

**CHARACTERISATION OF  
MESOSTRUCTURED FILMS AND SINGLE  
ZEOLITE NANOSHEETS**

A thesis submitted to the University of Manchester for  
the degree of Doctor of Philosophy in the Faculty of Science  
& Engineering

**2018**

**Shiyu Xu**

**School of Chemistry**

Table of Contents

|  |           |
|--|-----------|
| <b>TABLE OF CONTENTS</b> .....   | <b>2</b>  |
| <b>LIST OF ABBREVIATIONS</b> .....   | <b>5</b>  |
| <b>ABSTRACT</b> .....  | <b>6</b>  |
| <b>DECLARATION</b> .....   | <b>7</b>  |
| <b>COPYRIGHT STATEMENT</b> .....   | <b>8</b>  |
| <b>ACKNOWLEDGEMENTS</b> .....  | <b>9</b>  |
| <b>CHAPTER 1: INTRODUCTION</b> .....   | <b>10</b> |
| 1.1 AIMS .....   | 11        |
| 1.2. EARLY DISCOVERIES .....   | 11        |
| 1.3. MESOPOROUS MATERIALS .....  | 12        |
| <i>1.3.1. Synthesis, Characteristics and Mechanism of Ordered Mesoporous Materials</i> ..... | 13        |
| 1.3.1.1 Surfactant .....   | 13        |
| 1.3.1.2. The Interaction between Inorganics and Organics .....                               | 14        |
| 1.3.1.3 Synthesis Mechanism .....  | 15        |
| 1.3.1.4. Effective Packing Parameter: $g$ .....  | 17        |
| <i>1.3.2. Structure and Synthesis of Mesoporous Silica</i> .....                             | 19        |
| 1.3.2.1. 2D Hexagonal Structure: MCM-41 .....  | 19        |
| 1.3.2.2. 2-D Hexagonal Structure: SBA-15 .....   | 24        |
| 1.3.2.3. Cubic Channel Mesostructures: MCM-48 .....  | 27        |
| 1.3.2.4. Cubic Channel Mesostructures: SBA-16 .....  | 29        |
| 1.4. ZEOLITES .....  | 33        |
| <i>1.4.1. Structural Building Units of Zeolites</i> .....                                    | 33        |
| <i>1.4.2. Two-Dimensional Zeolites</i> .....   | 35        |
| <i>1.4.3. Structure and Synthesis of Two-Dimensional Zeolites</i> .....                      | 36        |
| 1.4.3.1. MWW family .....  | 36        |
| 1.4.3.2. MFI family .....  | 38        |
| 1.4.3.3. UTL family .....  | 39        |
| 1.5. REFERENCE .....   | 39        |
| <b>CHAPTER 2 ANALYTICAL TECHNIQUES</b> .....   | <b>45</b> |
| 2.1. X-RAY DIFFRACTION .....   | 46        |
| 2.2. ATOMIC FORCE MICROSCOPY .....   | 51        |
| 2.3. GAS ADSORPTION .....  | 54        |
| 2.4. SCANNING ELECTRON MICROSCOPY .....  | 59        |
| 2.5. REFERENCES .....  | 62        |
| <b>CHAPTER 3: PAPERS</b> .....   | <b>64</b> |
| PAPER 1: DIRECT VISUALIZATION OF MESOSTRUCTURED FILMS FORMING AT THE MICA-SOLUTION           |           |

|  |            |
|--|------------|
| INTERFACE .....  | 66         |
| PAPER 2. MECHANICAL EXFOLIATION OF NANOPOROUS MATERIALS .....                                      | 89         |
| PAPER 3. ENCAPSULATION OF PLATINUM NANO-CLUSTERS WITHIN EXFOLIATED ZEOLITE MFI NANOSHEETS.....     | 126        |
| <b>CHAPTER 4: SYNTHESIS AND CHARACTERIZATION OF MESOPOROUS MATERIALS.....</b>                      | <b>145</b> |
| 4.1. INTRODUCTION .....  | 146        |
| 4.2. SYNTHESIS AND CHARACTERIZATION OF MESOPOURS POWDER .....                                      | 146        |
| 4.2.1 Powder Synthesis: MCM-41 .....   | 146        |
| 4.2.1.1. Experimental .....  | 146        |
| 4.2.1.2. Result and Discussion .....   | 147        |
| 4.2.2. Powder Synthesis: MCM-48 .....  | 148        |
| 4.2.2.1. Experimental .....  | 148        |
| 4.2.2.2. Result and Discussion .....   | 149        |
| 4.2.3. Powder Synthesis: SBA-15.....   | 150        |
| 4.2.3.1. Experimental .....  | 150        |
| 4.2.3.2. Result and Discussion .....   | 151        |
| 4.2.4. Powder Synthesis: SBA-16.....   | 152        |
| 4.2.4.1. Experimental .....  | 152        |
| 4.2.4.2. Result and Discussion .....   | 152        |
| 4.3. SYNTHESIS AND CHARACTERIZATION OF MESOPOURS THIN FILMS .....                                  | 154        |
| 4.3.1. Thin Films Synthesis: FI27.....   | 154        |
| 4.3.1.1. Experimental .....  | 155        |
| 4.3.1.2. Result and Discussion .....   | 157        |
| 4.3.2. Thin Films Synthesis: CTAB.....   | 161        |
| 4.3.2.1. Experimental .....  | 161        |
| 4.3.2.2. Result and Discussion .....   | 163        |
| 4.4. CONCLUSIONS .....   | 167        |
| 4.5. REFERENCES .....  | 168        |
| <b>CHAPTER 5: ULTRA-THIN ZEOLITE MFI MEMBRANE AND PT-CONTAINING ALUMINOSILICATE NANOWIRES.....</b> | <b>169</b> |
| 5.1. FURTHER GROWTH OF EXFOLIATED MFI NANOSHEETS .....   | 170        |
| 5.1.1. Preparation of Multi-lamellar Zeolite MFI.....  | 170        |
| 5.1.2. Further Growth of Exfoliated MFI Nanosheets .....   | 175        |
| 5.1.2.1. Further Growth Experimental section .....   | 175        |
| 5.1.2.2. Atomic Force Microscopy .....   | 176        |
| 5.1.3. Future Work .....   | 181        |
| 5.2. PT-CONTAINING ALUMINOSILICATE NANOWIRES.....  | 182        |
| 5.2.1. Preparation of Pt-containing aluminosilicate Nanowires.....                                 | 182        |
| 5.2.2. Results and Discussion.....   | 183        |
| 5.2.2.1. XRD analysis of as-synthesized Pt-containing nanowires.....                               | 183        |
| 5.2.2.2. SEM analysis of as-synthesized Pt-containing nanowires.....                               | 184        |
| 5.2.2.3. N <sub>2</sub> adsorption isotherm of Pt-containing nanowires .....                       | 186        |
| 5.2.2.4. TEM analysis of Pt-containing MFI nanowires.....  | 186        |

---

|   |            |
|---|------------|
| 5.2.3. <i>Future Work</i> .....                         | 190        |
| 5.3. REFERENCE .....                                    | 190        |
| <b>CHAPTER 6 CONCLUSIONS AND FUTURE WORK</b> .....      | <b>192</b> |
| 6.1. CONCLUSION .....                                   | 193        |
| 6.2. FUTURE WORK .....                                  | 195        |
| <b>APPENDIX: LIST OF CONFERENCE PRESENTATIONS</b> ..... | <b>196</b> |

Word Count: 37165

## List of Abbreviations

ADOR - assembly-disassembly-organization-reassemble

AFM - atomic force microscopy

CMC- critical micelle concentration

CTAB - cetyltrimethylammonium bromide

EDX - energy dispersive x-ray spectroscopy

FFT - Fast Fourier transform

GID - grazing incidence diffraction

GISAXS - grazing-incidence small-angle x-ray scattering

HAADF-STEM - high-angle annular dark field scanning transmission electron microscopy

IUPAC - International Union of Pure and Applied Chemistry

LCT - liquid-crystal templating

NPs - nanoparticles

PBUs - the primary building units

PXRD - powder x-ray diffraction

SAXS - small-angle x-ray scattering

SBUs - the secondary building units

SEM - scanning electron microscopy

SPM - scanning probe microscopy

STM - scanning tunneling microscopy

TBOS – tetrabutyl orthosilicate

TEM - transmission electron microscopy

TEOS - tetraethyl orthosilicate

TMOS – tetramethyl orthosilicate

XRD - x-ray diffraction

## Abstract

Shiyu Xu

The University of Manchester

Doctor of Philosophy

Characterisation of Mesostructured Films and Single Zeolite Nanosheets

31/01/2018

Thin nanoporous films are attractive for many potential uses for example gas separation, catalysis, filtration of viruses, ore flotation, or as low-dielectric-constant materials. Zeolite and mesoporous materials are the two important nanoporous material classes. In this thesis, we synthesized and characterized two different thin nanoporous films; (i) mesostructured films at the mica-solution interface; (ii) mechanical exfoliated zeolites.

The mesoporous materials are well-defined pore size and size, and exhibit various morphologies, such as thin films, etc. In contrast, zeolites are a kind of perfect crystal and the morphologies are strongly related to their structures and are difficult to control.

Therefore, first we synthesis mesostructured films at mica-solution interface in acidic solution. *In-situ* Atomic Force Microscopy (AFM) has been used to reveal the formation process of organic and inorganic mesophase films at the molecular level.

Then, we synthesized two-dimensional zeolite structures *via* mechanical exfoliation process that does not involve any chemical intervention and can be applicable to a wide variety of structures with different chemical makeup. Three different zeolite structure nanosheets related to the structure code MWW, UTL, and MFI have been prepared. AFM and TEM have been used to characterized the exfoliated single nanosheet.

In order to broaden the application of the single zeolite nanosheet, platinum nano-clusters are encapsulated within mechanical exfoliated zeolite MFI nanosheets by ion exchange from aqueous solution of  $[\text{Pt}(\text{NH}_3)_4](\text{NO}_3)_2$ . High-angle annular dark field scanning transmission electron microscopy has been used to indicate the Pt clusters in the zeolite MFI structures.

Because of the property of the mechanically as-synthesised exfoliated MFI nanosheets that is the long hydrocarbon chains are essentially intact on both sides of the inorganic layer, and can prevent thickening of the zeolite MFI nanosheets along b-axis, we use the mechanically exfoliated MFI as seeds for further growth to form large scale MFI membrane with uniform nano-thickness.

Encapsulating noble metals within the channels or cavities of zeolites has already drawn numerous attentions because the well-defined zeolite structure is able to constrain the metal nanoparticle (NPs) aggregation size and enhance the diversity and activity for catalysis. We use the organic surfactant ( $\text{C}_{22-6-6}\text{Br}_2$ ) and  $[\text{Pt}(\text{NH}_3)_4](\text{NO}_3)_2$  as the structure and metal precursor to form Pt-containing nanowires; and use  $\text{F}^-$  to inhibit the premature precipitation of Pt precursors. After involving  $\text{F}^-$ , the Pt-containing nanowire structures were generated.

## **Declaration**

No portion of the work referred to in this thesis has been submitted in support of an application for another degree or qualification of this or any other university or other institute of learning.

## Copyright Statement

- i. The author of this thesis (including any appendices and/or schedules to this thesis) owns certain copyright or related rights in it (the “Copyright”) and s/he has given The University of Manchester certain rights to use such Copyright, including for administrative purposes.
- ii. Copies of this thesis, either in full or in extracts and whether in hard or electronic copy, may be made only in accordance with the Copyright, Designs and Patents Act 1988 (as amended) and regulations issued under it or, where appropriate, in accordance with licensing agreements which the University has from time to time. This page must form part of any such copies made.
- iii. The ownership of certain Copyright, patents, designs, trademarks and other intellectual property (the “Intellectual Property”) and any reproductions of copyright works in the thesis, for example graphs and tables (“Reproductions”), which may be described in this thesis, may not be owned by the author and may be owned by third parties. Such Intellectual Property and Reproductions cannot and must not be made available for use without the prior written permission of the owner(s) of the relevant Intellectual Property and/or Reproductions.
- iv. Further information on the conditions under which disclosure, publication and commercialisation of this thesis, the Copyright and any Intellectual Property and/or Reproductions described in it may take place is available in the University IP Policy (see <http://documents.manchester.ac.uk/DocuInfo.aspx?DocID=24420>), in any relevant Thesis restriction declarations deposited in the University Library, The University Library’s regulations (see <http://www.library.manchester.ac.uk/about/regulations/>) and in The University’s policy on Presentation of Theses.



## Acknowledgements

Firstly, I would like to thank my supervisor Professor Michael Anderson for his constant help and support throughout my PhD. Thank you also for allowing me the opportunity to attend many conferences and complete this research for your guidance.

I want to thank Dr. Christopher Muryn for his assistance with SAXS, AFM, Dr. Inigo Vitorica-yrezabal for help with PXRD, and Dr. John Waters for training with SEM. I would like to thank Dr. Barbara Gore for the support on the solid-state NMR. Thank you, Mr. Matthew Smith for training with TEM. My sincere thanks also go to Dr. Sarah Haigh and Dr. Eric Prestat for helping with TEM experiments and the TEM discussions.

I want to thank all the members of the Centre of Nanoporous Materials (CNM) for practical assistance and their friendship and moral support.

I would like to thank my family for supporting me spiritually throughout my studies.

---

## **Chapter 1: Introduction**

---

# 1. Introduction

## 1.1 Aims

One aim of this project was to synthesise thin nanoporous films in two different ways: (i) by surfactant-inorganic molecule self-assembling at mica surfaces in aqueous solutions; (ii) by mechanical exfoliation of hierarchical zeolites. The second aim was to directly visualize the mesostructured films forming at the mica-solution interface by AFM and investigate whether it is possible to produce two-dimensional zeolite structures *via* mechanical exfoliation process. A further aim was to encapsulate platinum clusters within exfoliated zeolite nanosheets.

## 1.2. Early Discoveries

Natural zeolites were discovered in 1756 by A.F. Cronstedt.<sup>1</sup> In the middle of the 20<sup>th</sup> century, the properties and applications of the natural zeolites have been further understood. R. Barrer synthesised the first low Si/Al ratio zeolites in hydrothermal conditions in 1948,<sup>2</sup> which laid the foundation of the great leap of zeolite industry and science. In 1992, scientists in Mobil Corporation utilized quaternary ammonium cationic surfactants as templates to synthesise a new family of mesoporous molecular sieves known as the M41S family,<sup>3</sup> this stimulated the rapid development of mesoporous materials.

The common characteristic of nanoporous materials is having regular and uniform porous structures, including the size and shape of pores and windows, the dimension of the pores, the direction of pores, the composition and properties of the walls. The size of the pores is the most important characteristic of the porous structures. According to the classification of IUPAC,<sup>4</sup> porous materials have three main categories, depending on their pore diameters, micropore (<2 nm), mesopore (2-50 nm), macropore (>50 nm).

### 1.3. Mesoporous Materials

The development of ordered mesoporous materials began in the 1980s by pillaring clays.<sup>5</sup> However, their pores could not be fully opened and that lead to coking in catalytic processes. In 1992, Japanese scientists and Mobil scientists successfully synthesized and characterised M41S family of silica/alumino silicate mesoporous molecular sieves, and proposed the liquid-crystal templating, LCT mechanism, for the formation of these materials.<sup>3,6,7</sup> To date, a tremendous research effort was put into the syntheses and applications of mesoporous materials. The structures (2D-hexagonal, space group  $P6mm$ , 2D-tetragonal  $C2mm$ , 3D-hexagonal  $P6_3/mmc$ , 3D-cubic  $Pm\bar{3}n$ ,  $Im\bar{3}m$ ,  $Fd\bar{3}m$ ,  $Fm\bar{3}m$ ,  $Pm\bar{3}m$ ,  $Ia\bar{3}d$ , *etc.*) and compositions (silica,<sup>8</sup> carbons,<sup>9</sup> and platinum,<sup>10</sup> germanium<sup>11,12</sup>, *etc.*) of these materials are extended and also many shortcomings have been overcome. Various systems and synthesis pathways for ordered mesoporous materials have been reported, but the core principle is still the sol-gel method. The sol-gel method is using surfactants as the template to form the ordered mesoporous materials with pore sizes in the range 2-50 nm. The synthesis media has a wide pH range from very acid to very basic. The synthesis temperature is from lower than room temperature to  $\sim 150$  °C and the surfactant may be cationic, anionic, nonionic, or amphoteric.<sup>13,14</sup>

The order mesoporous materials have many excellent properties, which other porous materials, such as amorphous materials or zeolites do not have. These properties include: highly ordered pore or channel structure system at nanometer level; well defined pore shape and size; various structure, wall composition and properties, mesoporous shape; high thermal and hydrothermal stability, if properly treated; various inorganics composition; high surface area and porosity; various controllable regular morphologies at different scale; having micropores in the wall, *etc.* The last but not the least distinct advantage of the order mesoporous materials over zeolites, is the ability of synthesise large thin films.

Having a high surface area and a large pore volume is a great advantage of the ordered mesoporous materials. Simultaneously, although the amorphous wall has some shortcomings, such as low hydrothermal stability, low catalytic acid strength, it has some special advantages, such as low limit to the structures (pores channels, windows), controllable structures at nanometer, easy doping. A distinct advantage of mesoporous materials over microporous materials such as zeolites, is the ability of synthesis of large thin films.

### 1.3.1. Synthesis, Characteristics and Mechanism of Ordered Mesoporous Materials

The mesoporous molecular sieves are obtained by organic template molecules, inorganic precursors, solvent, and an acid or base catalyst. The organic molecules or supramolecules such as biomacro molecules or amphiphilic surfactants, self-assemble from organic structures to organic templates. The most used templates are surfactants, which have one hydrophilic head group and one hydrophobic tail. The hydrophilic parts like water, which are the outer region of the micelle (contact water). And the hydrophobic parts do not like water, which are the internal region of the micelle (do not contact water). The inorganic network is generated by sol-gel chemistry. Driven by van der Waals forces, weak noncovalent bonds (hydrogen bonds), and electrovalent bonds between the surfactants and inorganic species, the ordered mesostructures was formed by assembly of organic-inorganic. Mesoporous materials can be obtained after the removal of surfactants. The common way to remove surfactants is calcination at high temperature or extraction with a solvent.

#### 1.3.1.1 Surfactant

The quaternary cationic surfactant  $C_nH_{2n+1}N(CH_3)_3Br$  ( $n=8-22$ ) is a typical surfactant and has been used efficiently in commercially synthesis of ordered mesoporous materials. The phase diagram of the system water/hexadecyltrimethyl ammonium bromide ( $C_{16}TMAB$ ) at varying

temperature is shown in Figure 1.1. The diagram for  $C_{16}TMAB$  shows L, E, I, D, and S phases.<sup>15</sup> The structures of the liquid-crystal phase depend on the surfactant concentration and temperature. When the surfactant concentration is higher than the critical micelle concentration (CMC), the micelle is generated in the phase L. As the surfactant concentration increases, first hexagonal phase E forms, then cubic phase I forms, at last lamellar phase D forms.

Other surfactants have the similar liquid-crystal phase behavior. They follow the same succession of phases, but the sizes of the phase range are different, even disappearing or forming new phases.

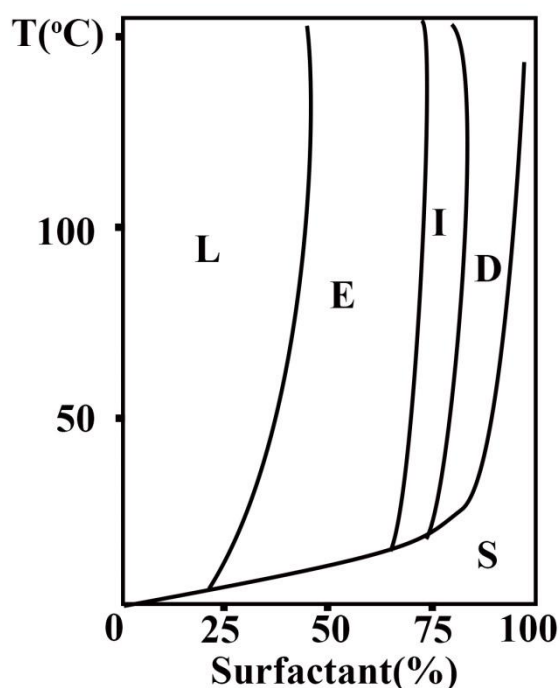


**Figure 1.1:** Phase diagrams of the system water/ $C_{16}TMAB$  at varying temperature. L is solution phase; E, I, and D represent hexagonal, cubic phase, and lamellar liquid crystalline phase, respectively; S is the undissolved surfactant solid.<sup>15</sup>

### 1.3.1.2. The Interaction between Inorganics and Organics

A large number of studies have been focused on the interaction between organics and inorganics, which is the key point of formation of mesoporous materials.<sup>16, 17</sup> Stucky has proposed the cooperative self-assembly to form

mesostructures based on four interaction routes between inorganic-organic species, which are  $S^+I^-$ ,  $S^-I^+$ ,  $S^+X^-I^+$ , and  $S^-X^+I^-$  ( $S^+$  is cationic surfactant;  $S^-$  is anionic surfactant;  $I^+$  is cationic inorganic precursor;  $I^-$  is anionic inorganic precursor;  $X^+$  is cationic counterions; and  $X^-$  is anionic counterions).<sup>18, 19</sup> Figure 1.2. depicts the four synthesis routes. In route 1, the anionic inorganic species ( $I^-$ ) match with the cationic surfactant ( $S^+$ ) through Coulomb forces, and the prototypic example is the synthesis of MCM-41. Route 2 is a similar to route 1, but  $S^-I^+$  interaction occurs. The surfactant and the inorganic precursor with the same charge are also possible. In route 3, the mesoporous materials synthesise by a  $S^+X^-I^+$  interaction, where  $X^-$  can be halogen ions ( $Cl^-$ ,  $Br^-$ ), etc. Route 4 can be described as the interaction of  $S^-X^+I^-$ , where  $X^+$  is  $Na^+$ ,  $K^+$ , etc.

According to this route prediction, various new mesoporous materials have been synthesized and new combinations of inorganic-organic species have been discovered.

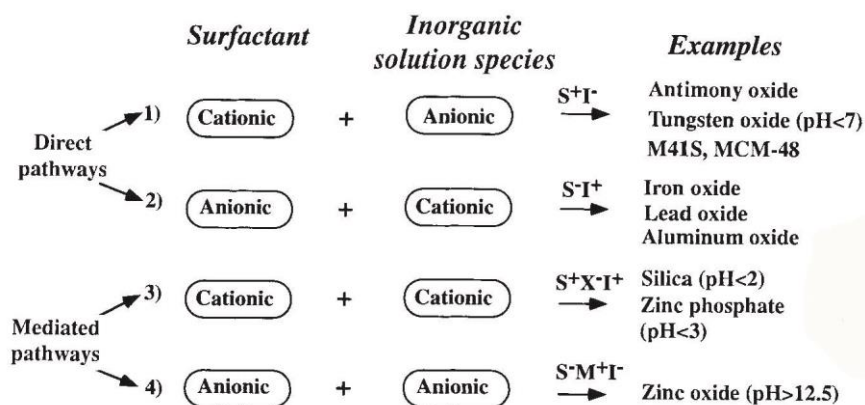


**Figure 1.2:** Synthesis routes for the self-assemble reaction of different inorganics precursors and surfactants.<sup>19</sup>

### 1.3.1.3 Synthesis Mechanism

Elaborate investigations have been carried out on the formation mechanism. However, the formation mechanism of mesoporous materials has not been fully understood. Here we give three synthesis mechanisms. They can explain the synthesis mechanism is some specific conditions.

In order to explain the synthesis mechanism of MCM-41, the Mobil's scientists proposed the 'liquid-crystal templating (LCT)' mechanism.<sup>3</sup> This

mechanism consists of the structures of hexagonal arrangement are pre-existing, then the inorganic silicate form around these to produce the final structure, finally the mesoporous materials obtained by removing the templates, for instance by calcination.(Figure 1.3.)

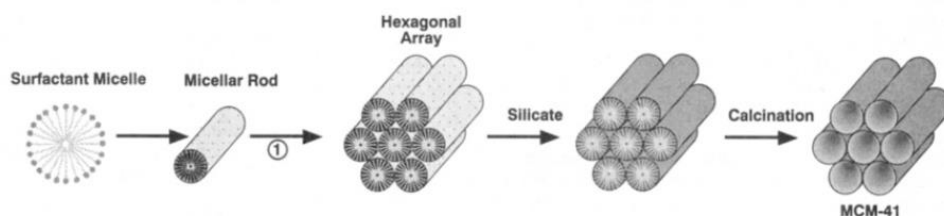


**Figure 1.3:** Liquid-crystal templating (LCT) mechanism.<sup>20</sup>

Davis and co-workers suggested the 'silicate rod assembly' mechanism. (see Figure 1.4.) The isolated surfactant micellar rods were covered by two or three monolayers. Then the silicate rods were randomly ordered, and eventually pack into the low energy structure - a hexagonal mesostructure.<sup>20, 21</sup>

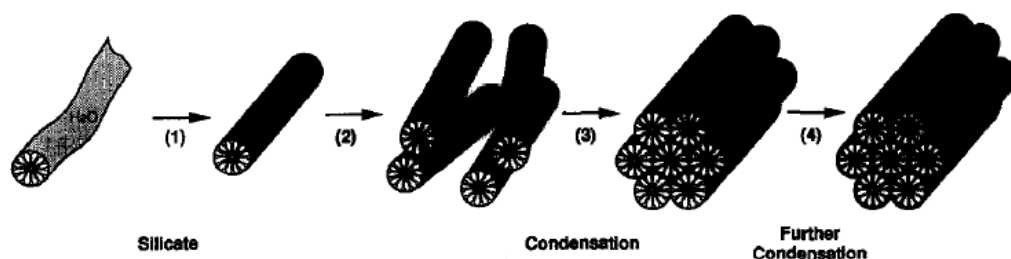


**Figure 1.4.** Davis's mechanism for the formation of MCM-41.<sup>21</sup>

The 'Charge-density matching mechanism' was postulated by Monnier and co-workers.<sup>22</sup> They gave a free energy formula:

$$\Delta G = \Delta G_{\text{inter}} + \Delta G_{\text{wall}} + \Delta G_{\text{intra}} + \Delta G_{\text{sol}} \quad (1.1)$$

where  $\Delta G_{\text{inter}}$  reflects the van der Waals forces and electrostatic effects associated with the interaction between inorganic walls and surfactant micelles.

$\Delta G_{\text{wall}}$  accounts for the structural free energy of inorganic frameworks.

$\Delta G_{\text{intra}}$  is the van der Waals and conformational energy of the surfactant.

$\Delta G_{\text{sol}}$  represents the chemical potential associated with the species in the mother



liquid solution.

$\Delta G_{\text{sol}}$  can be considered as a constant in a given solution system. Hence, the interaction between inorganics and surfactant is the key factor, such as the charge-density matching. If the  $\Delta G_{\text{inter}}$  is more negative, the assembly process can be more easily proceed.

#### 1.3.1.4. Effective Packing Parameter: $g$

The important question of the researcher in mesoporous materials is how to mathematically relate the molecular size, charge, and shape of surfactants, bonding energies, and morphology. Israelachvili and co-workers proposed the local effective surfactant packing parameter,  $g = V/a_0l$ <sup>23</sup>, to describe the classical and contemporary molecular description of surfactant organization in liquid-crystal arrays, where  $V$  is the total volume of the surfactant chains plus any co-covalent organic molecules between the chains,  $a_0$  is the effective head-group area at the micelle surface, including the charge and size on the surfactant hydrophilic head-group, and  $l$  is the kinetic surfactant tail length or the curvature elastic energy. The interface surface-bending energy can be written in terms of  $g$ , the actual surfactant packing parameter adopted by the aggregating chains in the phase.<sup>24</sup> The counterion in this classical model is not explicitly included.<sup>25</sup> In classical micelle chemistry, as the  $g$  value increases above critical values, mesophase transitions occur. Table 1.1 shows the relationship of the packing parameter  $g$  and the mesophase. These transitions reflect a decrease in surface curvature from cubic ( $Pm\bar{3}n$ ) through lamellar. For surfactant to associate in a spherical structure, the surface area occupied by the surfactants' polar head-group should be large. If the head-groups are permitted to pack tightly, on the other hand, the aggregation number will increase, and rod or lamellar packing will be favored. The values  $g$  (between  $\frac{1}{3}$  and  $\frac{1}{2}$ ) for  $P6mm$  and (between  $\frac{1}{2}$  and  $\frac{2}{3}$ ) for  $Ia\bar{3}d$  (cubic) depend upon the volume fraction of surfactant chains.<sup>25</sup>

In real synthesis processes, except the general reaction parameters and

conditions which can influence the LCT, (e.g., temperature, concentration, ion strength, pH, *etc.*) there are two main factors to affect the surfactant effective packing parameter,  $g$ . (1) The interactions between surfactant and inorganic species, such as charge density matching. (2) Charge, composition, surfactant molecular shape, and surfactant structure.

Block copolymer surfactants cannot be described with an effective packing parameter,  $g$ , as the simple surfactant, but can use the ratio of the hydrophilic part and hydrophobic part to give a description.<sup>26</sup> For example, different mesostructures can be obtained by varying the PEO fraction ( $x$  from 50 to 61), when the PPO fraction keeps similar in the triblock copolymer surfactants ( $\text{EO}_x\text{-PO}_y\text{-EO}_x$ ).<sup>27</sup> The number of EO units increase, equivalently the increasing of the head-group area,  $a_0$ , and a result of the decreasing of the packing parameter,  $g$ . The short EO chains ( $x=4$ , L101) surfactants can produce the lamellar structure. The medium-length EO chains ( $x=17$ , P103;  $x=27$ , P104;  $x=37$ , P105) can produce the hexagonal structure (SBA-15). And the long EO chains ( $x=132$ , F108) can produce the cubic structure (SBA-16). Figure 1.5 summarizes the transition from lamellar to 2-D hexagonal, 3-D hexagonal, and cubic symmetries as the size of hydrophilic EO head-group increases, when nonionic amphiphilic block copolymers blends were used as templates.<sup>28</sup>

**Table 1.1:** Relationship of the packing parameter  $g$  and mesophase

| Packing parameter $g$              | Mesophase                           |
|------------------------------------|-------------------------------------|
| $g < \frac{1}{3}$                  | Cubic ( $Pm\bar{3}n$ , $P6_3/mmc$ ) |
| $g = \frac{1}{3} \sim \frac{1}{2}$ | Hexagonal ( $P6mm$ )                |
| $g = \frac{1}{2} \sim \frac{2}{3}$ | Cubic ( $Ia\bar{3}d$ )              |
| $g = 1$                            | Lamellar                            |

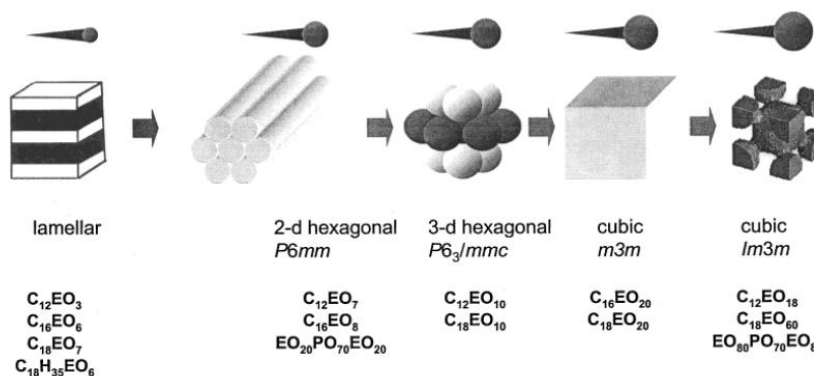


**Figure 1.5:** Suggested synthesis results with the nonionic surfactants.<sup>28</sup>

### 1.3.2. Structure and Synthesis of Mesoporous Silica

Silica materials are the most extensively researched area, because of properties of silica such as the tetrahedral structure flexibility, high thermal stability, easy modification, easy control of hydrolysis and polymerization. In addition, various natural structures, such as diatoms, is mainly composed by amorphous silica.

#### 1.3.2.1. 2D Hexagonal Structure: MCM-41

Figure 1.6 shows the 2D hexagonal symmetry (space group)  $P6mm$ .<sup>29</sup> The materials belonging to the 2D hexagonal symmetry are honeycomb arrays of



**Figure 1.6:** Pore models of mesostructures with symmetries of ( $P6mm$ ).<sup>29</sup>

hexagonally close packed channels. They are most easily produced, the classical products: MCM-41, SBA-15, SBA-3, *etc.*

The first reported of the synthesis of MCM-41 in the early of 1990s, by the scientists in the former Mobil Corporation,<sup>3, 6</sup> utilized the  $C_{16}H_{33}N(CH_3)_3Cl$  as template in a basic solution. The resulting mixture was placed in a static

---

autoclave at 150 °C for 48 h. The surfactant was removed by calcining at 540 °C for 1 h in flowing nitrogen, than in flowing air for 6 h. The cell parameter (~4 nm) was obtained from XRD and TEM.

The pore size for MCM-41 is adjustable in the range of 1.5~5 nm by varying of the alkylchain length of the surfactant molecules.<sup>30</sup> They also can be controlled by using the large head-group cationic surfactants, such as alkyltriethylammonium cations,<sup>25</sup> and certain auxiliary expander molecules, such as trialkylbenzenes.<sup>31,32</sup> The large pore size (4~10 nm) can be obtained by swelling surfactant micelle with organic molecules, such as aromatic hydrocarbons, alkanes, trialkylamines, and alkyldimethylamines.<sup>33</sup>

The 2D hexagonal structure for MCM-41 pore system is clear, but the shape of the channel is not clear. It is often simply approximated as cylinders,<sup>34</sup> although some experiments indicated it could be hexagonal, cylindrical, or changing from hexagonal to cylindrical as the surfactant concentration increased.

MCM-41 can be obtained in a very wide reaction conditions. The synthesis temperature can be from lower than room temperature to high temperature (150 °C). The reaction time can be from a few minutes to several days. The reaction media can be from very basic to neutral.

Various organic silicon compounds, such as TEOS, TMOS, TBOS, and inorganic silicon compounds, such as amorphous silica, soluble silicate, can be used as the silicon resource. Quaternary cationic surfactants, C<sub>n</sub>TMAB, are the best template for synthesis MCM-41.

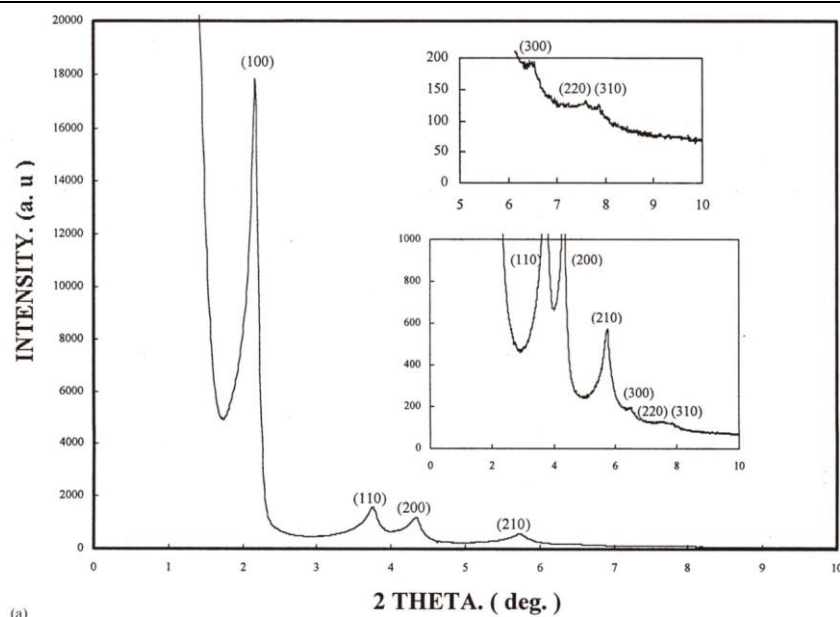


**Figure 1.7:** XRD patterns of the MCM-41 as-synthesis sample with extremely low surfactant concentration.<sup>35</sup>

The XRD pattern for a high-quality MCM-41 sample has more than four (hk0) diffraction peaks. Figure 1.7 shows XRD patterns of the MCM-41 as-synthesises sample, which exhibits a strong peak near  $2.26^\circ$ , and weak peaks around  $3.89$ ,  $4.50$ ,  $5.89$ ,  $6.70$ ,  $7.78$ ,  $8.10^\circ$ , respectively, corresponding to the diffraction of (100), (110), (200), (210), (300), (220) and (310).<sup>35</sup>

The high-resolution transmission electron microscopy (TEM) images of the calcined MCM-41 sample have been shown in Figure 1.8a and 1.8b. The uniform hexagonal arrangement of bright dots correspond to the straight channels of MCM-41 (see Figure 1.8a). The inset diffraction pattern of Figure 1.8a shows that the incident beam is along the [001] direction. There are slight differences between the brightness and the shape of the channels from different places, because of the slight change in diffraction conditions, which show a domain character. Note that all the TEM images are projected along the incident beam direction. Hence, in Figure 1.8 the projection of the pores along the [001] direction is the pore diameter value, but may be somewhat less than the actual value. The pore diameter which is calculated from Figure 1.8b, is uniformly about 3.2 nm. In principle, this value may be more reliable than the value

---

obtained from other methods, on the assumption that the channels are cylindrical. The TEM method requires appropriate data analysis method to avoid artifacts that can lead to an incorrect result.<sup>36</sup>

Gas adsorption is a prominent method for determining the specific surface area, pore volume, and pore size distribution as well as the surface properties for mesoporous solids. The typical MCM-41 adsorption isotherm belongs to the Type IV isotherm. (see Section 2.3.) For the high-quality MCM-41 sample, the pore size distribution is narrow, the surface area is higher than 1000 m<sup>2</sup>/g, and the pore volume is larger than 0.7 cm<sup>3</sup>/g.

Figure 1.9 shows the argon and nitrogen adsorption isotherms which were measured at 77 K for MCM-41 silicas with pores of diameter from 2.4-6.5 nm.<sup>37</sup> The same pattern of adsorption-desorption behavior is observed in both argon and nitrogen adsorbates case. Multilayer adsorption that takes place at the relative lower pressure, is followed by the capillary condensation gradually increasing with the pore diameter. The adsorption-desorption isotherm is reversible for the smaller pores. However, the hysteresis loop generates for the larger pores.<sup>25</sup> In the argon adsorption-desorption isotherms, the hysteresis loop disappears from the adsorption isotherm in the region corresponding to pore diameters between 3.2 and 3.5 nm. And in the nitrogen adsorption-desorption isotherms, the hysteresis loop disappears from the adsorption isotherm in the region corresponding to pores diameters between 3.9 and 4.2 nm, which is bigger than the argon one (see Figure 1.9).

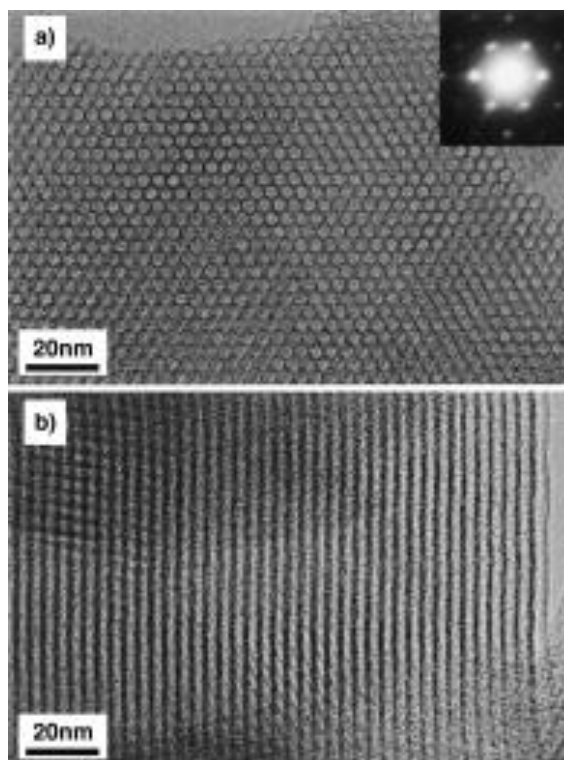


**Figure 1.8:** TEM images of calcined mesoporous MCM-41 along the channel direction (c axis; a) and perpendicular to it (b).<sup>36</sup>

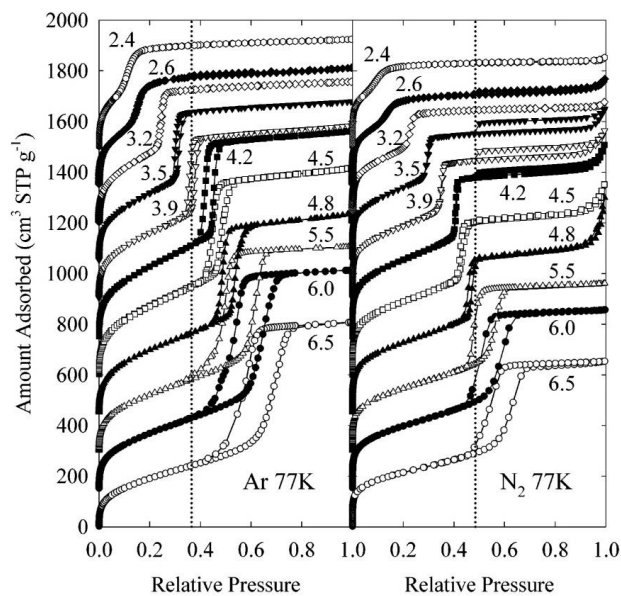


**Figure 1.9:** Argon and nitrogen adsorption-desorption isotherms measured at 77 K for a series of eleven MCM-41 silicas with approximately cylindrical pores of diameter 2.4-6.5 nm.<sup>37</sup>

## 1.3.2.2. 2-D Hexagonal Structure: SBA-15

The discovery of SBA-15 was one of the great breakthroughs in mesoporous materials synthesis.<sup>38</sup> SBA-15 is normally synthesized by using a poly (ethylene oxide) - poly (propylene oxide) - poly (ethylene oxide) (PEO-PPO-PEO) triblock copolymer as a structure directing agent under acidic synthesis system. The formation of SBA-15 is a  $(S^0H^+)(XI^+)$ . The triblock copolymer P123 would be the optimal template for SBA-15. The pore size from ~4 to 30 nm can be prepared by varying the synthesis composition and conditions, such as adding the swelling agent. Preparing with P123 at 40-100 °C would have the uniform pore sizes from ~6.5 to 10 nm. The small pore size can be prepared by Brij 56 ( $C_{16}H_{33}EO_{10}$ ). The silica wall (~3.1 to 4.8 nm) is much thicker than that of MCM-41. Therefore, it has higher thermal stability (>900 °C) and hydrothermal stability (to hot water) than MCM-41. The template can be removed by calcining at high temperature or extracting with a solvent.<sup>39</sup>

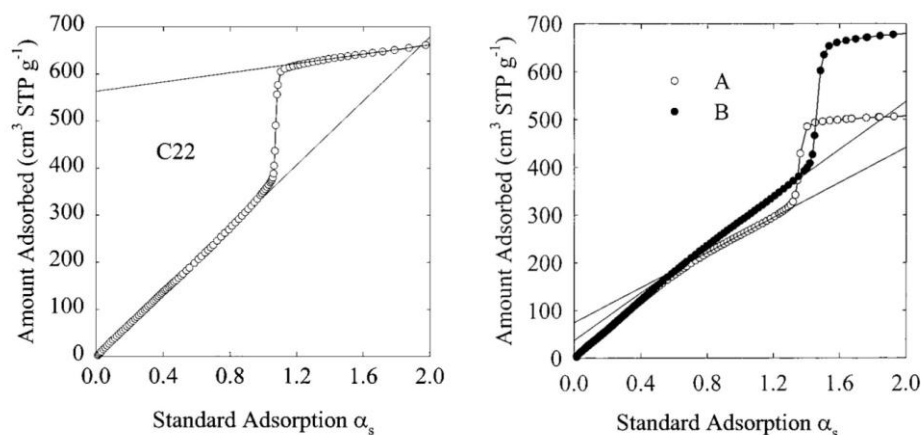


**Figure 1.10:**  $\alpha_s$ -plot for the calcined MCM-41 ( $C_{22}$ TMA as template) (left)<sup>40</sup> and  $\alpha_s$ -plots for calcined SBA-15 (sample A heated at 353 K for 1 day, sample B heated at 373 K for 2 days) (right).<sup>41</sup>

Another feature of a typical SBA-15 is the significant number of disordered micropore system in its framework (the wall for the mesopore).<sup>39</sup> The micropore volume is about  $0.1 \text{ cm}^3/\text{g}$ . This microporosity is the result from the insertion of hydrophilic PEO fingers of the template into the silica wall. Ryoo confirmed



the existence of the micropores in SBA-15 mesoporous silica wall, by successfully synthesising the stable mesoporous carbon by using SBA-15 as template.<sup>42</sup> SBA-15 sample shows a Type H1 hysteresis loop.<sup>43</sup> Figure 1.10 shows the difference between MCM-41 and SBA-15 adsorption results.<sup>41</sup> The  $\alpha_s$ -plot of MCM-41 at the relative low pressure range exhibits excellent linearity, and starting from their origin. That provided the evidence of the absence of any detectable amounts of micropores. The upward deviation at the higher pressure was generated by capillary condensation in mesopores. Other typical MCM-41 samples (using  $C_n$ TMA as template) give the similar results. The initial parts of the  $\alpha_s$ -plot for SBA-15 exhibits nonlinearity, which provide the evidence of the presence of micropores, and non steps, which indicates the broad pore size distributions in the micropore/small-mesopore range. In Figure 1.10 right the microporous volume of sample A is 0.12 cm<sup>3</sup>/g, and the microporous volume of sample B is 0.06 cm<sup>3</sup>/g. The template within both micropores and mesopores can be removed stepwise.<sup>44</sup>

Both mesopores and micropores of SBA-15 can be adjustable by the various synthesis conditions and post-synthesis treatment.<sup>45</sup> And the microporosity of SBA-15 can be retained, even after calcination at 900 °C, but probably disappearing at 1000 °C. At low synthesis temperature, the pore wall is too thick for the micropore to connect the adjacent mesopores. As the increasing of the synthesis temperature, the pore size increases and the thickness of the pore wall decreases. When the synthesis temperature is high, the micropores disappear, but the secondary mesopores bridging the main channels still occur. This is because of the influence of temperature on hydrophilicity of PEO. A hydrophilicity of PEO decreases with the increasing of the temperature. The decrease of micropores can also be obtained by the post-synthesis hydrothermal treatment. (Fig. 1.11)

Fan<sup>46</sup> developed a method to form a 3D SBA-15 material with the average mesostructure still being hexagonal  $P6mm$ , by high temperature and introducing TMB into the embryo of SBA-15 mesostructured. In Figure 1.12, the four

diffraction peaks can be observed and assigned to 100, 110, 200, and 210 reflections similar to those typical SBA-15. The cell parameter ( $a=13.0$  nm) for calcined 3D SBA-15 prepared with TMB is much larger than the typical SBA-15 ( $a=10.4$  nm). And it has many large connections (2-8 nm), which are randomly distributed as evidenced by TEM images. (see Figure 1.13) Figure 1.14 gives a description of the pore structure.

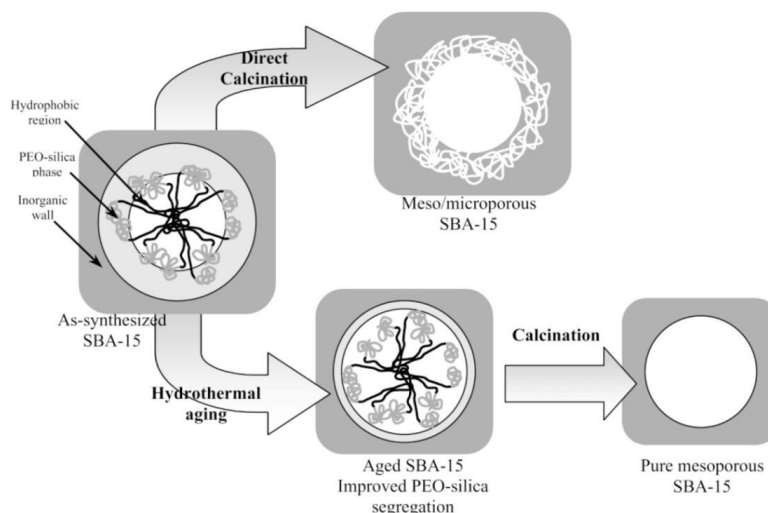


**Figure 1.11:** The effect of hydrothermal treatment on SBA-15 pore system.<sup>47</sup>

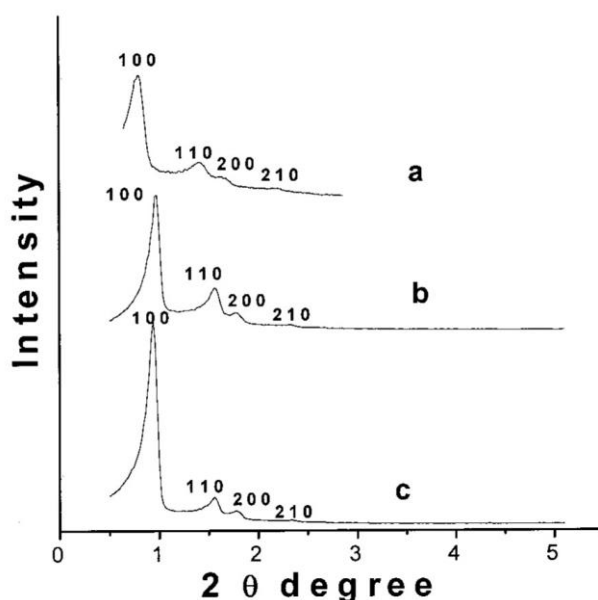


**Figure 1.12:** XRD pattern of calcined 3D mesoporous SBA-15 prepared at 403 K (a) with TMB, (b) without TMB, and (c) conventional SBA-15 prepared at 373 K.<sup>46</sup>

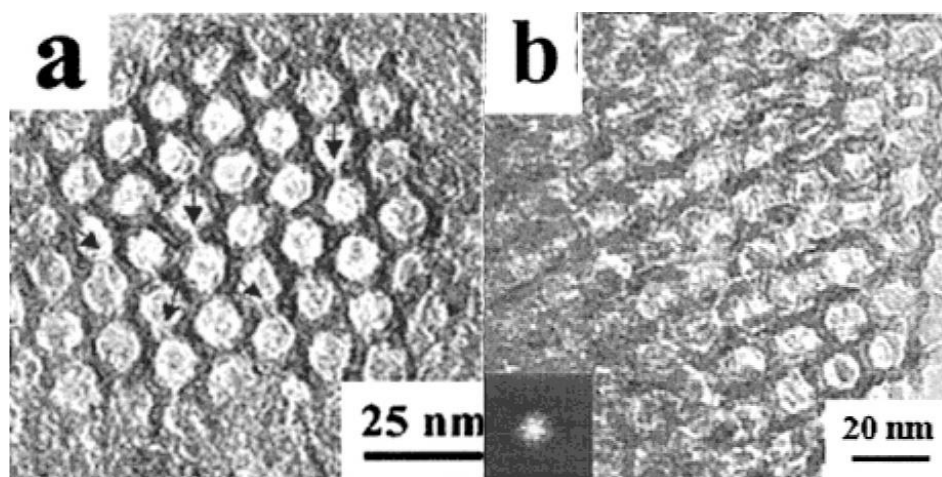


**Figure 1.13:** TEM images of calcined mesoporous SBA-15 prepared at 403 K along [100] directions. (a) without TMB, (b) with TMB.<sup>46</sup>

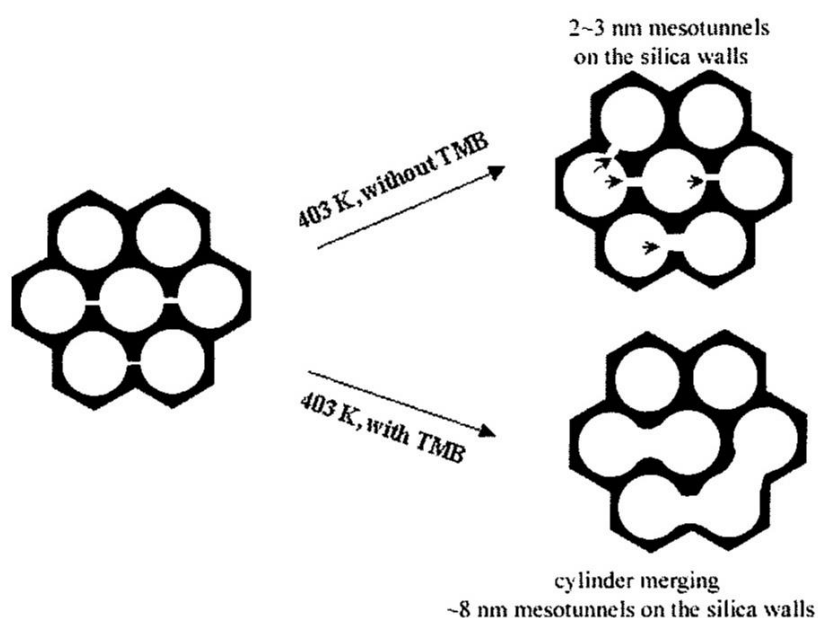


**Figure 1.14:** The description of the 3D Mesoporous SBA-15 pore structure.<sup>46</sup>

### 1.3.2.3. Cubic Channel Mesostructures: MCM-48

MCM-48 was first proposed by Monnier *et al.*<sup>22</sup> The structure of MCM-48 is bicontinuous cubic ( $Ia\bar{3}d$ ), (see Figure 1.15) which is wrapped by silica wall and defined by a so-called minimal surface, periodic G-surface, the gyroid. That means the space of MCM-48 was divided by the minimal surface into two enantiomeric separated 3D helical pore systems. The structure factors have been studied by powder X-ray pattern and high-resolution electron microscopy (HREM) images.

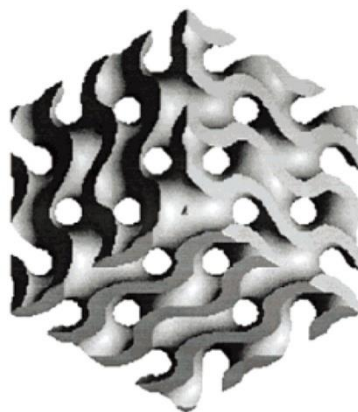


**Figure 1.15:** Pore models of mesostructures with symmetries of  $(Ia\bar{3}d)$ .<sup>48</sup>

Figure 1.16 shows the synchrotron XRD pattern (wavelength 0.17 nm) of as-made MCM-48.<sup>25</sup> (The unit cell  $a = 9.7$  nm) Figure 1.17 shows the TEM image of MCM-48 along [111] direction.<sup>22</sup> The sample was synthesised with quaternary cationic surfactants,  $C_{16}TACl$  at 100 °C. Figure 1.18 shows the adsorption-desorption isotherm of nitrogen of MCM-48 at different temperatures.<sup>49</sup> The sorption isotherms belong to Type IV, and the narrow pore size distribution at about 2 nm. The wall thickness is 0.8 nm, and the disordered micropores which were found to form interconnections between two main channels is about 0.5 to 0.8 nm.

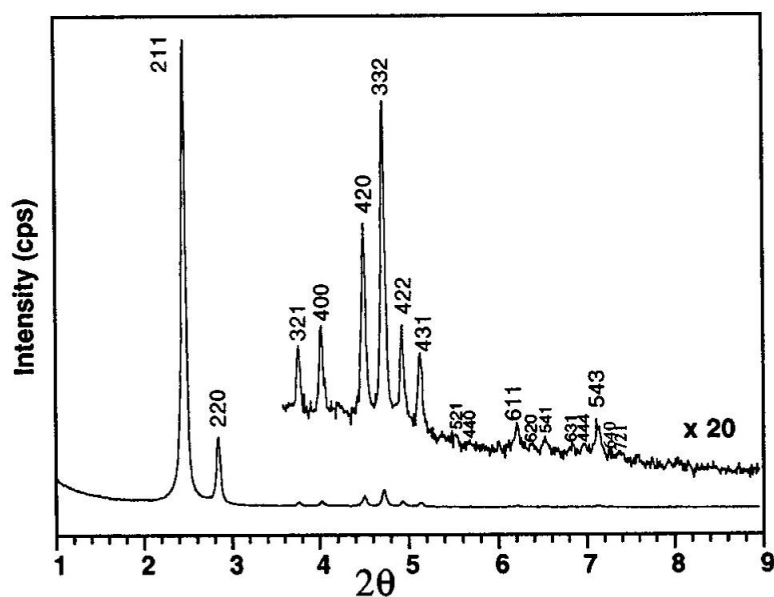


**Figure 1.16:** Synchrotron XRD pattern of as-made MCM-48.<sup>25</sup>

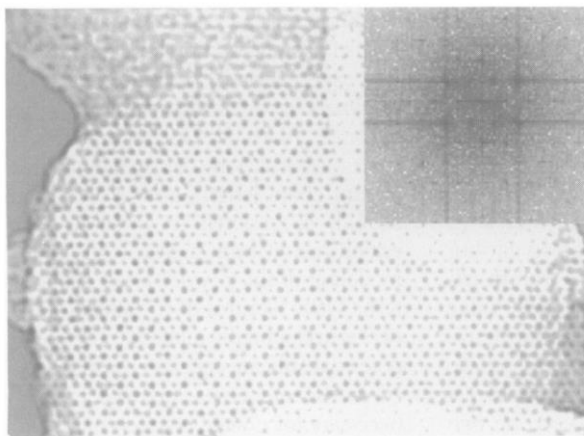


**Figure 1.17:** TEM image of MCM-48 viewed along its [111] axis.<sup>22</sup>

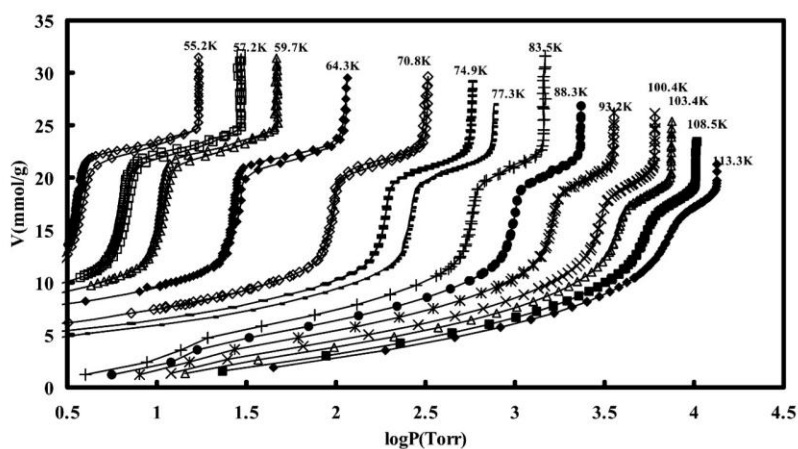


**Figure 1.18:** The adsorption-desorption isotherm of MCM-48 at different temperature.<sup>49</sup>

As one member of the M41S mesoporous family, the synthesis of MCM-48 is more difficult than MCM-41. In order to get a high quality MCM-48, the volume of the hydrophobic part which is near the head of the surfactant should be increased and the effective surfactant packing parameter,  $g$ , should be between  $1/2$  and  $2/3$ .

#### 1.3.2.4. Cubic Channel Mesostructures: SBA-16

Most mesoporous materials have 3D cage type pores. They have the same packing method, which is the close packing of cages (spheres, sphere-like, polyhedrons). Each cage has 12 cages as next neighbors, and they are interconnected via a window (or short channel).

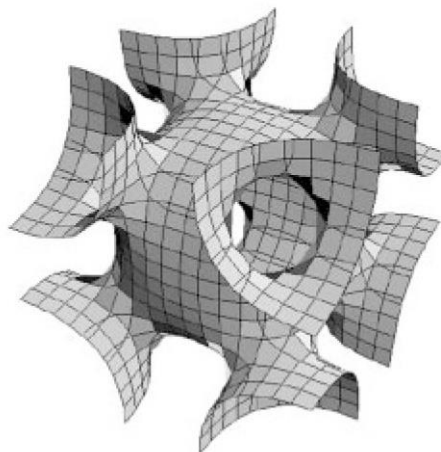


**Figure 1.19:** Pore models of mesostructures with symmetries of  $(Im\bar{3}m)$ .<sup>50</sup>

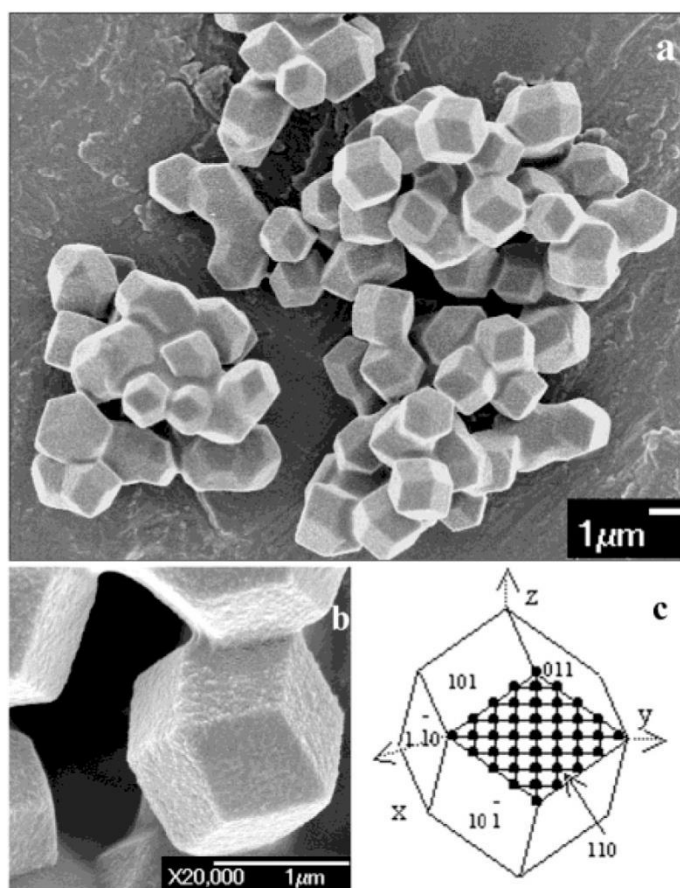


**Figure 1.20:** SEM images of mesoporous SBA-16: (a) at low magnification; (b) at high magnification; (c) index of a rhombicuboctahedron model, the mesopore array in  $xy$  plane is demonstrated.<sup>51</sup>

The SBA-16 mesostructure was described as the body-centered cubic symmetrical packing of spherical cages ( $Im\bar{3}m$ ).<sup>52</sup> (see Figure 1.19) Owing to the cage structure of SBA-16, the triblock copolymers with high PEO chains, such as F127, F108, and F98, are the preferred template for SBA-16. SBA-16 is usually synthesised in an acidic medium at low concentration (0.5 M HCl) in which the silica source (TEOS or TMOS) has a comparatively slow precipitation rate.<sup>53</sup> The reaction temperature is about 35 °C. The high quality SBA-16 can be obtained with the aid of inorganic salts, KCl, NaCl, Na<sub>2</sub>SO<sub>4</sub>, K<sub>2</sub>SO<sub>4</sub>, *etc.*, and hydrothermal treatment at 85-100 °C.<sup>54</sup>

Figure 1.20 shows the SEM of mesoporous SBA-16 single crystal synthesized with F108 at 38 °C with 0.5 mol/L K<sub>2</sub>SO<sub>4</sub>. All of these particles have the shape of a rhombododecahedron, consisting of 12 well-defined crystal faces. These 12 faces can be indexed to planes.

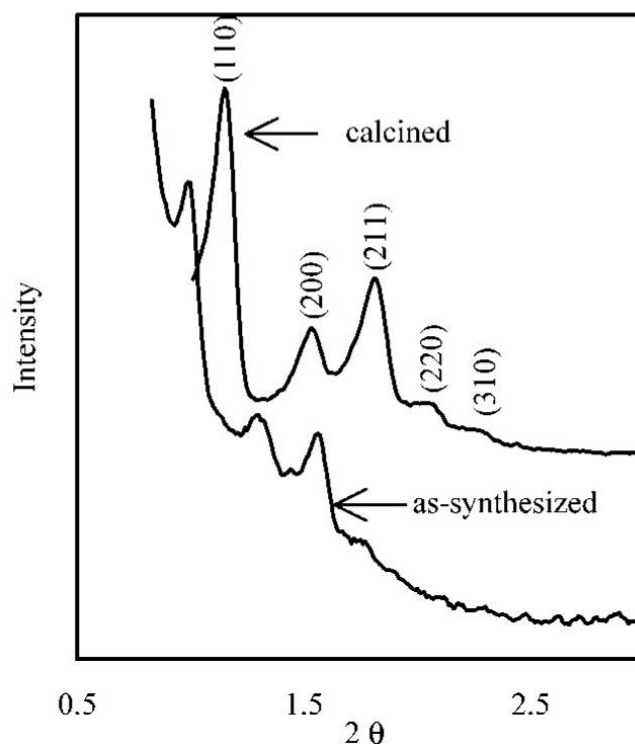


**Figure 1.21:** XRD patterns of as-synthesised and calcined mesoporous SBA-16.<sup>51</sup>

Figure 1.21 shows the XRD patterns of as-synthesised and calcined

mesoporous single crystals synthesised with F108 and 0.5 mol/L  $K_2SO_4$  at 38 °C. The as-synthesised powders show four well-resolved XRD peaks, which are indexed to the 110, 200, 211, and 220 diffraction peaks of  $Im\bar{3}m$  structure. The intensity of these peaks is much stronger after calcination. And the cell parameters  $a$ , are 13.7 nm and 11.6 nm for as-synthesised and calcined samples, respectively.<sup>51</sup> Figure 1.22 shows the nitrogen adsorption-desorption isotherm of SBA-16. The sorption isotherms belong to Type IV, and the hysteresis loop at the relative pressure between 0.4 and 0.5 indicates that SBA-16 has a cage structure. The BET surface area is 750 m<sup>2</sup>/g, and the pore size is 7.8 nm, and the pore volume is 0.52 cm<sup>3</sup>/g.<sup>51</sup>

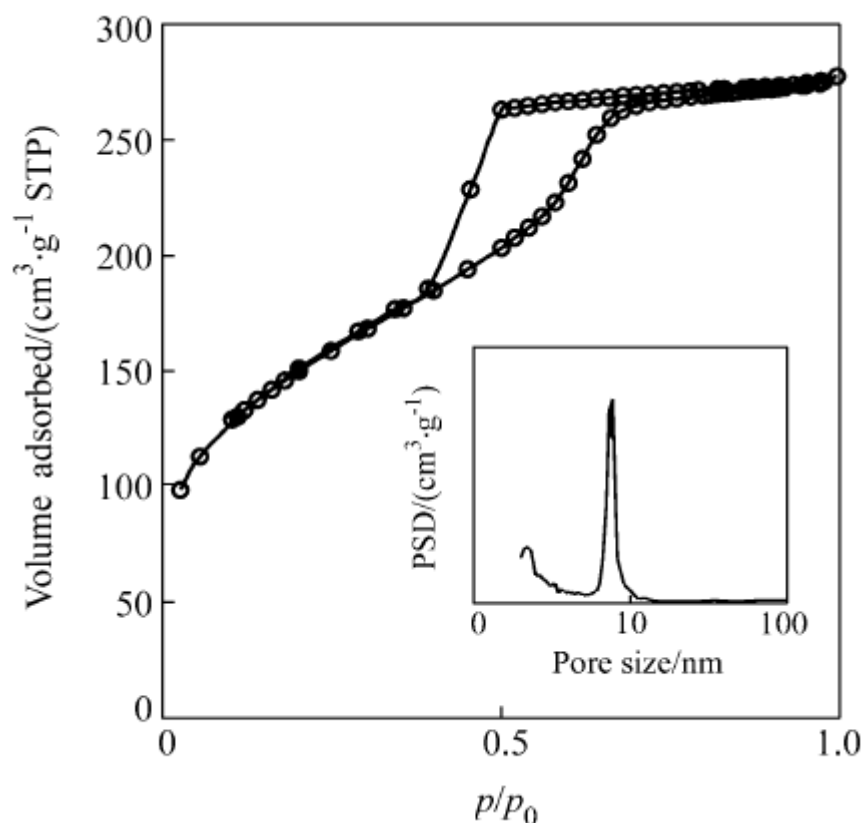


**Figure 1.22:** The nitrogen adsorption-desorption isotherm of SBA-16.<sup>51</sup>

The cage diameter and pore entrance size of SBA-16 silica which has  $Im\bar{3}m$  structure can be tailored using several synthesis strategies. Figure 1.23 illustrates the changes in SBA-16 structure brought about by increasing the hydrothermal treatment time or temperature, and by changing the relative ratios



of different copolymers in the copolymer mixture used as template.<sup>55</sup>

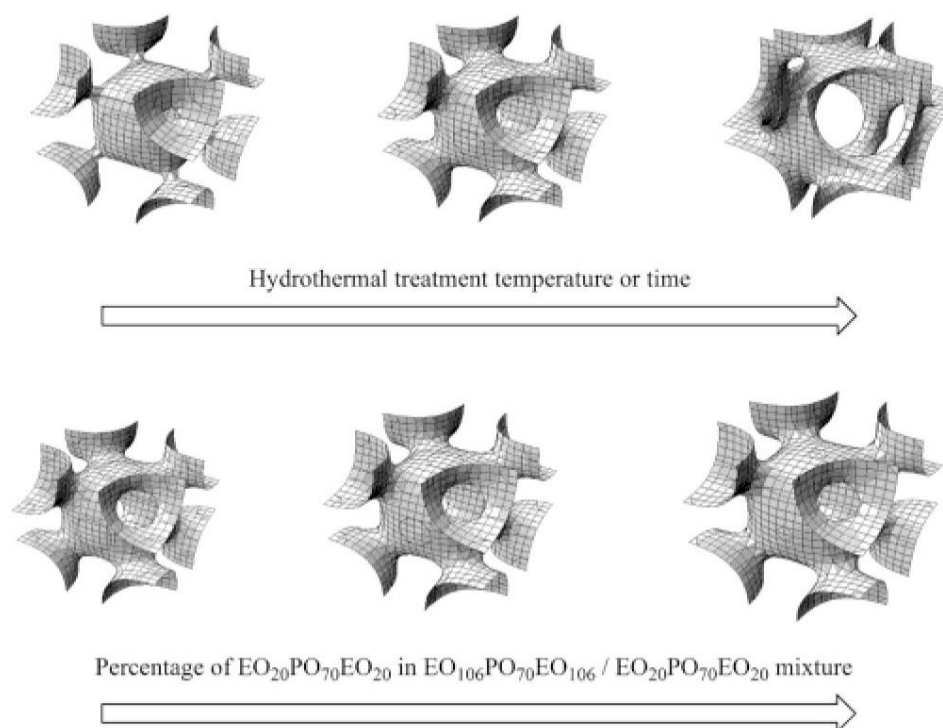


**Figure 1.23:** Illustration of changes in SBA-16 structure brought about by different synthesis strategies.<sup>55</sup>

## 1.4. Zeolites

### 1.4.1. Structural Building Units of Zeolites

Zeolites, which belong to the microporous group, are crystalline aluminosilicate polymorphs with three-dimensional frameworks that contain pores and cavities (*ca.* 3-15Å).<sup>56</sup> The 3D frameworks consist of  $TO_4$  (T=Si and Al). These  $[SiO_4]$  or  $[AlO_4]$  tetrahedra are the primary building units (PBUs) of the zeolite framework. In some cases, other T atoms, such as Ti, P, are also incorporated in the zeolite framework. In the zeolite framework, each T atom is coordinated to four oxygen atoms, and each oxygen atom is bridged to two T atoms. The aluminosilicate zeolite that is constructed with  $[SiO_4]$  and  $[AlO_4]$  tetrahedra carries a negative charge, which must be compensated by positively

charged cations. These cations along with intra-zeolite water are located in the channels and cages.<sup>57</sup> The aluminosilicate zeolite framework obeys Löwenstein rules, which states that two Al atoms cannot be adjacent to avoid Al-O-Al linkages and unfavourable charge-charge interactions.<sup>58</sup>

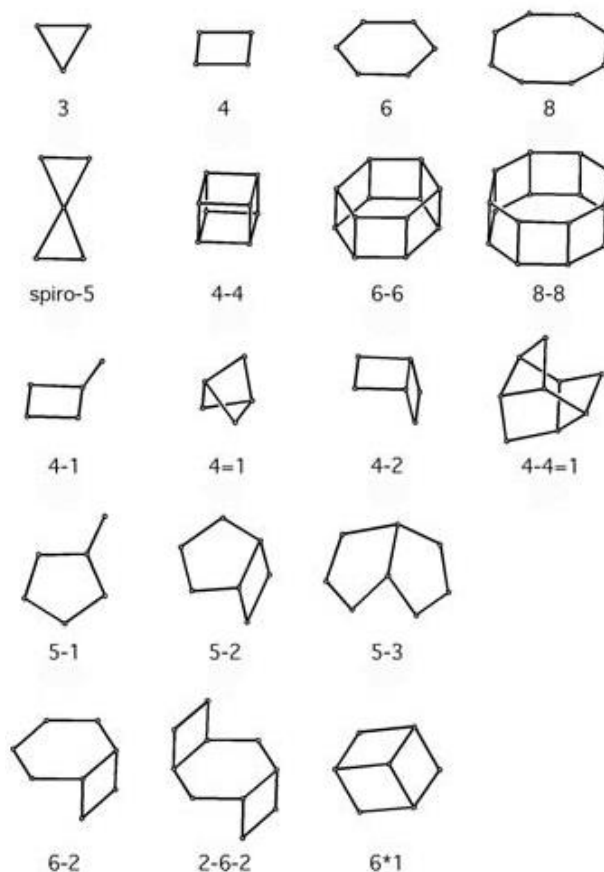


**Figure 1.24:** Secondary building units in zeolites.<sup>59</sup>

The secondary building units (SBUs) can be used to describe the zeolite framework. Figure 1.24 shows 16 kinds of SBUs that have been found in zeolite structures.<sup>59</sup> Each of the vertices represents a T atom and the oxygen atom between the two adjacent T-atoms has been omitted. The SBUs are only the theoretical topological building units, and they are not the existed species during the crystallization of zeolites. According to the Structural Commission of the International Zeolite Association, there are now 227 different framework structures have accepted and named as a unique three-letter code.<sup>60</sup>

### 1.4.2. Two-Dimensional Zeolites

In the traditional view, zeolites are crystalline solids with continuous bonding and extend to three-dimensional frameworks.<sup>61, 62</sup> However, zeolites contain one, two, or three-dimensional systems of channels which are interconnected in different ways. The two dimensional zeolites also contain the similar pores and cavities with the 3D zeolite structure. In principle, all zeolites can yield a 2D solid. However, so far 16 zeolite frameworks have been found to produce two-dimensional forms.<sup>63</sup>

**Table 1.2** Zeolites with known layered or 2D forms

|            |            |            |            |
|------------|------------|------------|------------|
| <b>AFO</b> | <b>AST</b> | <b>CAS</b> | <b>CDO</b> |
| <b>FER</b> | <b>HEU</b> | <b>MFI</b> | <b>MTF</b> |
| <b>MWW</b> | <b>NSI</b> | <b>OKO</b> | <b>PCR</b> |
| <b>RRO</b> | <b>RWR</b> | <b>SOD</b> | <b>UTL</b> |

At present, there are three different strategies to synthesise primary 2D zeolite materials.(Fig. 1.25)<sup>61</sup> The first is the hydrothermal synthesis of a layered precursor to produce 2D zeolites (MWW family). The second is a surfactant templated synthesis (MFI family). The third is a transformation from 3D to 2D (UTL family).

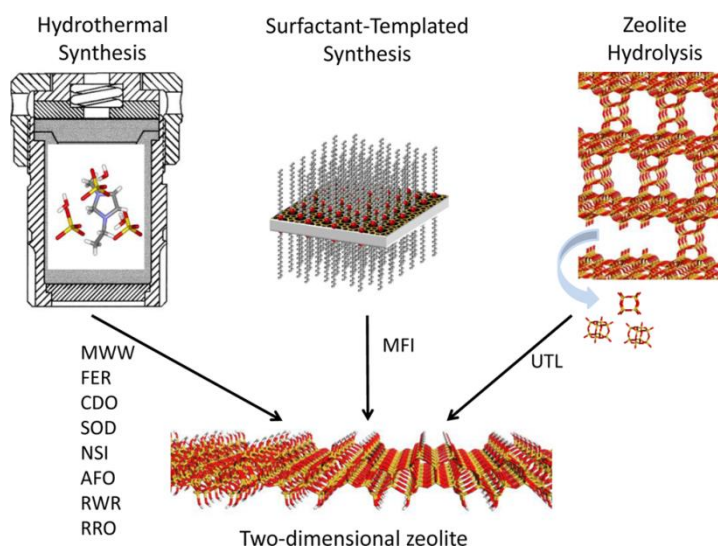


**Figure 1.25:** Schematic representation of possible routes to synthesise 2D zeolites: hydrothermal synthesis, surfactant-templated synthesis and zeolite hydrolysis.<sup>61</sup>

---

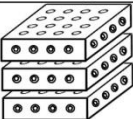
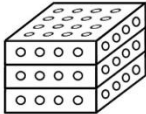
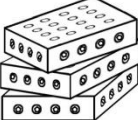
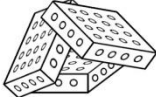
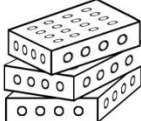
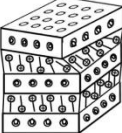
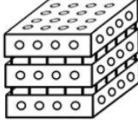
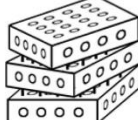
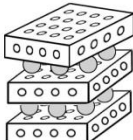
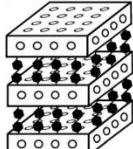
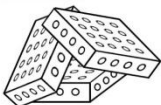
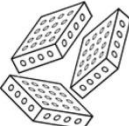
### 1.4.3. Structure and Synthesis of Two-Dimensional Zeolites

#### 1.4.3.1. MWW family

MWW is a structure code that corresponds to a family of materials that can be layered in nature depending upon the synthesis pathway. The fully connected three-dimensional borosilicate structure is known as MCM-22<sup>64</sup>, however, prior to complete condensation of the three-dimensional structure an ordered layer precursor, MCM-22P, is made which can be swollen and is suitable for pillaring.<sup>65</sup>

Normally, MCM-22P can be used as the onset materials to synthesis other MWW materials.(Fig. 1.25).<sup>61</sup> For example, the layers of MCM-22P can be separated by a post-synthesis treatment in nitric acid to make MCM-56P that results in a highly disorganized layering that prevents recondensation of the fully connected MWW framework.<sup>66</sup> After calcination of MCM-22P, the fully connected 3D structure MCM-22 is produced. In Fig. 1.26, the materials MCM-22P, MCM-22, EMM-10P, and MCM-56 can be obtained by direct synthesis, and the other eight zeolite materials only can be obtained by post-synthetic modifications.

MCM-22P nanosheets have the uniform thickness of each layer is 2.5 nm, and stack repeating about 0.2 nm greater than the 3D framework (MCM-22). Each layer corresponds to a single unit cell dimension along the c-axis ( $c=2.51980$  nm). The layers are interconnected via hydrogen bonding between silanol groups, with hexadecyltrimethyl ammonium chloride between the layers. Therefore, MCM-22P can be swollen with hexadecyltrimethyl ammonium chloride to produce MCM-22P SW. After swollen, the thickness of each layer increases to 5.1 nm.

| Layer ordering  | Type of material                      | Material Name   |
|---|---------------------------------------|-----------------|
|    | Ordered (multi)-layered precursor     | MCM-22P         |
|    | 3D Framework                          | MCM-22          |
|    | Disordered (multi)-layered precursor  | EMM-10P         |
|    | Mono-layer delaminated                | MCM-56          |
|    | Detemplated sub-zeolite               | MCM-56 analogue |
|    | Swollen precursor                     |                 |
|   | Stabilized ordered precursor (IEZ)    | IEZ-MWW         |
|  | Stabilized disordered precursor (IEZ) | EMM-12          |
|  | Pillared zeolite                      | MCM-36          |
|  | Organic pillared zeolite              | MCM-22-BETB     |
|  | Delaminated swollen precursor         | ITQ-2           |
|  | Colloidal suspension                  |                 |

**Figure 1.26:** Schematic representation of corresponding zeolite materials obtained from MCM-22P.<sup>61</sup>

## 1.4.3.2. MFI family

MFI is the structure code for the aluminosilicate zeolite ZSM-5<sup>67</sup> and the pure silica end-member known as silicalite<sup>68</sup>. As such it represents one of the most important structures for catalysis with ZSM-5, and its Ti-substituted cousin TS-1<sup>69</sup>, being used for a multitude of heterogeneous catalytic transformations. The crystals have a three-dimensional pore structure consisting of 10-tetrahedral atom rings to give a pore dimension of ca. 0.65 nm.

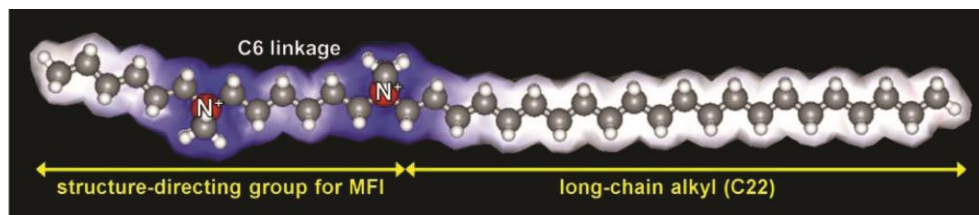


**Figure 1.27:** The schematic structure of the surfactants.<sup>70</sup>

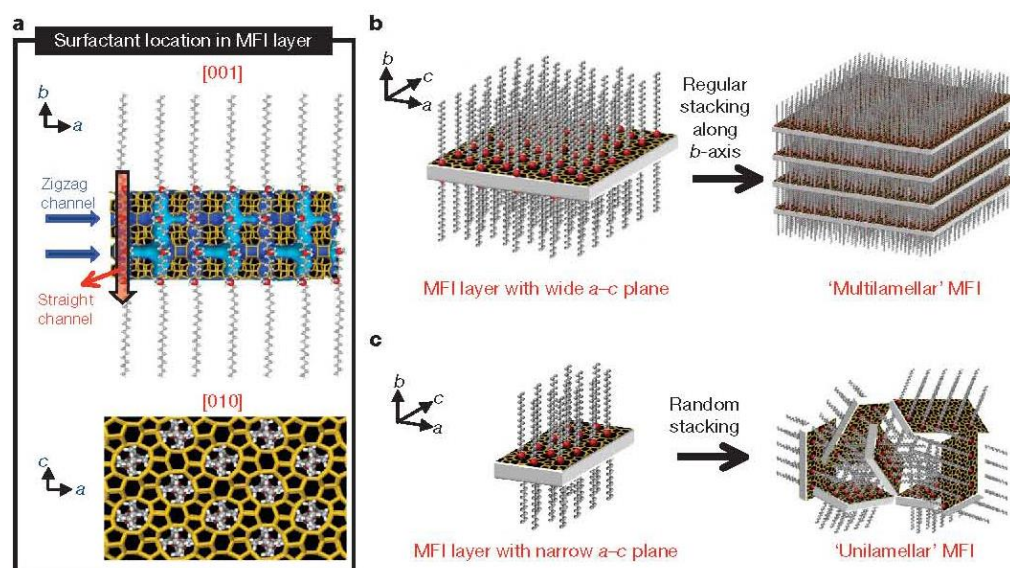


**Figure 1.28:** Use of a surfactant molecule with head-group that templates the MFI structure and long surfactant tail that separates the two-dimensional sheets. MFI nanosheets can form either in an ordered stacking structure along  $b$ -axis or a randomly stacking unilamellar structure.<sup>70</sup>

Ryoo's work has been to successfully synthesise the multilamellar zeolite MFI with 1.5 unit cell MFI nanosheets assembled along the  $b$ -axis generated by using di-quaternary ammonium surfactants ( $C_{22-6-6}Br_2$ ) with head-group that templates the MFI structure and long hydrocarbon chain that forms a lamellar

mesophase.<sup>70</sup> The schematic structure of the surfactants ( $C_{22-6-6}Br_2$ ) has been shown in Fig. 1.27, and can be identified by proton NMR.

Fig. 1.28 shows the single MFI nanosheet structure model. The disordered MFI nanosheets with large volume can be synthesized in a specific condition, requiring  $C_{22-6-6}(OH)_2$  and high concentration of  $Na^+$ .

#### 1.4.3.3. UTL family

UTL is a germanosilicate with crystals constructed from ferrierite layers where the germanium is preferentially sited between the layers permitting the layers to be separated by a hydrothermal treatment that dissolves this germanate coupling, which is the bridging of D4R units. The resulting material is known as IPC-1P and this can be further swollen by intercalation of hexadecyltrimethyl ammonium chloride to produce IPC-1SW. The IPC-1SW can be used as the building unit to prepare the pillared material. After an organized step, the organic amines (the blue oval) are incorporated into the structure. Finally, the new zeolite IPC-2 (OKO topology) or IPC-4 (PCR topology) was generated. These process was name as assembly-disassembly-organization-reassembly (ADOR) process.

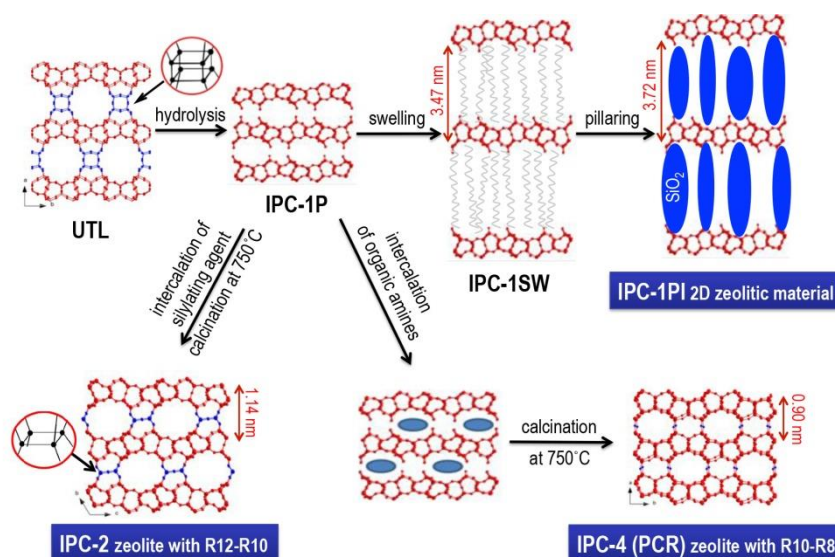


**Figure 1. 29:** ADOR process for preparation of zeolite UTL.<sup>71</sup>

## 1.5. Reference

- (1) Cronstedt, A. Natural Zeolite and Minerals. *Svenska Vetenskaps Akademiens Handlingar Stockholm* **1756**, 17, 120.
- (2) Barrer, R. M. Synthesis of a Zeolitic Mineral with Chabazite-like Sorptive Properties. *Journal of the Chemical Society* **1948**, 127-132.
- (3) Beck, J. S.; Vartuli, J. C.; Roth, W. J.; Leonowicz, M. E.; Kresge, C. T.; Schmitt, K. D.; Chu, C. T. W.; Olson, D. H.; Sheppard, E. W.; McCullen, S. B.; Higgins, J. B.; Schlenker, J. L. A New Family of Mesoporous Molecular Sieves Prepared with Liquid Crystal Templates. *Journal of the American Chemical Society* **1992**, 114, 10834-10843.
- (4) Corma, A. From Microporous to Mesoporous Molecular Sieve Materials and Their Use in Catalysis. *Chemical Reviews* **1997**, 97, 2373-2420.
- (5) Sing, K. S. W.; Everett, D. H.; Haul, R. A. W.; Moscou, L.; Pierotti, R. A.; Rouquerol, J.; Siemieniewska, T. Reporting Physisorption Data for Gas Solid Systems with Special Reference to the Determination of Surface Area and Porosity. *Pure And Applied Chemistry* **1985**, 57, 603-619.
- (6) Kresge, C. T.; Leonowicz, M. E.; Roth, W. J.; Vartuli, J. C.; Beck, J. S. Ordered Mesoporous Molecular Sieves Synthesized by a Liquid-crystal Template Mechanism. *Nature* **1992**, 359, 710-712.
- (7) Yanagisawa, T.; Shimizu, T.; Kuroda, K.; Kato, C. The Preparation of Alkyltriethylammonium–Kaneinite Complexes and Their Conversion to Microporous Materials. *Bulletin of the Chemical Society of Japan* **1990**, 63, 988-992.
- (8) Landskron, K.; Ozin, G. A. Periodic Mesoporous Dendrisilicas. *Science* **2004**, 306, 1529-1532.
- (9) Meng, Y.; Gu, D.; Zhang, F.; Shi, Y.; Yang, H.; Li, Z.; Yu, C.; Tu, B.; Zhao, D. Ordered Mesoporous Polymers and Homologous Carbon Frameworks: Amphiphilic Surfactant Templating and Direct Transformation. *Angewandte Chemie* **2005**, 117, 7215-7221.
- (10) Attard, G. S.; Bartlett, P. N.; Coleman, N. R. B.; Elliott, J. M.; Owen, J. R.; Wang, J. H. Mesoporous Platinum Films from Lyotropic Liquid Crystalline Phases. *Science* **1997**, 278, 838-840.
- (11) Armatas, G. S.; Kanatzidis, M. G. Mesostructured Germanium with Cubic Pore Symmetry. *Nature* **2006**, 441, 1122-1125.
- (12) Sun, D.; Riley, A. E.; Cadby, A. J.; Richman, E. K.; Korlann, S. D.; Tolbert, S. H. Hexagonal Nanoporous Germanium Through Surfactant-driven Self-assembly of Zintl Clusters. *Nature* **2006**, 441, 1126-1130.
- (13) Kim, A.; Bruinsma, P.; Chen, Y.; Wang, L.-Q.; Liu, J. Amphoteric Surfactant Templating Route for Mesoporous Zirconia. *Chemical Communications* **1997**, 161-162.
- (14) Zhang, Z.; Yan, X.; Tian, B.; Yu, C.; Tu, B.; Zhu, G.; Qiu, S.; Zhao, D. Synthesis of Ordered Small Pore Mesoporous Silicates with Tailorable Pore Structures and Sizes by Polyoxyethylene Alkyl Amine Surfactant. *Microporous and Mesoporous Materials* **2006**, 90, 23-31.
- (15) Wärnheim, T.; Jönsson, A. Phase Diagrams of Alkyltrimethylammonium Surfactants in Some Polar Solvents. *Journal of Colloid and Interface Science* **1988**, 125, 627-633.
- (16) Soler-Illia, G. J. A. A.; Crepaldi, E. L.; Grosso, D.; Durand, D.; Sanchez, C. Structural Control in Self-standing Mesostructured Silica Oriented Membranes and Xerogels. *Chemical Communications* **2002**, 2298-2299.
- (17) Ying, J. Y.; Mehnert, C. P.; Wong, M. S. Synthesis and Applications of Supramolecular-Templated Mesoporous Materials. *Angewandte Chemie International Edition*



1999, 38, 56-77.

- (18) Huo, Q. S.; Margolese, D. I.; Ciesla, U.; Demuth, D. G.; Feng, P. Y.; Gier, T. E.; Sieger, P.; Firouzi, A.; Chmelka, B. F.; Schuth, F.; Stucky, G. D. Organization of Organic-Molecules with Inorganic Molecular-Species into Nanocomposite Biphase Arrays. *Chemistry of Materials* **1994**, 6, 1176-1191.
- (19) Huo, Q.; Margolese, D. I.; Ciesla, U.; Feng, P.; Gier, T. E.; Sieger, P.; Leon, R.; Petroff, P. M.; Schuth, F.; Stucky, G. D. Generalized Synthesis of Periodic Surfactant/Inorganic Composite Materials. *Nature* **1994**, 368, 317-321.
- (20) Chen, C.-Y.; Burkett, S. L.; Li, H.-X.; Davis, M. E. Studies on Mesoporous Materials II. Synthesis Mechanism of MCM-41. *Microporous Materials* **1993**, 2, 27-34.
- (21) Chen, C.-Y.; Li, H.-X.; Davis, M. E. Studies on Mesoporous Materials. *Microporous Materials* **1993**, 2, 17-26.
- (22) Monnier, A.; Schüth, F.; Huo, Q.; Kumar, D.; Margolese, D.; Maxwell, R. S.; Stucky, G. D.; Krishnamurty, M.; Petroff, P.; Firouzi, A.; Janicke, M.; Chmelka, B. F. Cooperative Formation of Inorganic-Organic Interfaces in the Synthesis of Silicate Mesostructures. *Science* **1993**, 261, 1299-1303.
- (23) Israelachvili, J. N.; Mitchell, D. J.; Ninham, B. W. Theory of Self-assembly of Hydrocarbon Amphiphiles into Micelles and Bilayers. *Journal of the Chemical Society, Faraday Transactions 2: Molecular and Chemical Physics* **1976**, 72, 1525-1568.
- (24) Hyde, S. T. Interfacial Architecture in Surfactant Water Mixtures - Beyond Spheres, Cylinders and Planes. *Pure And Applied Chemistry* **1992**, 64, 1617-1622.
- (25) Huo, Q.; Margolese, D. I.; Stucky, G. D. Surfactant Control of Phases in the Synthesis of Mesoporous Silica-Based Materials. *Chemistry of Materials* **1996**, 8, 1147-1160.
- (26) Bates, F. S.; Fredrickson, G. H. Block Copolymers—Designer Soft Materials. *Physics Today* **1999**, 52, 32-38.
- (27) Kipkemboi, P.; Fogden, A.; Alfredsson, V.; Flodström, K. Triblock Copolymers as Templates in Mesoporous Silica Formation: Structural Dependence on Polymer Chain Length and Synthesis Temperature. *Langmuir* **2001**, 17, 5398-5402.
- (28) Kim, J. M.; Sakamoto, Y.; Hwang, Y. K.; Kwon, Y.-U.; Terasaki, O.; Park, S.-E.; Stucky, G. D. Structural Design of Mesoporous Silica by Micelle-Packing Control Using Blends of Amphiphilic Block Copolymers. *The Journal of Physical Chemistry B* **2002**, 106, 2552-2558.
- (29) Sun, J.; Zhang, H.; Ma, D.; Chen, Y.; Bao, X.; Klein-Hoffmann, A.; Pfander, N.; Su, D. S. Alkanes-Assisted Low Temperature Formation of Highly Ordered SBA-15 with Large Cylindrical Mesopores. *Chemical Communications* **2005**, 5343-5345.
- (30) Namba, S.; Mochizuki, A.; Kito, M., Preparation of Highly Ordered MCM-41 with Docosyltrimethylammonium Chloride (C22TMAC1) as A Template and Fine Control of Its Pore Size. In *Studies in Surface Science and Catalysis*, Bonneviot, L.; Bèland, F.; Danumah, C.; Giasson, S.; Kaliaguine, S., Eds. Elsevier: 1998; Vol. 117, pp 257-264.
- (31) Sayari, A.; Yang, Y. Highly Ordered MCM-41 Silica Prepared in the Presence of Decyltrimethylammonium Bromide. *The Journal of Physical Chemistry B* **2000**, 104, 4835-4839.
- (32) Galarneau, A.; Desplandier, D.; Dutartre, R.; Di Renzo, F. Micelle-Templated Silicates as A Test Bed for Methods of Mesopore Size Evaluation. *Microporous and Mesoporous Materials* **1999**, 27, 297-308.
- (33) Ulagappan, N.; Rao, C. N. R. Evidence for Supramolecular Organization of Alkane and Surfactant Molecules in the Process of Forming Mesoporous Silica. *Chemical Communications*

1996, 2759-2760.

- (34) Feuston, B. P.; Higgins, J. B. Model Structures for MCM-41 Materials: A Molecular Dynamics Simulation. *The Journal of Physical Chemistry* **1994**, *98*, 4459-4462.
- (35) Cai, Q.; Lin, W.-Y.; Xiao, F.-S.; Pang, W.-Q.; Chen, X.-H.; Zou, B.-S. The Preparation of Highly Ordered MCM-41 with Extremely Low surfactant Concentration. *Microporous and Mesoporous Materials* **1999**, *32*, 1-15.
- (36) Liu, Z.; Sakamoto, Y.; Ohsuna, T.; Hiraga, K.; Terasaki, O.; Ko, C. H.; Shin, H. J.; Ryoo, R. TEM Studies of Platinum Nanowires Fabricated in Mesoporous Silica MCM-41. *Angewandte Chemie International Edition* **2000**, *39*, 3107-3110.
- (37) Kruk, M.; Jaroniec, M. Argon Adsorption at 77 K as a Useful Tool for the Elucidation of Pore Connectivity in Ordered Materials with Large Cagelike Mesopores. *Chemistry of Materials* **2003**, *15*, 2942-2949.
- (38) Zhao, D.; Feng, J.; Huo, Q.; Melosh, N.; Fredrickson, G. H.; Chmelka, B. F.; Stucky, G. D. Triblock Copolymer Syntheses of Mesoporous Silica with Periodic 50 to 300 Angstrom Pores. *Science* **1998**, *279*, 548-552.
- (39) Rouquerol, J.; Avnir, D.; Fairbridge, C. W.; Everett, D. H.; Haynes, J. H.; Pernicone, N.; Ramsay, J. D. F.; Sing, K. S. W.; Unger, K. K. Recommendations for the Characterization of Porous Solids. *Pure And Applied Chemistry* **1994**, *66*, 1739-1758.
- (40) Kruk, M.; Jaroniec, M.; Sakamoto, Y.; Terasaki, O.; Ryoo, R.; Ko, C. H. Determination of Pore Size and Pore Wall Structure of MCM-41 by Using Nitrogen Adsorption, Transmission Electron Microscopy, and X-ray Diffraction. *The Journal of Physical Chemistry B* **2000**, *104*, 292-301.
- (41) Ryoo, R.; Ko, C. H.; Kruk, M.; Antochshuk, V.; Jaroniec, M. Block-Copolymer-Templated Ordered Mesoporous Silica: Array of Uniform Mesopores or Mesopore-Micropore Network? *The Journal of Physical Chemistry B* **2000**, *104*, 11465-11471.
- (42) Jun, S.; Joo, S. H.; Ryoo, R.; Kruk, M.; Jaroniec, M.; Liu, Z.; Ohsuna, T.; Terasaki, O. Synthesis of New, Nanoporous Carbon with Hexagonally Ordered Mesostructure. *Journal of the American Chemical Society* **2000**, *122*, 10712-10713.
- (43) Sayari, A.; Liu, P.; Kruk, M.; Jaroniec, M. Characterization of Large-Pore MCM-41 Molecular Sieves Obtained via Hydrothermal Restructuring. *Chemistry of Materials* **1997**, *9*, 2499-2506.
- (44) Lu, A.-H.; Schmidt, W.; Spliethoff, B.; Schüth, F. Synthesis and Characterization of Nanocast Silica NCS-1 with CMK-3 as a Template. *Chemistry – A European Journal* **2004**, *10*, 6085-6092.
- (45) Galarneau, A.; Cambon, H.; Di Renzo, F.; Ryoo, R.; Choi, M.; Fajula, F. Microporosity and Connections Between Pores in SBA-15 Mesostructured Silicas as a Function of the Temperature of Synthesis. *New Journal of Chemistry* **2003**, *27*, 73-79.
- (46) Fan, J.; Yu, C.; Wang, L.; Tu, B.; Zhao, D.; Sakamoto, Y.; Terasaki, O. Mesotunnels on the Silica Wall of Ordered SBA-15 to Generate Three-Dimensional Large-Pore Mesoporous Networks. *Journal of the American Chemical Society* **2001**, *123*, 12113-12114.
- (47) Soler-Illia, G. J. d. A. A.; Crepaldi, E. L.; Grosso, D.; Sanchez, C. Block Copolymer-Templated Mesoporous Oxides. *Current Opinion in Colloid & Interface Science* **2003**, *8*, 109-126.
- (48) Wan, Y.; Zhao. On the Controllable Soft-Templating Approach to Mesoporous Silicates. *Chemical Reviews* **2007**, *107*, 2821-2860.
- (49) Morishige, K.; Tateishi, N.; Fukuma, S. Capillary Condensation of Nitrogen in MCM-48 and SBA-16. *The Journal of Physical Chemistry B* **2003**, *107*, 5177-5181.
- (50) Sakamoto, Y.; Kaneda, M.; Terasaki, O.; Zhao, D. Y.; Kim, J. M.; Stucky, G.; Shin, H. J.; Ryoo, R. Direct Imaging of the Pores and Cages of Three-Dimensional Mesoporous Materials. *Nature*

---

2000, 408, 449-453.

- (51) Yu, C.; Tian, B.; Fan, J.; Stucky, G. D.; Zhao, D. Nonionic Block Copolymer Synthesis of Large-Pore Cubic Mesoporous Single Crystals by Use of Inorganic Salts. *Journal of the American Chemical Society* **2002**, 124, 4556-4557.
- (52) Mitchell, D. J.; Tiddy, G. J. T.; Waring, L.; Bostock, T.; McDonald, M. P. Phase Behaviour of Polyoxyethylene Surfactants with Water. Mesophase Structures and Partial Miscibility (Cloud Points). *Journal of the Chemical Society, Faraday Transactions 1: Physical Chemistry in Condensed Phases* **1983**, 79, 975-1000.
- (53) Barrett, E. P.; Joyner, L. G.; Halenda, P. P. The Determination of Pore Volume and Area Distributions in Porous Substances. I. Computations from Nitrogen Isotherms. *Journal of the American Chemical Society* **1951**, 73, 373-380.
- (54) Yu, C.; Tian, B.; Fan, J.; Stucky, G. D.; Zhao, D. Salt Effect in the Synthesis of Mesoporous Silica Templated by Non-Ionic Block Copolymers. *Chemical Communications* **2001**, 2726-2727.
- (55) Kim, T.-W.; Ryoo, R.; Kruk, M.; Gierszal, K. P.; Jaroniec, M.; Kamiya, S.; Terasaki, O. Tailoring the Pore Structure of SBA-16 Silica Molecular Sieve through the Use of Copolymer Blends and Control of Synthesis Temperature and Time. *The Journal of Physical Chemistry B* **2004**, 108, 11480-11489.
- (56) Cundy, C. S.; Cox, P. A. The Hydrothermal Synthesis of Zeolites: History and Development from the Earliest Days to the Present Time. *Chemical Reviews* **2003**, 103, 663-702.
- (57) Weitkamp, J. Zeolites and catalysis. *Solid State Ion.* **2000**, 131, 175-188.
- (58) Loewenstein, W. The Distribution of Aluminum in the Tetrahedra of Silicates and Aluminates. *Am. Miner.* **1954**, 39, 92-96.
- (59) Halliday, D.; Resnick, R.; Walker, J., *Principles of physics*. Wiley: Hoboken, N.J., 2011.
- (60) Database of Zeolite Structures. <http://www.iza-structure.org/databases/>
- (61) Roth, W. J.; Nachtigall, P.; Morris, R. E.; Čejka, J. Two-Dimensional Zeolites: Current Status and Perspectives. *Chemical Reviews* **2014**, 114, 4807-4837.
- (62) Perez-Ramirez, J.; Christensen, C. H.; Egeblad, K.; Christensen, C. H.; Groen, J. C. Hierarchical Zeolites: Enhanced Utilisation of Microporous Crystals in Catalysis by Advances in Materials Design. *Chemical Society Reviews* **2008**, 37, 2530-2542.
- (63) Layered Zeolites - 3D to 2D Paradigm Expansion. <http://layeredzeolites.com/>
- (64) Leonowicz, M. E.; Lawton, J. A.; Lawton, S. L.; Rubin, M. K. MCM-22: A Molecular Sieve with Two Independent Multidimensional Channel Systems. *Science* **1994**, 264, 1910-1913.
- (65) Roth, W. J.; Kresge, C. T.; Vartuli, J. C.; Leonowicz, M. E.; Fung, A. S.; McCullen, S. B., MCM-36: The First Pillared Molecular Sieve with Zeolite Properties. In *Studies in Surface Science and Catalysis*, Beyer, H. K.; Karge, H. G.; Kiricsi, I.; Nagy, J. B., Eds. Elsevier: 1995; Vol. 94, pp 301-308.
- (66) Wang, L.; Liu, Y.; Xie, W.; Wu, H.; Jiang, Y.; He, M.; Wu, P., Postsynthesis and Catalytic Properties of Metallosilicates Structurally Analogous to MCM-56. In *Studies in Surface Science and Catalysis*, Xu, R.; Gao, Z.; Chen, J.; Yan, W., Eds. Elsevier: 2007; Vol. 170, pp 635-640.
- (67) Kokotailo, G. T.; Lawton, S. L.; Olson, D. H.; Meier, W. M. Structure of Synthetic Zeolite ZSM-5. *Nature* **1978**, 272, 437-438.
- (68) Flanigen, E. M.; Bennett, J. M.; Grose, R. W.; Cohen, J. P.; Patton, R. L.; Kirchner, R. M.; Smith, J. V. Silicalite, A New Hydrophobic Crystalline Silica Molecular Sieve. *Nature* **1978**, 271, 512-516.
- (69) Taramasso, M.; Perego, G.; Notari, B., Preparation of Porous Crystalline Synthetic Material

---

Comprised of Silicon and Titanium Oxides. In Google Patents: 1983.

(70) Choi, M.; Na, K.; Kim, J.; Sakamoto, Y.; Terasaki, O.; Ryoo, R. Stable Single-Unit-Cell Nanosheets of Zeolite MFI as Active and Long-Lived Catalysts. *Nature* **2009**, 461, 246-249.

(71) Smith, R. L.; Eliášová, P.; Mazur, M.; Attfield, M. P.; Čejka, J.; Anderson, M. W. Atomic Force Microscopy of Novel Zeolitic Materials Prepared by Top-Down Synthesis and ADOR Mechanism. *Chemistry – A European Journal* **2014**, 20, 10446-10450.

---

## **Chapter 2 Analytical Techniques**

---

## 2. Analytical Techniques

### 2.1. X-ray Diffraction

X-rays are electromagnetic radiation, and have wave-particle duality. When x-rays are incident on matter with any form, they are partly absorbed by the atoms to produce photoelectric effect, and partly transmitted through the material, and partly scattered. The x-ray scattering process has two distinct forms, coherent scattering and incoherent scattering. Coherent scattering arises as a consequence of elastic collisions of x-rays with tightly-bound electrons in the atom. There is no change in energy between the scattered and the incident x-rays, and they have the same wavelength and frequency, and different directions.

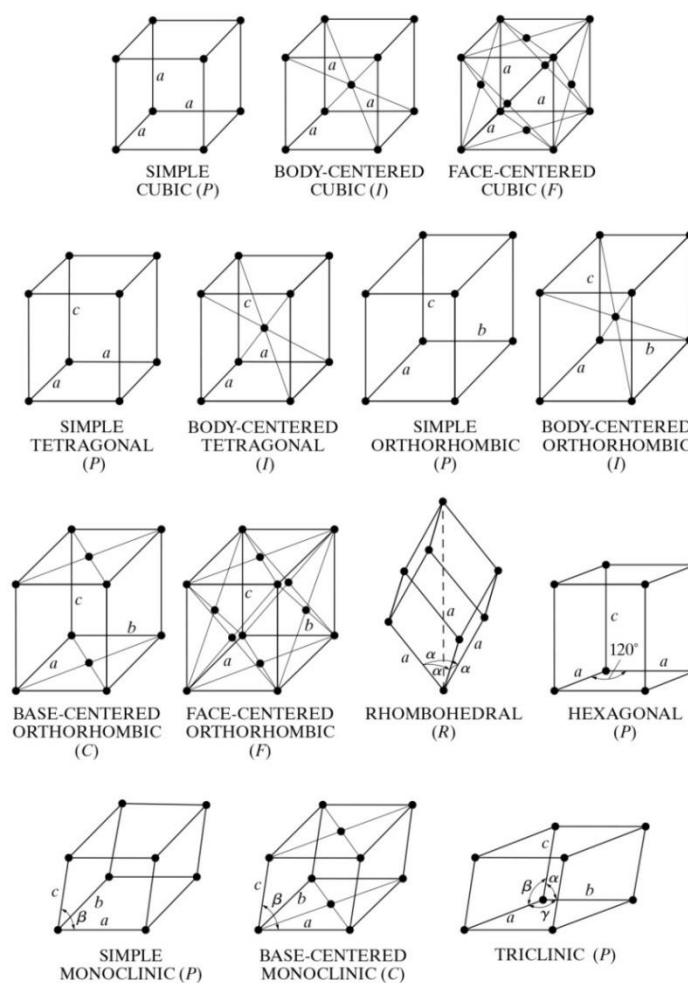


**Figure 2.1:** The fourteen Bravais lattices.<sup>1</sup>

Crystals are defined as solid materials where the atoms, molecules or ions arranged in a highly ordered pattern in three dimensions. The smallest repeat unit in the crystal lattice is known as the unit cell, and is represented by the side lengths ( $a, b, c$ ) and the inter-axial angles ( $\alpha, \beta, \gamma$ ). All crystals have been classified into seven lattice systems, and their point lattices can be obtained by putting the point at the corner of systems (Table 2.1). However, it is not the best classification to display the lattice symmetry. In 1848, Bravais discovered that there are fourteen possible point lattices and no more. The fourteen Bravais lattices are illustrated in Fig. 2.1. In order to describe the different crystal geometry, Miller indices are referred to describe the crystal plane or direction. The crystal plane is represented by  $(hkl)$ , the symmetry-related plane is represented by  $\{hkl\}$ , the direction is represented by  $[uvw]$ , and the symmetry-related direction is represented by  $\langle uvw \rangle$ .<sup>2</sup>

When x-rays of wavelength ( $\lambda$ ) are incident on a lattice plane, the incident angle, called the Bragg angle, equals to the diffraction angle. The incident beam, the diffraction beam and normal of the lattice plane are in the same plane (Fig. 2.2). The path difference ( $AB+AC$ ) must equal to a whole number ( $n$ ), called the order of diffraction, of wavelengths ( $\lambda$ ). From trigonometry, the path difference is equal to

$$n\lambda = 2d_{h'k'l'} \sin\theta_{hkl}$$

Where  $h = nh'$ ,  $k = nk'$ ,  $l = nl'$ ;  $d'$  represents the spacing between planes  $(hkl)$ . For convenient, Bragg's law can be written as

$$\lambda = 2d \sin\theta$$

**Table 2.1:** Formulas for calculating interplanar spacings  $d_{hkl}$

| System          | Axial Translation | Axial Angles   | $d_{hkl}$  |
|-----------------|-------------------|--|--|
| 1. Cubic        | $a=b=c$           | $\alpha=\beta=\gamma=90^\circ$                       | $a(h^2 + k^2 + l^2)^{-1/2}$  |
| 2. Tetragonal   | $a=b \neq c$      | $\alpha=\beta=\gamma=90^\circ$                       | $[h^2/a^2 + (k^2/b^2) + (l^2/c^2)]^{-1/2}$   |
| 3. Orthorhombic | $a \neq b \neq c$ | $\alpha=\beta=\gamma=90^\circ$                       | $[h^2/a^2 + (k^2/b^2) + (l^2/c^2)]^{-1/2}$   |
| 4. Hexagonal    | $a=b \neq c$      | $\alpha=\beta=90^\circ,$<br>$\gamma=120^\circ$       | $[(4/3a^2)(h^2 + k^2 + hk) + (l^2/c^2)]^{-1/2}$  |
| 5. Rhombohedral | $a=b=c$           | $\alpha=\beta=\gamma \neq 90^\circ$<br>$< 120^\circ$ | $a \left[ \frac{(h^2 + k^2 + l^2) \sin^2 \alpha + 2(hk + hl + kl)(\cos^2 \alpha - \cos \alpha)}{1 + 2\cos^3 \alpha - 3\cos^2 \alpha} \right]^{-1/2}$   |
| 6. Monoclinic   | $a \neq b \neq c$ | $\alpha=\gamma=90^\circ,$<br>$\beta > 90^\circ$      | $\left[ \frac{(h^2/a^2) + (l^2/c^2) - \left(\frac{2hl}{ac}\right) \cos \beta}{\sin^2 \beta} + \frac{k^2}{b^2} \right]^{-1/2}$  |
| 7. Triclinic    | $a \neq b \neq c$ | $\alpha \neq \beta \neq \gamma \neq 90^\circ$        | $\left[ \frac{h}{a} \left  \begin{array}{ccc} h/a & \cos \gamma & \cos \beta \\ k/b & 1 & \cos \alpha \\ l/c & \cos \alpha & 1 \end{array} \right  + \frac{k}{b} \left  \begin{array}{ccc} 1 & h/a & \cos \beta \\ \cos \gamma & k/b & \cos \alpha \\ \cos \beta & l/c & 1 \end{array} \right  + \frac{l}{c} \left  \begin{array}{ccc} \cos \gamma & \cos \beta & 1 \\ \cos \alpha & 1 & \cos \alpha \\ \cos \beta & \cos \alpha & 1 \end{array} \right  \right]^{-1/2}$ |



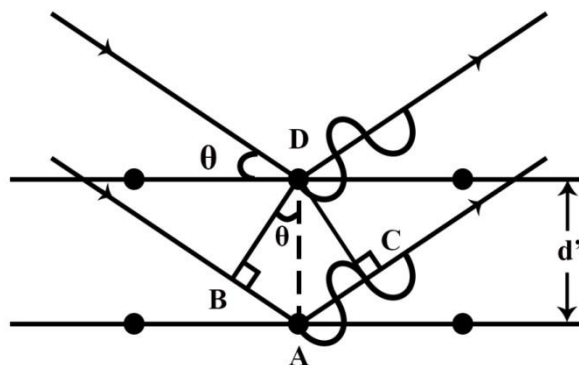


**Figure 2.2:** Diffraction of x-rays by a crystal.

X-rays can be produced in x-ray tubes with different shapes and ways. However, all x-rays tubes contain one cathode at high negative potential, and one anode normally at ground potential. The hot tungsten filament (cathode) produces electrons, and electrons accelerate by the high positive voltage electric field, and these electrons bombard a metal target (anode) to produce x-rays. Normally tungsten, molybdenum, chromium, copper can be used as the metal target. The voltages between the filament and target normally are 30 to 50kV.

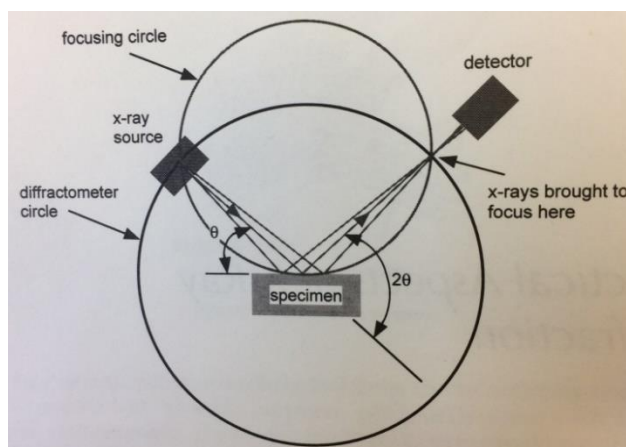


**Figure 2.3:** Geometry of the x-ray diffractometer.<sup>3</sup>

The powder x-ray diffraction method is an important application of x-rays. It yields plentiful information of the crystal structure. The essential geometry of the x-ray diffractometer is shown in Fig. 2.3. X-ray source, specimen, and x-ray detector are three basic modules of an x-ray diffractometer. They are located on the focusing circle. The Bragg angle ( $\theta$ ) is the angle between x-ray source and the surface of specimen. Hence, the angle between the projection of the x-ray

source and the detector is  $2\theta$ . The surface of the specimen must be tangent to the focusing circle, which means that a flat specimen is required before measuring. Normally, the measuring angle ( $2\theta$ ) is plotted on the abscissa, and intensity is plotted on the ordinate, and the peak (called reflection) corresponds to the specific crystal plane of the specimen. Each material has their characteristic x-ray diffraction pattern (called fingerprint), which can be used to determine the crystal structure and the lattice parameters.

Much information, for instance the shape and size of very small particle, characteristic distances and pore size of partially ordered materials, can be learned at the angular range ( $2\theta \leq 10^\circ$ ).<sup>4</sup> However, to measure the small angle scattering, the problem of scattered intensity near the direct beam must be overcome. Therefore, this angular range data are more appropriate to be collected by SAXS (small-angle x-ray scattering) instruments. Because of the weakness of the small angle scattering, vacuum systems are required from the x-ray source to the detector in SAXS instruments to decrease the beam attenuation and air scattering. Grazing-incidence small-angle x-ray scattering (GISAXS) is the scattering technique frequently used to study nano- and micro-structured thin films. GISAXS combines the features of three techniques<sup>5</sup>: GID, SAXS, and diffuse scattering. The geometry picture of the GISAXS is shown in Fig.2.4. The position of the sample represented by the spatial coordinates  $x$ ,  $y$ , and  $z$  as well as by its azimuthal orientation  $\omega$ .  $\alpha_i$  represents the incident angle,  $\alpha_f$  represents the exit angle, and  $\psi$  represents the out-of-plane angle. The calculation process of the results will be discussed in Chapter 4.

In this project, we use the PANalytical X'Pert Pro Diffractometer by a Philips PW3040/60 with Cu  $K\alpha$  x-ray radiation, which has a characteristic wavelength  $\lambda = 0.154184$  nm. The x-rays were generated from a Cu anode supplied with 30 mA current and 40 kV. SAXS and GISAXS were performed using Hecus S3-MICRO system equipped with a 2D SAXeye CCD-detector, with monochromatized Cu-radiation as x-ray source, which has a weighted wavelength  $\lambda = 0.15406$  nm. (Sample to CCD distance of 290.94 mm, CCD

pixel size of 0.172 mm, Beam center of 270.281 and 96.0281).

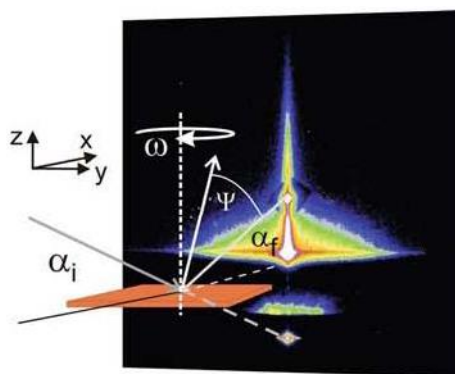


**Figure 2.4:** The geometry picture of the GISAXS.<sup>6</sup>

## 2.2. Atomic Force Microscopy

Scanning tunneling microscopy (STM) was first established by Binnig and Rohrer in 1981 as a method to image the atomic structure of conductive materials. In order to image insulating samples, Binnig and his co-workers invented the atomic force microscope (AFM) in 1986.<sup>7</sup> Both STM and AFM can be classified in the category of scanning probe microscopy (SPM) that depend on the interaction between the sharp probe and the sample surface. STM works by the tunneling current between the conducting sample and the metallic tip, and AFM measures the van der Waals force between the tip and sample surfaces. AFM can be performed over a wide range of temperatures (5-1000K) and under different conditions including air, fluid, gas and vacuum.<sup>8</sup>

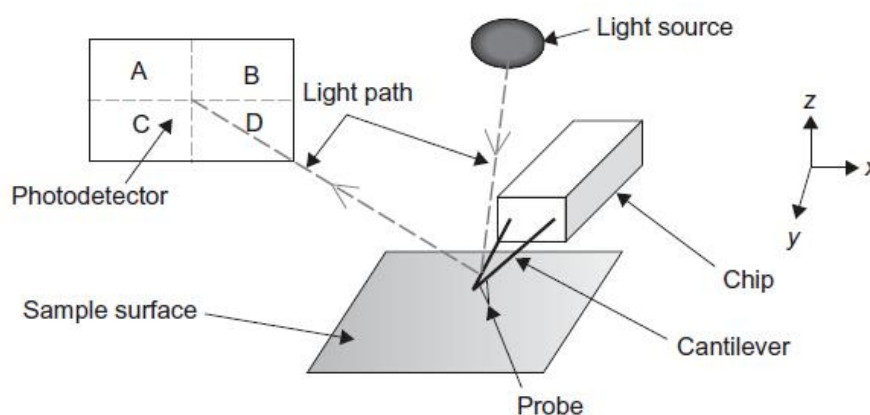


**Figure 2.5:** Schematic representation of the AFM.<sup>9</sup>

Figure 2.5 shows the schematic to illustrate the main features of an AFM. AFM works by scanning a very sharp tip which is mounted on the end of a cantilever, over the surface with a very low force. The sample surface is mounted on a piezoelectric crystal. A laser beam is focused on the end of the cantilever, preferably the position of the tip and the reflected on a photo detector. Therefore, the deflection of the cantilever can be monitored by the change in the path of the laser beam deflected by a photodetector. Therefore, when the sample is scanned by the movement of the piezoelectric crystals, the topography of the sample causes the cantilever to deflect as the force between the probe and sample changes.

The scanner normally consists of a hollow tube made of ceramic piezoelectric materials, which move very precisely and accurately with atomic dimensions. The motion of the sample can be controlled in three orthogonal directions: x and y (for sample scanning) and z (for controlling the tip-sample distance).

Optical beam detection has now become the most common detection method in commercial systems. In this method, the most common configuration for the photodetector is that of a quadrant photodiode divided into four parts with a horizontal and a vertical dividing line.<sup>9</sup> Each section is labeled from A to D (see Figure 2.5). Then the deflection signal can be calculated by the difference in signal detected by the (A+B)-(C+D) quadrants. Comparison of the signal strength detected by (A+C)-(B+D) will allow detection of lateral or torsional bending of the lever.

In order to obtain high-resolution AFM surface imaging, the control system should be accurate and fast. This is achieved by using three controls: proportional, integral and derivative (PID) controls. Proportional control simply amplifies the error between input and set point. Integral control monitors how the error signal changes with time (cumulative error). Derivative control looks at the rate of change of the error signal with time.

When the AFM probe approaches the sample surface, the forces between

the tip and sample will produce a deflection of the cantilever. The most relevant forces when performing experiments in air are long range, van der Waals interactions, short-range repulsive interactions, capillary and adhesion forces. In liquids, additional forces appear at the solid-liquid interface, such as solvation and electric double-layer interactions. These forces can be divided into two types: repulsive and attractive. Figure 2.6 shows the force-distance curve. At large separations between the tip and the sample surface, there is no force. As the probe approaches the surface, attractive van der Waals interactions begin to pull the tip towards the surface. As the distance is reduced, short-range repulsive forces reduce. The tip bends in the opposite way. According to the force-distance curve, there can be three different scanning modes: contact, intermittent contact and non-contact.

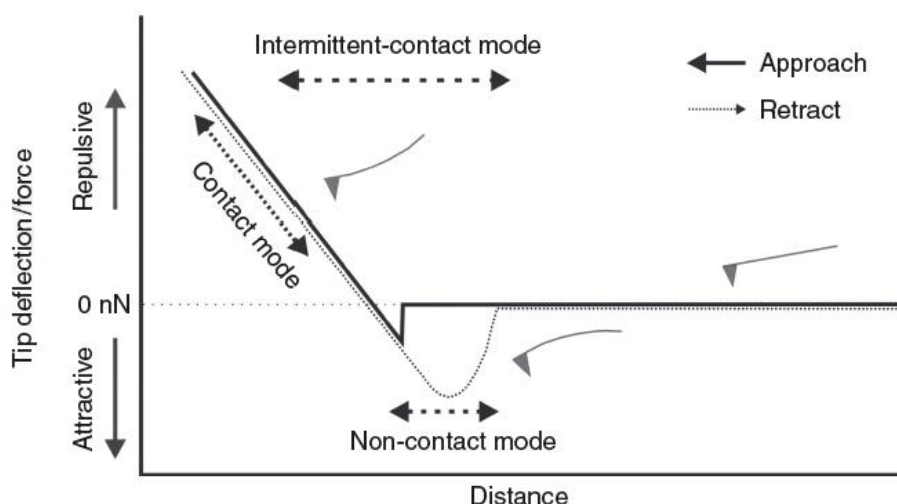


**Figure 2.6:** An ideal force-distance curve.<sup>10</sup>

Contact mode is so called because the tip is in direct contact with the sample at all times. The interaction between the tip and sample belongs to repulsive regime. This process can be performed either in air or under a liquid, and usually be used for sub-molecular resolution studies.

Intermittent contact mode is also known as tapping mode. Here the probe is oscillated at a value close to its resonant frequency. The advantages of using intermittent contact mode are increased lateral resolution and reduced damage

due to load, making the method easier to use with a softer sample. This process can also be performed either in air or under a liquid.

In non-contact mode, the tip never actually touches the surface of the sample. The tip oscillates with an amplitude of a few nm. There are only long range van der Waals attractive force between the tip and the sample.<sup>8</sup>

In this project, we use Bruker Multimode8-U AFM, and operate by Peak Force Tapping Mode in the air and Fluid. Height histogram images were derived using the NanoScope Analysis software from the AFM height images. First, export the data scale that displays a histogram of the height data from the color bar along the right side of the height image. (Fig. 2.7a) Second, taking the height as the x-axis, the percentage of the corresponding height as the y-axis, draw the standard curve. The first peak at  $0.00 \pm 0.01$  nm represents the average height of the substrate, and the second peak at  $2.65 \pm 0.01$  nm represents the average height of the exfoliated MWW flakes after calcination. (Fig. 2.7b) Third, Height histogram images were derived from the AFM height image, and the distance *ca.* 2.65 nm between the two peaks represents the thickness of the exfoliated MWW flakes after calcination.

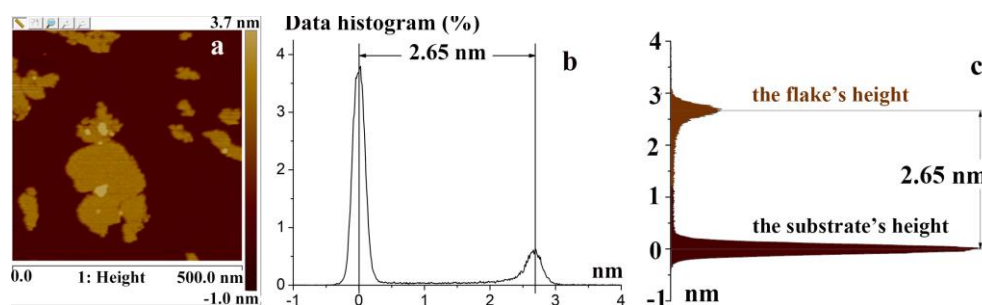


**Figure 2.7:** The derive method of height histograms from associated AFM height images.

## 2.3. Gas adsorption

### Classification of adsorption isotherms

Apart from the crystalline structure, the specific surface area, pore volume, and pore size distribution as well as the surface properties are also of great

interest by scientists for their structural investigation and industrial applications. Gas adsorption is usually used to determine these properties.<sup>11</sup> The majority of gas adsorption isotherms commonly fall into five categories according to the IUPAC classification, shown in Figure 2.8.<sup>12</sup> The limiting value of the relative pressure  $p/p^0$  axis is 1, and the vertical axis is the amount adsorbed  $n^a$ .

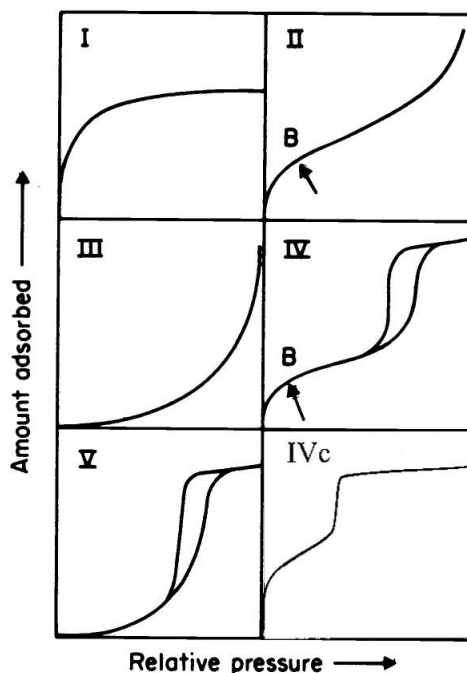


**Figure 2.8:** Type of gas adsorption isotherms.<sup>12</sup>

Type I isotherms exhibit prominent adsorption at low relative pressures and then level off. The strong adsorption exhibits the strong adsorbent-adsorbate interactions, which indicates the adsorption in micropores or monolayer adsorption. (It may be the case for chemisorption, which involves chemical bonding between the adsorbate and the adsorbent surface, we will not discuss chemisorption here).<sup>12</sup> Nonpolar gases usually were used for characterization of porous solids ( $N_2$ , Ar). Therefore, the chemisorption is unlikely. Nitrogen is the most widely used, due to the low-cost, easily obtained and environmentally friendly.

In the case of adsorption of  $N_2$  at 77 K or Ar at both 77 and 87 K in

cylindrical pores, the result would indicate the micropores, when Type I have to level off below  $p/p^0$  of about 0.1. The limiting uptake has been governed by the accessible micropore volume rather than by the internal surface area.

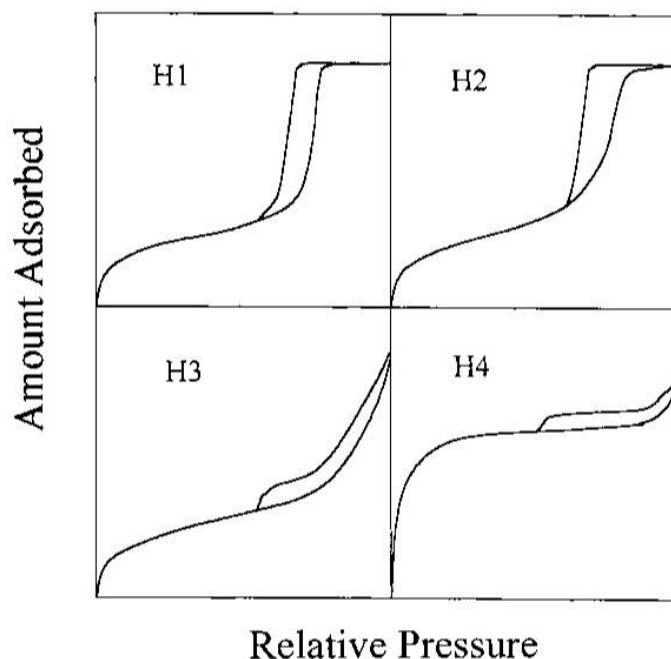


**Figure 2.9:** Type of adsorption - desorption hysteresis loops.<sup>12</sup>

The reversible Type II and Type III isotherm obtain with macroporous solids via multilayer formation. As the relative pressure increases, the amount adsorbed increases gradually, although near the saturation vapor pressure, the amount adsorbed may increase quite steeply.

Type II isotherm is given rise to the unrestricted monolayer-multilayer adsorption. There may be a pronounced stage (Point B) at the beginning of the almost linear middle section. It is usually taken to represent the stage at which monolayer formation is complete and multilayer adsorption about to begin. The reversible Type II and Type III isotherm obtain with macroporous solids via multilayer formation. As the relative pressure increases, the amount adsorbed increases gradually, although near the saturation vapor pressure, the amount adsorbed may increase quite steeply.



Type III isotherm may be convex in the whole pressure range and therefore does not exhibit a Point B. Type IV and Type V isotherms are obtained with mesoporous solids via multilayer adsorption followed by capillary condensation. The initial part of the isotherm is similar to that on macroporous solids, but over a range of high pressures the amount adsorbed rises quite abruptly due to the capillary condensation in mesopores. After these pores filled up, the adsorption isotherm levels off. The characteristic features of the Type IV and Type V isotherm are their hysteresis loop, which produced because the capillary condensation and capillary evaporation usually take place at the different pressure. The difference between Type IV and Type V is similar to that between Type II and III. Type IVc isotherm represents that the capillary condensation and capillary evaporation in mesopores may also be reversible.<sup>13</sup> Type IV is general, and IVc in particular, is typical for many ordered mesoporous solids.

#### **Classification of Adsorption-Desorption Hysteresis Loops**

A large number of studies have been carried out to investigate the hysteresis phenomenon, but its origin is still not fully understood. The hysteresis loops usually arise from the thermodynamic effects or network effects or some combination of these two effects.<sup>14</sup> The metastability of the adsorption or desorption branches in the isotherm leads to the thermodynamic effects. The pressure of the gas-like and liquid-like phases coexistent in the pore, is higher or lower than the pressure, when the capillary condensation or evaporation take place or delay.

The network (pore connectivity) effects which give rise to the hysteresis are expected to play an important role in desorption processes. If the larger pores have access to the surrounding only through the narrower pores, the larger pores cannot be emptied at the relative pressure of their capillary evaporation. Due to this narrower pores are still filled with the condensed adsorbate. So the larger pores may be completely emptied at the relative pressure of the capillary evaporation of the narrower pores. Another possible explanation is that the desorption originates from the core of mesopores. The radius of the local

meniscus is smaller than those of pores, requiring a lower pressure to evaporate. Consequently, at the pressure where the adsorbate condenses on the adsorption branch, evaporation is resisted until a lower equilibrium pressure has been reached.

There are four types of hysteresis loops according to the IUPAC classification, shown in Figure 2.9.<sup>12</sup>

In the Type H1 loop, the two branches are parallel and nearly vertical, which is often associated with the materials that consisted of agglomerates or compacts of approximately uniform spheres in a fairly uniform way.<sup>12</sup> At present, Type H1 loop is also characteristic of materials with high pore size uniformity and facile pore connectivity.<sup>15</sup> The Type H2 loop which has a triangular shape and a steep desorption branch, is especially difficult to interpret. It often attributed to the pore connectivity effects occurring in pores with narrow mouths and wide bodies (ink-bottle pores),<sup>13</sup> but it may provide an oversimplified picture. The Type H3 loop that does not level off at the high relative pressure, is reported for aggregates of plate-like particle forming slit-shaped pores. In the Type H4 loop, the two branches are parallel and almost horizontal, which is often associated with adsorption-desorption in narrow slit-like pores.

### Assessment of Mesoporosity

Mesopore size calculations are usually made with the aid of the Kelvin equation in the form

$$\ln \frac{p}{p^0} = - \frac{2\gamma\bar{V}}{rRT}$$

which relates the radius,  $r$ , of curvature of the liquid meniscus (which is assumed to be hemispherical) in the pore to the relative pressure,  $p/p^0$ , at which condensation occurs; here  $\gamma$  is the surface tension of the liquid condensate and  $\bar{V}$  is its molar volume.  $R$  is the universal gas constant, at the constant temperature  $T$ .

### Determination of surface area

The Brunauer-Emmett-Teller (BET) method<sup>16</sup> has become the widely used

standard procedure to evaluate specific surface area. According to the BET method, the evaluation of the monolayer capacity, which is the number of adsorbed molecules in the monolayer of the material surface, can be calculated by the BET equation. Thus, the specific cross-sectional area of the adsorbed molecule in monolayer formed on the given surface can be obtained.

The BET equation:

$$\frac{p}{n^a(p^o - p)} = \frac{1}{n_m^a C} + \frac{(C - 1)p}{n_m^a C p^o}$$

where  $n^a$  is the amount adsorbed at the relative pressure  $p/p^o$  and  $n_m^a$  is the monolayer capacity,  $C$  is the constant related to the enthalpy of adsorption in the first adsorbed layer. According to the major assumptions, the  $N_2$  BET calculations only use the adsorption data at relative pressures between 0.05 and 0.3.<sup>17</sup>

### Determination of Pore Size

The pore size at the corresponding relative pressure can be obtained simply by the Kelvin equation. However, the calculated radius (Kelvin radius) is not the real pore radius. There are many methods for calculation of pore size distributions. The Barrett-Joyner and Halenda (BJH)<sup>17</sup> is commonly used in mesoporous materials characterisation. However, the BJH method significantly underestimates the mesopore size since some of its simplified assumptions, such as the independence of surface tension on the pore radius and the same thermal-physical properties of pre-adsorbed multilayer to bulk liquid, are inapplicable. To this end, non-local density functional theory (NLDFT) has been developed.<sup>18</sup> It is found that the NLDFT equilibrium isotherm is in good agreement with the reversible experimental isotherm while the NLDFT prediction for capillary condensation fits the adsorption branch of the isotherm with hysteresis loop better.

## 2.4. Scanning Electron Microscopy

SEM focuses electrons into a beam by using magnetic fields in high vacuum, and then scans line by line over the surface of the specimen in the

---

evacuated microscope column and forms signals based on the interactions between the beam and the sample, which are electronically detected and amplified by suitable equipment.<sup>19</sup> The beam of electrons imparts charge to the sample so it is important for the sample either to be conducting or coated in a conductive layer to prevent charge building up which reduces the quality of the image.

Electrons accelerated onto the surface of the sample lead to numerous interactions with the atoms of the specimen. The accelerated electrons can pass through the sample without interaction, which was experienced the elastic scattering and inelastic scattering. (Fig. 3.0) The scattering generates numerous signals that are used for imaging, semi-quantitative, and quantitative information of the specimen and bringing about an x-ray source. Secondary electrons (SEs), backscattered electrons (BSEs) are two important signals used for imaging.

SEs are generated during the diffusion of the primary electrons (PEs), but possess only a small amount of energy. Thus only the SEs produced by the surface layers can leave the surface and reach the detector. The image provided by SEs can give the information about morphology and surface topography. The numbers of SEs are different from the different areas of the sample, that determine the contrast in a SE image. A higher point on the sample surface correspond to the brighter spot in the image. This effect is called the edge effect.

Backscattered electrons are generated by elastic scattering. They can provide information about the elemental composition of the sample. Namely the intensity of the electron signal detected is dependent upon the atomic weight of the sample, and determine the brightness of the image.

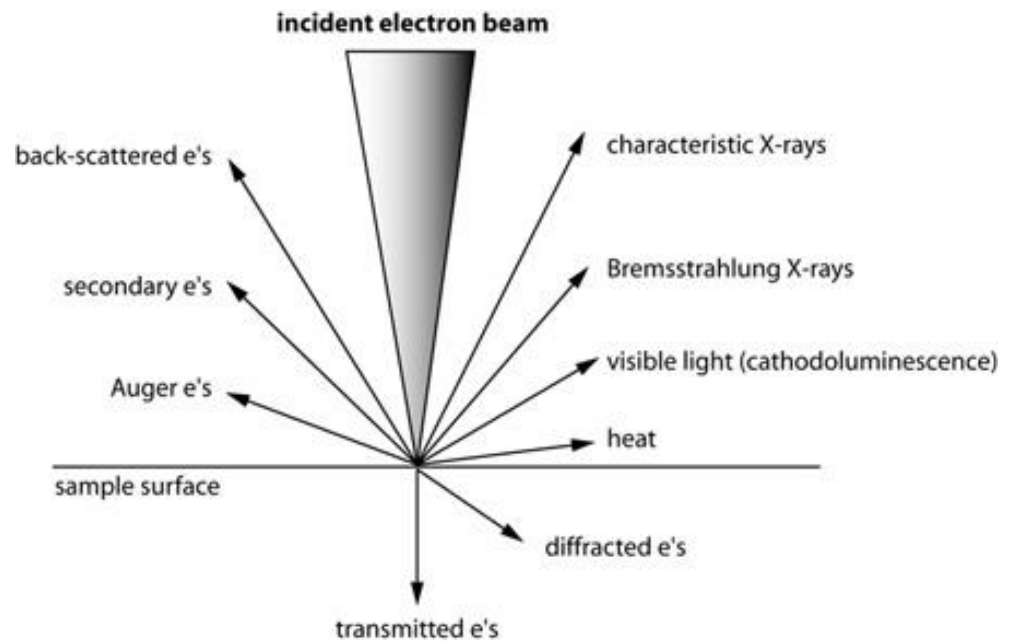


**Figure 3.0:** Types of interactions between electrons and a sample.<sup>20</sup>

In this project, we used an FEI XL30 Environmental scanning electron microscope-field emission gun. The FEI XL30 ESEM-FEG is used for imaging a wide range of samples. With carbon or gold coated samples, the ESEM can be used as a traditional SEM utilising either secondary electron or backscattered electron detectors.<sup>21</sup>

## 2.5. References

- (1) Cullity, B. D.; Stock, S. R., *Elements of X-ray Diffraction*. Prentice Hall: Upper Saddle River, NJ, 2001.
- (2) Putnis, A., *Introduction to Mineral Sciences*. Cambridge University Press: Cambridge, 1992.
- (3) Dorset, D. L., *X-ray Diffraction: A Practical Approach*. Cambridge University Press: 1998; Vol. 4, p 513-515.
- (4) Surhone, L. M.; Timpledon, M. T.; Marseken, S. F., *Small-angle x-ray scattering : small-angle scattering, x-ray, x-ray scattering techniques, macromolecule, protein, crystallography, NMR spectroscopy*. Betascript Publishing: USA, 2010.
- (5) Müller-Buschbaum, P., Structure Determination in Thin Film Geometry Using Grazing Incidence Small-Angle Scattering. In *Polymer Surfaces and Interfaces: Characterization, Modification and Applications*, Stamm, M., Ed. Springer Berlin Heidelberg: Berlin, Heidelberg, 2008; pp 17-46.
- (6) Müller-Buschbaum, P., A Basic Introduction to Grazing Incidence Small-Angle X-Ray Scattering. In *Applications of Synchrotron Light to Scattering and Diffraction in Materials and Life Sciences*, Gomez, M.; Nogales, A.; Garcia-Gutierrez, M. C.; Ezquerro, T. A., Eds. Springer Berlin Heidelberg: Berlin, Heidelberg, 2009; pp 61-89.
- (7) Binnig, G.; Quate, C. F.; Gerber, C. Atomic Force Microscope. *Physical Review Letters* **1986**, 56, 930-933.
- (8) Cubillas, P.; Anderson, M. W., Atomic Force Microscopy. In *Multi Length-Scale Characterisation*, John Wiley & Sons, Ltd: 2014; pp 121-193.
- (9) Morris, V. J.; Kirby, A. R.; Gunning, A. P., *Atomic Force Microscopy for Biologists*. Imperial College Press: London, 2009.
- (10) Johansson, E. M.; Córdoba, J. M.; Odén, M. Synthesis and Characterization of Large Mesoporous Silica SBA-15 Sheets with Ordered Accessible 18 nm Pores. *Materials Letters* **2009**, 63, 2129-2131.
- (11) Kruk, M.; Jaroniec, M. Gas Adsorption Characterization of Ordered Organic-Inorganic Nanocomposite Materials. *Chemistry of Materials* **2001**, 13, 3169-3183.
- (12) Sing, K. S. W.; Everett, D. H.; Haul, R. A. W.; Moscou, L.; Pierotti, R. A.; Rouquerol, J.; Siemieniewska, T. Reporting Physisorption Data for Gas Solid Systems with Special Reference to the Determination of Surface Area and Porosity. *Pure And Applied Chemistry* **1985**, 57, 603-619.
- (13) Franke, O.; Schulz-Ekloff, G.; Rathousky, J.; Starek, J.; Zukal, A. Unusual Type of Adsorption Isotherm Describing Capillary Condensation without Hysteresis. *Journal of the Chemical Society, Chemical Communications* **1993**, 724-726.
- (14) Ball, P. C.; Evans, R. Temperature Dependence of Gas Adsorption on a Mesoporous Solid: Capillary Criticality and Hysteresis. *Langmuir* **1989**, 5, 714-723.
- (15) Kruk, M.; Jaroniec, M.; Sayari, A. Application of Large Pore MCM-41 Molecular Sieves To Improve Pore Size Analysis Using Nitrogen Adsorption Measurements. *Langmuir* **1997**, 13, 6267-6273.
- (16) Brunauer, S.; Emmett, P. H.; Teller, E. Adsorption of Gases in Multimolecular Layers. *Journal of the American Chemical Society* **1938**, 60, 309-319.
- (17) Rouquerol, J.; Avnir, D.; Fairbridge, C. W.; Everett, D. H.; Haynes, J. H.; Pernicone, N.; Ramsay, J. D. F.; Sing, K. S. W.; Unger, K. K. Recommendations for the Characterization of Porous Solids. *Pure And Applied Chemistry* **1994**, 66, 1739-1758.

- (18) Barrett, E. P.; Joyner, L. G.; Halenda, P. P. The Determination of Pore Volume and Area Distributions in Porous Substances. I. Computations from Nitrogen Isotherms. *Journal of the American Chemical Society* **1951**, 73, 373-380.
- (19) Shi, K.; Peng, L.-M.; Chen, Q.; Wang, R.; Zhou, W. Porous Crystalline Iron Oxide Thin Films Templated by Mesoporous Silica. *Microporous and Mesoporous Materials* **2005**, 83, 219-224.
- (20) Electron-Sample Interactions.  
[http://serc.carleton.edu/research\\_education/geochemsheets/electroninteractions.html](http://serc.carleton.edu/research_education/geochemsheets/electroninteractions.html)
- (21) Environmental Scanning Electron Microscope.  
<http://www.seaes.manchester.ac.uk/our-research/research-areas/mes/facilities/environmental-sem/>

---

## **Chapter 3: Papers**

---



---

**Paper 1. Direct visualization of mesostructured  
films forming at the mica-solution interface**

---

## **Paper 1: Direct visualization of mesostructured films forming at the mica-solution interface**

Shiyu Xu<sup>1</sup>, Michael W. Anderson<sup>1\*</sup>

<sup>1</sup>Centre for Nanoporous Materials, School of Chemistry, The University of Manchester, Oxford Road, Manchester M13 9PL, UK.

\*e-mail: [m.anderson@manchester.ac.uk](mailto:m.anderson@manchester.ac.uk)

Paper not submitted for publication.

---

## Direct visualization of mesostructured films forming at the mica-solution interface

Shiyu Xu<sup>1</sup>, Michael W. Anderson<sup>1\*</sup>

<sup>1</sup>Centre for Nanoporous Materials, School of Chemistry, The University of Manchester, Oxford Road, Manchester M13 9PL, UK.

\*e-mail: [m.anderson@manchester.ac.uk](mailto:m.anderson@manchester.ac.uk)

### Abstract

Mesostructured films have been formed at a mica-solution interface in acidic surfactant cetyltrimethylammonium bromide (CTAB) solution. After introducing an inorganic precursor tetraethoxysilane (TEOS) acidic solution, the silicon hydroxide monomers reacted with a pre-existing organic mesophase film to form an inorganic film. The mesostructured films can be directly visualization by *in-situ* AFM that reveals the cylindrical structure, with spacing 5.1 to 5.5 nm, oriented parallel to the mica-solution interface and the thickness of each layer was consistently  $2.6 \pm 0.1$  nm, comparable to the alkyl chain length of the surfactant. The concentration of surfactant, pH, and CTAB/TEOS ratio affect the structure quality but have little effect on the structure spacing. The structure transformation process of the surfactant self-assembly on mica and reaction with the inorganic precursor after introducing TEOS can be tracked by AFM. The *in-situ* AFM method was used to demonstrate the formation process of both organic and inorganic mesophase films at the molecular level. This yields valuable information useful for developing architectural design strategies, and also provides an opportunity to reveal structure transformations at the solid-liquid interface at different solution compositions.

### Introduction

The mesophase formed by surfactant plus inorganic molecules self-assembling at the solid surfaces in aqueous solutions has been investigated extensively owing to potential uses in for example wear protection<sup>1</sup> and

corrosion prevention<sup>2</sup>. In addition, their intriguing physical and chemical biomimetic properties can be used in colloidal stabilization<sup>3</sup>, ore flotation<sup>4</sup> and as biochemical sensors<sup>5</sup>. As a consequence, it is important to understand the mechanism of the mesophase formation at the solid-solution interface. Hitherto, a substantial number of researchers have studied different structures of surfactants aggregating on various surface substrates. For example, Aksay et al. have studied the cationic surfactant cetyltrimethylammonium chloride (CTAC) in a dilute acidic solution of tetraethoxy silane (TEOS) (as inorganic precursor) growth on mica, graphite and amorphous silica substrates, respectively.<sup>6</sup> They observe that CTAC forms cylinders on mica, hemicylinders on graphite and spheres on silica. In addition, anionic<sup>7</sup>, neutral<sup>8</sup> and zwitterionic<sup>9</sup> surfactants in aqueous media and their mixtures<sup>10</sup> with<sup>11</sup> and without<sup>12-15</sup> inorganic precursors on other well-defined substrates, such as H-terminated Si(111) surface<sup>16</sup>, have been studied. However, the formation process of surfactant self- assembling at the solution-substrate interface, and the structure transformation after introducing the inorganic precursor into the solution is not yet well understood. *In-situ* atomic force microscopy (AFM) can make a significant contribution to the investigation of the interaction at the solid-solution interface, and is able to directly reveal the presence of defects and structural imperfection.

In this paper we use a much greater variety of experimental conditions compared to previous work.<sup>6</sup> This includes using much lower concentrations of silicate precursor than previously used including studying the surfactant mesophase in the absence of this precursor. In addition we have investigated a wide range of both pH conditions and surfactant concentrations. Finally, we have varied the order of addition of different components during the mesophase formation, such as, performing the surfactant mesophase followed by the addition of silicate precursor. In terms of AFM technology we have used PeakForce tapping mode which is a great leap in AFM technology, and provides the lowest available imaging forces between probe and sample surface, that can produce high-resolution AFM images for a wide variety of samples with

different rigidity, from biological cells to hard inorganic materials. We used mica as substrate because it has an atomically flat surface,<sup>17</sup> and can support the integrity of the mesostructural film forming on top. To avoid surface contamination, the mica was freshly cleaved. The cetyltrimethylammonium bromide (CTAB,  $C_{16}H_{33}N^+(CH_3)_3Br^-$ ) was used as surfactant, with critical micelle concentration (cmc)  $0.9 \text{ mM}^{14}$ . A dilute solution of TEOS is used as inorganic precursor for the assembly of mesostructures<sup>18</sup> and the formation was directly visualized by *in-situ* AFM.

## Experimental

Mica sheets (Agar Scientific Ltd.), were cut into  $1 \times 1 \text{ cm}^2$  squares and mounted on magnetic stainless steel AFM discs by carbon double sided adhesive discs.

CTAB ( $\geq 99\%$ , Sigma-Aldrich), TEOS (99.999%, Sigma-Aldrich), hydrochloric acid (37%, Sigma-Aldrich), and deionized water ( $18.2 \text{ M}\Omega \text{ cm}^{-1}$  at  $25 \text{ }^\circ\text{C}$ , Milli-Q Direct 8, Merck Millipore) were used as received. The aqueous solution for AFM experiments with molar composition is listed in Table 3.1-1.

All AFM images were obtained by PeakForce QNM (Quantitative Nano Mechanics) from MultiMode 8 AFM (Bruker). A sharpened silicon tip, and silicon nitride cantilever (ScanAsyst-Fluid+, Bruker) with spring constant  $0.7 \text{ N/m}$ , resonant frequency  $150 \text{ kHz}$ , E scanner ( $XY = 9.3 \text{ }\mu\text{m}$ ,  $Z = 3.5 \text{ }\mu\text{m}$ ) were used. Before operation, scanning parameters were adjusted as follows: scan size= $100 \text{ nm}$ ; scan rate= $2 \text{ Hz}$ ; the preferable engage setpoint  $\leq 0.05 \text{ V}$ ; amplitude preferably  $\leq 20 \text{ nm}$ ; and Z limit preferably  $\leq 500 \text{ nm}$ , but as small as possible. A higher peakforce setpoint can either damage the sample or the tip, however the sufficient sample deformation is required in order to achieve accurate elastic modulus measurement, therefore the peakforce setpoint needs to be continually adjusted during scanning with the starting setting preferably  $0.01 \text{ V}$ . A schematic representation of the *in-situ* AFM fluid cell is shown in Figure 3.1-S1 of supporting information. All the experiments were carried out at room

temperature.

Images were analyzed using the NanoScope Analysis software. The noise in height images was removed by three steps. First, a Fast Fourier Transform (FFT) was applied to the height image. Second, the mesophase signal was masked and an inverse FFT applied only to the noise. Third, the noise image product was subtracted from the original height image to give a noise-reduced image. Peak force error images were unprocessed.

### **AFM Experiments of the Self-assembled Organic Layers (S1-S7)**

The appropriate AFM parameters were adjusted and the mica was freshly cleaved before introducing the acidic surfactant solution (sample S1-S7) into the AFM fluid cell. During the AFM image collection, the force between the tip-sample was around 100 pN. For further investigation of the organic films the surfactant solution was removed from the AFM fluid cell and the sample dried in nitrogen. The AFM analysis of the films was performed in air after drying. In order to obtain high-resolution AFM images of the organic films deionized water was injected into the AFM fluid cell to avoid capillary forces.<sup>19</sup> Time was measured from the point that the surfactant solution was dropped onto the freshly cleaved mica.

### **AFM Experiments of the mesophase layers after introducing TEOS(SI1-SI3)**

The appropriate AFM parameters were set before experiments. 0.1 mL acidic surfactant solution with molar composition 2CTAB:9.4HCl:1000H<sub>2</sub>O was dropped on the freshly cleaved mica. 0.1 mL dilute acidic TEOS solution with molar composition 9.4HCl:1000H<sub>2</sub>O:nTEOS (where n was 0.008, 0.04 and 0.08 in sample SI1, SI2, and SI3, respectively) was dropped on the tip in the AFM fluid cell. After engaging the probe onto the mica surface, the timer was started as soon as the surfactant solution and the TEOS solution were mixed. The final molar composition for AFM analysis is shown in Table 3.1-1. The *ex-situ* AFM images of these films forming on mica were collected after removing the

---

solution mixture from the AFM fluid cell and drying the sample in nitrogen.

## Results

In order to protect the probes and sample surface small engage setpoints were used in order to reduce the engage force. It normally took 15 minutes to obtain the first AFM image after the solution was dropped on the mica surface. In the acidic aqueous systems (samples S1-S7) that contain surfactant CTAB and acid HCl, without TEOS, the mesophase films form at the mica surface spontaneously.

Figure 3.1-1 shows *in-situ* AFM height images of the film formed by the self-assembly of surfactants with different concentrations in the solution without TEOS. (samples S1-S4) The cylindrical micelles aggregated at the mica-solution interface. Figure 3.1-1a reveals the undulating cylindrical structure with low quality, many cross-links, and poor orientation forming in the 10.6 mM surfactant solution. As the surfactant concentration was increased to 21.3 mM, 31.9 mM, and 106.5 mM (Figs. 3.1-1b, 1c and 1d), mesostructures with higher quality and greater orientation were formed. If the surfactant concentration is lower than 10.6 mM the surfactant micelle did not form a mesophase on the mica surface; at higher than 106.5 mM, the surfactant self-assembles in bulk solution instead of forming at the mica-solution interface. The mesostructured cylinders, with repeat 5.1 to 5.5 nm, orient parallel to the mica-solution interface. The mesophase repeat was more-or-less independent of the surfactant concentration.

Figures 3.1-2 (a, b, c and d) reveal the mesophase formed at different acid concentrations of 0.4 M (sample S5), 0.5M (sample S4), 0.7M (sample S6) and 1.5M (sample S7), respectively. An acid solution is the essential condition to form mesophase at mica-solution interface. On the other hand, when the HCl concentration is lower than 0.4 M, the mesostructured films cannot be formed at the mica-solution interface. The structure and orientation of the mesophase films did not vary with the concentration of HCl. However, the mesophase forming

rate was pH dependent.<sup>20</sup> Comparing sample S4, S6, and S7 (see Fig. 3.1-2b, c, and d respectively), the pH values gradually increase, and more cross-links have been measured by AFM. This is due to the formation of mesophase at the mica surface being accelerated by lowering acid concentration of the solution. Higher formation rates give rise to the lower quality of the product. Highly concentrated HCl (>1.5 M) is not recommended, because a low-quality product was obtained, and the meandering cylinder mesophase disappeared from AFM measurements. In contrast, using the lower acid concentration, with an HCl concentration of 0.5 M (Sample S4, see Fig. 3.1-2b), a high-quality mesophase was characterized by AFM.

After removing the surfactant solution from the AFM fluid cell, sample S4 was dried in nitrogen, and was scanned by AFM in air. Figure 3.1-3 indicates that multilayers are formed on the surface of mica, and the thickness of each layer was consistently  $2.6 \pm 0.1$  nm. By drying in nitrogen the mesostructure might become strained in the direction perpendicular to the mica surface. Therefore, the thickness of each layer might be less than that in solution before drying.

To obtain high-resolution AFM images deionized water was injected into the AFM fluid cell. The unstable structures were revealed in Fig. 3.1-4d, and layers were formed by the cylindrical micelles. Peak force error is the feedback signal in PeakForce QNM and is a useful imaging mode to highlight transient processes such as dissolution of the mesophase films. Figs. 3.1-4(a, b, c) show the peak force error images of the films with two different layers, the higher islands (Fig.3.1-4b region I) and the outside edges of the film (Fig.3.1-4b region II). It was difficult to obtain the structure of the higher layer (Fig.3.1-4b region I), with the same peak force setting, and the soft structure in the higher layer disrupted by the scanning tip. The unstable layers gave rise to system noise during AFM scanning, that causes the feedback system to lose control of the tip position temporarily, and some structures in Fig. 3.1-4 tended to be blurred. After 5 minutes, the islands in the blue region (in Fig. 3.1-4b) were dissolved



(see Fig. 3.1-4c).

In conclusion of the experiments (sample S1-S7), we suggest that the surfactant CTAB self-assembled to meandering cylinders on the hydrophilic mica surface in the solution without the inorganic precursor TEOS at room temperature. The surfactant is kept adsorbing to the freshly formed organic mesophase surface, and this process can be reversed by adding deionized water.

In order to investigate the interaction between inorganic precursor and pre-existing surfactant layers, a dilute acidic TEOS solution with different concentrations was introduced into the AFM fluid cell (sample SI1, SI2, and SI3). The CTAB/TEOS ratios of sample SI1, SI2, and SI3 are 246, 49, and 25, respectively, listed in Table 3.1-1. Figures 3.1-5(b,d,f) show *in-situ* AFM height images of the mesophase structures layers after introducing TEOS solution, and Figures 3.1-5(a,c,e) are the same area of Figures 3.1-5(b,d,f), respectively, measured by AFM after 5 minutes. At high CTAB/TEOS=246 ratio (sample SI1), the cylindrical structure tended to rod-like (Fig. 3.1-5a), and more diffuse compared with the structure in Figs. 3.1-5c, and e. If the CTAB/TEOS ratio is higher than 246, the structure disappeared in AFM scanning images, this could be the consequence of a change in the mesophase structure to, for example, a lamellar mesophase although we have no crystallographic confirmation of this. At low CTAB/TEOS=12.5 ratio, particles with micro-size precipitated on mica, and the transparent solution became turbid, and cannot be measured by AFM. The cylinder repeat (5.1 to 5.5 nm) did not vary with CTAB/TEOS ratio in the range from 25 to 246. During the reaction between silicon hydroxide monomers and surfactant layer, the mesostructured film was unstable. Hence, it had the same phenomenon with the organic surfactant film dissolving in deionized water. The feedback system lost control of the tip position temporarily, and the mesostructure was not well-packed. When the tip traversed through the film, the scanning images were lost. The probe had to be withdrawn and re-engaged, and the scanning area drifted a little after each engagement.

After removal of the solution from the AFM fluid cell, sample SI3 was

dried in nitrogen, and was scanned by AFM in air. Figure 3.1-6 reveals the *ex-situ* peak force error image of sample SI3 after drying in nitrogen. A mesostructured silica multilayer was formed on mica, and the thickness point in Figure 6 was about 400 nm, consistently 150 layers. These films were stable and well-packed and cannot be dissolved in deionized water.

### Discussion

The AFM results directly demonstrate that surfactant CTAB above the CMC self-assemble on mica in acidic solutions in the absence of TEOS to form meandering cylinders. The cylinders are oriented parallel to the mica-solution interface and exhibit mesostructure with spacing 5.1 to 5.5 nm, i.e. about twice the length of the  $C_{16}H_{33}(CH_3)_3N^+$  ion,<sup>14</sup> and did not vary with the concentration of surfactant CTAB and acid HCl.

Imaging mesophase formation is successful in the solution with the concentration of surfactant CTAB between 10.6 mM to 106.5 mM. In this concentration range, higher surfactant concentration favours higher mesostructure quality. When the surfactant concentration is GREATER than 106.5 mM, the structure disappears in the AFM scanning image. This is because heterogeneous nucleation occurs at far lower free energy cost and hence is favoured over homogeneous nucleation at lower degrees of supersaturation.<sup>21</sup> The surfactant self-assembles in bulk solution instead of on mica surface at a high level of supersaturation. This theory is also suitable to explain the importance to maintain relatively low levels of supersaturation to minimize the mesostructure silica forming in bulk solution after introducing the silica species. The pH affects the formation rate of the mesophase films. Undulating cylinders obtained at a slower formation rate at lower pH and high formation rate leads to poor quality mesostructure at high pH. Hence, an optimum surfactant concentration and pH is important to form stable, well-packed mesophase films.

As the cylindrical micelle aggregation continues more surfactant is adsorbed onto the freshly formed organic mesophase films. The thickness of

each layer is consistently  $2.6 \pm 0.1$  nm, and is comparable to the length of the surfactant CTAB alkyl chain and about half length of the cylinder spacing. The result suggests that the cationic surfactant head group  $C_{16}H_{33}(CH_3)_3N^+$  adsorbs vertically at the mica interface forming a cylindrical mesophase with the unique axis parallel to the mica surface. The formation process can be reversed by immersing the film into deionized water such that the mesostructured film is dissolved.

The surfactant micelles grow parallel to the mica surface to form undulated or meandering cylinders due to the small bending energy along the long axes of the cylinder, and can be explained by the Helfrich model.<sup>22, 23</sup>

The minimization bending energy

$$w_b = \frac{k_c}{2} (2H - C_0)^2 + k_G K$$

Where,  $H = (C_1 + C_2)/2$  is the mean curvature, i.e. the average of the principal curvatures  $C_1$  and  $C_2$ ;  $C_0$  is the spontaneous curvature, about  $1/2.6$  nm<sup>-1</sup> in the experiments;  $K = C_1 C_2$  is the Gaussian curvature, and is a constant in closed topology object<sup>25</sup>;  $k_c$  is the constant bending modulus;  $k_G$  is the Gaussian modulus. In the long cylinder formation,  $C_1 \gg C_2$ ,  $2H = C_1 + C_2$  approaches to  $C_0$ . When external forces are imposed, such as the interaction between silicon hydroxide monomers and the surfactant head groups,  $w_b$  increases and produces more cross-links along the long cylinder. The organic and inorganic multilayer structure can both be explained by this model.

The experiments of the organic mesophase layer show the surfactant CTAB self-assembles into meandering cylinders on the hydrophilic mica surface. One possible reason might be that in the acidic surfactant solution, the head group of single chain quaternary ammonium surfactant  $C_{16}H_{33}(CH_3)_3N^+$  was vertically bound at the mica-solution interface by the ion-exchange with the  $K^+$  ions.<sup>17</sup> The adsorption process only interacted with the head group and did not involve bromine or chlorine ions as these were not detected by x-ray photoelectron spectroscopy (XPS).<sup>26</sup> It is known from XPS measurements that the potassium ions are unevenly distributed on the mica surface and this disorder might be

reflected in the meandering nature of the cylindrical growth. Multi-layers are then formed with the mesophase orientation conforming to that of the first layer.

After introducing a TEOS solution, the cationic inorganic species was polymerized on the pre-existing mesophase film surface. As the polymerization continues, surfactant micelles were adsorbed onto the freshly formed inorganic mesophase surface. The process repeated to form inorganic mesostructured layers, until the CTAB/TEOS ratio dropped below the critical value of 25. This inorganic film is stable in the deionized water.

At a CTAB/TEOS ratio in the range from 25 to 246, the cylinders with repeat 5.1 to 5.5 nm form on mica. Lamellar or structures other than cylindrical should form at higher CTAB/TEOS ratio, but these have not been characterized by AFM at present. At lower CTAB/TEOS ratio, the solution became turbid, and cannot be measured by AFM, this is because of the reason we discussed before that the homogeneous nucleation is favoured over heterogeneous nucleation, and the mesostructured silica formed in bulk solution instead forming at mica surface at a high level of supersaturation.

As a contrast, two more experiments were carried out to study the hydrolysis reaction of TEOS in acidic solution. (i) We followed the procedure reported by Aksay *et al.*<sup>6</sup> whereby the freshly prepared acidic CTAB/TEOS=2 mixture solution with the same molar ratios of the solution (1TEOS:2CTAB:9.4HCl:1000H<sub>2</sub>O), was injected into AFM fluid cell. The meandering cylindrical structure was formed on mica, and after 2 hours reaction *in-situ* AFM images were difficult to obtain. This was because the mesostructured silica formed on the cantilever and in bulk solution and this influenced the nature of the tip and the reflection of the laser beam. (ii) The freshly prepared CTAB/TEOS=2 mixture solution (1TEOS:2CTAB:9.4HCl:1000H<sub>2</sub>O) was stirred at room temperature for 4 hours to allow the TEOS to sufficiently hydrolyse in the acidic solution, then injected into AFM fluid cell. The mesostructured silica formed in bulk solution in a few minutes, and the solution became turbid. The homogeneous nucleation occurred

at high levels of supersaturation and the mesostructured silica formed in bulk solution.

The results of the organic mesophase layer forming on mica measured by AFM, suggests that for CTAB between the concentration ranges 10.6 mM to 106.5 mM self-assembly on the mica surface occurs in the acidic solution. The comparison between the two experiments, (i) the introduction of the fully hydrolyzed acidic TEOS solution into the CTAB solution AFM fluid cell, (ii) injection of the mixture CTAB and TEOS solution in to the AFM fluid cell, suggests that the TEOS hydrolyzes to silicon hydroxide monomers in the acidic solution and then the inorganic monomers react with the pre-existing organic film. This promotes the surfactant micellar formation on the freshly formed inorganic surface. The CTAB/TEOS ratio in the thin film formation at the mica-solution interface is far below the CTAB/TEOS ratio for film formation induced by evaporation<sup>27</sup>. This is the same for other interfaces such as the air-water interface<sup>28</sup> and also for powder preparations.<sup>29, 30</sup>

## Conclusions

The formation of the organic and inorganic mesophase can be directly visualized at the mica-solution interface by AFM. The repeat of the structure did not vary with the concentration surfactant CTAB or pH, CTAB/TEOS ratio, but the structure quality depends on them. Understanding the processing of mesophase formation not only has significant contribution to design useful material architectures, but also provides important experimental support to the theory or model of interfaces and colloids science. The *in-situ* AFM methods on a molecular level can be applicable to a wide range of different solution and substrates, especially can extend to demonstrate the process and structure transformation on solid-liquid when two different composition liquids react.

## References

- (1) Li, J.; Zhang, C.; Cheng, P.; Chen, X.; Wang, W.; Luo, J. AFM Studies on Liquid Superlubricity between Silica Surfaces Achieved with Surfactant Micelles. *Langmuir* **2016**, *32*, 5593-5599.

- 
- (2) Volentiru, E.; Nyari, M.; Szabo, G.; Horvolgyi, Z.; Muresan, L. M. Silica Sol - Gel Protective Coatings Against Corrosion of Zinc Substrates. *Period. Polytech.-Chem. Eng.* **2014**, *58*, 61-66.
  - (3) Jódar-Reyes, A. B.; Martín-Rodríguez, A.; Ortega-Vinuesa, J. L. Effect of the Ionic Surfactant Concentration on the Stabilization/Destabilization of Polystyrene Colloidal Particles. *Journal of Colloid and Interface Science* **2006**, *298*, 248-257.
  - (4) Weng, X.; Mei, G.; Zhao, T.; Zhu, Y. Utilization of Novel Ester-Containing Quaternary Ammonium Surfactant as Cationic Collector for Iron Ore Flotation. *Separation and Purification Technology* **2013**, *103*, 187-194.
  - (5) Guo, Y.; Guadalupe, A. R. Screen-Printable Surfactant-Induced Sol-Gel Graphite Composites for Electrochemical Sensors. *Sensors and Actuators B: Chemical* **1998**, *46*, 213-219.
  - (6) Aksay, I. A.; Trau, M.; Manne, S.; Honma, I.; Yao, N.; Zhou, L.; Fenter, P.; Eisenberger, P. M.; Gruner, S. M. Biomimetic Pathways for Assembling Inorganic Thin Films. *Science* **1996**, *273*, 892-898.
  - (7) Wanless, E. J.; Ducker, W. A. Organization of Sodium Dodecyl Sulfate at the Graphite-Solution Interface. *The Journal of Physical Chemistry* **1996**, *100*, 3207-3214.
  - (8) Holland, N. B.; Ruegsegger, M.; Marchant, R. E. Alkyl Group Dependence of the Surface-Induced Assembly of Nonionic Disaccharide Surfactants. *Langmuir* **1998**, *14*, 2790-2795.
  - (9) Ducker, W. A.; Grant, L. M. Effect of Substrate Hydrophobicity on Surfactant Surface-Aggregate Geometry. *The Journal of Physical Chemistry* **1996**, *100*, 11507-11511.
  - (10) Davey, T. W.; Warr, G. G.; Almgren, M.; Asakawa, T. Self-Assembly of Hydrocarbon and Fluorocarbon Surfactants and Their Mixtures at the Mica-Solution Interface. *Langmuir* **2001**, *17*, 5283-5287.
  - (11) Li, B.; Fujii, M.; Fukada, K.; Kato, T.; Seimiya, T. In Situ AFM Observation of Heterogeneous Growth of Adsorbed Film on Cleaved Mica Surface. *Thin Solid Films* **1998**, *312*, 20-23.
  - (12) Sokolov, I.; Yang, H.; Ozin, G. A.; Henderson, G. S. Beyond the Hemicylindrical Micellar Monolayer on Graphite: AFM Evidence for a Lyotropic Liquid Crystal Film. *Advanced Materials* **1997**, *9*, 917-921.
  - (13) Manne, S.; Gaub, H. E. Molecular Organization of Surfactants at Solid-Liquid Interfaces. *Science* **1995**, *270*, 1480-1482.
  - (14) Manne, S.; Cleveland, J. P.; Gaub, H. E.; Stucky, G. D.; Hansma, P. K. Direct Visualization of Surfactant Hemimicelles by Force Microscopy of the Electrical Double Layer. *Langmuir* **1994**, *10*, 4409-4413.
  - (15) Teschke, O.; Ceotto, G.; de Souza, E. F. Dielectric Exchange-Force Effect on the Rupture Force of Adsorbed Bilayers of Self-assembled Surfactant Films. *Applied Physics Letters* **2001**, *78*, 3064-3066.
  - (16) Imanishi, A.; Suzuki, M.; Nakato, Y. In Situ AFM Studies on Self-Assembled Monolayers of Adsorbed Surfactant Molecules on Well-Defined H-Terminated Si(111) Surfaces in Aqueous Solutions. *Langmuir* **2007**, *23*, 12966-12972.
  - (17) Yang, H.; Kuperman, A.; Coombs, N.; Mamiche-Afara, S.; Ozin, G. A. Synthesis of Oriented Films of Mesoporous Silica on Mica. *Nature* **1996**, *379*, 703-705.
  - (18) Huo, Q.; Margolese, D. I.; Ciesla, U.; Feng, P.; Gier, T. E.; Sieger, P.; Leon, R.; Petroff, P. M.; Schuth, F.; Stucky, G. D. Generalized Synthesis of Periodic Surfactant/Inorganic Composite Materials. *Nature* **1994**, *368*, 317-321.
  - (19) Butt, H.-J.; Cappella, B.; Kappl, M. Force Measurements with the Atomic Force Microscope:
-

- Technique, Interpretation and Applications. *Surface Science Reports* **2005**, 59, 1-152.
- (20) Wan, Y.; Zhao. On the Controllable Soft-Templating Approach to Mesoporous Silicates. *Chemical Reviews* **2007**, 107, 2821-2860.
- (21) Berg, J. C., *An Introduction to Interfaces & Colloids: The Bridge to Nanoscience*. World Scientific: 2010.
- (22) Guckenberger, A.; Gekle, S. Theory and Algorithms to Compute Helfrich Bending Forces: A Review. *J. Phys.-Condes. Matter* **2017**, 29, 30.
- (23) Helfrich, W. Elastic Properties of Lipid Bilayers - Theory and Possible Experiments. *Zeitschrift Fur Naturforschung C-a Journal Of Biosciences* **1973**, C 28, 693-703.
- (24) Chaikittisilp, W.; Suzuki, Y.; Mukti, R. R.; Suzuki, T.; Sugita, K.; Itabashi, K.; Shimojima, A.; Okubo, T. Formation of Hierarchically Organized Zeolites by Sequential Intergrowth. *Angewandte Chemie International Edition* **2013**, 52, 3355-3359.
- (25) Capovilla, R.; Guven, J.; Santiago, J. A. Lipid Membranes with an Edge. *Phys. Rev. E* **2002**, 66, 7.
- (26) Li, B. Y.; Fujii, M.; Fukada, K.; Kato, T.; Seimiya, T. Time Dependent Anchoring of Adsorbed Cationic Surfactant Molecules at Mice/Solution Interface. *Journal Of Colloid And Interface Science* **1999**, 209, 25-30.
- (27) Grosso, D.; Cagnol, F.; Soler-Illia, G. J. d. A. A.; Crepaldi, E. L.; Amenitsch, H.; Brunet-Bruneau, A.; Bourgeois, A.; Sanchez, C. Fundamentals of Mesostructuring Through Evaporation-Induced Self-Assembly. *Advanced Functional Materials* **2004**, 14, 309-322.
- (28) Yang, H.; Coombs, N.; Sokolov, I.; Ozin, G. A. Free-Standing and Oriented Mesoporous Silica Films Grown at the Air-Water Interface. *Nature* **1996**, 381, 589-592.
- (29) Beck, J. S.; Vartuli, J. C.; Roth, W. J.; Leonowicz, M. E.; Kresge, C. T.; Schmitt, K. D.; Chu, C. T. W.; Olson, D. H.; Sheppard, E. W.; McCullen, S. B.; Higgins, J. B.; Schlenker, J. L. A New Family of Mesoporous Molecular Sieves Prepared with Liquid Crystal Templates. *Journal of the American Chemical Society* **1992**, 114, 10834-10843.
- (30) Kresge, C. T.; Leonowicz, M. E.; Roth, W. J.; Vartuli, J. C.; Beck, J. S. Ordered Mesoporous Molecular Sieves Synthesized by a Liquid-crystal Template Mechanism. *Nature* **1992**, 359, 710-712.

## Figures

**Table 3.1-1:** Molar Compositions of the Sample for AFM Characterization

| Sample name <sup>a</sup> | CTAB (mM) <sup>b</sup> | HCl (M) <sup>c</sup> | CTAB/TEOS <sup>d</sup> | Molar ratios <sup>e</sup> |
|--------------------------|------------------------|----------------------|------------------------|---------------------------|
| S1                       | 10.6                   | 0.5                  | /                      | 0.2:9.4:1000:/            |
| S2                       | 21.3                   | 0.5                  | /                      | 0.4:9.4:1000:/            |
| S3                       | 31.9                   | 0.5                  | /                      | 0.6:9.4:1000:/            |
| S4                       | 106.5                  | 0.5                  | /                      | 2:9.4:1000:/              |
| S5                       | 106.5                  | 0.4                  | /                      | 2:7.4:1000:/              |
| S6                       | 106.5                  | 0.7                  | /                      | 2:13.4:1000:/             |
| S7                       | 106.5                  | 1.5                  | /                      | 2:30.9:1000:/             |
| SI1                      | 106.5                  | 0.5                  | 246                    | 1:9.4:1000:0.004          |
| SI2                      | 106.5                  | 0.5                  | 49                     | 1:9.4:1000:0.02           |
| SI3                      | 106.5                  | 0.5                  | 25                     | 1:9.4:1000:0.04           |

<sup>a</sup> Samples S1-S7 show the self-assembled organic layers growing in the solution absence of the TEOS inorganic precursor. Sample SI1-SI3 show the films growing after the TEOS being included in the solution.

<sup>b</sup> The concentration of surfactant CTAB (mmol/L)

<sup>c</sup> The concentration of acid HCl (mol/L, the pH values is between 0.15–0.65.)

<sup>d</sup> The molar ratios of surfactant CTAB and inorganic precursor TEOS

<sup>e</sup> The molar ratios of the solution (CTAB:HCl:H<sub>2</sub>O:TEOS) This is the final composition for AFM characterization.



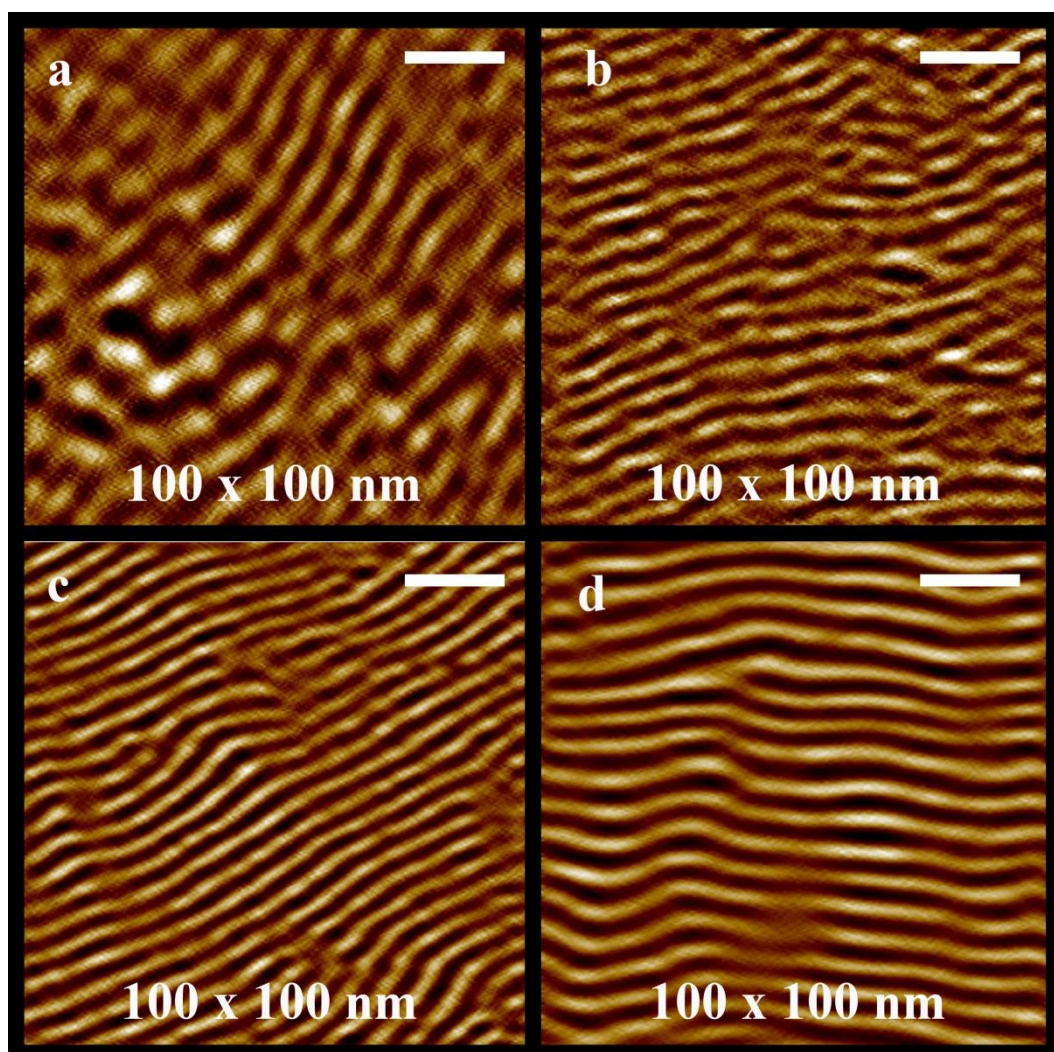


**Figure 3.1-1:** *In-situ* AFM height images of mesophase films forming on mica by the self-assembly of surfactant CTAB with different surfactant concentrations. (a,b,c,d) illustrate the sample S1, S2, S3, and S4, respectively, and the molar composition was listed in Table 3.1-1. All the meandering cylinders are parallel to the mica-solution inter face with spacing 5.1 to 5.5 nm. Scale bars in (a-d) are 20 nm.

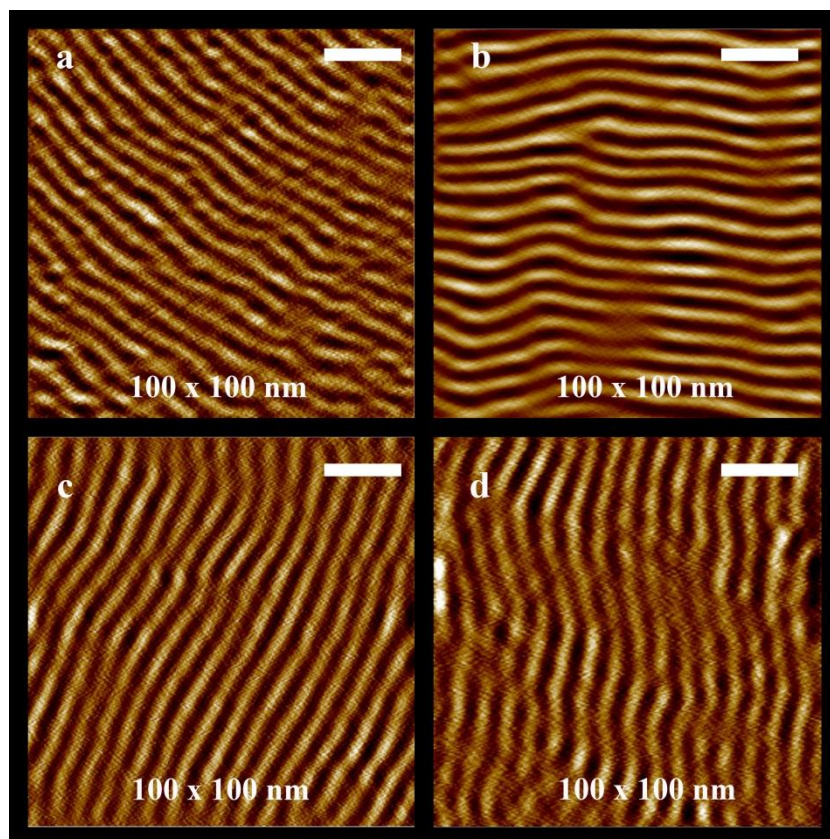


**Figure 3.1-2:** *In-situ* AFM height images of mesophase films forming on mica by the self-assembling of surfactant CTAB with different pH values. (a,b,c,d) illustrate the samples S5, S4, S6, and S7, respectively, and the molar composition listed in Table 3.1-1. Scale bars in (a-d) are 20 nm.

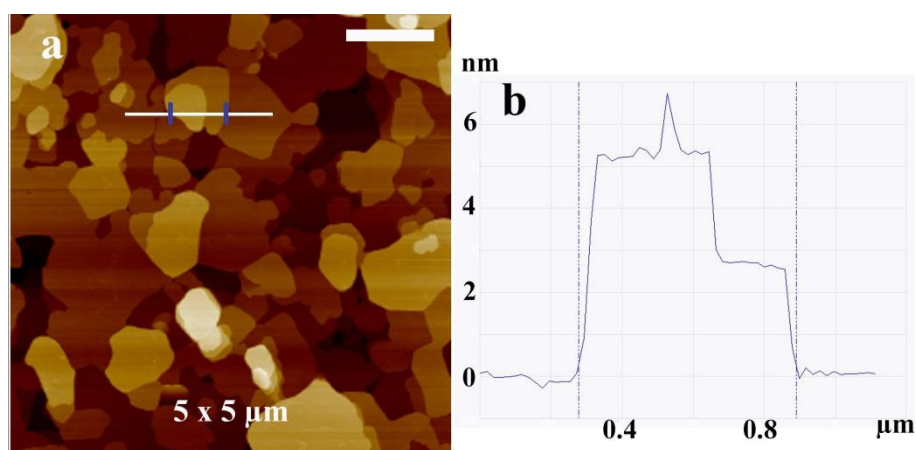


**Figure 3.1-3:** *Ex-situ* AFM height image of mesophase films forming on mica by the self-assembling of surfactant CTAB (sample S4) after drying in nitrogen. The average step-height data of the line highlighted in (a) are plotted in (b). The thickness of each layer are consistently  $2.6 \pm 0.1$  nm. The scale bar in (a) is 1  $\mu\text{m}$ .

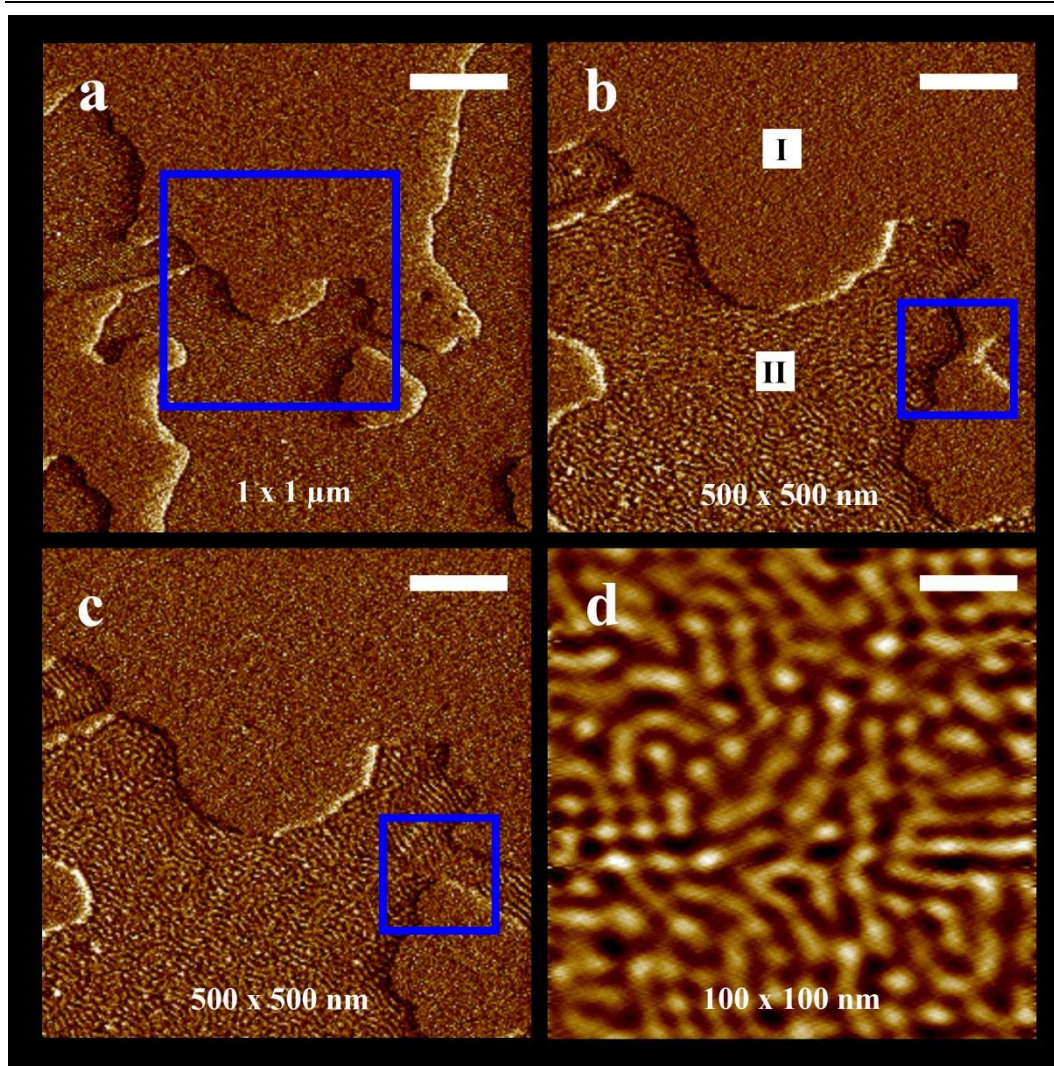


**Figure 3.1-4:** *In-situ* AFM images of mesophase films forming on mica (sample S4) after injected the deionized water into the AFM fluid cell. (a, b, and c) reveal the peak force error images of the two different organic layers dissolving in deionized water. The zoom in scanning of the blue region in (a) is shown in (b). Region I in (b) is the layer higher than the outside layer in region II. After 5 minutes, the island in the blue region of (b) was dissolved, seen in (c). (d) shows the height image of the unstable mesostructure. Scale bars from (a) to (d) are 200 nm, 100 nm, 100 nm and 20 nm.

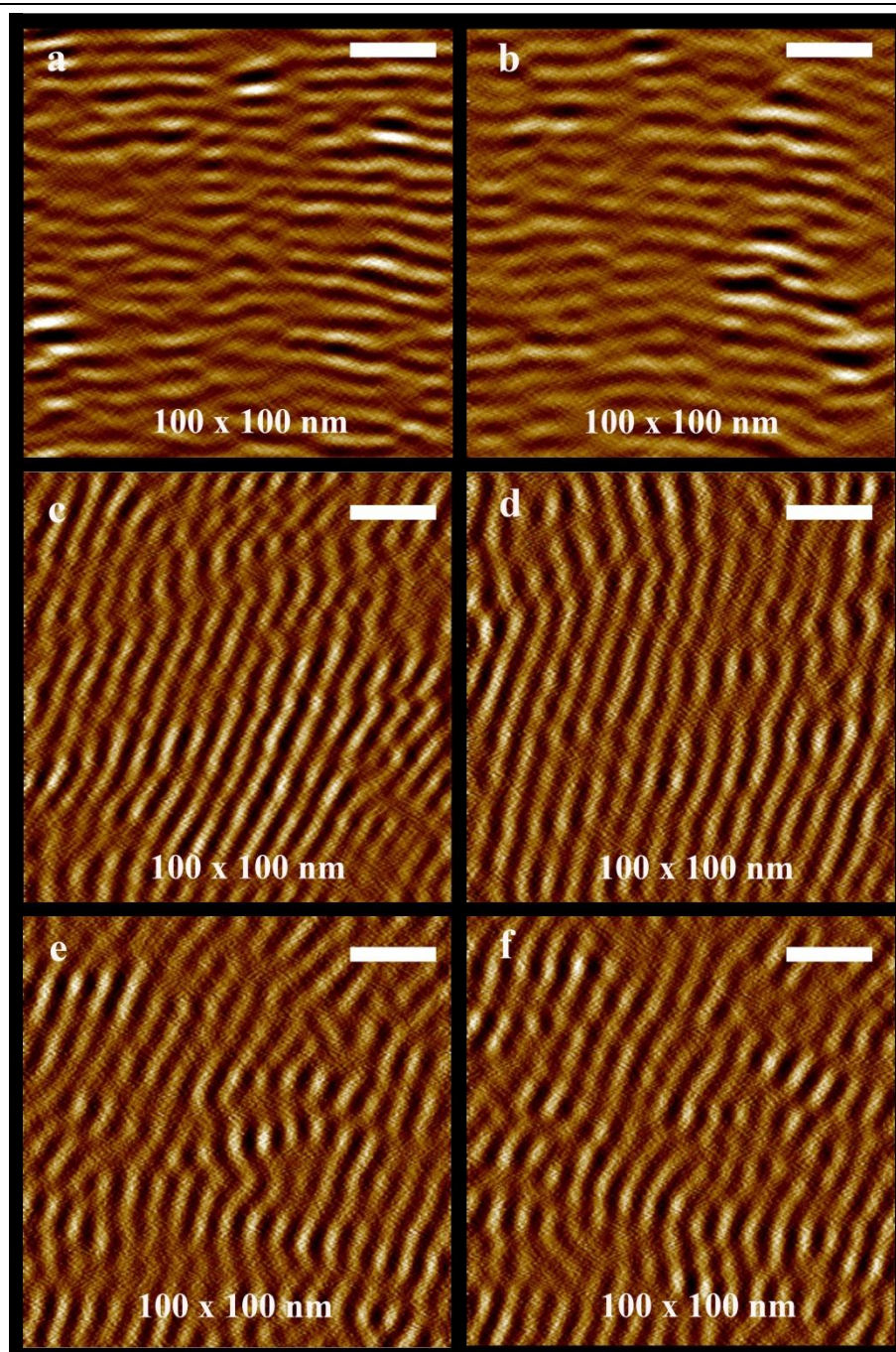


**Figure 3.1-5:** *In-situ* AFM height images of mesophase films forming on mica after introducing TEOS into the surfactant solution in the AFM fluid cell. (a, c, and e) illustrate sample SI1, SI2, and SI3, respectively, and the molar composition was listed in Table 3.1-1. (b, d, and f) show the cylindrical mesostructured growth after 5 minutes of the same area in (a, c, and e). Scale bars in (a-f) are 20 nm.

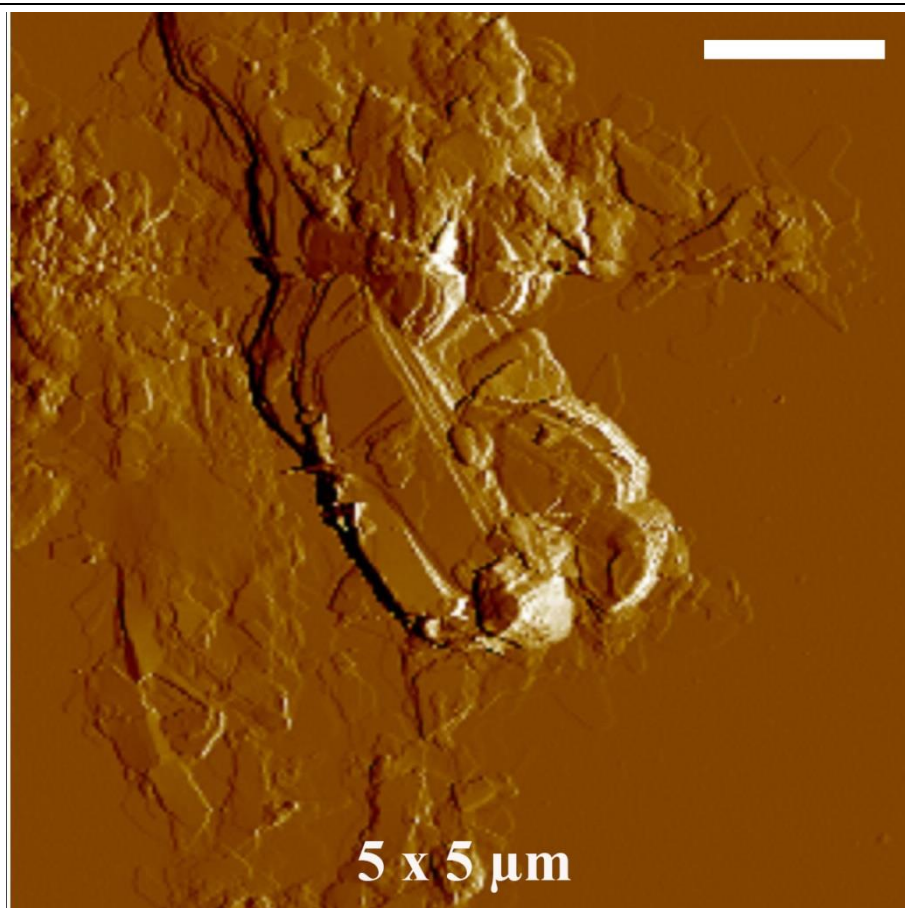


**Figure 3.1-6:** *Ex-situ* AFM peak force error image of mesostructured silica films forming on mica after drying in nitrogen. (sample SI3) The stable layers with differed thickness have been measured, and the thickness point is about 400 nm. The scale bar is 1  $\mu\text{m}$ .

---

## **Paper 1. Supporting Information**

---

## Supporting Information

### Direct visualization of mesostructured films forming at the mica-solution interface

Shiyu Xu<sup>1</sup>, Michael W. Anderson<sup>1\*</sup>

<sup>1</sup>Centre for Nanoporous Materials, School of Chemistry, The University of Manchester, Oxford Road, Manchester M13 9PL, UK.

\*e-mail: [m.anderson@manchester.ac.uk](mailto:m.anderson@manchester.ac.uk)

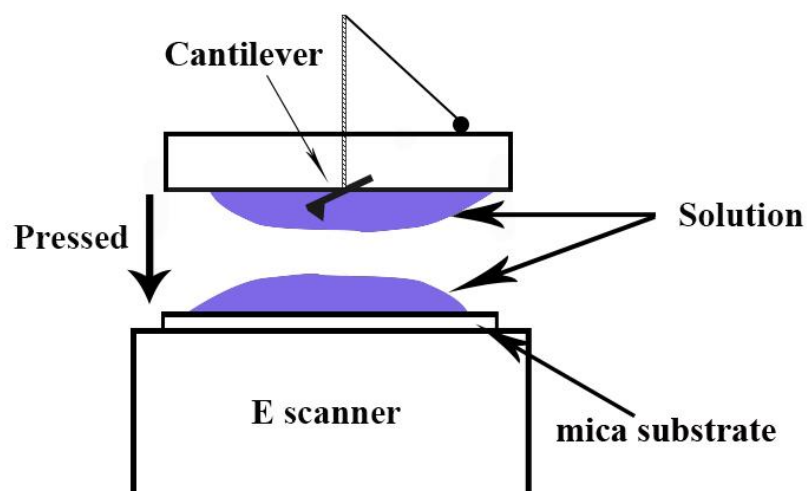


**Figure 3.1-S1:** Schematic illustration of the in-situ AFM fluid cell.

---

## **Paper 2. Mechanical Exfoliation of Nanoporous Materials**

---



---

## Paper 2. Mechanical Exfoliation of Nanoporous Materials

Shiyu Xu<sup>1</sup>, Yun-Hao Hsieh<sup>1</sup>, Michael W. Anderson<sup>1\*</sup>, Konstantin S. Novoselov<sup>2</sup>, Colin R. Woods<sup>2</sup>, Sarah J. Haigh<sup>3</sup>, Eric Prestat<sup>3</sup>, Lan Nguyen<sup>3</sup>, and Jiří Čejka<sup>4</sup>

<sup>1</sup> Centre for Nanoporous Materials, School of Chemistry, The University of Manchester, Oxford Road, Manchester M13 9PL, UK.

<sup>2</sup> School of Physics, The University of Manchester, Oxford Road, Manchester M13 9PL, UK.

<sup>3</sup> School of Materials, The University of Manchester, Oxford Road, Manchester M13 9PL, UK.

<sup>4</sup> Department of Synthesis and Catalysis, J. Heyrovský Institute of Physical Chemistry, Academy of Sciences of the Czech Republic, v.v.i., Dolejškova 3, CZ-182 23 Prague 8, Czech Republic.

\*e-mail: [m.anderson@manchester.ac.uk](mailto:m.anderson@manchester.ac.uk)

Paper not submitted for publication.

### Author Contributions:

The zeolites were synthesized by S. Xu and Y.H. Hsieh. XRD, SEM, exfoliation, AFM and modelling were performed by S. Xu. The TEM experiments were performed by C.R. Woods, E. Prestat, and L. Nguyen. The article was written by S. Xu. All author contributed to analysis of the data and discussions.

## Mechanical Exfoliation of Nanoporous Materials

Shiyu Xu<sup>1</sup>, Yun-Hao Hsieh<sup>1</sup>, Michael W. Anderson<sup>1\*</sup>, Konstantin S. Novoselov<sup>2</sup>, Colin R. Woods<sup>2</sup>, Sarah J. Haigh<sup>3</sup>, Eric Prestat<sup>3</sup>, Lan Nguyen<sup>3</sup>, Jiří Čejka<sup>4</sup>

### Abstract

The discovery of graphene<sup>1</sup> has highlighted the importance of two-dimensional materials and the intriguing properties that may be generated. Indeed, in order to create pencil lead, from which graphene can be extracted, graphite is mixed with another ubiquitous layered material, clay, in order to produce different degrees of hardness and, like graphite, clay can be readily exfoliated.<sup>2</sup> Here we show that certain three-dimensional nanoporous materials, zeolites a structural cousin of clay,<sup>3</sup> may be mechanically exfoliated in a similar manner to the original production of graphene. The nanosheets of insulating silica produced are several microns in lateral dimension, a couple of nanometers thick and possess an ordered array of sub-nanometer holes or depressions separated by about one nanometer. The technique is applicable to a variety of structural types to produce materials with pores either running across the short dimension of the nanosheet or parallel to the plane of the nanosheet. Other nanosheets product have ordered nanoscopic pockets arranged on the nanosheet separated by insulating silica. The simple production of such structures could be used to create devices such as nanoscopic capacitors whereby the nanopores could be filled with a wide variety of nanowires.

---

<sup>1</sup> Centre for Nanoporous Materials, School of Chemistry, The University of Manchester, Oxford Road, Manchester M13 9PL, UK.

<sup>2</sup> School of Physics, The University of Manchester, Oxford Road, Manchester M13 9PL, UK.

<sup>3</sup> School of Materials, The University of Manchester, Oxford Road, Manchester M13 9PL, UK.

<sup>4</sup> Department of Synthesis and Catalysis, J. Heyrovský Institute of Physical Chemistry, Academy of Sciences of the Czech Republic, v.v.i., Dolejškova 3, CZ-182 23 Prague 8, Czech Republic.

\*e-mail: m.anderson@manchester.ac.uk

Nanoporous membranes have many potential uses for example gas separation, filtration of viruses or as biosensors. In gas separation there are five main industrial applications: hydrogen recovery; air separation; CO<sub>2</sub> separation; separation and recovery of organics from gas streams; air and natural gas dehydration.<sup>4-7</sup> As a consequence there has been a substantial effort to create highly efficient and selective membranes consisting of ever-thinner nanoporous structures. One of the most important nanoporous crystalline material class is zeolites that find widespread utility in heterogeneous catalysts, gas separation and storage and ion-exchange. Typically zeolite crystals grow from a hydrothermal gel to produce crystals with a size from 100s of nanometers to 100s of microns. For heterogeneous catalysis applications it is often desirable to grow very small crystals with size less than 100 nm in order to reduce the diffusion path-length of guest species within the pores thereby providing access to a greater proportion of the internal reaction centres. Controlling the crystal habit is also crucial for the same reason especially, for example, in materials with one-dimensional pores such as zeolite L where it is crucial to minimize the crystal size along the pore direction for catalytic applications such as the dehydrocyclization of light naphtha.<sup>8</sup> This necessitates modifying the growth conditions usually by adding a growth inhibitor that slows growth on selective crystal faces. In the extreme this crystal growth modification can almost terminate growth in one direction and stabilize thin platelets with thickness one or two unit cells (one or two nanometers).<sup>9</sup> This has been achieved by using long surfactant-like organic molecules with dual functionality. One end of the molecule is designed to specifically template the zeolite structure by fitting hand-in-glove in the pores of the zeolite. The other end is a long hydrocarbon chain that has a tendency to form a lamellar mesophase and prevent thickening of the zeolite platelet. Epitaxial growth is another route to control the crystallization and encourage two-dimensionality and has achieved some success with zeolites<sup>10</sup> but much more so with metal-organic frameworks.<sup>11</sup> All the strategies rely on controlling the growth in two-dimensions. Another strategy

is to deconstruct a three-dimensional material following synthesis and relies on some pre-encoded two-dimensionality within the starting structure. As mentioned before materials that are obviously layered, such as clays, micas, graphite etc are particularly amenable to exfoliation post synthesis. The success depends to some extent on the strength of the interlayer connectivity or the ability to weaken this connectivity through intercalation. In this manner materials even with quite strong interlayer bonding such as titanates can be prized apart and even subsequently pillared with new interlayer guest species.<sup>12</sup> In the case where the initial three-dimensional material contains full covalent bonding in all directions then exfoliation will depend upon the strength of bonding in one direction being much less than bonding strength in other directions. In particular the recent work of Tsapatsis *et al.*<sup>13, 14</sup> has shown that it is possible to exfoliate a variety of two- and three-dimensional nanoporous materials through a process of melt-compounding and extrusion. This involves embedding the three-dimensional material within a polymer matrix followed by blending at temperatures between 120 °C and 200 °C under high shear forces. The extruded nanocomposite blend could then be dissolved in organic solvent to produce a suspension containing both polymer and zeolite. Centrifugation is then able to separate out thin nanosheets from the less exfoliated particles. Finally the suspension of nanosheets could be used to coat materials and form membranes which, after subsequent hydrothermal growth, could produce pinhole free structures for gas separation.

Here we have used a process of mechanical exfoliation in order to investigate whether it is possible to produce two-dimensional nanoporous structures *via* a process that does not involve any chemical intervention and, thereby, is potentially applicable to a wide variety of structures with different chemical makeup. We have used a method similar to the original production of graphene<sup>1</sup> from graphite whereby a solid is repeatedly cleaved by the application of a sticky tape (Fig. 3.2-1). Three structure types have been considered related to the zeolite structure codes UTL,<sup>15</sup> MWW<sup>16</sup> and MFI<sup>17</sup> that can all be initially

constructed in a two-dimensional layered form. Structures and syntheses of the three different two-dimensional zeolites materials UTL, MWW, and MFI have been discussed in Section 1.4.3. The structure of exfoliated zeolites is shown in Figure 3.2-5.

UTL is a germanosilicate with crystals (Figs. 3.2-S4a,b) constructed from ferrierite layers where the germanium is preferentially sited between the layers permitting the layers to be separated by a hydrothermal treatment<sup>18, 19</sup> that dissolves this germanate coupling. The resulting material is known as IPC-1P and this can be further swollen by intercalation of hexadecyltrimethyl ammonium chloride to produce IPC-1SW. Upon exfoliation of IPC-1SW nanoflakes are produced with a consistent thickness of  $1.1 \pm 0.1$  nm (Figs. 3.2-2a,b). High-resolution transmission electron microscopy (HRTEM) was performed by carefully transferring the flakes from the substrate to a TEM grid through a sequence of polymer coating and dissolution steps (Fig. 3.2-S16). Indexing of the associated selected area diffraction (SAED) patterns (Fig. 3.2-S15) indicates that, as expected, the nanoflakes have a surface normal along [100]. The layer thickness corresponds exactly to the thickness of the ferrierite layers (Fig 3.2-S17a) and is in accordance with the d-spacing of the lowest angle x-ray diffraction reflection that is recorded for the unswollen IPC-1P structure (Fig. 3.2-S2). Although the original UTL structure contains both large 14-T atom and 12-T atom pores these run parallel to the ferrierite layers and, therefore, the nanoflake structure does not have nanopores passing through the layer but retains the periodic impression of the pore topography (Figs. 3.2-5a and S16). Although the synthesis of UTL involves the organic structure directing agent (6R,10S)-6,10-dimethyl-5-azoniaspiro[4.5]decane and the swelling of the layers is achieved with hexadecyltrimethyl ammonium chloride the thickness of the nanoflakes created suggests that they consist only of the inorganic agent. This is not surprising since both organic agents will be intercalated with only a weak physical interaction to the inorganic structure. If the IPC-1P layers are not swollen prior to exfoliation it is not possible to exfoliate individual layers but

the structure is split into tens of layers (Figs 3.2-S8a,b). This indicates that inter-layer interaction is still significant even following the dissolution of interconnecting germanate units. Sometimes a second layer is observed with a layer height *ca.*  $1.4 \pm 0.1$  nm (Fig. 3.2-S8c,d) which is closer to half a unit cell of the original UTL structure suggesting that there may be incomplete removal of the interconnected germanate units. Lateral flake dimensions up to about 600 nm have been observed for the UTL structure.

MWW is a structure code that corresponds to a family of materials that can be layered in nature depending upon the synthesis pathway. The fully connected three-dimensional borosilicate structure is known as MCM-22,<sup>16</sup> however, prior to complete condensation of the three-dimensional structure an ordered layer precursor, MCM-22P, is made which can be intercalated and swollen if the condensation step is avoided.<sup>20</sup> The layers can also be separated by a post-synthesis treatment in nitric acid to make MCM-56P that results in a highly disorganized layering that prevents recondensation of the fully connected MWW framework.<sup>21</sup> In this work we have used both MCM-22P swollen with hexadecyltrimethyl ammonium chloride and MCM-56P for mechanical exfoliation. Similar to the UTL structure, MWW results in crystals with a flakey appearance (Fig. 3.2-S4c,d). Upon swelling of the MCM-22P material a new low-angle reflection appears in the SAXS pattern (Fig. 3.2-S1a,b) at a d-spacing of 5.1 nm. Exfoliation of MCM-22P SW (swollen) material results in layers with a consistent thickness  $5.0 \pm 0.1$  nm (Fig. 3.2-2c,d) and the HRTEM and indexing of the selected area diffraction pattern confirms (Fig. 3.2-S13) that the surface normal is along the [001] direction. These results taken together indicate that the exfoliated layer consists of both inorganic structure and the swelling agent. This is confirmed after calcination of the exfoliated flakes at 500 °C in air that resulted in removal of the organic swelling agent and the formation of an inorganic flake with thickness  $2.6 \pm 0.1$  nm (Fig. 3.2-2e,f). This thickness is consistent with one unit cell in the c-direction (Fig. 3.2-5b and S18) of the MWW structure, in other words the thickness of the MCM-22P layers. The

largest pore through the MWW layer is only a 6-tetrahedral atom ring with pore size *ca.* 0.2 nm. However, the layer consists of surface pockets on both sides with width 0.7 nm and depth 0.8 nm and an ordered separation of 1.4 nm on a hexagonal lattice. The HRTEM shows that both single and multi-layer nanosheets of MWW structure can be formed (Fig. 3.2-S14) with single layers yielding sharp diffraction spots and multilayers showing streaking owing to misalignment of the layers in the a- and b-directions. The AFM of multilayers (Fig. 3.2-S8e,f) reveals the alternation of inorganic layer and swelling agent although it is not possible to determine which component is initially in contact with the substrate. Direct mechanical exfoliation of MCM-56P is also successful (Fig. 3.2-S8g,h) without any need for pre-swelling indicating that the layers are weakly agglomerated in the starting material. Lateral flake dimensions up to about 500 nm have been observed for the MWW structure.

MFI is the structure code for the aluminosilicate zeolite ZSM-5<sup>22</sup> and the pure silica end-member known as silicalite.<sup>23</sup> As such it represents one of the most important structures for catalysis with ZSM-5, and its Ti-substituted cousin TS-1,<sup>24</sup> being used for a multitude of heterogeneous catalytic transformations. The crystals have a three-dimensional pore structure consisting of 10-tetrahedral atom rings to give a pore dimension of *ca.* 0.65 nm. In this work the precursor for exfoliation has been prepared by using a surfactant molecule with head-group that templates the MFI structure according to reference 62. This yields platey crystals (Figs. 3.2-S4e,f, S5, S6 and S7) that form petal-shaped clusters. As the crystals already contain surfactant tails separating the two-dimensional sheets no further preparation is required prior to crystal exfoliation (Fig. 3.2-S11). The x-ray diffraction pattern of the nano-platelet MFI structure (Fig. 3.2-S3a) is consistent with a structure with layer normal parallel to [010] and the SAXS pattern (Fig. 3.2-S3b) shows two reflections – (010) with  $d = 6.3$  nm and the (030) reflection. The absence of the (020) reflection is consistent with a layered structure that oscillates between high and low electron density with nearly equal thickness of each layer. That is, the 6.3 nm repeat is

divided into two layers each with thickness *ca.* 3.15 nm that will correspond to the inorganic component and the intervening organic tails respectively. Mechanical exfoliation of MFI results in flakes that are consistently  $5.3 \pm 0.1$  nm thick (Figs. 3.2-3a,b,c 3g,h,i and S9a,b) and following calcination the flakes become consistently  $3.1 \pm 0.1$  nm thick (Figs. 3.2-3d,e,f and S9c,d). This suggests that before calcination the template molecules are essentially intact on both sides of the inorganic layer, however, as the layer thickness is not the full basal plane separation of the starting material it is probable that the organic template molecules are no longer in their original configuration (see Fig. 3.2-S11). The exfoliated MFI flakes can be tracked by AFM before and after calcination. (Figs. 3.2-3a,d S10c,d). Moreover, the organic layer with thickness consistently  $1.6 \pm 0.1$  nm deposits on substrate after exfoliation was detected (Figs. 3.2-S10). Therefore the schematic representation in Figs. 3.2-3c,f and S11 seems plausible. The lateral dimension of the MFI sheets is consistently greater than 1  $\mu\text{m}$  and up to 10  $\mu\text{m}$  in some cases (Fig. 3.2-3i). Also, it is possible to observe where the inorganic layer is stripped from the organic layer (Fig. 3.2-3g,h) where the organic layer is pockmarked with holes. TEM of as-synthesised MFI flakes (Fig. 3.2-4a,d) and the associated selected area diffraction pattern are consistent with predominantly single-layer sheets oriented with the [010] direction normal to the sheet. The unit cell parameters of  $a = 1.98$  nm,  $c = 1.42$  nm can be calculated by the fast Fourier transform of the select region (Figs. 3.2-4a,b). After calcination the MFI structure unit cell parameter become consistently  $a = 1.94$  nm,  $c = 1.28$  nm (Figs. 3.2-4g,h). The calcination results a shrinkage on flakes structure in *c*-direction, but not notable in *a*-direction. HR-TEM images (Figs. 3.2-4d, S12) display that the mechanically exfoliated MFI structure contain the straight nanoporous about 0.6 nm wide.

Consequently, the MFI flake thickness is consistent with that from the x-ray diffraction studies and indicates that the structure is 1.5 unit cells thick in the *b*-direction (Figs. 3.2-5c and S19), and with straight nanopores running through the sheet, *ca.* 0.65 nm wide with centres separated by 1.3 nm. Because of the



property of the mechanically exfoliated MFI structure flakes, the future effort towards into two directions. First, use the mechanically exfoliated MFI flakes as seeds for further growth to form large scale MFI membrane with uniform nano-thickness. Directly synthesis nanosheets has been reported recently, by using 30 nm MFI crystal seeds to trigger the epitaxial growth of MFI nanosheets with thickness about 5 nm in b-direction,<sup>25</sup> and the seed-crystal can be removed by rubbing. The mechanically exfoliated MFI layer seeds before calcination contain the hydrocarbon chain template molecules on the both side, which can prevent thickening the layer growth in b-axis. Second, preparing MFI structures flakes on conducting substrates to fabricate the metal-insulator device, and filling the straight pores, running through the sheet with optoelectronic materials, it may be possible to generate materials with exotic properties.

These three mechanically exfoliated nanoporous, insulating silica structures, UTL, MWW and MFI, yield three very different sheets with (i) continuous structure, (ii) nano-sized, regularly arranged nanopockets and (iii) regularly arranged nanopores respectively.

## Methods

**Synthesis of UTL.** 4.9 g (6R,10S)-6,10-dimethyl-5-azoniaspiro[4.5]decane was dissolved in 24 mL distilled water and converted into hydroxide form by ion exchange with Dowex Marathon A resin (8.36 g, SUPELCO) for 2 h (this is termed SDA-OH for structure-directing agent). After filtering out the resin, 3.05 g germanium oxide (Aldrich) was added to the SDA-OH solution with stirring for complete dissolution. 3.5 g silica (Cab-osil M-5, Riedel-de Haen) was added into the solution and stirred at room temperature for 30 min. The pH value of the parent gel was adjusted to 9-10 by 1 M SDA-OH solution and then sealed in a Teflon-lined autoclave. The autoclave was heated at 175°C for 6 days with rotation (~60 rpm). The solid product was recovered by filtration with distilled water and dried overnight at 90°C. The as-synthesized product was calcined in air at 550°C for 6 h with a temperature ramp of 2 °C min<sup>-1</sup> to remove the

---

template. The parent gel composition was  $0.8\text{SiO}_2: 0.4\text{GeO}_2: 0.4\text{SDA}: 30\text{H}_2\text{O}$ .

**Hydrolysis of UTL.** 1 g of calcined UTL zeolite was hydrolysed in 200 mL 0.1 M HCl (Fisher Scientific) at  $99^\circ\text{C}$  for overnight (~12 h). The product was separated by filtration, washed with distilled water and dried at  $60^\circ\text{C}$ .

**Swelling of IPC-1P.** 1 g IPC-1P was added to 40 g of a mixture of 40% tetrapropyl ammonium hydroxide (TPA-OH, Merck) and 25% hexadecyltrimethyl ammonium chloride (CTMA-Cl, Aldrich) ( $w/w = 1/9$ ). The slurry was stirred at room temperature for 10 h. The product was separated by centrifugation and washed with water twice and then dried at  $80^\circ\text{C}$ .

**Synthesis of MCM-22P.** 0.42 g sodium aluminate (41 w/w%  $\text{Na}_2\text{O}$ , 54 w/w%  $\text{Al}_2\text{O}_3$ , Riedel-de Haen), and 0.58 g sodium hydroxide (Fisher Scientific) were dissolved in 48 g distilled water. 3.3 g hexamethyleneimine (HMI, Aldrich) and 4 g silica (Cab-osil M-5, Riedel-de Haen) were added to the solution with vigorous stirring for 30 min. After that, the parent gel was heated in a Teflon-lined autoclave at  $150^\circ\text{C}$  with rotation (~60 rpm) for 6 days. After quenching in cold water, the product was separated by filtration, washed with distilled water and dried at  $80^\circ\text{C}$ . The parent gel composition was  $\text{SiO}_2: 0.033\text{Al}_2\text{O}_3: 0.3\text{OH}^-: 0.3\text{Na}^+: 0.5\text{HMI}: 40\text{H}_2\text{O}$ .

**Swelling of MCM-22P.** 1 g MCM-22P was added to 40 g of a mixture of 25% tetramethylammonium hydroxide (TMA-OH, Merck) and 25% hexadecyltrimethyl ammonium chloride (CTMA-Cl, Aldrich) ( $w/w = 1/6$ ). The slurry was stirred at room temperature for 10 h. The product was separated by centrifugation and washed with water five times and then dried at  $80^\circ\text{C}$ .

**Synthesis of MCM-56P.** 1 g 50% sodium hydroxide solution (Fisher Scientific), and 2.23 g sodium aluminate solution (19.5 w/w%  $\text{Na}_2\text{O}$ , 25.5 w/w%  $\text{Al}_2\text{O}_3$ , Riedel-de Haen) were dissolved in 43 g distilled water. 8.57 g silica (ULTRASIL) and 4.52 g hexamethyleneimine (HMI, Aldrich) were added to the solution with vigorous stirring for 30 min. The reaction gel was heated in a Teflon-lined autoclave at  $145^\circ\text{C}$  with rotation (~400 rpm) for 36 h. After quenching in cold water, the product was separated by filtration, washed with

distilled water to form a wet cake and dried at 110°C. The parent gel composition was  $\text{SiO}_2: 0.044\text{Al}_2\text{O}_3: 0.21\text{OH}^-: 0.21\text{Na}^+: 0.35\text{HMI}: 20\text{H}_2\text{O}$ .

**Synthesis of organic surfactant ( $\text{C}_{22-6-6}\text{Br}_2$ ).** 3.9 g 1-bromodocosane (0.100 mol, TCI) and 17.2 g N,N,N',N'-tetramethyl-1,6-diaminohexane (1 mol, Aldrich) were dissolved in 100 ml acetonitrile/toluene mixture (1: 1 vol/vol) and heated under reflux at 70 °C for 10 h. Then, the mixture was cooled down to room temperature. After filtering and washing with diethyl ether, the product was dried in a vacuum oven at 50 °C. 5.62 g product (0.1 mol) and 24.6 g 1-bromohexane (0.2 mol, Aldrich) were dissolved in 30 ml acetonitrile and refluxed for 10 h. After filtering and washing with diethyl ether, the product was dried in a vacuum oven at 50 °C.

**Synthesis of lamellar MFI.** Tetraethylorthosilicate (TEOS, TCI),  $\text{Al}_2(\text{SO}_4)_3 \cdot 18\text{H}_2\text{O}$  (Aldrich), NaOH, organic surfactant ( $\text{C}_{22-6-6}\text{Br}_2$ ),  $\text{H}_2\text{SO}_4$  and water were mixed to obtain a gel composition of  $30\text{Na}_2\text{O}: 1\text{Al}_2\text{O}_3: 100\text{SiO}_2: 10\text{C}_{22-6-6}\text{Br}_2: 18\text{H}_2\text{SO}_4: 4000\text{H}_2\text{O}$ . The gel was heated in a Teflon-lined autoclave at 150°C with rotation (~60 rpm) for 5 days. The solid product was recovered by filtration with distilled water and dried overnight at 120°C.

**Mechanical exfoliation.** To separate the layered zeolite, nitto processing tape (BT-150E-CM, TELTEC) was used to perform repeat peeling of the sample. A silicon wafer with 290 nm oxide coating (Mi-Net) was used as the substrate for the exfoliated samples. The silicon wafer was cleaned with acetone and isopropyl alcohol (IPA) by ultrasonic cleaner for 10 min, respectively. Then, the tape was stuck on the silicon wafer and the wafer examined by filtered-light optical reflection microscopy. The zeolite layers interfere with light causing a shift in colours that allows distinction between wafer and zeolite, and few-layer zeolite from multi-layers zeolite.

**TEM sample transfer.** For transfer of the exfoliated samples for TEM before the mechanical exfoliation the silicon wafer was spin coated with polymethylglutarimide (PMGI). The exfoliated samples were then attached to the silicon wafer with PMGI coating. The wafer was examined by filtered-light

optical reflection microscopy and the flake thickness determined by AFM. The wafer was then spin coated with poly(methyl methacrylate) (PMMA). The exfoliated sample was now sandwiched between PMGI and PMMA. The selected area on the wafer was marked with a tweezer and MF319 solvent (2.2 % tetramethylammonium hydroxide with <1.0 % surfactant) was used to etch the PMGI. The wafer was put slowly into water to separate the selected area with PMMA coating. The selected area with PMMA coating floated on the water and a TEM grid was used to fish it up. The dried TEM grid was washed with acetone to remove the PMMA coating on the exfoliated samples.

**Calcination of exfoliated flakes.** The resulting exfoliated flakes on the substrates and TEM grids were calcined at 550 °C in air for 4h to remove the templates.

## References

- (1) Novoselov, K. S.; Geim, A. K.; Morozov, S. V.; Jiang, D.; Zhang, Y.; Dubonos, S. V.; Grigorieva, I. V.; Firsov, A. A. Electric Field Effect in Atomically Thin Carbon Films. *Science* **2004**, 306, 666-669.
- (2) Lan, T.; Kaviratna, P. D.; Pinnavaia, T. J. Mechanism of Clay Tactoid Exfoliation in Epoxy-Clay Nanocomposites. *Chemistry of Materials* **1995**, 7, 2144-2150.
- (3) Volkmer, D. Microporous Framework Solids. By Paul A. Wright. *Angewandte Chemie International Edition* **2008**, 47, 7163-7163.
- (4) Rao, M. B.; Sircar, S. Nanoporous Carbon Membranes for Separation of Gas Mixtures by Selective Surface Flow. *Journal of Membrane Science* **1993**, 85, 253-264.
- (5) Bernardo, P.; Drioli, E.; Golemme, G. Membrane Gas Separation: A Review/State of the Art. *Industrial & Engineering Chemistry Research* **2009**, 48, 4638-4663.
- (6) Hatori, H.; Takagi, H.; Yamada, Y. Gas Separation Properties of Molecular Sieving Carbon Membranes with Nanopore Channels. *Carbon* **2004**, 42, 1169-1173.
- (7) Rao, M. B.; Sircar, S. Performance and Pore Characterization of Nanoporous Carbon Membranes for Gas Separation. *Journal Of Membrane Science* **1996**, 110, 109-118.
- (8) Bernard, J., *Hydrocarbons Aromatization on Platinum Alkaline Zeolites*. 1980; p 686.
- (9) Choi, M.; Na, K.; Kim, J.; Sakamoto, Y.; Terasaki, O.; Ryoo, R. Stable single-unit-cell nanosheets of zeolite MFI as active and long-lived catalysts. *Nature* **2009**, 461, 246-249.
- (10) Nair, S.; Villaescusa, L. A.; Cambor, M. A.; Tsapatsis, M. Zeolite-Beta Grown Epitaxially on SSZ-31 Nanofibers. *Chemical Communications* **1999**, 921-922.
- (11) Yoo, Y.; Jeong, H.-K. Heteroepitaxial Growth of Isoreticular Metal–Organic Frameworks and Their Hybrid Films. *Crystal Growth & Design* **2010**, 10, 1283-1288.
- (12) Anderson, M. W.; Klinowski, J. Layered Titanate Pillared with Alumina. *Inorganic Chemistry* **1990**, 29, 3260-3263.

- (13) Varoon, K.; Zhang, X.; Elyassi, B.; Brewer, D. D.; Gettel, M.; Kumar, S.; Lee, J. A.; Maheshwari, S.; Mittal, A.; Sung, C.-Y.; Cococcioni, M.; Francis, L. F.; McCormick, A. V.; Mkhoyan, K. A.; Tsapatsis, M. Dispersible Exfoliated Zeolite Nanosheets and Their Application as a Selective Membrane. *Science* **2011**, 334, 72-75.
- (14) Maheshwari, S.; Jordan, E.; Kumar, S.; Bates, F. S.; Penn, R. L.; Shantz, D. F.; Tsapatsis, M. Layer Structure Preservation during Swelling, Pillaring, and Exfoliation of a Zeolite Precursor. *Journal of the American Chemical Society* **2008**, 130, 1507-1516.
- (15) Paillaud, J.-L.; Harbuzaru, B.; Patarin, J.; Bats, N. Extra-Large-Pore Zeolites with Two-Dimensional Channels Formed by 14 and 12 Rings. *Science* **2004**, 304, 990-992.
- (16) Leonowicz, M. E.; Lawton, J. A.; Lawton, S. L.; Rubin, M. K. MCM-22: A Molecular Sieve with Two Independent Multidimensional Channel Systems. *Science* **1994**, 264, 1910-1913.
- (17) Kokotailo, G. T.; Lawton, S. L.; Olson, D. H.; Meier, W. M. Structure of synthetic zeolite ZSM-5. *Nature* **1978**, 272, 437.
- (18) Roth, W. J.; Nachtigall, P.; Morris, R. E.; Čejka, J. Two-Dimensional Zeolites: Current Status and Perspectives. *Chemical Reviews* **2014**, 114, 4807-4837.
- (19) Roth, W. J.; Shvets, O. V.; Shamzhy, M.; Chlubná, P.; Kubů, M.; Nachtigall, P.; Čejka, J. Postsynthesis Transformation of Three-Dimensional Framework into a Lamellar Zeolite with Modifiable Architecture. *Journal of the American Chemical Society* **2011**, 133, 6130-6133.
- (20) Roth, W. J.; Kresge, C. T.; Vartuli, J. C.; Leonowicz, M. E.; Fung, A. S.; McCullen, S. B., MCM-36: The First Pillared Molecular Sieve with Zeolite Properties. In *Studies in Surface Science and Catalysis*, Beyer, H. K.; Karge, H. G.; Kiricsi, I.; Nagy, J. B., Eds. Elsevier: 1995; Vol. 94, pp 301-308.
- (21) Wang, L.; Liu, Y.; Xie, W.; Wu, H.; Jiang, Y.; He, M.; Wu, P., Postsynthesis and catalytic properties of metallosilicates structurally analogous to MCM-56. In *Studies in Surface Science and Catalysis*, Xu, R.; Gao, Z.; Chen, J.; Yan, W., Eds. Elsevier: 2007; Vol. 170, pp 635-640.
- (22) Kokotailo, G. T.; Lawton, S. L.; Olson, D. H.; Meier, W. M. Structure of Synthetic Zeolite ZSM-5. *Nature* **1978**, 272, 437-438.
- (23) Flanigen, E. M.; Bennett, J. M.; Grose, R. W.; Cohen, J. P.; Patton, R. L.; Kirchner, R. M.; Smith, J. V. Silicalite, a new hydrophobic crystalline silica molecular sieve. *Nature* **1978**, 271, 512.
- (24) Taramasso, M.; Perego, G.; Notari, B., Preparation of porous crystalline synthetic material comprised of silicon and titanium oxides. In Google Patents: 1983.
- (25) Jeon, M. Y.; Kim, D.; Kumar, P.; Lee, P. S.; Rangnekar, N.; Bai, P.; Shete, M.; Elyassi, B.; Lee, H. S.; Narasimharao, K.; Basahel, S. N.; Al-Thabaiti, S.; Xu, W.; Cho, H. J.; Fetisov, E. O.; Thyagarajan, R.; DeJaco, R. F.; Fan, W.; Mkhoyan, K. A.; Siepmann, J. I.; Tsapatsis, M. Ultra-Selective High-Flux Membranes from Directly Synthesized Zeolite Nanosheets. *Nature* **2017**, 543, 690-694.

### Author Contributions

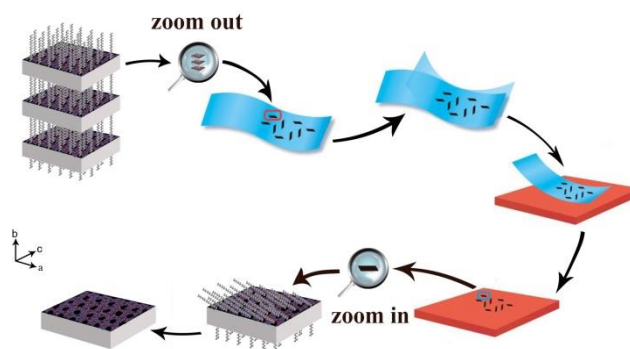
S.X and Y.H.H contributed to the synthesis, exfoliation and characterization of the samples. C.R.W, E.P. and L.N. contributed to the electron microscopy. All authors contributed to analysis of the data, discussions and the production of the manuscript.

**Additional information**

Supplementary information is available in the online version of the paper. Reprints and permissions information is available online at [www.nature.com/reprints](http://www.nature.com/reprints). Correspondence and requests for materials should be addressed to M.W.A.

**Competing financial interests**

The authors declare no competing financial interests.

**Figures**

**Figure 3.2-1: Exfoliation procedure.** To separate the layered zeolite, nitro processing tape was used to perform repeat peeling of the sample. A silicon wafer with 290 nm oxide coating was used as the substrate for the exfoliated samples. The tape was stuck on the silicon wafer and the wafer examined by filtered-light optical reflection microscopy. The zeolite layers interfere with light causing a shift in colours that allows distinction between wafer and zeolite, and few-layer zeolite from multi-layers zeolite. The thickness of flakes were measured by AFM to obtain accurate value. Following exfoliation the flakes were calcined to yield the inorganic nanosheet.

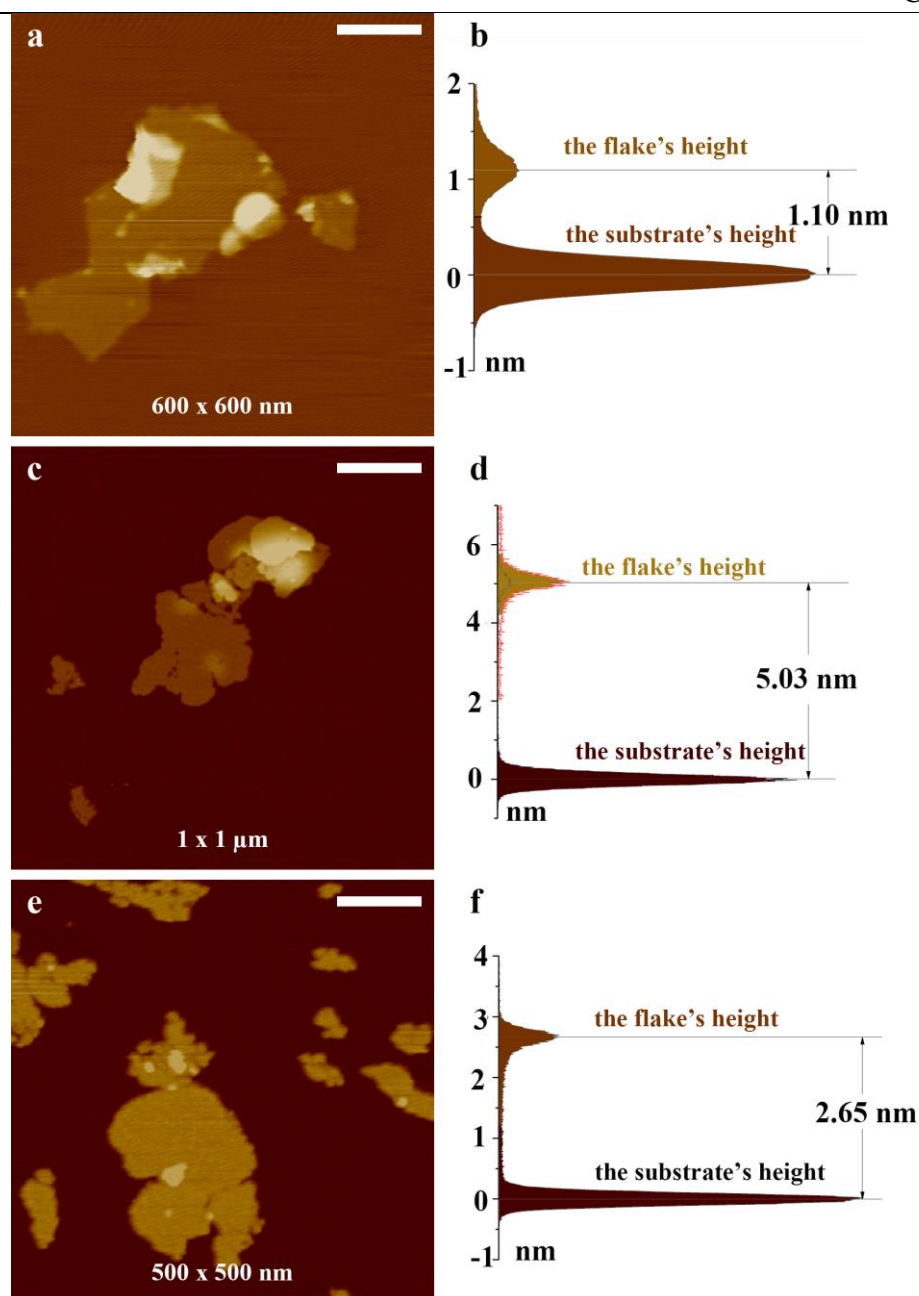


**Figure 3.2-2: AFM of exfoliated flakes, UTL and MWW.** AFM (tapping mode) images (a,c,e) and associated height histograms (b,d,f) show two different zeolite structures of exfoliated flakes. (a,b) IPC-1SW flake derived from UTL is  $1.1 \pm 0.1$  nm thick. (c,d) MCM-22P SW flake is  $5.0 \pm 0.1$  nm thick for the as-synthesised samples. (e,f) Following calcination of MCM-22P SW flake to remove the swelling agent the layer thickness is  $2.6 \pm 0.1$  nm which is consistent with one unit cell in the c-direction of the MWW structure. The derive method of height histograms from associated AFM images has been discussed in Section 2.2. Scale bars from (a) (c) and (e) are 120 nm, 200 nm and 100 nm.



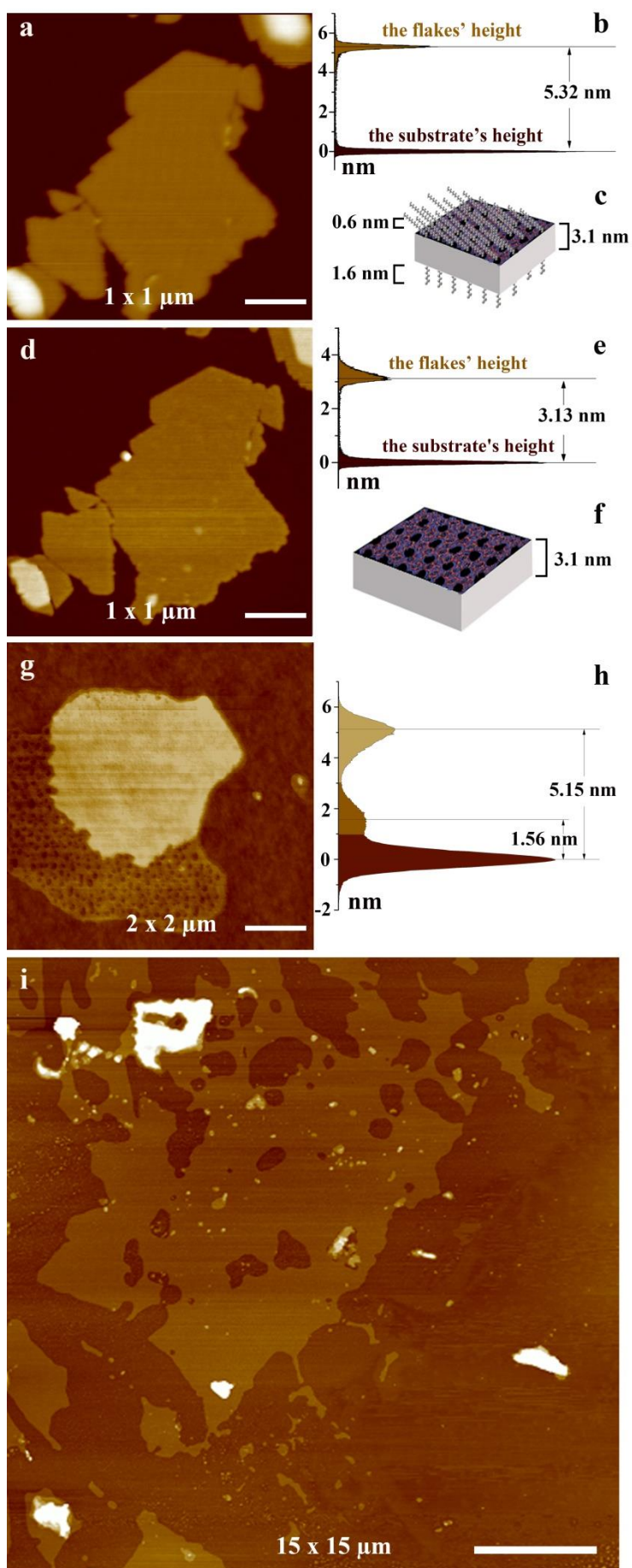


**Figure 3.2-3: AFM of exfoliated flakes, MFI.** AFM (tapping mode) images (a,d,g,i) and associated height histograms (b,e,h) show exfoliated flakes derived from the lamellar MFI structure. (a,b) shows flakes of the as-synthesised flakes that have a thickness  $5.3 \pm 0.1$  nm, and the schematic representation shows in (c). After calcination (d,e) to remove the templating surfactant the thickness reduces to on average  $3.1 \pm 0.1$  nm consistent with one and a half unit cells in the b-direction of the MFI structure, and the schematic representation shows in (f). The same flake in (a,d) can be track by AFM before and after calcination. In the as-synthesised sample the templating agent and the inorganic framework sometimes become detached and both layers can be seen independently (g,h). The largest MFI sheets are larger than  $10 \mu\text{m}$  in lateral dimension (i). The faint trace of the templating agent can also be seen in this image. Scale bars from (a) (d), (g) and (i) are 200 nm, 200 nm, 400 nm and  $3 \mu\text{m}$ .

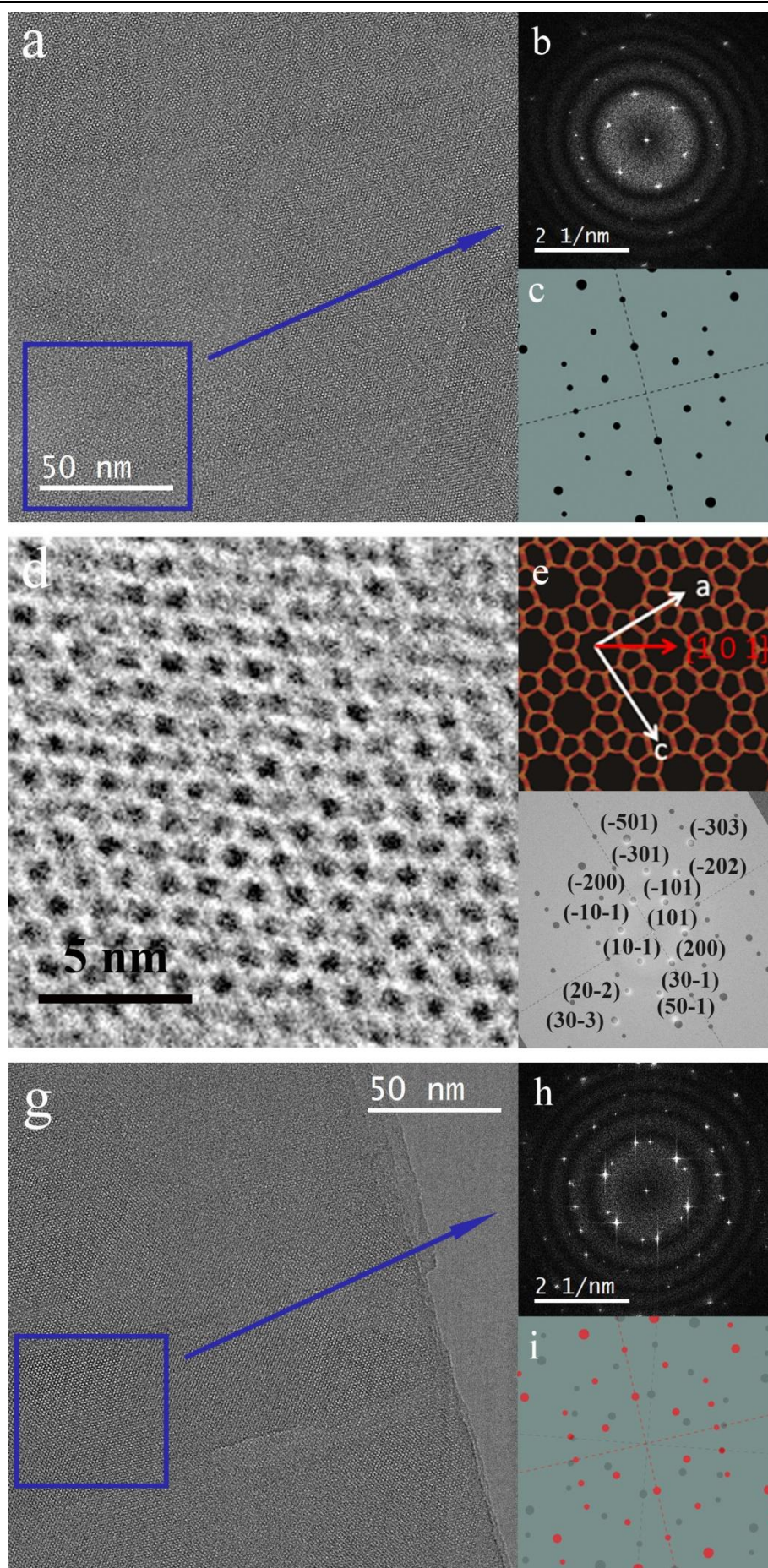


**Figure 3.2-4: TEM of exfoliated MFI.** The TEM images display the flake like morphology. The uniform contrast observed from the areas selected in the TEM image suggests these small areas have relatively uniform thickness. The as-synthesised monolayer of MFI nanosheet is just visible in the TEM images (a,d). However, the crystallinity of the structure can be confirmed from the sharp spots visible in the fast Fourier transform of the blue region in (a) is shown in (b). The FFT in (b) shows sharp spots instead of diffuse rings of contrast consistent with a single layer. Moreover, the simulation of electron diffraction pattern (c) of the MFI nanosheet can be used to confirm the orientation of the nanosheet. (d) HR-TEM images of the as-synthesised MFI monolayer oriented with the [010] direction normal to the sheet. (e) the model of MFI structure monolayer viewed along b-axis. (f) the simulation of electron diffraction pattern index the FFT of area (d). The TEM image of exfoliated flakes after calcination is shown in (g). The FFT of the blue region in (g) is shown in (h), and (i) shows the simulation of electron diffraction pattern of two single layers with different orientations.

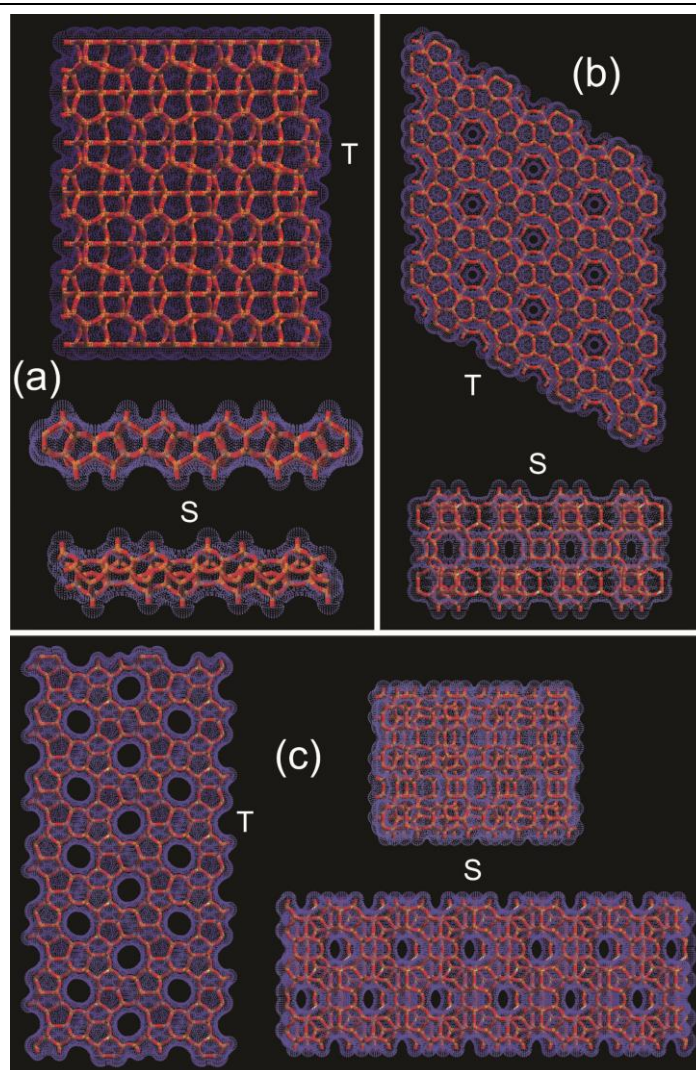


**Figure 3.2-5: Structures of exfoliated zeolites.** Top down (T) and side (S) views of the exfoliated zeolite structures. The underlying zeolite structure is shown within a van der Waals skin to illustrate the available pore space. (a) The UTL structure does not have any nanoporous passing through the nanosheet, however, the side-view shows how the corrugated nature of the pores that ran parallel to the nanosheet are retained. In a similar fashion the MWW structure (b) only has very small pores,  $< 0.2$  nm, passing through the sheets. This structure, however, has nanopockets decorating the sheet on both sides. The MFI nanosheets (c) show straight nanopores, ca 0.65 nm diameter, running through the sheet. There is also a secondary channel system that runs parallel to the sheet in a zig-zag pattern.

---

## **Paper 2. Supporting Information**

---

## Supporting Information

### Paper 2. Mechanical Exfoliation of Nanoporous Materials

Shiyu Xu<sup>1</sup>, Yun-Hao Hsieh<sup>1</sup>, Michael W. Anderson<sup>1\*</sup>, Konstantin S. Novoselov<sup>2</sup>,  
Colin R. Woods<sup>2</sup>, Sarah J. Haigh<sup>3</sup>, Eric Prestat<sup>3</sup>, Lan Nguyen<sup>3</sup>, and Jiří Čejka<sup>4</sup>

<sup>1</sup> Centre for Nanoporous Materials, School of Chemistry, The University of Manchester, Oxford Road, Manchester M13 9PL, UK.

<sup>2</sup> School of Physics, The University of Manchester, Oxford Road, Manchester M13 9PL, UK.

<sup>3</sup> School of Materials, The University of Manchester, Oxford Road, Manchester M13 9PL, UK.

<sup>4</sup> Department of Synthesis and Catalysis, J. Heyrovský Institute of Physical Chemistry, Academy of Sciences of the Czech Republic, v.v.i., Dolejškova 3, CZ-182 23 Prague 8, Czech Republic.

\*Correspondence to [m.anderson@manchester.ac.uk](mailto:m.anderson@manchester.ac.uk)

## Figures

## 1 X-ray diffraction

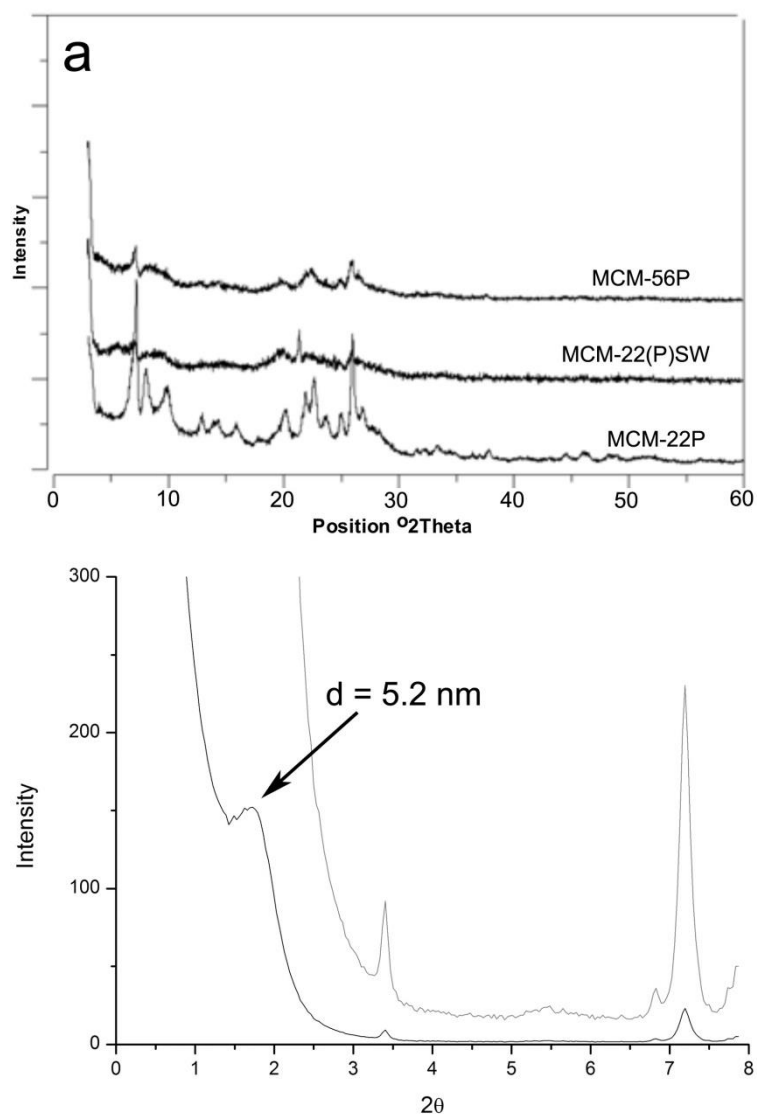


**Figure 3.2-S1: MWW structure.** (a) Powder x-ray diffraction patterns of MCM-56P and MCM-22P precursor materials and MCM-22(P)SW swollen material. (b) Small-angle x-ray diffraction showing low angle peak from basal plane of swollen MWW structure.



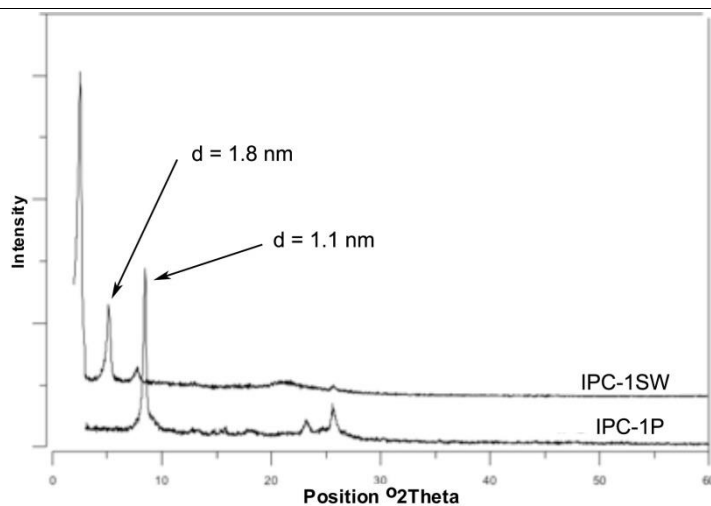


**Figure 3.2-S2: UTL structure.** Powder x-ray diffraction patterns of IPC-1P precursor material and IPC-1SW swollen material.

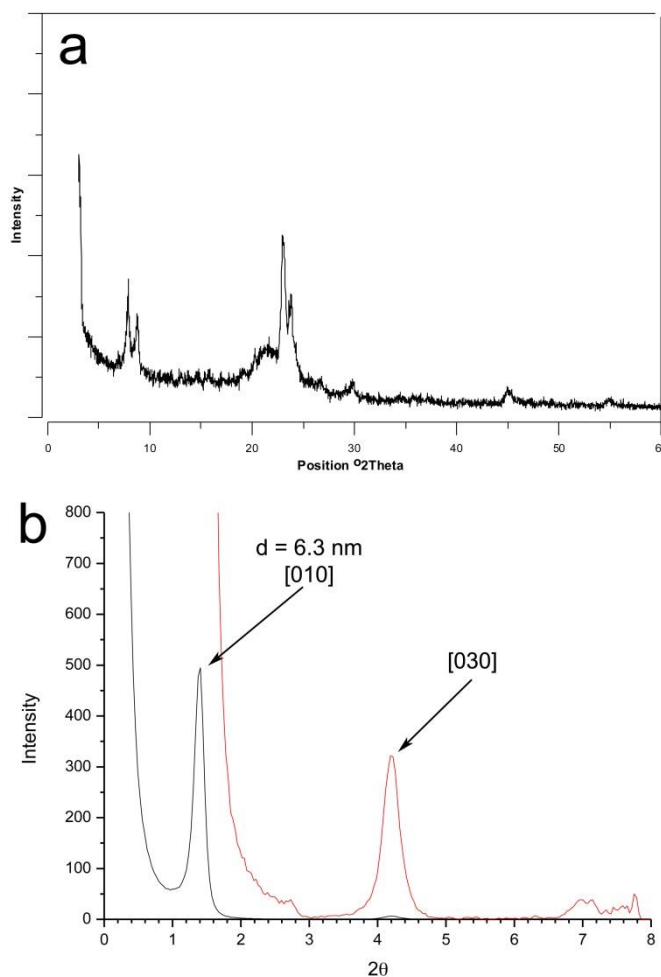


**Figure 3.2-S3: MFI structure.** (a) Powder x-ray diffraction patterns of lamellar MFI material, (b) small angle x-ray pattern showing diffraction from basal plane of layered material.

## 2 SEM

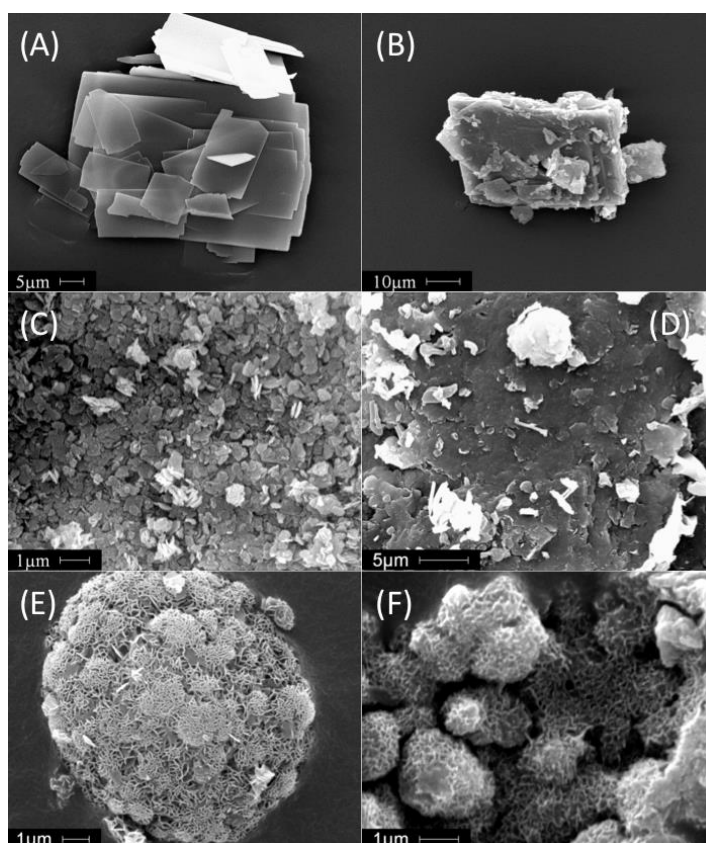


**Figure 3.2-S4: Scanning electron micrographs.** SEM images of zeolites: (A) IPC-1P, (B) IPC-1SW, (C) MCM-22P, (D) MCM-22(P)SW, (E) MCM-56P, (F) lamellar MFI.

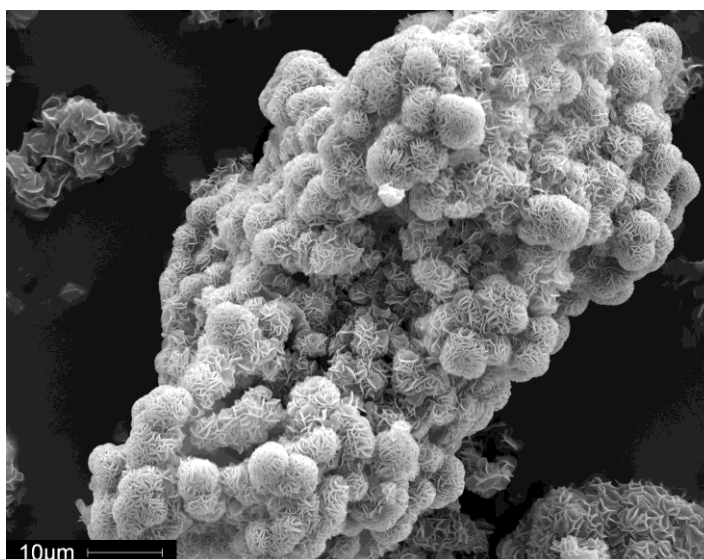


**Figure 3.2-S5: Scanning electron micrograph.** SEM image of lamellar MFI, low resolution.

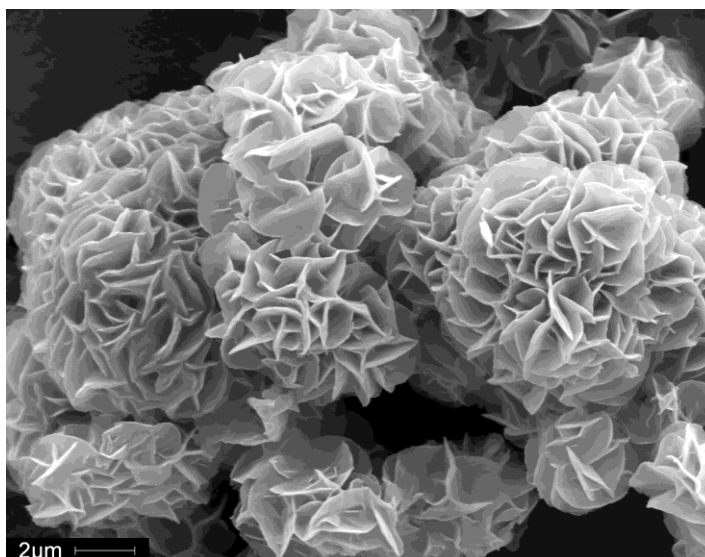


**Figure 3.2-S6: Scanning electron micrograph.** SEM image of lamellar MFI, medium resolution.

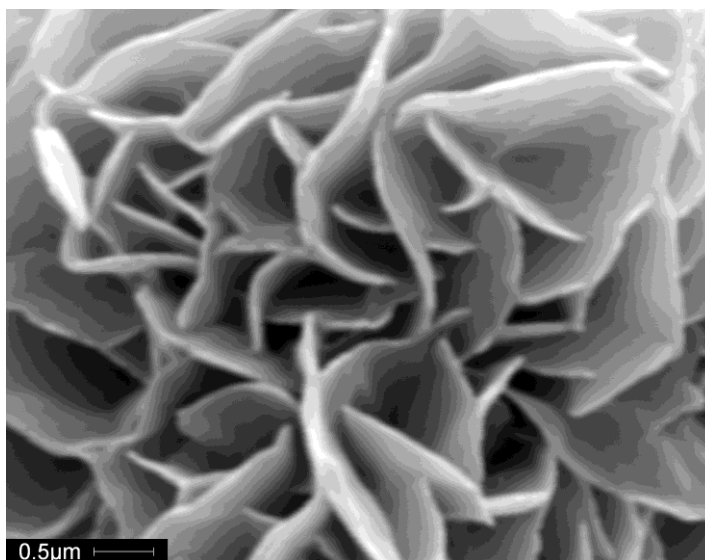


**Figure 3.2-S7: Scanning electron micrograph.** SEM image of lamellar MFI, high resolution.

## 3 AFM

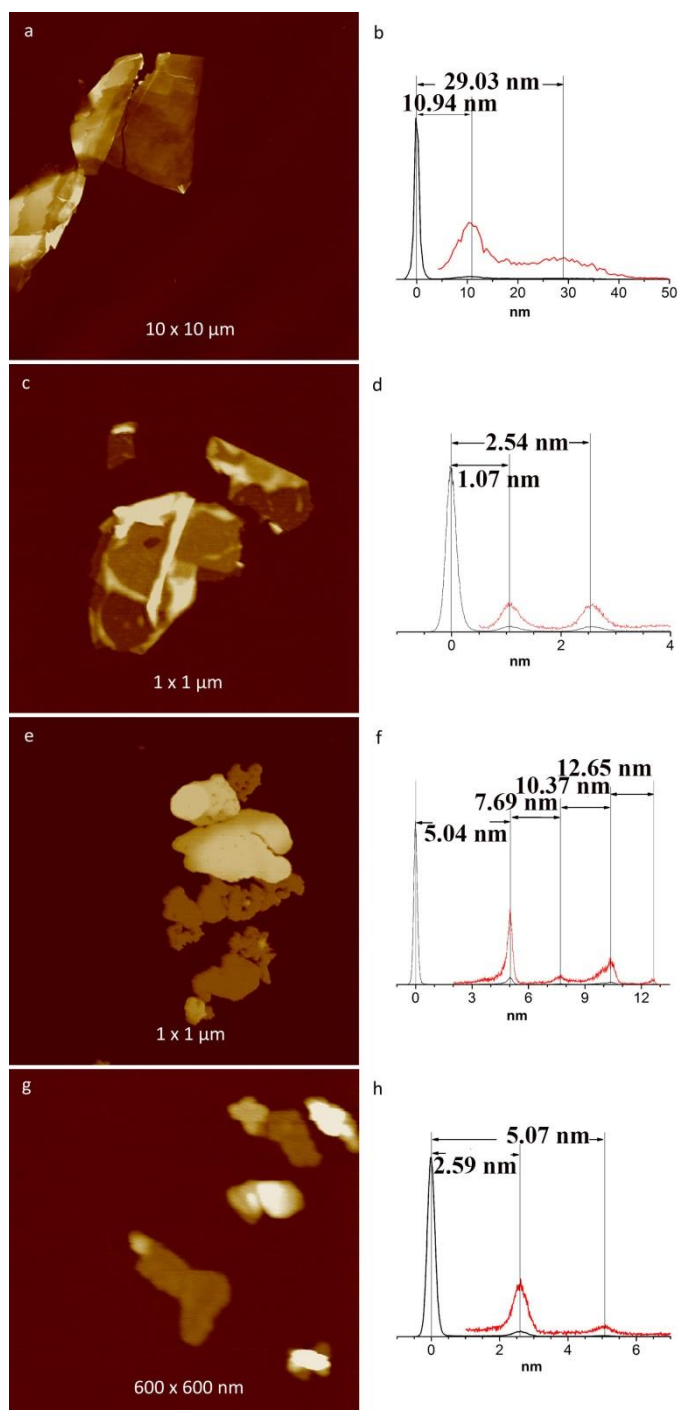


**Figure 3.2-S8: Atomic force micrographs and height histograms.** (a,b) IPC flakes from non-swollen precursor, (c,d) flakes from IPC swollen showing double layer, (e,f) flakes from MCM-22 swollen, as-synthesised showing multiple layers, (g,h) exfoliated MCM-56P. The first peak in the height histograms (b,d,f,h) represents the relative height of substrate measured by AFM and other peaks represent the relative height of zeolite flakes.

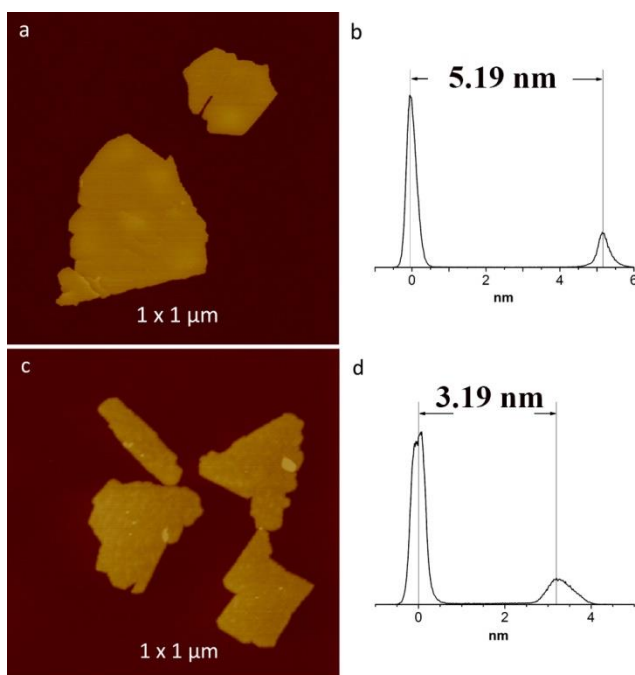


**Figure 3.2-S9: Atomic force micrographs and height histograms of MFI.**

(a,b) exfoliated sample, (c,d) exfoliated sample following calcination.

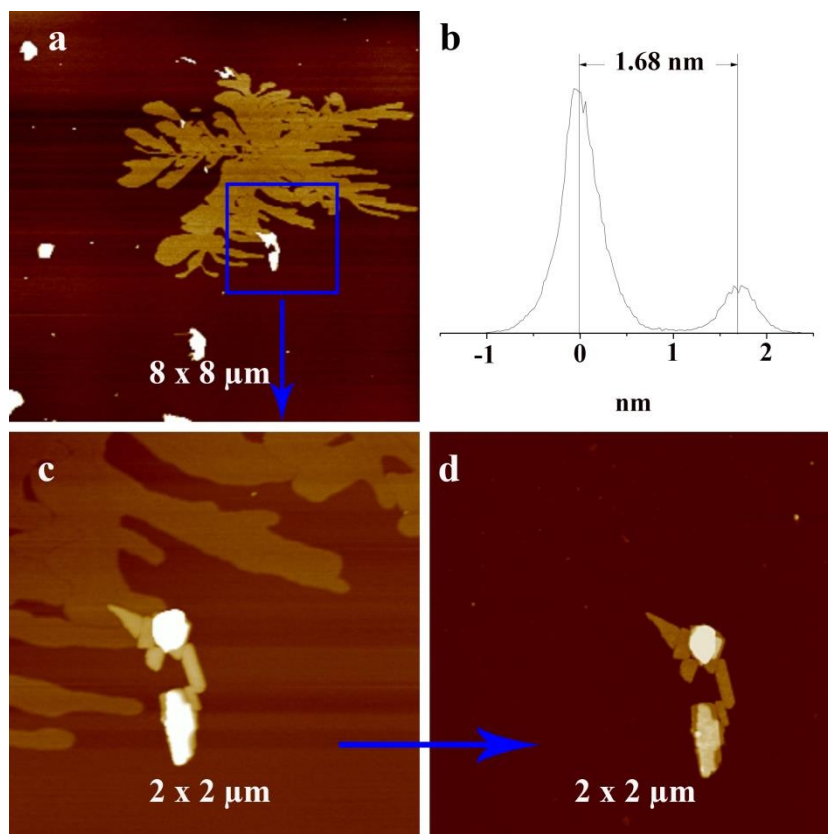


**Figure 3.2-S10: Atomic force micrographs and height histograms of deposited organic layer after exfoliation of MFI nanosheets.** (a,b) exfoliated sample, (c) the zoom-in scanning of the blue region in (a). (d) exfoliated sample following calcination. The deposited organic layer consistently  $1.6 \pm 0.1$  nm thick was removed by calcination.

#### 4 MFI nanosheet arrangements

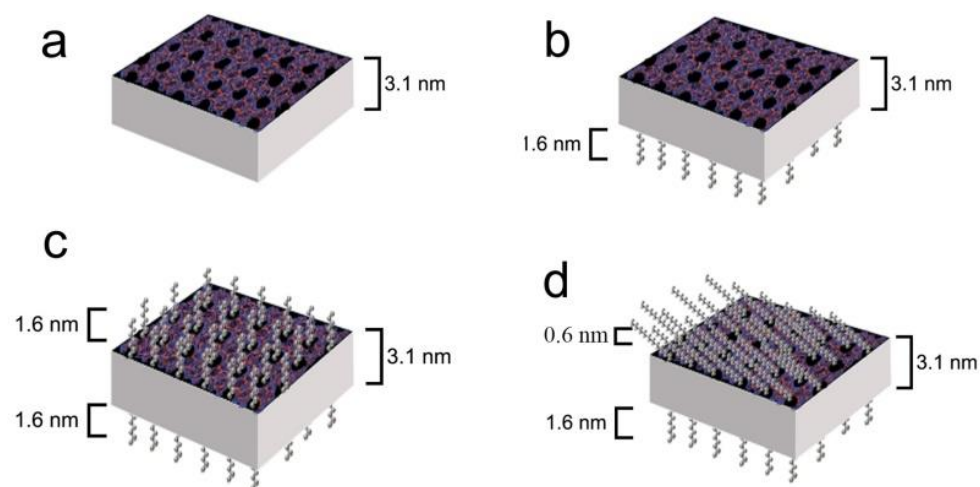


**Figure 3.2-S11: Schematic representations of possible MFI nanosheets.** (a) the nanosheet after exfoliation and calcination to remove organic templating agents. (b, c and d) are possible configurations as a result of exfoliation. (c) is the likely arrangement in the original layered MFI where the basal plane spacing is measured as 6.3 nm. (d) is the most likely arrangement after exfoliation where the nanosheet is 5.3 nm thick. The configuration of the organic templating agents is clearly different to the starting material as the layer thickness is only 5.3 nm. However, we measure organic layer deposits of 1.6 nm (see Fig. 3.2-S10) and therefore configuration (d) seems plausible.

## 5 TEM nanoporous nanosheets

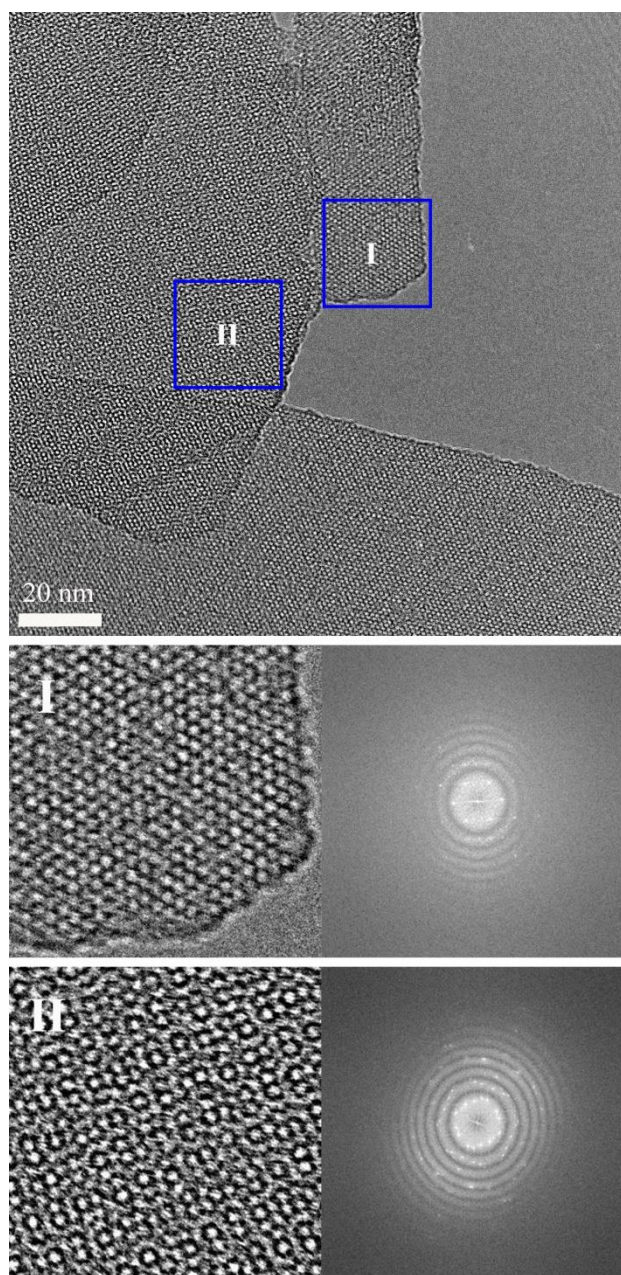


**Figure 3.2-S12: TEM of as-synthesised single- and multi-layer nanosheet MFI.** The HR-TEM images of the blue region (I), (II) and their fast Fourier transform display the single- and multi-layer MFI nanosheet oriented with the [010] direction.

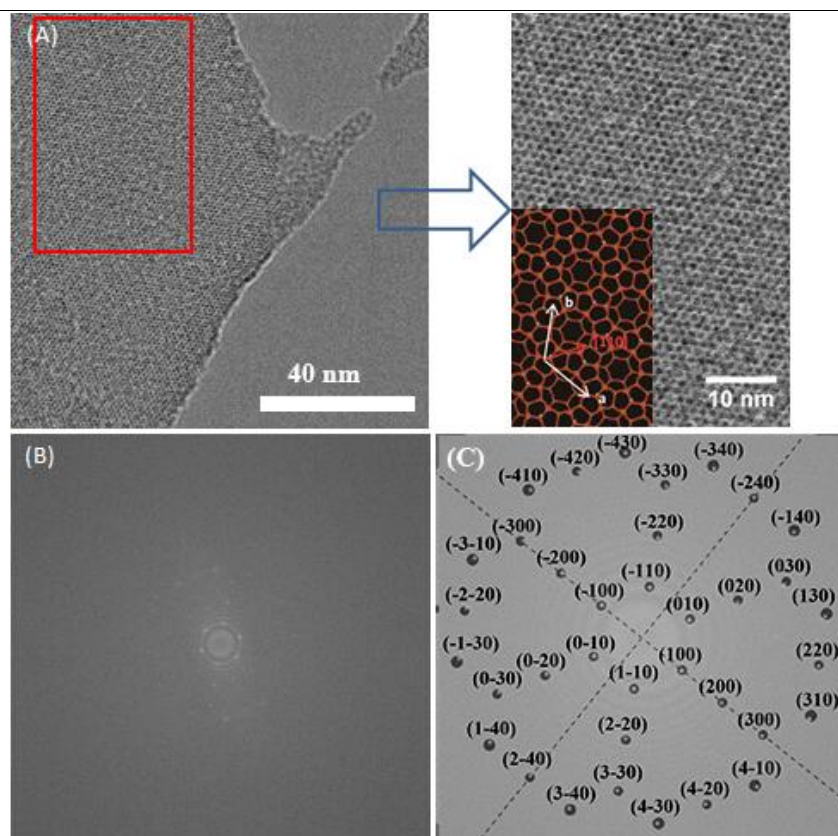


**Figure 3.2-S13: TEM of as-synthesised single-layer nanosheet MWW.** TEM images of (A) selected area of MWW monolayer with fast Fourier transform (B); (C) indexing of the selected area FFT.

**Figure 3.2-S14: TEM of as-synthesised single- and multi- layer nanosheet MWW.** TEM images of (A) selected area of MWW mono- and multi-layer with fast Fourier transform (B); (C) indexing of the selected area FFT.



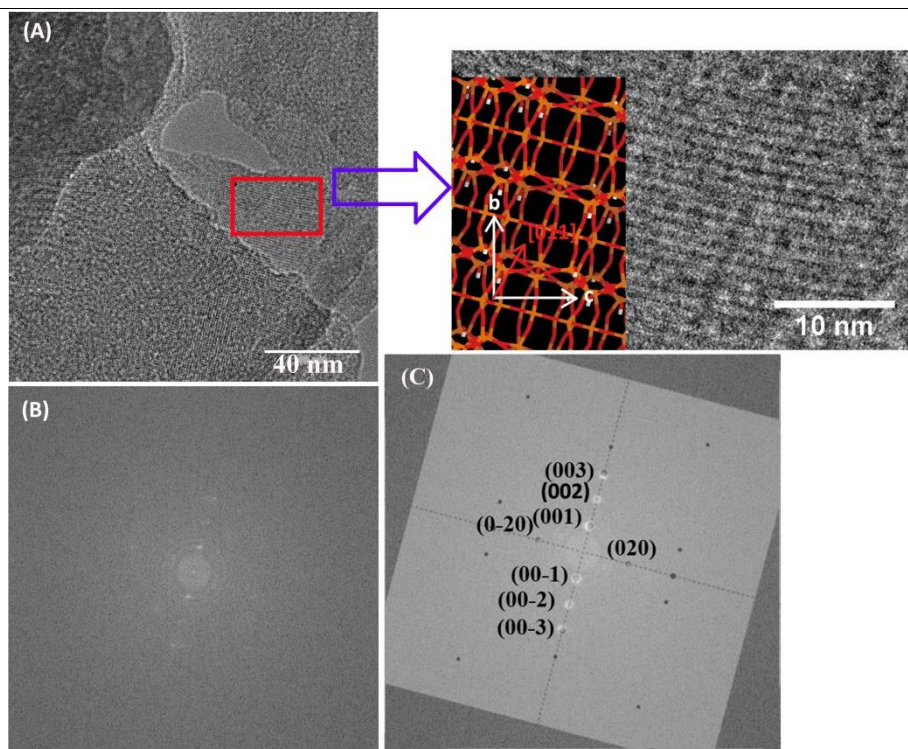


**Figure 3.2-S15: TEM of as-synthesised single- and multi-layer nanosheet UTL.** TEM images of single- and multi-layer UTL showing a selected area of the single-layer (A); fast Fourier transform (B); (C) indexing of the selected area FFT.

## 6 TEM transfer

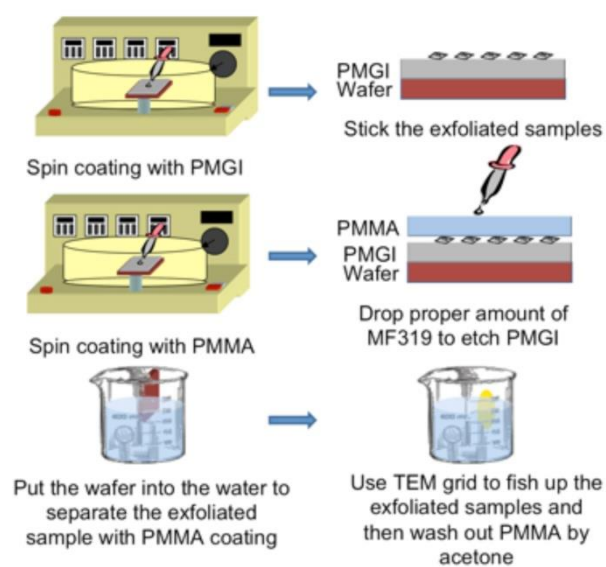


**Figure 3.2-S16: Transfer of nanosheets for TEM.** TEM sample transfer preparation methodology.

## 7 Zeolite nanosheet structures

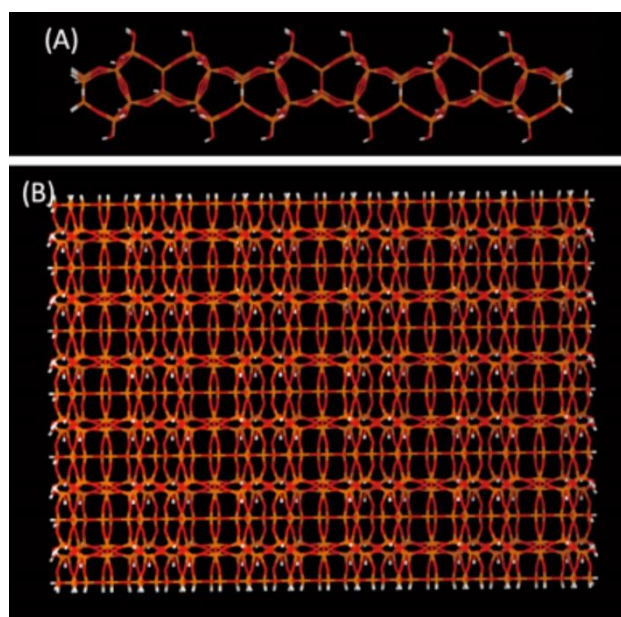


**Figure 3.2-S17: UTL nanosheet structure.** The model of IPC-1P monolayer (A) viewed along c-axis; (B) viewed along a-axis. Si, O and H atoms are colored in brown, red and white, respectively.

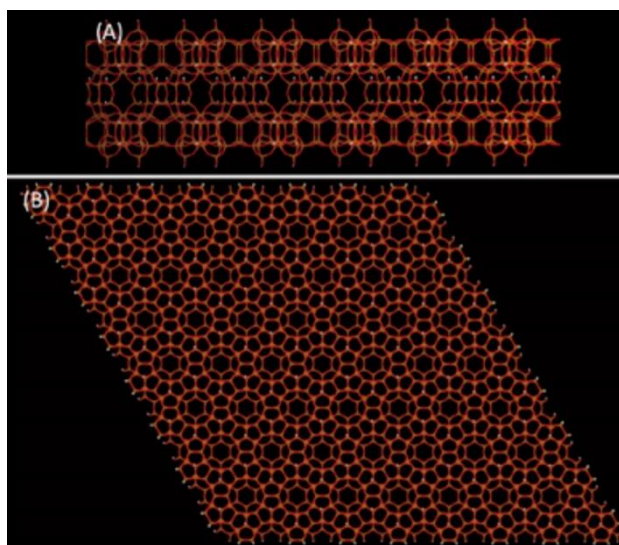


**Figure 3.2-S18: MWW nanosheet structure.** The model of MWW structure monolayer (A) viewed along a (or b)-axis; (B) viewed along c-axis. Si, O and H atoms are colored in brown, red and white, respectively.

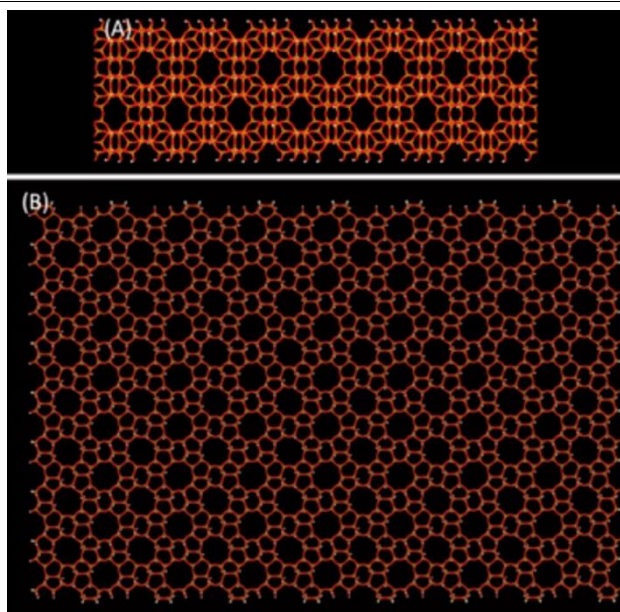


**Figure 3.2-S19: MFI nanosheet structure.** The model of MFI structure monolayer (A) viewed along a-axis; (B) viewed along b-axis. Si, O and H atoms are colored in brown, red and white, respectively.

---

**Paper 3. Encapsulation of platinum nano-clusters  
within exfoliated zeolite MFI nanosheets**

---

---

## **Paper 3. Encapsulation of platinum nano-clusters within exfoliated zeolite MFI nanosheets**

Shiyu Xu<sup>1</sup>, Michael W. Anderson<sup>1\*</sup>, Konstantin S. Novoselov<sup>2</sup>, Hague Lee<sup>2</sup>, Sarah J. Haigh<sup>3</sup>, Eric Prestat<sup>3</sup>

<sup>1</sup>Centre for Nanoporous Materials, School of Chemistry, The University of Manchester, Oxford Road, Manchester M13 9PL, UK.

<sup>2</sup>School of Physics, The University of Manchester, Oxford Road, Manchester M13 9PL, UK.

<sup>3</sup>School of Materials, The University of Manchester, Oxford Road, Manchester M13 9PL, UK.

\*e-mail: [m.anderson@manchester.ac.uk](mailto:m.anderson@manchester.ac.uk)

Paper not submitted for publication.

### **Author Contributions:**

The synthesis of exfoliated zeolite MFI nanosheets and encapsulation experiments were performed by S. Xu. The TEM experiments were performed by H. Lee and E. Prestat. XRD, SEM, NMR, AFM and simulation experiments were performed by S. Xu, and the article was written by S. Xu. All author contributed to analysis of the data and discussions.

---

## Encapsulation of platinum nano-clusters within exfoliated zeolite MFI nanosheets

Shiyu Xu<sup>1</sup>, Michael W. Anderson<sup>1\*</sup>, Konstantin S. Novoselov<sup>2</sup>, Hague Lee<sup>2</sup>, Sarah J. Haigh<sup>3</sup>, Eric Prestat<sup>3</sup>

<sup>1</sup>Centre for Nanoporous Materials, School of Chemistry, The University of Manchester, Oxford Road, Manchester M13 9PL, UK.

<sup>2</sup>School of Physics, The University of Manchester, Oxford Road, Manchester M13 9PL, UK.

<sup>3</sup>School of Materials, The University of Manchester, Oxford Road, Manchester M13 9PL, UK.

\*e-mail: [m.anderson@manchester.ac.uk](mailto:m.anderson@manchester.ac.uk)

### Abstract

Platinum nano-clusters are successfully encapsulated within exfoliated zeolite MFI nanosheets by ion exchange from aqueous solution of  $[\text{Pt}(\text{NH}_3)_4](\text{NO}_3)_2$ . The Pt clusters are well dispersed and uniform within the MFI nanosheets. Simulation suggests that the Pt clusters are located in both the straight channels and the sinusoidal channels of the MFI structure. High-angle annular dark field scanning transmission electron microscopy studies indicate that the Pt clusters size (~0.99 to 1.65 nm) is mediated in the zeolite MFI structures by the post-processes. This technique can integrate both the nanoporous architecture and the inherent insulating characteristic of the single zeolite nanosheets, and the encapsulated Pt clusters within the MFI structure might broaden the application beyond the traditional uses, such as micromechanical, optoelectronic, nanoscopic capacitors or other devices.

### Introduction

Zeolites are nanoporous crystalline materials, containing regular arrays of channels and cavities.<sup>1</sup> Encapsulating metals within these channels or cavities has already drawn much attention because of the well-defined structure that is able to constrain the metal nanoparticle (NPs) aggregation size and enhance the diversity and activity for catalysis.<sup>2</sup> MFI is a structure type for the aluminosilicate or

silicate zeolites, that has a three-dimensional pore structure consisting of 10-tetrahedral atom rings to give a pore dimension of *ca.* 0.65 nm.<sup>3</sup> A number of strategies have hitherto been used to successfully encapsulate metal clusters of Pt, Ru, Rh and Pd into bulk zeolite MFI.<sup>4-6</sup>

Multi-lamellar zeolite MFI, with thickness 1.5 unit cells with the b-axis orthogonal to the nanosheet, have been generated by using di-quaternary ammonium surfactants with head-group that templates the MFI structure and long hydrocarbon chain that forms a lamellar mesophase.<sup>7</sup> Two different methods have been reported to load Pt NPs on the MFI nanosheets: ion-exchange to load the Pt NPs inside the pores of the zeolite MFI nanosheets and colloidal impregnation to load the Pt NPs on the external surface of the zeolite MFI nanosheets.<sup>8</sup>

The single MFI nanosheet are 3 nm thick in the b-direction with straight 0.65 nm nanopores traversing the nanosheet each separated by 1.3 nm (see Figure 3.3-S6). Until now, the single zeolite MFI nanosheets could be obtained by three different methods: (i) by using 30 nm MFI crystal seeds to trigger the epitaxial growth of zeolite MFI nanosheets with thickness about 5 nm;<sup>9</sup> (ii) melt-blend the mixture of polymer and multilamellar zeolite MFI and centrifuge to separate out the exfoliated zeolite MFI nanosheets with thickness about 3 nm;<sup>10</sup> (iii) the multilamellar zeolite MFI is repeatedly cleaved by the application of a sticky tape resulting in the mechanical exfoliation of zeolite MFI nanosheets with thickness about 3 nm.

To date, most applications requiring incorporation of metal clusters within zeolites structure are for use as catalysts. However, with the development of the preparation of single zeolite nanosheets, encapsulation of metal nano-clusters within the ultrathin insulating zeolite nanosheets has broadened the application beyond the traditional uses. The integration of both the nanoporous architecture and the inherent insulating characteristic of the single zeolite nanosheets provide the possibility for some new applications, for example, as components in micromechanical, optoelectronic, nanoscopic capacitors or other devices.

Here, we investigate encapsulation of Pt clusters within the exfoliated zeolite



MFI nanosheets and the Pt NPs size mediated in the zeolite MFI structures by related post-process that are listed in Table 3.3-1. The exfoliated zeolite MFI nanosheets were prepared by mechanical exfoliation of the multilamellar zeolite MFI with a 1.5 unit cell thick of each MFI nanosheet along the b-axis. An aqueous solution of  $[\text{Pt}(\text{NH}_3)_4](\text{NO}_3)_2$  has been used as the metal precursor. Zeolite MFI structure require high synthesis temperatures ( $>150\text{ }^\circ\text{C}$ ) that decompose the even ligand-stabilized precursor  $[\text{Pt}(\text{NH}_3)_4](\text{NO}_3)_2$ . Thus, the Pt particles precipitate before the zeolite crystalizing at the high temperature ( $>150\text{ }^\circ\text{C}$ ), and it is inaccessible to encapsulate the Pt clusters within MFI via direct hydrothermal synthesis. The Pt clusters were encapsulated within the exfoliated zeolite MFI nanosheets by ion exchange. The platinum ions were reduced using hydrogen as the reducing agent. In order to investigate the Pt cluster distribution and mediation in the zeolite MFI structures, the exfoliated Na-MFI nanosheets were used for subsequent ion exchange with platinum, and the platinum ions in zeolite MFI structure were thermally treated in air prior to reduction.

## Experiment

**Chemicals.** 1-bromodocosane (96%, Sigma-Aldrich), N,N,N',N'-tetramethyl-1,6-diaminohexane (99%, Sigma-Aldrich), acetonitrile (99.8%, Sigma-Aldrich), toluene (99.8%, Sigma-Aldrich), diethyl ether (99%, Fisher Scientific), 1-bromohexane (98%, Sigma-Aldrich), ethanol ( $\geq 99.8\%$ , Sigma-Aldrich), Tetraethylorthosilicate (TEOS, 99.999%, Sigma-Aldrich), Aluminum sulfate hydrate ( $\text{Al}_2(\text{SO}_4)_3 \cdot \text{H}_2\text{O}$ ,  $\geq 98\%$ , Sigma-Aldrich), NaOH (99.995%, Sigma-Aldrich),  $\text{H}_2\text{SO}_4$  (99.999%, Sigma-Aldrich), deionized water (18.2  $\text{M}\Omega\text{ cm}^{-1}$  at 25  $^\circ\text{C}$ , Milli-Q Direct 8, Merck Millipore), polymethylglutarimide (PMGI, MicroChem Corp.), poly(methyl methacrylate) (PMMA, MicroChem), NaCl ( $\geq 99\%$ , Sigma-Aldrich),  $[\text{Pt}(\text{NH}_3)_4](\text{NO}_3)_2$  (99.995%, Sigma-Aldrich), and isopropyl alcohol (IPA,  $\geq 99\%$ , Sigma-Aldrich).

**Synthesis of organic surfactant ( $\text{C}_{22-6-6}\text{Br}_2$ ).** 10 g 1-bromodocosane and 43 g N,N,N',N'-tetramethyl-1,6-diaminohexane were dissolved in 250 ml acetonitrile

/toluene mixture (1: 1 vol/vol) and heated under reflux at 70 °C overnight. Then, the mixture was cooled down to room temperature. After filtering and washing with diethyl ether, the product was dried in oven at 50 °C overnight. 6.9 g product and 3.4 g 1-bromohexane were dissolved in 130 ml acetonitrile and 12 ml ethanol to reflux overnight, then cooled down to room temperature. After filtering and washing with diethyl ether, the product was dried in oven at 50 °C overnight.

**Synthesis of lamellar MFI.** Tetraethylorthosilicate, Aluminum sulfate hydrate ( $\text{Al}_2(\text{SO}_4)_3 \cdot \text{H}_2\text{O}$ ), NaOH, organic surfactant,  $\text{H}_2\text{SO}_4$ , and deionized water were mixed to obtain a gel composition of  $30\text{Na}_2\text{O}: 1\text{Al}_2\text{O}_3: 100\text{SiO}_2: 10\text{C}_{22-6-6}\text{Br}_2: 18\text{H}_2\text{SO}_4: 4000\text{H}_2\text{O}$ . The gel was heated in a Teflon-lined autoclave at 158 °C with rotation (~60 rpm) for 8 days. The solid product was recovered by filtration with deionized water and dried overnight at 100 °C.

**Mechanical exfoliation.** To separate the layered zeolite, nitto processing tape (BT-150E-CM, TELTEC) was used to perform repeat peeling of the sample. A silicon wafer with 290 nm oxide coating (Mi-Net) was used as the substrate for the exfoliated samples. Then, the tape was stuck on the silicon wafer and peeled the tape. The exfoliated single and multi-layers zeolite MFI were on the substrates.

**TEM sample transfer.** For transfer of the exfoliated samples for TEM before the mechanical exfoliation the silicon wafer was spin coated with polymethylglutarimide (PMGI). The exfoliated samples were then attached to the silicon wafer with PMGI coating. The wafer was then spin coated with poly(methyl methacrylate) (PMMA,). The exfoliated sample was now sandwiched between PMGI and PMMA. The selected area on the wafer was marked with a tweezer and MF-319 developer was used to etch the PMGI. The wafer was put slowly into water to separate the selected area with PMMA coating. The selected area with PMMA coating floated on the water and a TEM grid was used to fish it up. The dried TEM grid was washed with acetone to remove the PMMA coating on the exfoliated samples.

**Calcination of the exfoliated layers.** The resulting exfoliated layers on the

TEM grids were calcined at 550 °C in air for 4h to remove the templates.

**Encapsulation of Pt clusters within exfoliated MFI layers.** <sup>a</sup>The TEM grids with exfoliated layers on it were immersed into NaCl (1M) solution at room temperature overnight, then the TEM grids were washed with deionized water and dried in the oven at 100 °C overnight. The resulting grids were used for subsequent ion exchange with platinum. <sup>b</sup>Platinum was encapsulated within exfoliated MFI layers by ion exchange from [Pt(NH<sub>3</sub>)<sub>4</sub>](NO<sub>3</sub>)<sub>2</sub> (~1% wt metal content) aqueous solution at room temperature overnight, then washed with deionized water and dried in the oven at 100 °C overnight. <sup>c</sup>The sample was treated in flowing air and heated to 350 °C at 15 °C/min and held for 2 h. <sup>d</sup>The sample was reduced in flowing H<sub>2</sub>/N<sub>2</sub> and heated to 300 °C at 15 °C/min and held for 2 h. The four procedures (a,b,c,d) were not all executed for samples S1-S5. Table 3.3-1 indicates the different procedures that were executed for samples S1, S2, S3, S4, and S5, respectively.

**Structural characterization.** Scanning electron microscopy (SEM) images were taken with an FEI XL30 Environmental scanning electron microscope. Transmission electron microscopy (TEM) images were taken with the Titan G2 chemiSTEM electron microscope operated at 200 kV. The holey silicon nitride support TEM grids (Protochips) should be cleaned by rising with isopropyl alcohol (IPA), before use, then the grids were coated with 5 nm PdAu to eliminate the electron charging during TEM process. The averaged diameter  $d_{\text{TEM}}$  was calculated by ImageJ software. Atomic force microscopy (AFM) images were obtained by PeakForce QNM (Quantitative Nano Mechanics) from MultiMode 8 AFM (Bruker). The simulation was performed by Material Studio software.

## Results and discussion

The XRD and SAXS patterns of the nanoplatelet MFI structure for exfoliation are shown in Figs. 3.3-S1 and S2. The only (*h0l*) reflections in the XRD pattern index the structure with layer normal parallel to [010], and SAXS assigned the first reflection (010) with  $d = 6.3$  nm and third the (030) reflection.

The SEM image (Fig. 3.3-S3) shows petal-shaped zeolite has been formed. To introduce the metals into the zeolite by ion exchange, normally Al needs to be first introduced in order to create a framework charge. The  $^{29}\text{Si}$  MAS spectrum (Fig. 3.3-S4) shows three strong signals at -102 ppm, 107 ppm and -112 ppm that corresponds to  $\text{Q}^3=\text{Si}(\text{OSi})_3(\text{OH})$ ,  $\text{Q}^4(1\text{Al})=\text{Si}(\text{OSi})_3(\text{OAl})$  and  $\text{Q}^4(0\text{Al})=\text{Si}(\text{OSi})_4$  silicon environments. According to the formula

$$(\text{Si}/\text{Al})_{\text{NMR}} = \frac{I_4 + I_3 + I_2 + I_1 + I_0}{I_4 + 0.75I_3 + 0.5I_2 + 0.25I_1} \quad 11$$

Where  $I_n$  is the area of the NMR peak corresponding to the  $\text{Si}(n\text{Al})$  building unit, the Si/Al of the MFI nanosheets is *ca.* 42 and the corresponding  $^{27}\text{Al}$  MAS NMR spectrum is shown in Fig. 3.3-S5. The strong signal around 53 ppm corresponds to tetrahedral framework Al sites.<sup>12</sup>

After mechanical exfoliation to produce the MFI flakes the organic template is removed by calcination. The TEM image in Fig. 3.3-1a shows the single inorganic MFI nanosheets. The fast Fourier transform spectrum of this (Fig. 3.3-1b) indicates the [010] incidence of MFI structure, and the crystallinity can be confirmed by the sharp spots. Fig. 3.3-1c shows the model of MFI structure monolayer viewed along b-axis. In order to study the small nanoparticles that consist of heavy elements HAADF-STEM (high-angle annular dark field scanning transmission electron microscopy) was used to characterize the MFI nanosheets after Pt loading.<sup>13</sup>

The Pt clusters are well-dispersed and uniform on the MFI nanosheets. The average size of the Pt clusters in Figure 3.3-1 is 1.33 nm, 1.62 nm, 1.55 nm and 0.99 nm for sample S2, S3, S4, and S5, respectively.<sup>14</sup> The Pt clusters are identified in the HAADF-STEM images as the bright contrast features, superimposed on the darker flakes that correspond to the exfoliated MFI nanosheets. Figs. 3.3-1(f-o) show the particle size distribution based on measurements from Figs. 3.3-1(e-h).

All the exfoliated MFI nanosheets for encapsulation have been calcined to yield the inorganic nanosheet. Sample S3-5 were prepared by immersing the exfoliated MFI nanosheets into NaCl solution to yield Na-zeolite nanosheets, and

the resulting materials were used for subsequent ion exchange with Pt and other post-treatments. Comparing with sample S5 (see Figs. 3.3-1 m-o), the Pt clusters in Sample S4 (see Figs. 3.3-1 j-i) were reduced by H<sub>2</sub> after ion exchange to produce Pt NPs. After reduction the size of Pt clusters increased from 0.95 nm to 1.55 nm. Sample S3 (see Figs. 3.3-1 g-i) was thermally treated in flowing air that contains 21% O<sub>2</sub> prior to the H<sub>2</sub> reduction, and this treatment promoted the Pt clusters to be homogeneously distributed within zeolite structure. Comparing with sample S3, The Pt clusters were encapsulated within exfoliated zeolite MFI nanosheets by directly immersing the sample into [Pt(NH<sub>3</sub>)<sub>4</sub>](NO<sub>3</sub>)<sub>2</sub> solution instead of forming Na-zeolite nanosheets first. (see Figs. 3.3-1 d-f).

Comparing Fig. 3.3-1e with Fig. 3.3-1h, in the same size area (20 nm x 20 nm), the Pt clusters density of sample S3 (see Fig. 3.3-1e) is higher than the Pt clusters density of sample S2 (see Fig. 3.3-1h). Because the precursor [Pt(NH<sub>3</sub>)<sub>4</sub>](NO<sub>3</sub>)<sub>2</sub> decompose and yield HNO<sub>3</sub> in the aqueous solution, that could break the zeolite structure. After immersing the exfoliated Na-MFI nanosheet into [Pt(NH<sub>3</sub>)<sub>4</sub>](NO<sub>3</sub>)<sub>2</sub> solution, the solution is mediated by counterions of Na<sup>+</sup> that can protect the zeolite framework and promote the ion exchange of metal Pt. The Pt cluster size increases with thermal treatments, from 0.99 nm (see Fig. 3.3-1o) to 1.55 nm (see Fig. 3.3-1l) and 1.62 nm (see Fig. 3.3-1i) due to an Ostwald ripening process, in order to minimize the surface free energy by growing larger crystals.<sup>15</sup> Except for the Ostwald ripening process other post-treatments such as producing the Na-MFI nanosheets before ion exchange of metal Pt also varies the encapsulated Pt clusters over a considerable size range. However, at the individual nanoparticle level discrepancies suggesting that the atom mediation also relates to the local environment.

The Pt NPs observed in Figure 1 were about 0.99- 1.62 nm, which is larger than the MFI channels 0.65 nm diameter as well as the intersectional channels 0.9 nm.<sup>16</sup> The high-resolution HAADF-STEM images (Fig. 3.3-2a) strikingly show some small Pt clusters about 0.26, 0.39 and 0.49 nm in sample S3, that might be located in both the straight channels and the sinusoidal channels. The simulation

(Fig. 3.3-2d) was performed by universal force field to predict the location of the guest species of Pt. The larger size of Pt NPs observed (Fig. 3.3-1) might be due to two reasons, (i) the Pt NPs aggregate on the surface of the exfoliated MFI flakes; (ii) the visual aggregation of the Pt NPs within adjacent channels in the MFI structures. The FFT spectrum in Fig. 3.3-2b indicated that the Pt clusters were encapsulated into two single MFI layer with different orientations, and the MFI structure remains intact under the diffraction. Fig. 3.3-2c shows the Pt-MFI nanosheets (sample S5) without H<sub>2</sub> reduction and thermal treatment in flowing air.

AFM images of sample S3 are shown in Fig. 3.3-3. The bright contrast features in the height images correspond to the second layer of the MFI flakes. The height data of the line highlighted in Fig. 3.3-3a is plotted in Fig. 3.3-3b. The nanoparticles of *ca.* 1.62 nm size have, therefore, not been found on the surface of the exfoliated MFI nanosheets, that can prove the Pt clusters are consequently encapsulated within the exfoliated structure.

So far two-dimensional atomic crystals such as graphene<sup>17</sup> are molybdenum disulphide (MoS<sub>2</sub>)<sup>18</sup> have been studied in the nearly a decade. The new growing interest develops in putting a monolayer on top of another monolayer or few-layer crystal to fabric new architecture devices<sup>19</sup> that are being considered as electronic, optoelectronic, micromechanical and other devices. Extending the building blocks from these 2D atomic crystals to the 3D compounds monolayers and stacking on top of other isolating 2D crystals are two important directions to the further work. Pt clusters that have small electrical resistivity  $\rho$  ( $1.06 \times 10^{-7} \Omega \cdot \text{m}$  at 20 °C)<sup>20</sup> were achieved to encapsulate within the insulating single nanosheet that contain zeolite MFI nanoporous architecture. The single Pt-MFI nanosheet as 3D compounds monolayers extend the diversity of building blocks. Therefore, encapsulation of Pt clusters within exfoliated zeolite MFI nanosheets is an important attempt to broaden the application beyond the traditional uses of 2D zeolites, and develop into a large field of their own.

## Conclusions

Platinum nano-clusters are successfully encapsulated within exfoliated zeolite MFI nanosheets with 3 nm thickness (1.5 unit cells of each nanosheet along b-axis) by ion-exchange from aqueous solution of  $\text{Pt}(\text{NH}_3)_4][\text{NO}_3]_2$ . Moreover, the HAADF-STEM images show that the encapsulated Pt clusters size within the exfoliated MFI nanosheets was followed by an Ostwald ripening process. The Pt particle size is ca 0.95 nm after ion exchange. After reduced by  $\text{H}_2$  at 300 °C, the Pt particle size increases to ca 1.55 nm. After the thermally treatment flowing in air at 350 °C, the Pt particle size increases to ca 1.62 nm. Preparing the exfoliated Na-MFI nanosheet for subsequent ion exchange with Pt can protect the zeolite framework and promote the ion exchange of metal Pt. AFM measurements are combined to confirm the Pt clusters are encapsulated within the exfoliated structure instead of locating on the surface.

## References

- (1) Cundy, C. S.; Cox, P. A. The Hydrothermal Synthesis of Zeolites: History and Development from the Earliest Days to the Present Time. *Chemical Reviews* **2003**, 103, 663-702.
- (2) Farrusseng, D.; Tuel, A. Perspectives on Zeolite-Encapsulated Metal Nanoparticles and Their Applications in Catalysis. *New Journal of Chemistry* **2016**, 40, 3933-3949.
- (3) Framework Type MFI. <http://europe.iza-structure.org/IZA-SC/framework.php?STC=MFI>
- (4) Goel, S.; Zones, S. I.; Iglesia, E. Encapsulation of Metal Clusters within MFI via Interzeolite Transformations and Direct Hydrothermal Syntheses and Catalytic Consequences of Their Confinement. *Journal of the American Chemical Society* **2014**, 136, 15280-15290.
- (5) Gu, J.; Zhang, Z.; Hu, P.; Ding, L.; Xue, N.; Peng, L.; Guo, X.; Lin, M.; Ding, W. Platinum Nanoparticles Encapsulated in MFI Zeolite Crystals by a Two-Step Dry Gel Conversion Method as a Highly Selective Hydrogenation Catalyst. *ACS Catalysis* **2015**, 5, 6893-6901.
- (6) Wang, N.; Sun, Q.; Bai, R.; Li, X.; Guo, G.; Yu, J. In Situ Confinement of Ultrasmall Pd Clusters within Nanosized Silicalite-1 Zeolite for Highly Efficient Catalysis of Hydrogen Generation. *Journal of the American Chemical Society* **2016**, 138, 7484-7487.
- (7) Choi, M.; Na, K.; Kim, J.; Sakamoto, Y.; Terasaki, O.; Ryoo, R. Stable Single-Unit-Cell Nanosheets of Zeolite MFI as Active and Long-Lived Catalysts. *Nature* **2009**, 461, 246-249.
- (8) Kim, J.; Kim, W.; Seo, Y.; Kim, J.-C.; Ryoo, R. n-Heptane Hydroisomerization over Pt/MFI Zeolite Nanosheets: Effects of Zeolite Crystal Thickness and Platinum Location. *Journal of Catalysis* **2013**, 301, 187-197.
- (9) Jeon, M. Y.; Kim, D.; Kumar, P.; Lee, P. S.; Rangnekar, N.; Bai, P.; Shete, M.; Elyassi, B.; Lee, H. S.; Narasimharao, K.; Basahel, S. N.; Al-Thabaiti, S.; Xu, W.; Cho, H. J.; Fetisov, E. O.; Thyagarajan, R.; DeJaco, R. F.; Fan, W.; Mkhoyan, K. A.; Siepmann, J. I.; Tsapatsis, M. Ultra-Selective High-Flux Membranes from Directly Synthesized Zeolite Nanosheets. *Nature* **2017**, 543, 690-694.
- (10) Varoon, K.; Zhang, X.; Elyassi, B.; Brewer, D. D.; Gettel, M.; Kumar, S.; Lee, J. A.; Maheshwari,

- S.; Mittal, A.; Sung, C.-Y.; Cococcioni, M.; Francis, L. F.; McCormick, A. V.; Mkhoyan, K. A.; Tsapatsis, M. Dispersible Exfoliated Zeolite Nanosheets and Their Application as a Selective Membrane. *Science* **2011**, 334, 72-75.
- (11) Zhan, B.-Z.; White, M. A.; Lumsden, M.; Mueller-Neuhaus, J.; Robertson, K. N.; Cameron, T. S.; Gharghour, M. Control of Particle Size and Surface Properties of Crystals of NaX Zeolite. *Chemistry of Materials* **2002**, 14, 3636-3642.
- (12) Wu, L.; Magusin, P. C. M. M.; Degirmenci, V.; Li, M.; Almutairi, S. M. T.; Zhu, X.; Mezari, B.; Hensen, E. J. M. Acidic Properties of Nanolayered ZSM-5 Zeolites. *Microporous and Mesoporous Materials* **2014**, 189, 144-157.
- (13) Girleanu, M.; Lopes Silva, S.; Ihiawakrim, D.; Chaumonnot, A.; Bonduelle-Skrzypczak, A.; Lefebvre, F.; Dufaud, V.; Gay, A.-S.; Ersen, O. HAADF-STEM High-Resolution Study of Nanometric MoS<sub>2</sub> inside Mesoporous SBA-15. *Microporous and Mesoporous Materials* **2015**, 217, 190-195.
- (14) Bergeret, G.; Gallezot, P., Particle Size and Dispersion Measurements. In *Handbook of Heterogeneous Catalysis*, Wiley-VCH Verlag GmbH & Co. KGaA: 2008.
- (15) Simonsen, S. B.; Chorkendorff, I.; Dahl, S.; Skoglundh, M.; Sehested, J.; Helveg, S. Direct Observations of Oxygen-induced Platinum Nanoparticle Ripening Studied by In Situ TEM. *Journal of the American Chemical Society* **2010**, 132, 7968-7975.
- (16) Trout, B. L.; Chakraborty, A. K.; Bell, A. T. Diffusion and Reaction in ZSM-5 Studied by Dynamic Monte Carlo. *Chemical Engineering Science* **1997**, 52, 2265-2276.
- (17) Novoselov, K. S.; Geim, A. K.; Morozov, S. V.; Jiang, D.; Zhang, Y.; Dubonos, S. V.; Grigorieva, I. V.; Firsov, A. A. Electric Field Effect in Atomically Thin Carbon Films. *Science* **2004**, 306, 666-669.
- (18) Novoselov, K. S.; Jiang, D.; Schedin, F.; Booth, T. J.; Khotkevich, V. V.; Morozov, S. V.; Geim, A. K. Two-Dimensional Atomic Crystals. *Proceedings of the National Academy of Sciences of the United States of America* **2005**, 102, 10451-10453.
- (19) Geim, A. K.; Grigorieva, I. V. Van der Waals Heterostructures. *Nature* **2013**, 499, 419-425.
- (20) Halliday, D., *Principles of physics*. 9th ed., International student version. ed.; Hoboken, N.J. : John Wiley & Sons: Hoboken, N.J., 2011.



## Figures

**Table 3.3-1:** The execute procedures for encapsulation of Pt clusters within exfoliated MFI samples.

| Sample name | NaCl <sup>a</sup> | [Pt(NH <sub>3</sub> ) <sub>4</sub> ](NO <sub>3</sub> ) <sub>2</sub> <sup>b</sup> | flowing air at 350 °C <sup>c</sup> | flowing H <sub>2</sub> /N <sub>2</sub> at 300 °C <sup>d</sup> |
|-------------|-------------------|--|------------------------------------|---|
| S1          | x                 | x  | x                                  | x   |
| S2          | x                 | √  | √                                  | √   |
| S3          | √                 | √  | √                                  | √   |
| S4          | √                 | √  | x                                  | √   |
| S5          | √                 | √  | x                                  | x   |

<sup>a</sup>Immersed the samples into NaCl ( $\geq 99\%$ , Sigma-Aldrich, 1M) solution at room temperature overnight.

<sup>b</sup>Immersed the samples into [Pt(NH<sub>3</sub>)<sub>4</sub>](NO<sub>3</sub>)<sub>2</sub> (99.995%, Sigma-Aldrich, 1% wt metal content) aqueous solution at room temperature overnight.

<sup>c</sup>The sample was treated in flowing air and heated to 350 °C at 15 °C/min and held for 2 h.

<sup>d</sup>The sample reduced in a flowing H<sub>2</sub>/N<sub>2</sub> and heated to 300 °C at 15 °C/min and held for 2 h.

“√” represents the procedures execute in the Pt encapsulation steps.

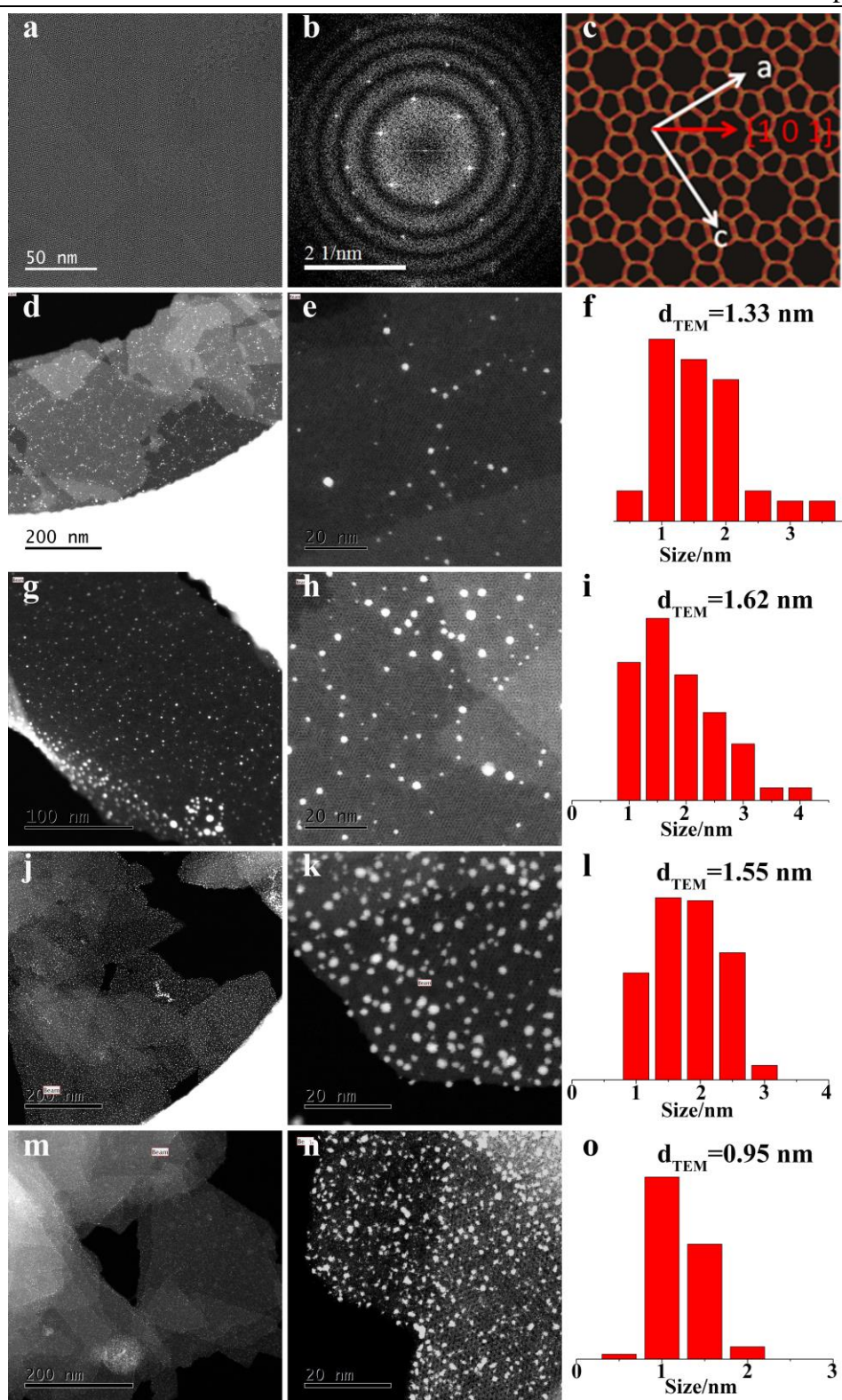


**Figure 3.3-1:** HAADF-STEM image of Sample S1 (a,b,c), Sample S2 (d,e,f), Sample S3(g,h,i), Sample S4 (j,k,l) and Sample S5 (m,n,o). The fast Fourier transform of (a) is shown in (b). (c) the model of MFI structure nanosheets viewed along b-axis. (f-o) are the Pt particle size distribution corresponded to (e-n), respectively, and were calculated using  $d_{TEM} = \sum n_i d_i^3 / \sum n_i d_i^2$ , where  $n_i$  is the number of clusters having diameter  $d_i$ .

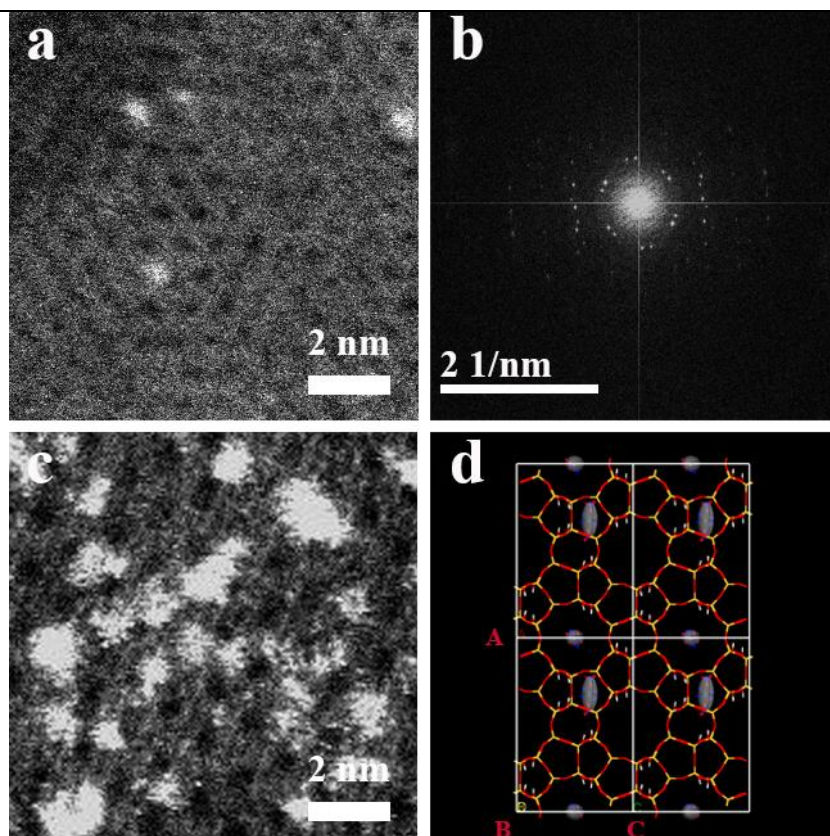


**Figure 3.3-2:** High-resolution HAADF-STEM images (a,c) of Sample S3 and Sample S5, respectively. The ultra-small Pt clusters 0.26, 0.39, and 0.49 nm can be observed in the centre of (a). The FFT spectrum of (a) shows two single MFI nanosheets with different orientations. The images size of (a,c) is 10 nm. (d) is the simulation of framework structure of MFI with Pt (or Pt(NH<sub>3</sub>)<sub>4</sub><sup>2+</sup> cations) encapsulated within the channels.

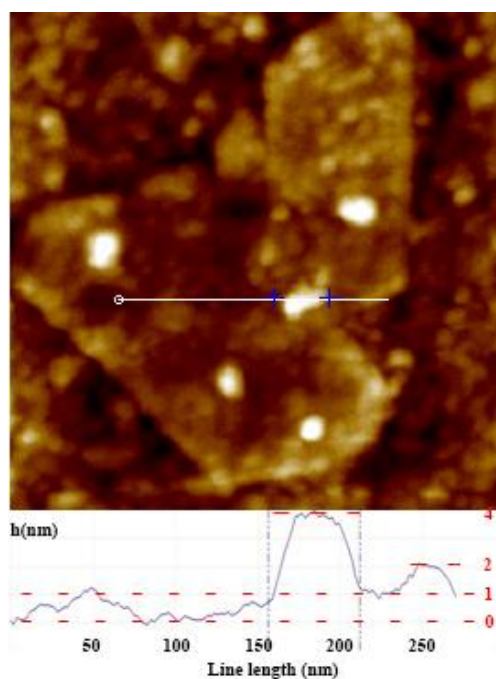


**Figure 3.3-3:** (a) AFM image of Sample S3 with size 500 nm. The height data of the line highlighted in (a) is plotted in (b).

---

## **Paper 3. Supporting Information**

---

---

## Supporting Information

### Encapsulation of ultra-small platinum clusters within exfoliated zeolite MFI nanosheets

Shiyu Xu<sup>1</sup>, Michael W. Anderson<sup>1\*</sup>, Konstantin S. Novoselove<sup>2</sup>, Hague Lee<sup>2</sup>,  
Sarah J. Haigh<sup>3</sup>, Eric Prestat<sup>3</sup>

<sup>1</sup>Centre for Nanoporous Materials, School of Chemistry, The University of  
Manchester, Oxford Road, Manchester M13 9PL, UK.

<sup>2</sup>School of Physics, The University of Manchester, Oxford Road, Manchester  
M13 9PL, UK.

<sup>3</sup>School of Materials, The University of Manchester, Oxford Road, Manchester  
M13 9PL, UK.

\*e-mail: [m.anderson@manchester.ac.uk](mailto:m.anderson@manchester.ac.uk)

## 1 X-ray diffraction

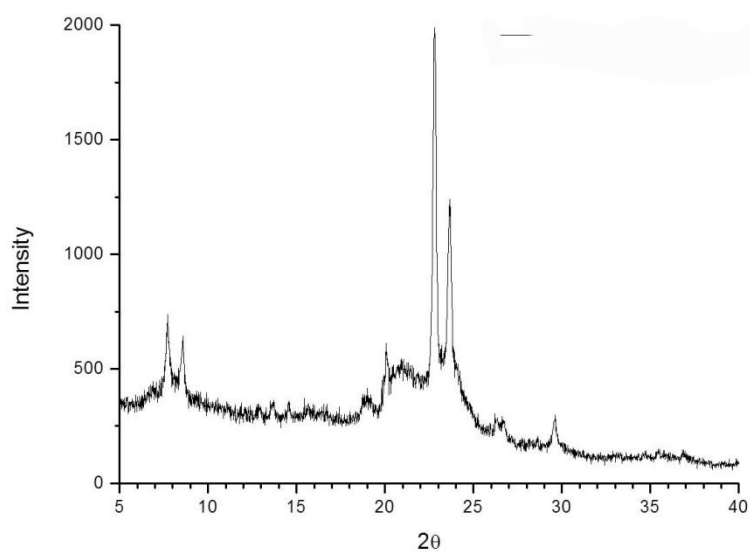


**Figure 3.3-S1:** XRD image of lamellar MFI material.

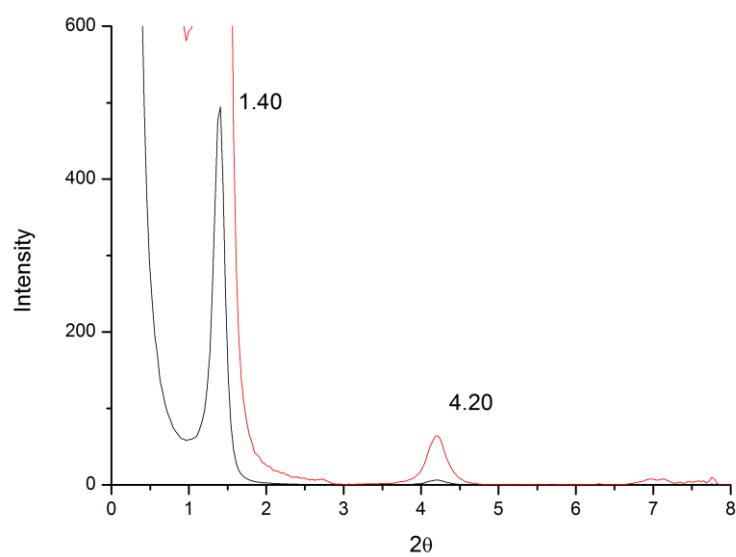


**Figure 3.3-S2:** SAXS image of lamellar MFI material.

## 2 SEM

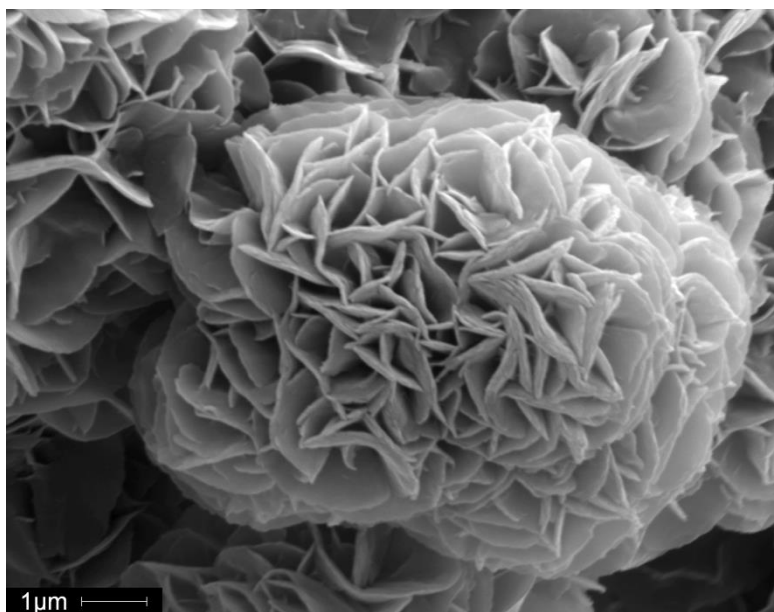


Figure 3.3-S3: SEM image of lamellar MFI material.

## 3 1D $^{29}\text{Si}$ cross-polarization (CP) MAS spectra

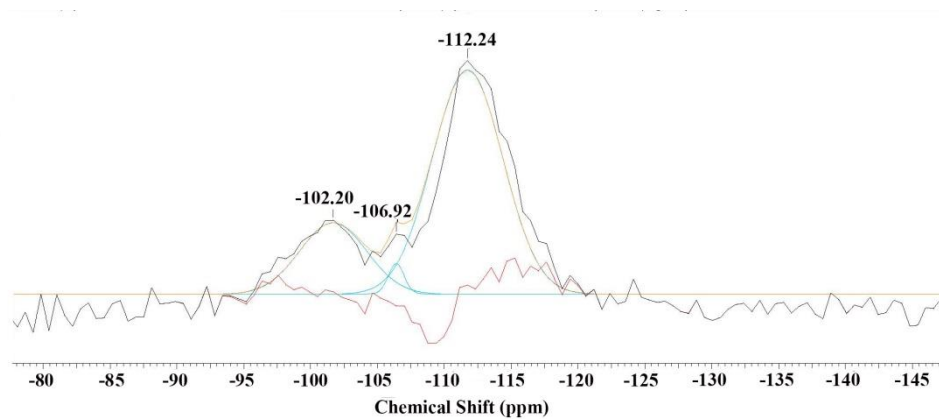
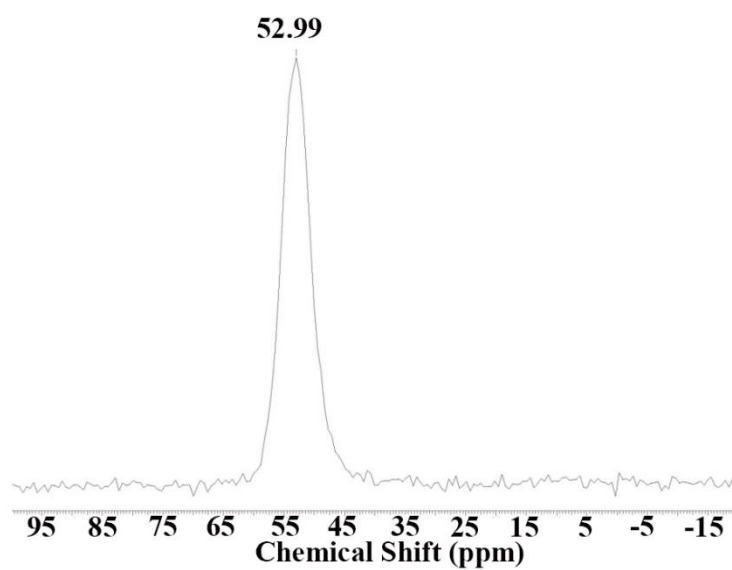


Figure 3.3-S4: 1D  $^{29}\text{Si}$  MAS spectra of lamellar MFI material.

#### 4 $^{27}\text{Al}$ MAS NMR spectra



**Figure 3.3-S5:**  $^{27}\text{Al}$  MAS NMR spectra of lamellar MFI material.

#### 5 MFI nanosheet structure

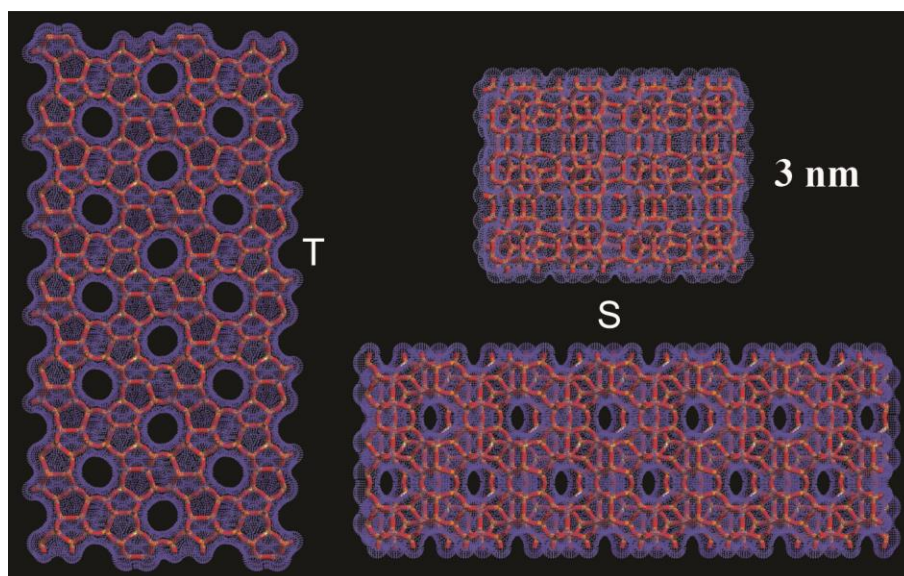


**Figure 3.3-S6:** Top down (T) and side (S) views of the single MFI nanosheet structure within a van der Waals skin to illustrate the available pore space



---

## **Chapter 4: Synthesis and Characterization of Mesoporous Materials**

---

---

## 4. Synthesis and Characterization of Mesoporous Materials

### 4.1. Introduction

The mesoporous materials are obtained from organic template molecules, inorganic precursors, solvent, acid or base catalyst. Driven by van der Waals forces, weak noncovalent bonds (hydrogen bonds), and electrovalent bonds between the surfactants and inorganic species, the ordered mesostructures was formed by assembly of organic-inorganic. Mesoporous materials can be obtained after the removal of surfactants.

In this Chapter, we report successful syntheses of four mesoporous silicas powders with different structures, MCM-41, MCM-48, SBA-15, SBA-16, and the characterization of these mesoporous materials was by SAXS, SEM, and N<sub>2</sub> adsorption. We also report successful syntheses of two mesoporous silicas thin films, *P6mm* and *Im $\bar{3}m$* . The quality of these films is normally characterized by GISAXS that readily reveal the type and consistency of the crystal structure. However, the diffraction techniques are not able to reveal the presence of defects and structural imperfections. In order to probe such short-range features AFM techniques are more appropriate.

### 4.2. Synthesis and Characterization of Mesopours powder

#### 4.2.1 Powder Synthesis: MCM-41

##### 4.2.1.1. Experimental

In a typical preparation of MCM-41,<sup>1</sup> 2.4 g of CTAB ( $\geq 99\%$ , Sigma-Aldrich) was dissolved in mixture of 120 mL of deionized water ( $18.2 \text{ M}\Omega \text{ cm}^{-1}$  at 25 °C, Milli-Q Direct 8, Merck Millipore) and 8 mL of ammonium hydroxide (NH<sub>4</sub>OH,  $\geq 35\%$ , Sigma-Aldrich) and stirred for 8 min at room temperature. Then 10 mL of TEOS (99.999%, Sigma-Aldrich) was added while stirring. The molar composition of the gel was:



The reaction was stirred overnight after which the solution was filtered and washed with deionized water and dry in the oven at 100 °C for 4 h. The template was removed by calcination at 823 K (550 °C) for 5 h.

#### 4.2.1.2. Result and Discussion

Powder SAXS pattern of calcined mesoporous silica material synthesized by CTAB is shown in Figure 4.1. It gives more than four well-resolved XRD reflections. The strong peak near 2.25° and the weak peak in the region of 4-8° can be indexed with 2-D hexagonal P6mm symmetry. The strong peak near 2.25° corresponds to the diffraction of (100). According to the Bragg's law  $\lambda = 2d \sin\theta$  ( $\lambda = 0.154184 \text{ nm}$ ),  $d_{100} = 3.92 \text{ nm}$ . In hexagonal  $d = \left[ \left( \frac{4}{3a^2} \right) (h^2 + k^2 + hk) + \left( \frac{l^2}{c^2} \right) \right]^{-1/2}$ , the cell parameter,  $a$ , is 4.53 nm. The N<sub>2</sub> adsorption isotherm for MCM-41 belongs to the Type IV isotherm. (Fig. 4.2) The surface area is about 1037.5150 m<sup>2</sup>/g, the pore volume is about 0.864187 cm<sup>3</sup>/g, and the pore diameter is about 3.238 nm. The approximate pore size calculated by nitrogen adsorption (3.24 nm) is less than the cell parameter,  $a$ , as determined by x-ray diffraction. Because the cell parameter includes the pore wall. This difference, (1.29 nm) between these two determination gives an indication of the pore wall thickness.

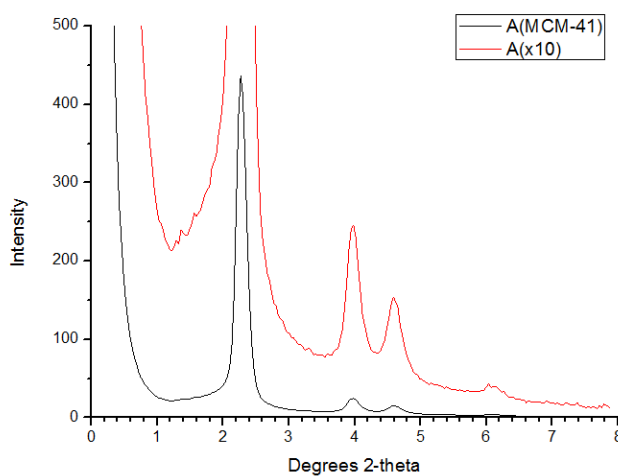


**Figure 4.1:** The SAXS pattern of calcined MCM-41.

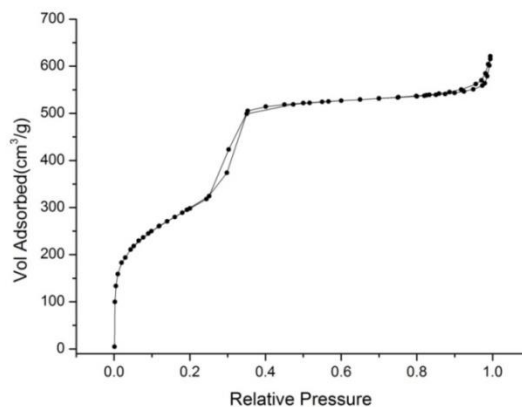


**Figure 4.2:** N<sub>2</sub> adsorption isotherm for calcined MCM-41.

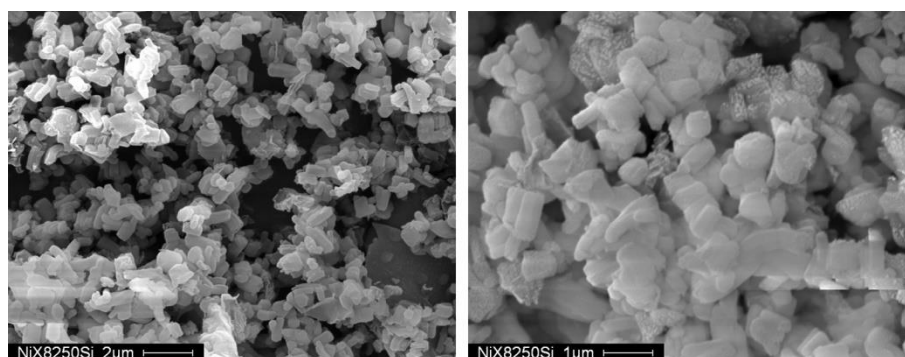


**Figure 4.3:** SEM images of calcined hexagonal mesoporous silica MCM-41.

SEM image (Fig. 4.3) reveals that the calcined MCM-41 sample consists of many rope-like domains with relative sizes of  $\sim 1 \mu\text{m}$ . The as-synthesised MCM-41 shows a similar particle morphology, and the morphology of MCM-41 depends on synthesis conditions.

## 4.2.2. Powder Synthesis: MCM-48

### 4.2.2.1. Experimental

To synthesise powder MCM-48<sup>2</sup>, 2.4 g of CTAB was dissolved in 11.3 mL deionized water and the added 0.2 g sodium hydroxide (NaOH,  $\geq 98\%$ , Sigma-Aldrich), and stirred for 5 min at room temperature. 2.24 mL of TEOS was added into this solution, and stirred for 1 h. The molar composition of the gel was:

$$\text{TEOS}:\text{Na}_2\text{O}:\text{CTAB}:\text{H}_2\text{O}=1:0.25:0.65:62.$$

The solution was changed into an autoclave and heated at 383 K for 3 days. The

product was filtered and washed with deionized water and dried in the oven at 100 °C overnight. The template was removed by calcined at 823 K (550 °C) for 6 h.

#### 4.2.4.2. Result and Discussion

The SAXS pattern of calcined mesoporous silica material synthesized by CTAB is shown in Figure 4.4. The result upon indexing the diffraction peaks of MCM-48 shows a good correspondence to those predicted by the cubic  $Ia\bar{3}d$  symmetry. The strong peak near  $2.5^\circ$  corresponds to the diffraction of (211). According to the Bragg's law  $\lambda = 2d \sin\theta$  ( $\lambda = 0.154184 \text{ nm}$ ),  $d_{211} = 3.53 \text{ nm}$ . In cubic structure  $d = a (h^2 + k^2 + l^2)^{-1/2}$ , the cell parameter,  $a$ , is 8.6 nm. Comparing with MCM-41 (Fig. 4.1), MCM-48 exhibits a larger unit cell. The  $N_2$  adsorption isotherm for MCM-48 belongs to the Type IV isotherm. (Fig. 4.5). SEM images (Fig. 4.6) reveal that the calcined MCM-48 sample consists of many the mixture spheres and polyhedrons with relatively size of  $\sim 2.5 \mu\text{m}$ . The as-synthesised MCM-48 shows a similar particle morphology.

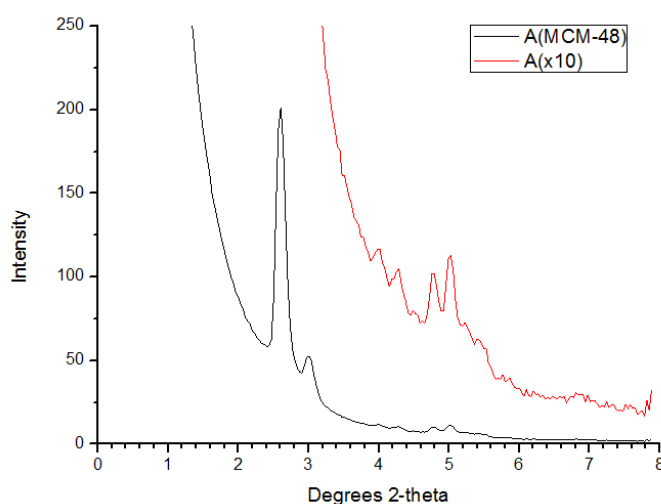


**Figure 4.4:** The SAXS pattern of calcined MCM-48.

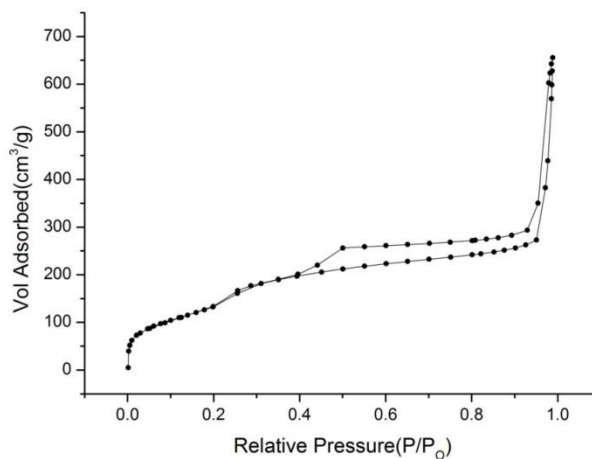


**Figure 4.5:** N<sub>2</sub> adsorption isotherm for calcined MCM-48.

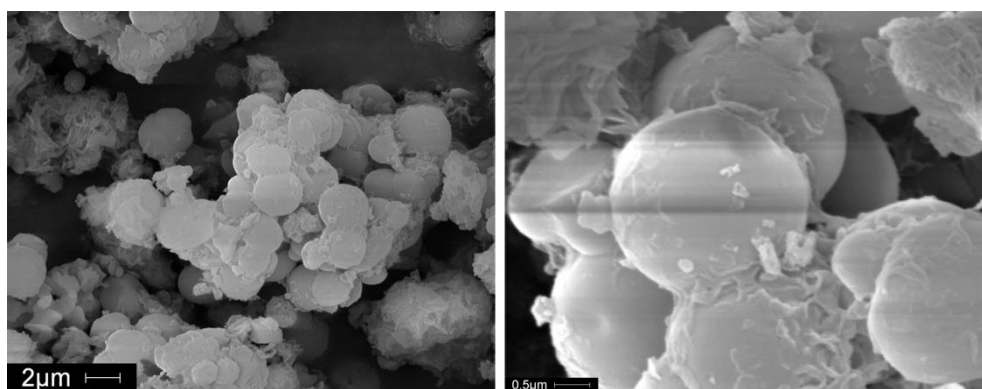


**Figure 4.6:** SEM images of calcined cubic mesoporous silica MCM-48.

### 4.2.3. Powder Synthesis: SBA-15

#### 4.2.3.1. Experimental

The SBA-15 is templated by triblock copolymer P123 (PEO<sub>20</sub>-PPO<sub>70</sub>-PEO<sub>20</sub>, Sigma-Aldrich). To synthesise powder SBA-15,<sup>3</sup> 1.14 g Pluronic P123 was dissolved in 35.66 mL deionized water and the added 0.013 g ammonium fluoride (NH<sub>4</sub>F, ≥98%, Sigma-Aldrich) and 4.34 mL hydrochloric acid (HCl wt.37%, Fisher Scientific), and stirred for 3 h at room temperature. In a separate beaker, 2.6 mL TEOS and *n*-octane (CH<sub>3</sub>(CH<sub>2</sub>)<sub>6</sub>CH<sub>3</sub>, ≥99%, Sigma-Aldrich) mixed for 10 min at room temperature. The second mixture was slowly added to the first and stirring for 24 h at 25 °C. The molar composition of the gel was:

$$\text{TEOS:P123:NH}_4\text{F:HCl:C}_8\text{H}_8\text{:H}_2\text{O}=1:0.017:0.03:4.44:4.06.$$

The solution was charged into an autoclave and heated at 383 K for 2 days. The product was filtered and washed with deionised water and dried in the oven at 100 °C overnight. The template was removed by calcination at 823 K (550 °C) for 5 h.

#### 4.2.3.2. Result and Discussion

The SAXS patterns of calcined mesoporous silica material synthesized by P123 are shown in Figure 4.7. The result upon indexing the diffraction peaks of SBA-15 shows a good correspondence to those predicted by the 2D hexagonal (P6mm) symmetry. The strong peak near 0.8° correspond the diffraction of (100). According to the Bragg's law  $\lambda = 2d \sin\theta$  ( $\lambda = 0.154184 \text{ nm}$ ),  $d_{100} = 11.04 \text{ nm}$ . In hexagonal structure,  $d = \left[ \left( \frac{4}{3a^2} \right) (h^2 + k^2 + hk) + \left( \frac{l^2}{c^2} \right) \right]^{-1/2}$ , the cell parameter,  $a$ , is 12.75 nm. The N<sub>2</sub> adsorption-desorption isotherm for the samples obtained show a Type IV isotherm with H1-type hysteresis at the relative pressure of 0.8-1, which is characteristic for mesoporous materials with cylindrical channels in hexagonal arrangement. (Fig. 4.8) The surface area is about 501.2871 m<sup>2</sup>/g, the pore volume is about 0.9485 cm<sup>3</sup>/g, and the pore diameter is about 7.3376 nm.

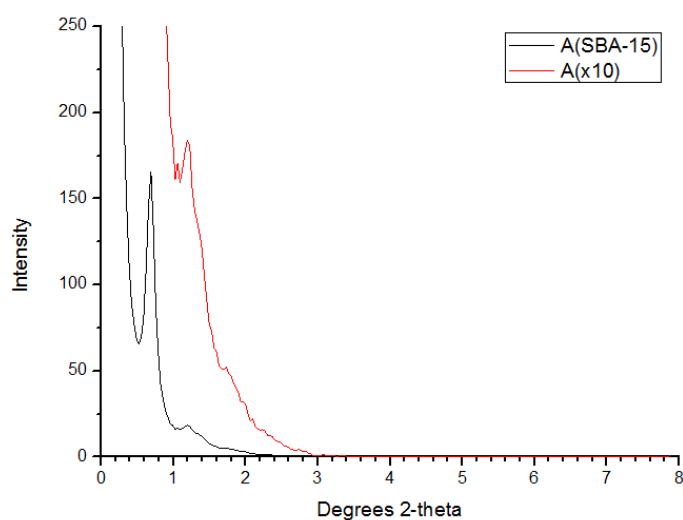


**Figure 4.7:** The SAXS pattern of calcined SBA-15.

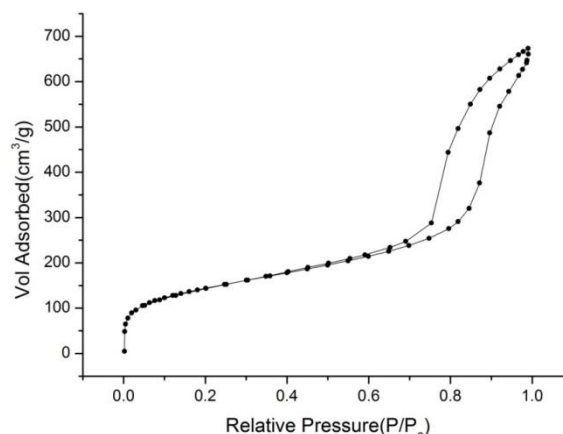


**Figure 4.8:** N<sub>2</sub> adsorption isotherm for calcined SBA-15.

#### 4.2.4. Powder Synthesis: SBA-16

##### 4.2.4.1. Experimental

The SBA-16 is templated by triblock copolymer F127 (PEO<sub>106</sub>-PPO<sub>70</sub>-PEO<sub>106</sub>, Sigma-Aldrich). To synthesis powder SBA-16, 1.003 g Pluronic F127 was dissolved in 123.891 mL deionized water and the added 0.118 g CTAB and 4.72 mL hydrochloric acid (HCl wt.37%), and stirred for 24 h at 28 °C. The molar composition of the gel was:

$$\text{TEOS:F127:CTAB:HCl:H}_2\text{O}=1:0.00008:0.02:9.43:472.73.$$

A transparent solution was obtained after the agitation. Finally the agitation was stopped and the temperature of oil bath was raised to 90 °C. The crystal growth of SBA-16 was developed under this static condition for another 6 days. The white precipitate was filtrated and was washed with deionised water and dried at room temperature overnight. The template was removed by calcination at 823 K (550 °C) for 5 h.

##### 4.2.4.2. Result and Discussion

The SAXS patterns of calcined mesoporous silica material synthesized by F127 are shown in Figure 4.9. The result upon indexing the diffraction peaks of SBA-16 shows a good correspondence to those predicted by the cubic  $Im\bar{3}m$  symmetry. The strong peak near  $0.8^\circ$  correspond the diffraction of (110).



According to the Bragg's law  $\lambda = 2d \sin\theta$  ( $\lambda = 0.154184 \text{ nm}$ ),  $d_{110} = 11.04 \text{ nm}$ .

In cubic structure  $d = a (h^2 + k^2 + l^2)^{-1/2}$ , the cell parameter,  $a$ , is  $15.62 \text{ nm}$ .

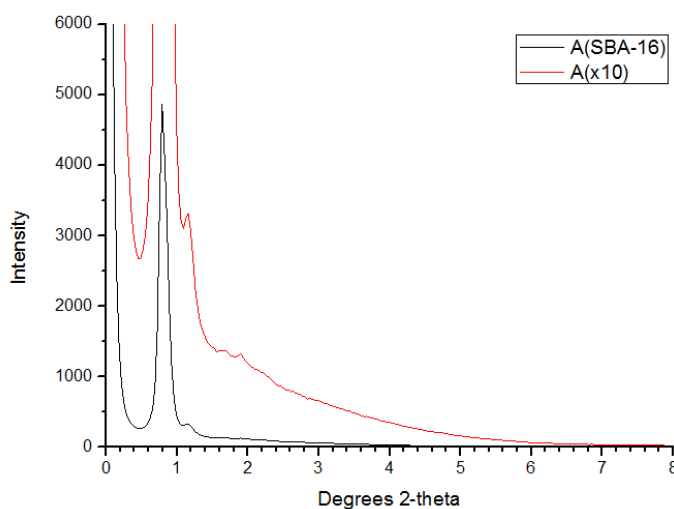


**Figure 4.9:** The SAXS pattern of calcined SBA-16.

The  $\text{N}_2$  adsorption-desorption isotherm for the obtained samples show a Type IV isotherm with H2-type hysteresis loop, which indicates that SBA-16 has a cage structure. (Fig. 4.10) The surface area is about  $713.9185 \text{ m}^2/\text{g}$ , the pore volume is about  $0.44 \text{ cm}^3/\text{g}$ . SEM images (Fig. 4.11) reveal that the calcined SBA-16 sample consists of many large polyhedrons with relatively sizes of  $\sim 5 \mu\text{m}$ . Some of these particles have the shape of a rhombododecahedron, consisting of 12 well-defined crystal faces. These 12 faces can be indexed to (110) planes. The crystal has four three-fold axes and three four-fold axes and exhibits cubic symmetry which belongs to  $m\bar{3}m$  point group class.

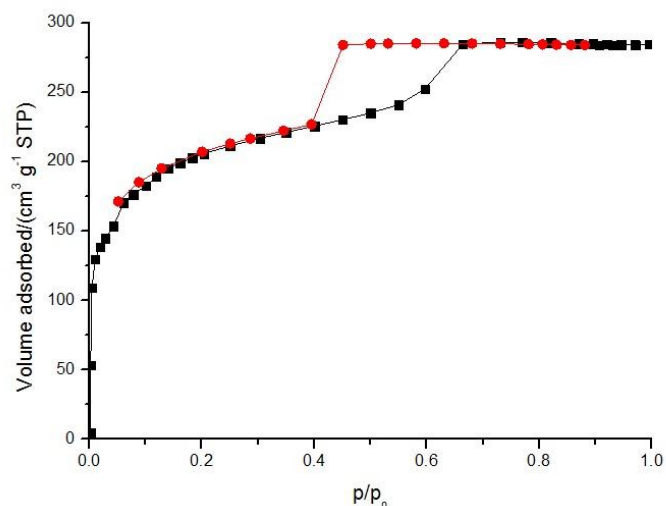


**Figure 4.10:** N<sub>2</sub> adsorption isotherm for calcined SBA-16.

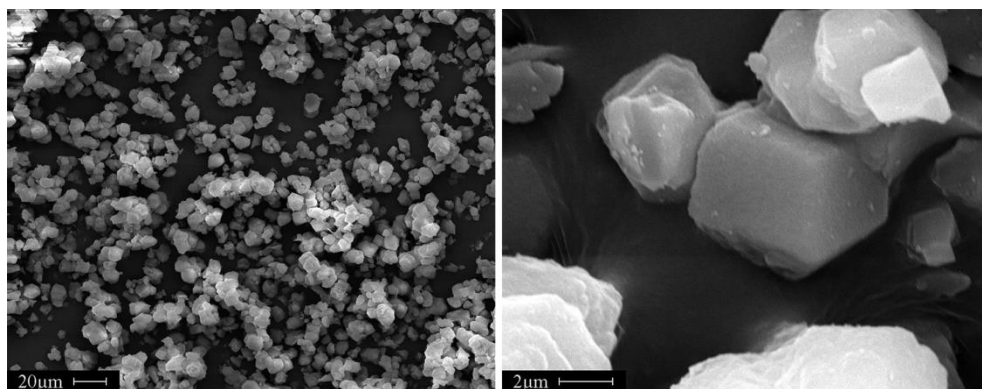


**Figure 4.11:** SEM images of calcined cubic mesoporous silica SBA-16.

## 4.3. Synthesis and Characterization of Mesoporous Thin Films

### 4.3.1. Thin Films Synthesis: F127

Mesoporous silica films can be grown at solid-liquid and liquid-vapor interface through an interfacial silica-surfactant self-assembly process.<sup>4</sup> In this project, we have synthesised the continuous mesoporous silica thin films by dip-coating on polished cover glasses, which has been reported by Lu.<sup>5</sup> The coating solutions are prepared by the addition of an ethanol solution using acidic conditions.<sup>6,7</sup> These films respectively used F127 and CTAB as surfactants. The mesostructured thin films are formed by evaporation induced self-assembly (EISA).<sup>8</sup> The thickness of the films can be uniform and varied by adjusting the

coating solution concentration or dip-coating rate.

#### 4.3.1.1. Experimental

Substrate preparation, especially the cleaning of substrates, is critically important in the thin film experiments, as any dust or dirt will affect the properties of the finished film. In this project, the glass has been used as the substrate. The glass was cleaned by soaking in 5% Teepol L multi-purpose detergent for 24 h, followed by ultrasonication for 15 min. The substrate was then washed with deionised water and ultrasonicated for another 15 min, and dried with nitrogen and kept in a closed container for further use.

The formation of continuous mesoporous silica thin films with large cage and pore structures using F127 as the structure template with dip-coating processing. The preparation began by dissolving 2.2286 g surfactant F127 as structure-directing agent in 0.549 mL hydrochloric acid (HCl, wt.37%) and 15 mL methanol ( $\geq 99.8\%$ , Sigma-Aldrich) with continuous stirring for 2 h at 35 °C. In a separate beaker, 10 mL TEOS, 103.92 mL EtOH ( $\geq 99.8\%$ , Sigma-Aldrich), 2.364 mL H<sub>2</sub>O were mixed for 30 min at room temperature. The second mixture was slowly added to the first and stirring continued for another 1 h at 35 °C. The molar composition of the gel was:

$$\text{TEOS:MeOH:EtOH:H}_2\text{O:HCl:F127}=1:8.37:40:5:0.15:0.004:8.37.$$

After mixing, the solution was kept under static conditions for 20 min in the oven at 80 °C (hydrothermal treatment), then cool at the room temperature for 4 h. Dip-coating process was in a static environment at a controlled relative humidity (RH) of 45-55%, temperature around 23-25 °C and pull rate at 1 mm/s. The film was kept in dip-coating container for another 10 min after the dip-coating process to allow it to dry. Then the film dried at room temperature for 24 h. The complete recipes for tested thin films synthesised by F127 were summarized in Table 4.1.

**Table 4.1:** Recipes of the films synthesised by F127. (a is the molar ratios of different sample. b includes the applied temperature and duration)

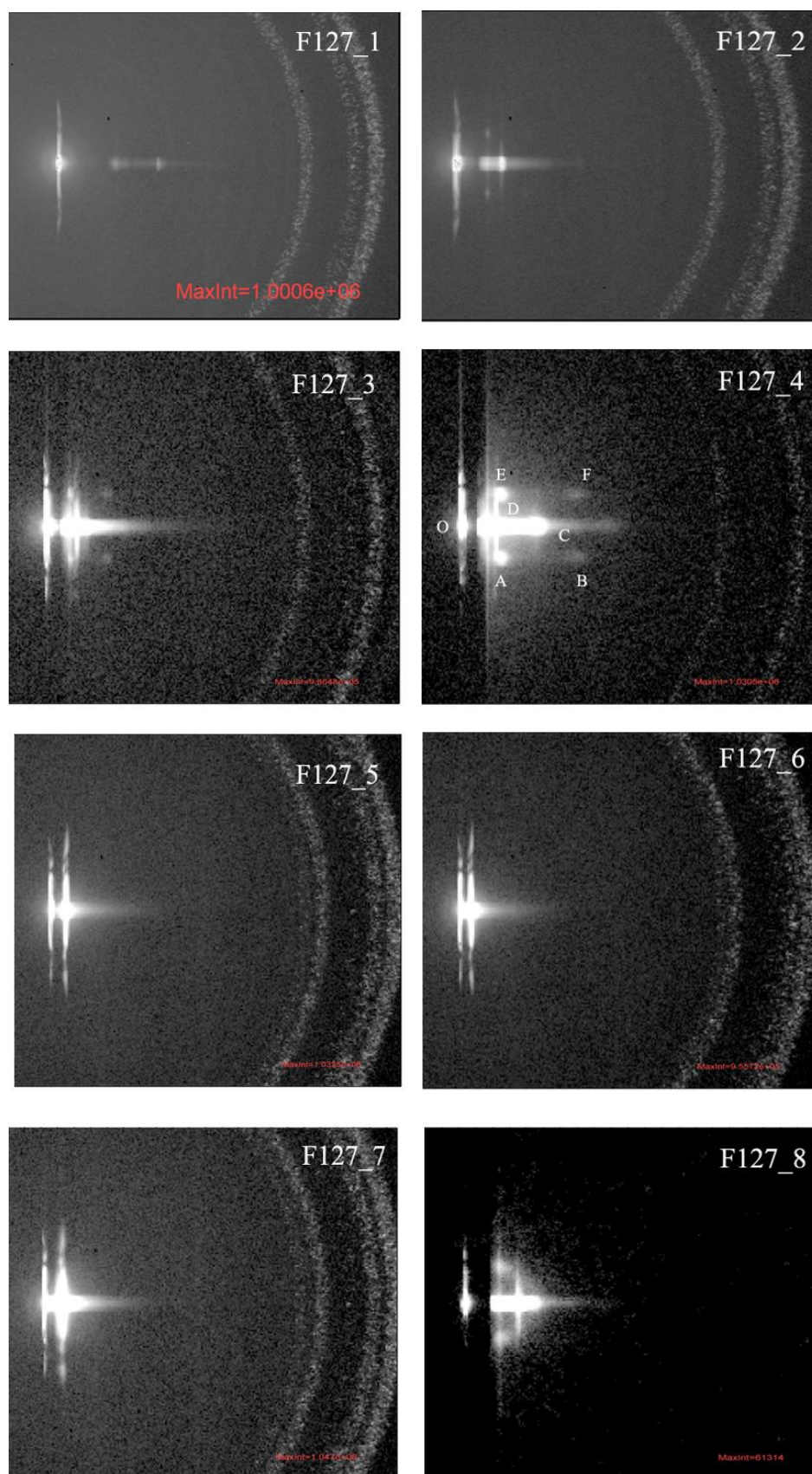
(a)

| Sample              | TEOS | EtOH | H <sub>2</sub> O | HCl  | F127  | MtOH |
|---------------------|------|------|------------------|------|-------|------|
| <b>F127_1 to 2</b>  | 1    | 40   | 5                | 0.15 | 0.004 | 8.37 |
| <b>F127_3 to 6</b>  | 1    | 35   | 5                | 0.02 | 0.004 | -    |
| <b>F127_7 to 10</b> | 1    | 35   | 5                | 1.18 | 0.004 | -    |

(b)

| Sample         | Silica sol-gels preparation | Hydrothermal treatment | After dip-coating  |
|----------------|-----------------------------|------------------------|--|
| <b>F127_1</b>  | Room temperature, 30 min    | 80 °C, 20 min          | -  |
| <b>F127_2</b>  | Room temperature, 30 min    | 80 °C, 20 min          | A closed container, 90 °C, 24 h                              |
| <b>F127_3</b>  | 75 °C, 1 h                  | 75 °C, 1 d             | -  |
| <b>F127_4</b>  | 75 °C, 1 h                  | 75 °C, 1d              | Calcined at 450 °C, 4 h                                      |
| <b>F127_5</b>  | 75 °C, 1 h                  | 75 °C, 1 d             | 80 °C in deionized water, overnight                          |
| <b>F127_6</b>  | 75 °C, 1 h                  | 75 °C, 1 d             | 80 °C in deionized water, overnight, calcined at 450 °C, 4 h |
| <b>F127_7</b>  | 75 °C, 1 h                  | 75 °C, 1 d             | -  |
| <b>F127_8</b>  | 75 °C, 1 h                  | 75 °C, 1 d             | Calcined at 450 °C, 4 h                                      |
| <b>F127_9</b>  | 75 °C, 1 h                  | 75 °C, 1 d             | 80 °C in deionized water, overnight                          |
| <b>F127_10</b> | 75 °C, 1 h                  | 75 °C, 1 d             | 80 °C in deionized water, overnight, calcined 450 °C, 4 h    |

## 4.3.1.2. Result and Discussion



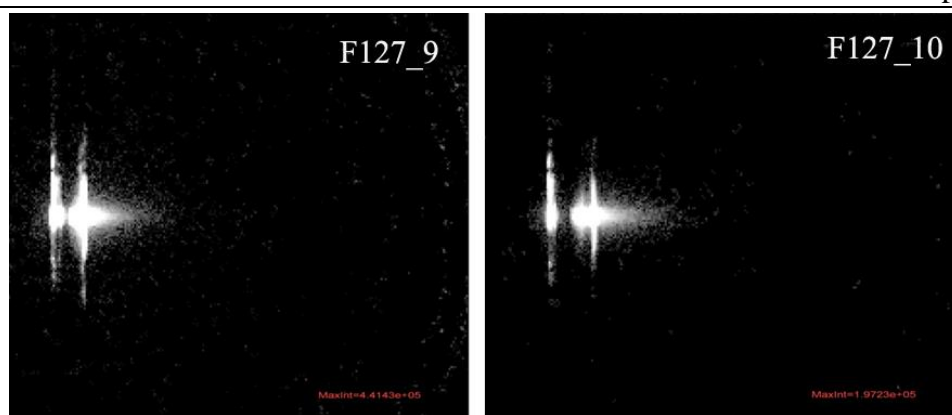


**Figure 4.12:** GISAXS patterns of the thin films synthesised by F127.

The GISAXS image of the mesostructure thin films synthesised by F127 is shown in Figure 4.12. Based on the GISAXS pattern comparisons of various samples, 1 day at 75 °C hydrothermal treatment will be an efficient method to improve mesoscopic regularity of the thin films. And the thin films do not have good hydrothermal stability. F127\_3 is selected as the representative way to make the as-synthesised thin films synthesised by F127, and F127\_4 is the calcined one.

The order parameter with respect to the 110 direction is practically equal to 1. As the 110 direction is perpendicular to the Si surface, the (110) net planes are lying parallel to the surface.<sup>9</sup> Figure 4.13 shows an arrangement of micelles on the Si surface assuming the  $Im\bar{3}m$  phase.

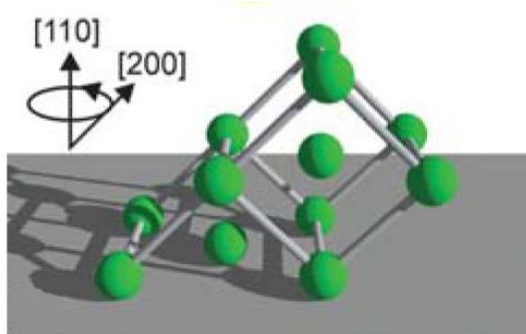


**Figure 4.13:** An arrangement of micelles on the Si surface assuming the  $Im\bar{3}m$  phase is of the micellar type.<sup>9</sup>

In this project, we use the Hecus S3-MICRO system equipped with a 2D SAXeye CCD-detector, with monochromatized Cu-radiation as x-ray source,

which has a weighted wavelength  $\lambda = 0.15406$  nm, Sample to CCD distance of 290.94 mm, CCD pixel size of 0.172 mm.

In Figure 4.12 F127\_4, there are six bright spots, labelled A to F. The beam center labelled O. The spots coordinates show as follows: O(96.0281, 270.281), D(96.0281, 294), C(96.0281, 318), A(114, 297), B(114, 342).

$$OD = (294 - 270.281) * 0.172 = 4.123 \text{ mm}$$

$$OC = (318 - 270.281) * 0.172 = 8.208 \text{ mm}$$

$$OA = \sqrt{(114 - 96.0281)^2 + (297 - 270.281)^2} * 0.172 = 5.575 \text{ mm}$$

$$OB = \sqrt{(114 - 96.0281)^2 + (342 - 270.281)^2} * 0.172 = 12.759 \text{ mm}$$

In cubic structures:

$$a=b=c, \alpha=\beta=\gamma=90^\circ$$

the interplanar spacing  $d = a(h^2 + k^2 + l^2)^{-1/2}$

Spot D, is the diffraction of the plane (110):

$$\tan\theta = \frac{4.123}{290.247}, \text{ according to the Bragg's law } \lambda = 2d \sin\theta,$$

the interplanar spacing  $d_D = 5.42$  nm.

the cell parameter  $a = 7.7$  nm

As the same calculation method, the following results can be obtained:

C, the diffraction of the plane (220),  $d_C = 2.72$  nm,  $a = 7.7$  nm.

A, the diffraction of the plane (200),  $d_A = 4.01$  nm,  $a = 8.0$  nm.

B, the diffraction of the plane (420),  $d_B = 1.75$  nm,  $a = 7.8$  nm.

Hence, the cell parameter,  $a \approx 7.8$  nm.

The molecular resolution AFM images of the mesostructure thin films synthesised by F127 are shown in Figure 4.12. It confirms that we have synthesised continuous, crack-free film.

In order to record high-resolution AFM images, Scan Parm Settings suggestusing the following parameters:

Scan size: ~15 nm, Scan rate: ~2 Hz, Samples/line: 256, XYCL: Off, Scan Asyst Auto Control: Off, Feedback Gain: 1.00, Peak Force Setpoint: ~0-20 mV depending on probe, *etc.* LP Deflection BW: 10-20 KHz, Peak Force Amplitude:

5-25 nm, Deflection limit: 4 V, Z limit: 0.5-1.0  $\mu\text{m}$ . The engage settings Peak Force Engage Setpoint prefer  $\leq 0.02$  V, but as small as possible. Use the E scanner (10x10  $\mu\text{m}$  XY, 2 $\mu\text{m}$  Z).

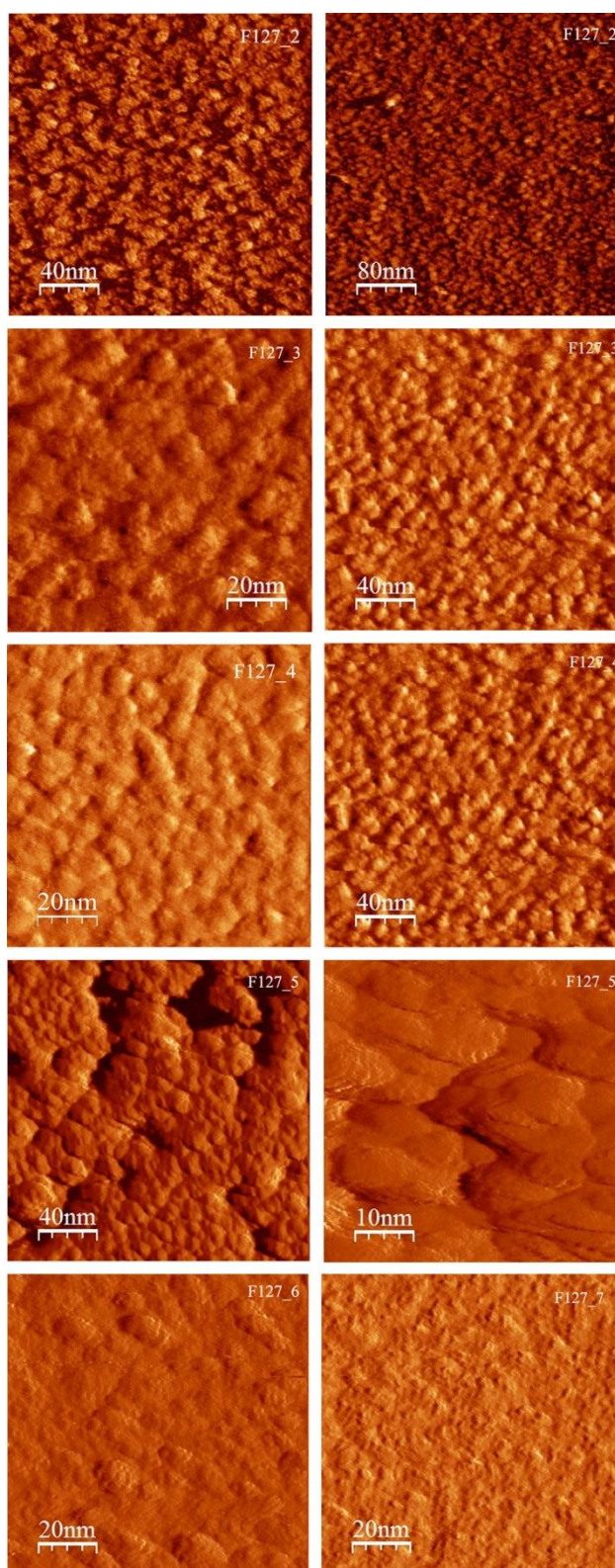


**Figure 4.14:** AFM height images of the thin films synthesised by F127.



However, the AFM images are not really clear, even some of them have disorder shapes, that is maybe generated by the contamination from the sample surfaces. The contamination can hide the underlying lattice. Select F127\_3 and F127\_4 to analyse.(Fig. 4.14) The cell parameters,  $a$ , are 10 and 8 nm for as-synthesised and calcined samples, respectively, which correspond to the result given by GISAXS. However, the smaller mesopores are not visible by these AFM experiments, being embedded in the nanocrystals.

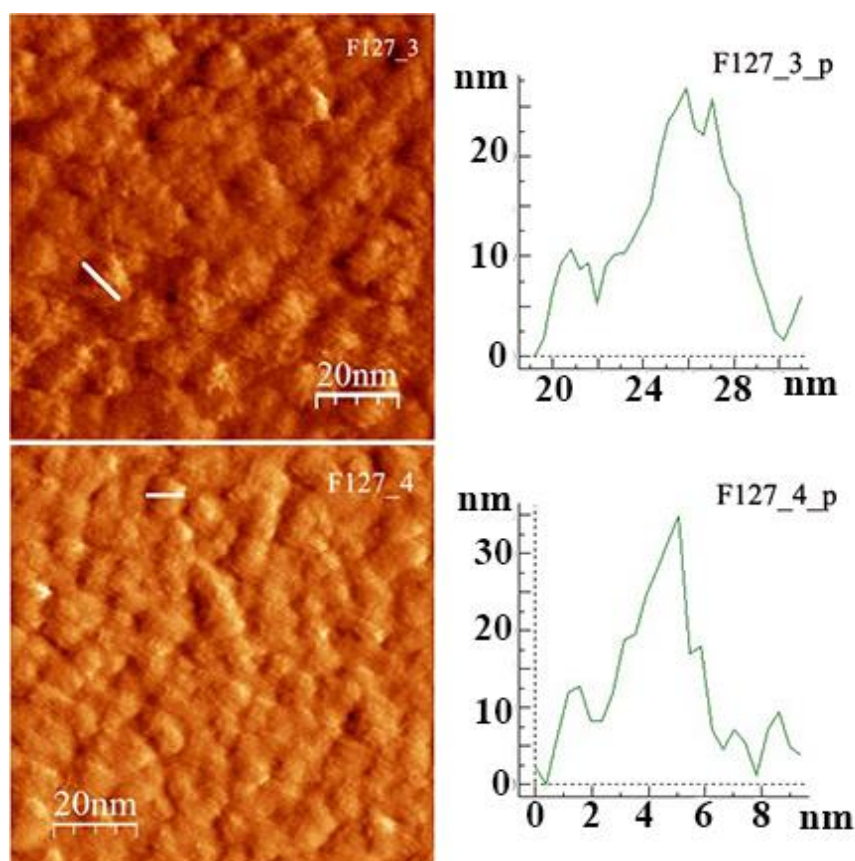


**Figure 4.15:** AFM height images of the thin films synthesised by F127. (F127\_3 is the as-synthesised, F127\_4 is the calcined mesoporous thin films. F127\_3\_p, F127\_4\_p are their unit cell Peak Force profile images, respectively)

### 4.3.2. Thin Films Synthesis: CTAB

#### 4.3.2.1. Experimental

The formation of continuous mesoporous silica thin films use CTAB as the structure template with dip-coating processing. The preparation began by

dissolving 3.2231 g surfactant CTAB as structure-directing agent in 0.48 mL hydrochloric acid (HCl wt.37%) and 72 mL ethanol with continuous stirring for 2 h at 35 °C. In a separate beaker, 10 mL TEOS, 7.79 mL EtOH, 0.52 mL H<sub>2</sub>O were mixed for 1 h at 50 °C. The second mixture was slowly added to the first and stirring continued for another 1 h at 35 °C. The molar composition of the gel was:

$$\text{TEOS:EtOH:HCl:H}_2\text{O:CTAB}=1:35:0.13:5:0.2.$$

After mixing, the solution was kept under static conditions for 20 min in the oven at 80 °C (hydrothermal treatment), then cooled at the room temperature for 4 h.

The dip-coating process was in a static environment at a controlled relative humidity (RH) of 45-55%, temperature around 23-25 °C and pull rate at 1 mm/s. The film was kept in dip-coating container for another 10 min after the dip-coating process to allow it to dry. Then the film dried at room temperature for 24 h. The complete recipes for tested thin films synthesised by F127 were summarized in Table 4.2.

**Table 4.2:** Recipes of the films synthesised by CTAB. (a is the molar ratios of different sample. b includes the applied temperature and duration)

(a)

| Sample      | TEOS | EtOH | H <sub>2</sub> O | HCl  | CTAB |
|-------------|------|------|------------------|------|------|
| CTAB_1      | 1    | 35   | 5                | 0.13 | 0.08 |
| CTAB_2 to 3 | 1    | 35   | 5                | 0.13 | 0.2  |
| CTAB_4      | 1    | 35   | 5                | 0.13 | 0.35 |
| CTAB_5 to 6 | 1    | 35   | 5                | 0.13 | 0.35 |
| CTAB_7 to 8 | 1    | 35   | 5                | 0.02 | 0.35 |

(b)

| Sample | Silica sol-gels preparation | Hydrothermal treatment | After dip-coating |
|--------|-----------------------------|------------------------|-------------------|
|--------|-----------------------------|------------------------|-------------------|

|               |            |               |                                 |
|---------------|------------|---------------|---------------------------------|
| <b>CTAB_1</b> | 50 °C, 1 h | -             | A closed container, 90 °C, 24 h |
| <b>CTAB_2</b> | 50 °C, 1 h | -             | A closed container, 90 °C, 24 h |
| <b>CTAB_3</b> | 50 °C, 1 h | 80 °C, 20 min | A closed container, 90 °C, 24 h |
| <b>CTAB_4</b> | 50 °C, 1 h | -             | A closed container, 90 °C, 24 h |
| <b>CTBA_5</b> | 50 °C, 1 h | -             | -                               |
| <b>CTAB_6</b> | 50 °C, 1 h | -             | A closed container, 90 °C, 24 h |
| <b>CTAB_7</b> | 75 °C, 1 h | 75 °C, 1 d    | -                               |
| <b>CTAB_8</b> | 75 °C, 1 h | 75 °C, 1 d    | Calcined at 450 °C, 4 h         |

#### 4.3.2.2. Result and Discussion

The GISAXS image of the mesostructure thin films synthesised by CTAB is shown in Figure 4.16. Based on the GISAXS pattern comparisons of various samples, hydrothermal treatment is not necessary, but a stronger signal can be obtained by heating in a close container at 90 °C for 24 h after dip-coating. CTAB\_4 is selected as the representative way to make the as-synthesis thin films synthesised by CTAB.

In this project, we use the Hecus S3-MICRO system equipped with a 2D SAXeye CCD-detector, with monochromatized Cu-radiation as x-ray source, which has a weighted wavelength  $\lambda = 0.15406$  nm, Sample to CCD distance of 290.94 mm, CCD pixel size of 0.172 mm.

In Figure 4.16 CTAB\_4, there are five bright spots, labelled from A to E. The beam center labelled O. The spots coordinates show as follows:

O(96.0281, 270.281), A (96.0281, 348), E(148, 310), D(148, 388).

$$OA = (348 - 270.281) * 0.172 = 13.368 \text{ nm}$$

$$OE = \sqrt{(148 - 96.0281)^2 + (310 - 270.281)^2} * 0.172 = 11.25 \text{ nm}$$

$$OD = \sqrt{(148 - 96.0281)^2 + (388 - 270.281)^2} * 0.172 = 22.13 \text{ nm}$$

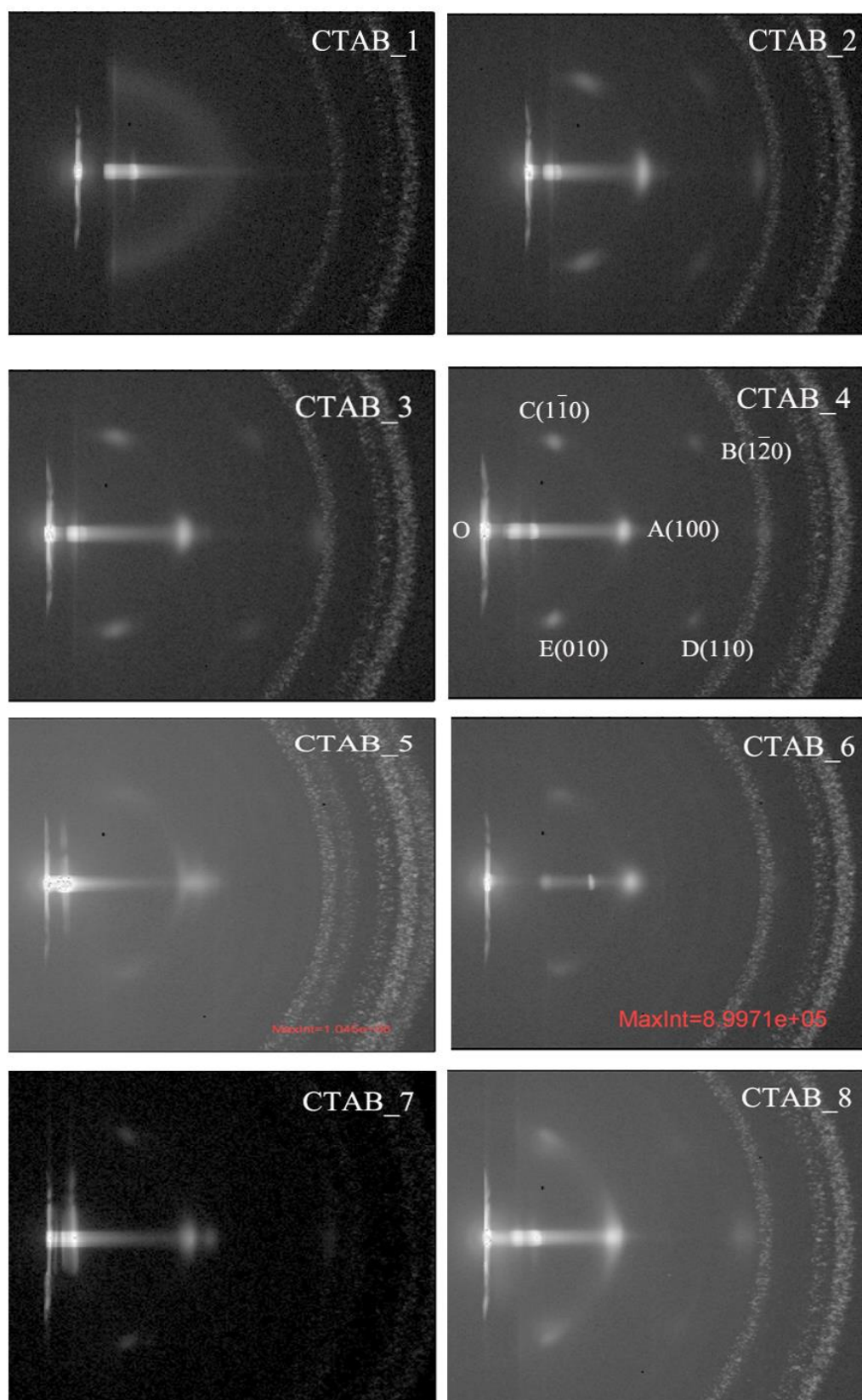


**Figure 4.16:** GISAXS patterns of the thin films synthesised by CTAB.

In hexagonal structures:

Spot A, is the diffraction of the plane (100):

$$\tan\theta = \frac{13.368}{290.247}, \text{ according to the Bragg's law } \lambda = 2d \sin\theta,$$

the interplanar spacing  $d_A = 1.67$  nm.

As the same calculation method, the following results can be obtained:

E, the diffraction of the plane (010),  $d_E = 1.99$  nm.

D, the diffraction of the plane (110),  $d_D = 1.01$  nm.

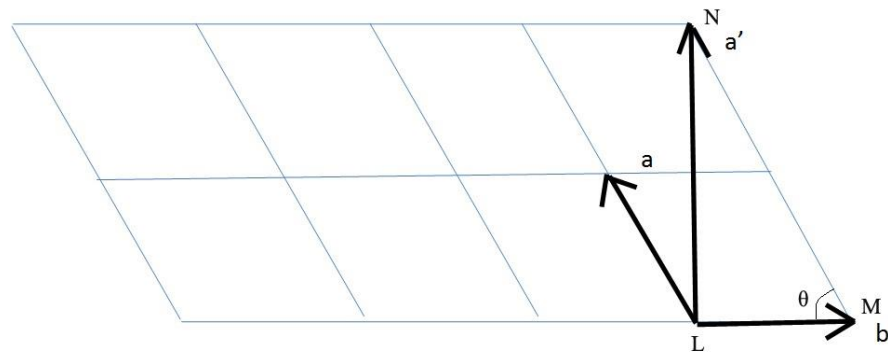


**Figure 4.17:** A point lattice ( $a, b$  are the cell parameter of the hexagonal structures,  $a \neq b, c \rightarrow \infty$ .  $a', b$  are the cell parameter of the orthorhombic structures,  $a \neq b, \alpha = 90^\circ, c \rightarrow \infty$ ).

The hexagonal structures have been compressed after dip-coating by calculation. It is not the real hexagonal structures. ( $a \neq b$ ) In order to find out the cell parameter, the hexagonal structures would be transformed into the orthorhombic structures. (Fig. 4.17)

$$a = \frac{d_A}{d_E} b = \frac{1.68}{1.995} * b = 0.84b$$

$$LN^2 = LM^2 + MN^2 - 2 * MN * LM * \cos\theta$$

$$= b^2 + (2a)^2 - 2 * (2a) * b * \cos[90 - \arctan\left(\frac{310 - 270.281}{148 - 96.0281}\right)]$$

$$= b^2 + 2.82 b^2 - 3.36 b^2 * \cos 52.63^\circ$$

$$= 1.78 b^2$$

$$a' = LN = 1.33b$$

In hexagonal structures:

$$a = b \neq c, \alpha = \beta = 90^\circ, \gamma = 120^\circ, c \rightarrow \infty.$$

the interplanar spacing  $d = \left[ \left( \frac{4}{3a^2} \right) (h^2 + k^2 + hk) + \left( \frac{l^2}{c^2} \right) \right]^{-1/2}$

$$d^2 = \frac{3a^2}{4(h^2+k^2+hk)} = \frac{3b^2}{4(h^2+k^2+hk)}$$

In orthorhombic structures:

$$a \neq b \neq c, \alpha = \beta = \gamma = 90^\circ, c \rightarrow \infty.$$

the interplanar spacing  $d' = \left[ \left( \frac{h^2}{a^2} \right) + \left( \frac{k^2}{b^2} \right) + \left( \frac{l^2}{c^2} \right) \right]^{-1/2}$

$$d'^2 = \frac{a^2 * b^2}{b^2 h^2 + a^2 k^2} = \frac{3b^2}{h^2 + 3k^2}$$

Spot A, (100)  $\rightarrow$  (200)

$$d^2 = d'^2 = \frac{3b^2}{4}$$

Spot E, (010)  $\rightarrow$  (110)

$$d^2 = d'^2 = \frac{3b^2}{4}$$

Spot D, (110)  $\rightarrow$  (310)

$$d^2 = d'^2 = \frac{b^2}{4}$$

Hence, the hexagonal structures can transform into the orthorhombic structures.

In orthorhombic structures:

the interplanar spacing

$$d' = \left[ \left( \frac{h^2}{a'^2} \right) + \left( \frac{k^2}{b^2} \right) \right]^{-1/2} = \left[ \left( \frac{h^2}{1.33b^2} \right) + \left( \frac{k^2}{b^2} \right) \right]^{-1/2} = \sqrt{\frac{1.33^2 * b^2}{h^2 + 1.33^2 k^2}}$$

Spot A, is the diffraction of the plane (200):

$$\text{the interplanar spacing } d_A = 1.67 \text{ nm} = \sqrt{\frac{1.33^2 * b^2}{4}}$$

$$b = 2.51 \text{ nm}, a' = 1.33b = 3.34 \text{ nm}$$

The cell parameter,  $a'$ , is 3.34 nm;  $b'$ , is 2.51 nm.

The molecular resolution AFM images of the mesostructure thin films synthesised by CTAB are shown in Figure 4.18. It confirms that we have synthesised continuous, crack-free film. However, the AFM images are not really clear enough. And they do not reveal the shape as we predict, such as the tubes lie on the surface, even some of them have disorder shapes. We speculate it maybe generate by the contamination from the sample surfaces or the geometry of the tips. Hence, the

lattices have been hidden.

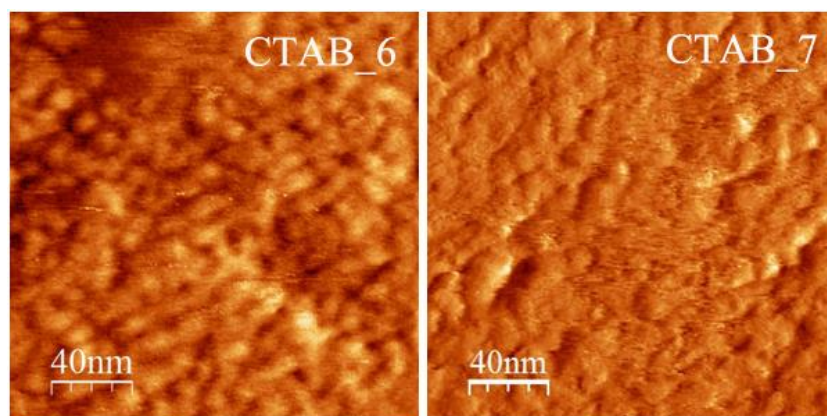


**Figure 4.18:** AFM height images of the thin films synthesized by CTAB.

#### 4.4. Conclusions

Four different structures mesoporous silicas powders with good regularities, MCM-41, MCM-48, SBA-15, SBA-16, have been prepared. The structures are calculated from the diffraction intensities, which are collected from the SAXS patterns of the samples, and be confirmed successfully as reported in the literature. The different morphology have been obtained depending on synthesis conditions and been examined and analyzed by SEM. The specific surface area, pore volume, and pore size distribution as well as the surface properties have been determined by  $N_2$  adsorption.

Compared with powder precipitation, thin films can be attained with a high precision in their dimensions, such as thickness. Moreover, thin films are highly interesting owing an expectation that they will be useful in many potential applications (e.g. molecular detection, separation, environmental science, medicine, catalysis, optics, and other still evolving fields of activities).

Two different structure mesoporous silicas thin films, SBA-16 with symmetry  $Im\bar{3}m$ , MCM-41 with symmetry  $P6mm$ , have been prepared. The structures have been confirmed by the GISAXS patterns of the samples. The molecular resolution AFM images of the thin film surface have been obtained by using AFM operating by Peak Force Tapping Mode in the liquid. The molecular

---

defects and structural imperfections have been investigated by AFM.

## 4.5. References

- (1) Kumar, D.; Schumacher, K.; du Fresne von Hohenesche, C.; Grün, M.; Unger, K. K. MCM-41, MCM-48 and Related Mesoporous Adsorbents: Their Synthesis and Characterisation. *Colloids and Surfaces A: Physicochemical and Engineering Aspects* **2001**, 187–188, 109-116.
- (2) Monnier, A.; Schüth, F.; Huo, Q.; Kumar, D.; Margolese, D.; Maxwell, R. S.; Stucky, G. D.; Krishnamurty, M.; Petroff, P.; Firouzi, A.; Janicke, M.; Chmelka, B. F. Cooperative Formation of Inorganic-Organic Interfaces in the Synthesis of Silicate Mesostructures. *Science* **1993**, 261, 1299-1303.
- (3) Sun, J.; Zhang, H.; Ma, D.; Chen, Y.; Bao, X.; Klein-Hoffmann, A.; Pfander, N.; Su, D. S. Alkanes-Assisted Low Temperature Formation of Highly Ordered SBA-15 with Large Cylindrical Mesopores. *Chemical Communications* **2005**, 5343-5345.
- (4) Aksay, I. A.; Trau, M.; Manne, S.; Honma, I.; Yao, N.; Zhou, L.; Fenter, P.; Eisenberger, P. M.; Gruner, S. M. Biomimetic Pathways for Assembling Inorganic Thin Films. *Science* **1996**, 273, 892-898.
- (5) Lu, Y.; Ganguli, R.; Drewien, C. A.; Anderson, M. T.; Brinker, C. J.; Gong, W.; Guo, Y.; Soyez, H.; Dunn, B.; Huang, M. H.; Zink, J. I. Continuous Formation of Supported Cubic and Hexagonal Mesoporous Films by Sol-Gel Dip-Coating. *Nature* **1997**, 389, 364-368.
- (6) Huo, Q.; Margolese, D. I.; Ciesla, U.; Feng, P.; Gier, T. E.; Sieger, P.; Leon, R.; Petroff, P. M.; Schuth, F.; Stucky, G. D. Generalized Synthesis of Periodic Surfactant/Inorganic Composite Materials. *Nature* **1994**, 368, 317-321.
- (7) Huo, Q. S.; Margolese, D. I.; Ciesla, U.; Demuth, D. G.; Feng, P. Y.; Gier, T. E.; Sieger, P.; Firouzi, A.; Chmelka, B. F.; Schuth, F.; Stucky, G. D. Organization of Organic-Molecules with Inorganic Molecular-Species into Nanocomposite Biphase Arrays. *Chemistry of Materials* **1994**, 6, 1176-1191.
- (8) Grosso, D.; Cagnol, F.; Soler-Illia, G. J. d. A. A.; Crepaldi, E. L.; Amenitsch, H.; Brunet-Bruneau, A.; Bourgeois, A.; Sanchez, C. Fundamentals of Mesostructuring Through Evaporation-Induced Self-Assembly. *Advanced Functional Materials* **2004**, 14, 309-322.
- (9) Weber, C. H. M.; Liu, F.; Zeng, X.-b.; Ungar, G.; Mullin, N.; Hobbs, J. K.; Jahr, M.; Lehmann, M. Body-Centered Cubic Phase in 3-arm Star Mesogens: a Torsional Tapping AFM and GISAXS Study. *Soft Matter* **2010**, 6, 5390-5396.



---

## **Chapter 5: Ultra-thin Zeolite MFI Membrane and Pt-containing aluminosilicate nanowires**

---

## 5. Ultra-thin Zeolite MFI Membrane and Pt-containing aluminosilicate nanowires

### 5.1. Further Growth of Exfoliated MFI Nanosheets

Until now, a single zeolite MFI nanosheet could be obtained by three different methods: (i) by using 30 nm MFI crystal seeds to trigger the epitaxial growth of zeolite MFI nanosheets with thickness about 5 nm;<sup>1</sup> (ii) melt-blend the mixture of polymer and multilamellar zeolite MFI and centrifuge to separate out the exfoliated zeolite MFI nanosheets with thickness about 3 nm;<sup>2</sup> (iii) a multi-lamellar zeolite MFI is repeatedly cleaved by the application of a sticky tape resulting in the mechanical exfoliation of zeolite MFI nanosheets with thickness about 3 nm.(see Chapter 3 paper 2)

Here, we use the third method that is using the mechanical exfoliation process to obtain the single zeolite MFI nanosheets to obtain the single zeolite MFI nanosheet. After exfoliation, the schematic presentation of possible as-synthesised single MFI nanosheets has been discussed in Chapter 3 paper 2. (see Fig. 3.2-S11) The long hydrocarbon chains are essentially intact on both sides of the inorganic layer, and can prevent thickening of the zeolite MFI nanosheets along b-axis. Therefore, in this chapter 5.1, we use the single zeolite MFI nanosheets as seeds to investigate whether it is possible to further grow and produce the large scale MFI membrane with uniform nano-thickness.

#### 5.1.1. Preparation of Multi-lamellar Zeolite MFI

Multi-lamellar zeolite MFI, with a thickness of 1.5 unit cells along the b-axis, have been generated by using di-quaternary ammonium structure directing agents (SDA) with a sufficiently long hydrophobic tail, i.e.,  $[\text{C}_{22}\text{H}_{45}\text{-N}^+(\text{CH}_3)_2\text{-C}_6\text{H}_{12}\text{-N}^+(\text{CH}_3)_2\text{-C}_6\text{H}_{13}]\text{Br}_2$  (denoted as  $\text{C}_{22-6-6}\text{Br}_2$ ).<sup>3</sup> The schematic figure has been shown in Fig. 1.27.

The organic surfactant ( $\text{C}_{22-6-6}\text{Br}_2$ ) was synthesized by the procedure outlined

before.<sup>3</sup> 3.9 g 1-bromodocosane (0.100 mol, TCI) and 17.2 g N,N,N',N'-tetramethyl-1,6-diaminohexane (1 mol, Aldrich) were dissolved in 100 ml acetonitrile/toluene mixture (1: 1 vol/vol) and heated under reflux at 70 °C for 10 h. Then, the mixture was cooled down to room temperature. After filtering and washing with diethyl ether, the product was dried in a vacuum oven at 50 °C. 5.62 g product (0.1 mol) and 24.6 g 1-bromohexane (0.2 mol, Aldrich) were dissolved in 30 ml acetonitrile and refluxed for 10 h. After filtering and washing with diethyl ether, the product was dried in a vacuum oven at 50 °C.

The product was identified as  $[\text{C}_{22}\text{H}_{45}\text{-N}^+(\text{CH}_3)_2\text{-C}_6\text{H}_{12}\text{-N}^+(\text{CH}_3)_2\text{-C}_6\text{H}_{13}]\text{Br}_2$  by solution  $^1\text{H}$  NMR (Bruker Avance instrument 400 MHz). (Fig. 5.1) The reference peak at 7.26 ppm presents the chemical shifts of the solvent  $\text{CDCl}_3$ .<sup>4</sup> Except the reference peak, there are 4 basic types of H present in the ratio of 20:8:48:6. Using the chemical shift charts, the H in the surfactant  $\text{C}_{22-6-6}\text{Br}_2$  can be assigned to the same color peaks in Figure 5.1.

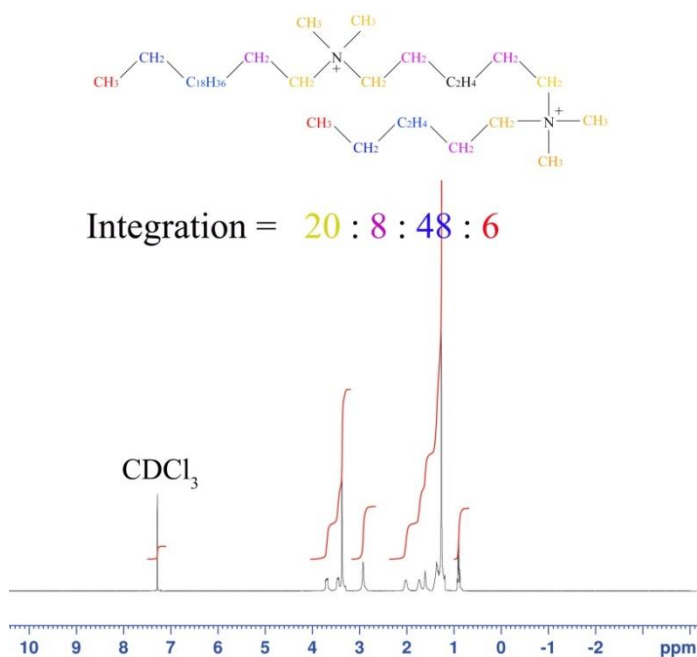


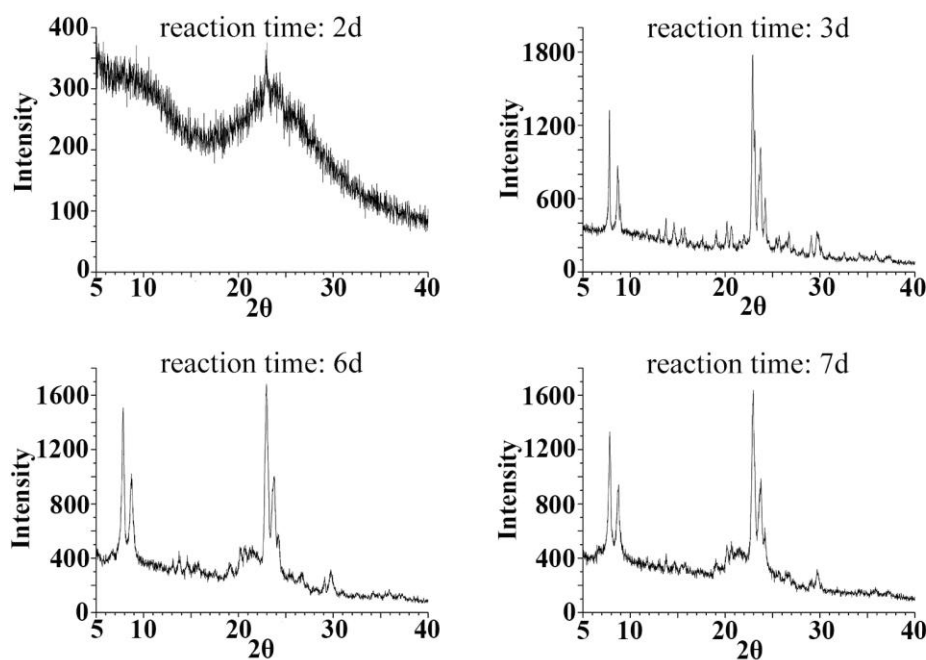
**Figure 5.1:**  $^1\text{H}$  NMR spectrum of the organic surfactant

$[\text{C}_{22}\text{H}_{45}\text{-N}^+(\text{CH}_3)_2\text{-C}_6\text{H}_{12}\text{-N}^+(\text{CH}_3)_2\text{-C}_6\text{H}_{13}]\text{Br}_2$ , which was taken from a  $\text{CDCl}_3$  solution.

The multi-lamellar MFI zeolite nanosheets were prepared by the hydrothermal synthesis procedure follow by the method of Choi *et al.*<sup>3</sup>

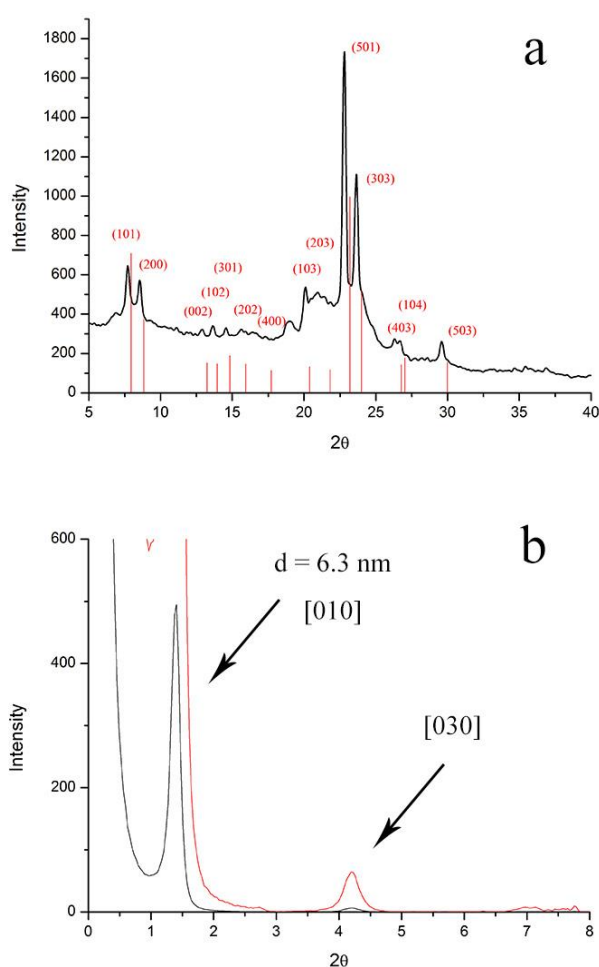
Tetraethylorthosilicate (TEOS, TCI),  $\text{Al}_2(\text{SO}_4)_3 \cdot 18\text{H}_2\text{O}$  (Aldrich), NaOH, organic surfactant ( $\text{C}_{22-6-6}\text{Br}_2$ ),  $\text{H}_2\text{SO}_4$  and water were mixed to obtain a gel composition of  $30\text{Na}_2\text{O} : 1\text{Al}_2\text{O}_3 : 100\text{SiO}_2 : 10\text{C}_{22-6-6}\text{Br}_2 : 18\text{H}_2\text{SO}_4 : 4000\text{H}_2\text{O}$ . The gel was heated in a Teflon-lined autoclave at  $150^\circ\text{C}$  with rotation ( $\sim 60$  rpm) for 3-7 days. The solid product was recovered by filtration with distilled water and dried overnight at  $120^\circ\text{C}$ .

Figure 5.2 shows XRD patterns for the products of as-synthesised multi-lamellar MFI nanosheets, heating for 2d, 3d, 6d, and 7d, respectively. After heating for 2 days, an unknown amorphous phase without indexing peaks was generated. When the reaction time of the MFI nanosheets was beyond 3 days, only the  $h0l$  reflections were sufficiently sharp for indexing. (Fig. 5.2 and 5.3a) The result confirms that the zeolite layers with wide  $a$ - $c$  planes, while the framework thickness along the  $b$ -axis was extremely small. With increasing of the reaction time (from 3d to 7d), the impure peaks (the unindexed peaks from Fig. 5.3a) decreased. This indicates that the multi-lamellar structural order increased by a crystal ripening process that was orthogonal to the nanosheets and along the  $b$ -axis and increase in the  $a$ - $c$  plane area.



**Figure 5.2:** XRD patterns for as-synthesized MFI zeolite nanosheets.

Figure 5.3a shows that the XRD pattern of as-synthesised MFI zeolite nanosheets, heated for 7 days, was compared with the  $h0l$  reflection of MFI framework.<sup>5</sup> The SAXS pattern (Fig. 5.3b) shows two reflections – (010) at  $2\theta=1.4^\circ$  with  $d = 6.3$  nm and the (030) reflection. The absence of the (020) reflection is consistent with a layered structure that oscillates between high and low electron density with nearly equal thickness of each layer.<sup>6</sup> That is, the 6.3 nm repeat is divided into two layers each with thickness ca. 3.15 nm that will correspond to the inorganic component and the intervening organic tails respectively.



**Figure 5.3:** (a) XRD pattern and (b) SAXS pattern of as-synthesised MFI zeolite nanosheets, heating for 7 days.

The SEM images show that the multi-lamellar MFI nanosheets have a plate-like morphology. (see Chapter 3 paper 2 Figs. 3.2-S5-S7)

Fig. 5.4 shows  $^{29}\text{Si}$  MAS spectrum of multi-lamellar MFI zeolites heating for 7 days. The spectrum shows three signals at -102, -108 and -112 ppm that corresponds to  $\text{Q}^3=\text{Si}(\text{OSi})_3(\text{OH})$ ,  $\text{Q}^4(1\text{Al})=\text{Si}(\text{OSi})_3(\text{OAl})$  and  $\text{Q}^4(0\text{Al})=\text{Si}(\text{OSi})_4$  silicon environments. According to the formula

$$(\text{Si}/\text{Al})_{\text{NMR}} = \frac{I_4 + I_3 + I_2 + I_1 + I_0}{I_4 + 0.75I_3 + 0.5I_2 + 0.25I_1} \quad 7$$

Where  $I_n$  is the area of the NMR peak corresponding to the  $\text{Si}(n\text{Al})$  building unit, the Si/Al ratio of the MFI nanosheets is *ca.* 42. The Si/Al ratio for the original preparing solution is *ca.* 50, and is slightly higher than the Si/Al ratio calculated from NMR result.

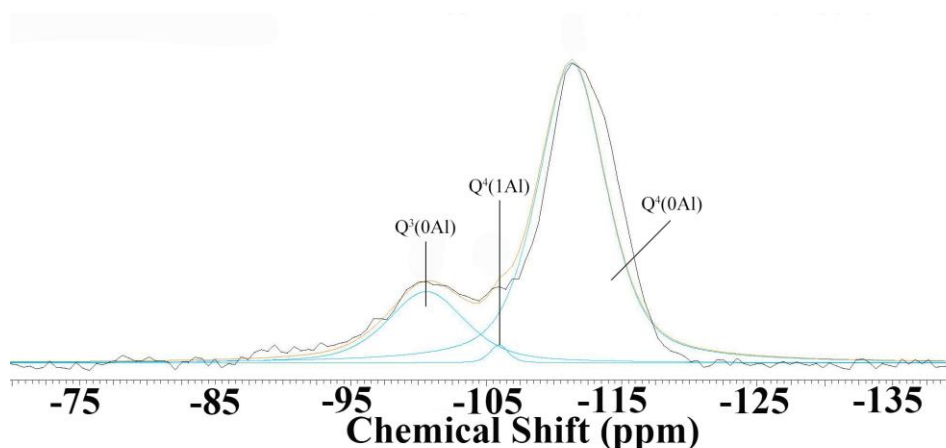


**Figure 5.4:**  $^{29}\text{Si}$  MAS spectrum of as-synthesized MFI zeolite nanosheets, heating for 7 days. The blue line indicate the three peaks at -102, -108, -112, have been find the best fit of the calculated spectrum to the experimental data.

$^{27}\text{Al}$  MAS NMR spectrum is shown in Fig. 5.5. The spectrum shows a strong signal at 56 ppm corresponds to tetrahedral framework Al sites.<sup>8</sup>

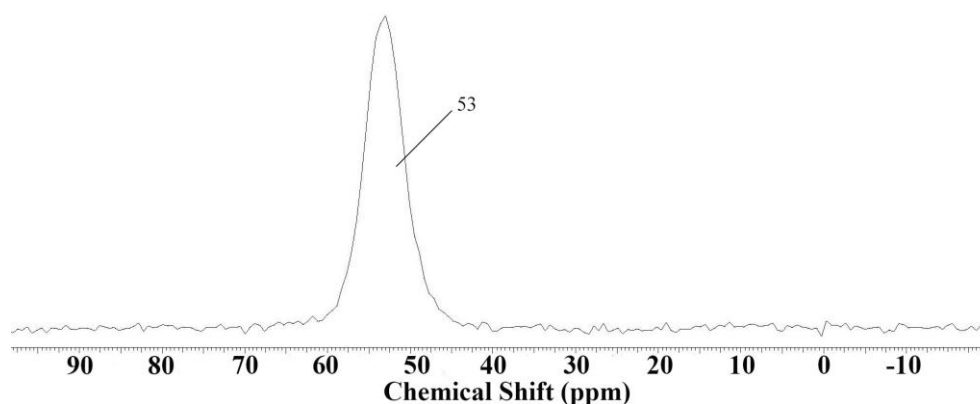


**Figure 5.5:**  $^{27}\text{Al}$  MAS spectrum of as-synthesized MFI zeolite nanosheets, heating for 7 days.

### 5.1.2. Further Growth of Exfoliated MFI Nanosheets

The multi-lamellar zeolite MFI is repeatedly cleaved by the application of a sticky tape resulting in the mechanical exfoliation of zeolite MFI nanosheets with thickness about  $5.3 \pm 0.1$  nm. (see Chapter 3 paper 2) After calcination, the organic template has been removed, the inorganic layers become consistently  $3.1 \pm 0.1$  nm thick, which correspond to 1.5 unit cell along the b-axis ( $b=1.9738$  nm). The experiment and characterization of the exfoliated MFI nanosheets are described in Chapter 3 paper 2. Here, we are focus on further growth section, and the single MFI nanosheets were exfoliated on mica following the same process of paper 2 in Chapter 3.

#### 5.1.2.1. Further Growth Experimental section

Tetraethylorthosilicate (TEOS, TCI), NaOH, organic surfactant ( $C_{22-6-6}Br_2$ ),  $H_2SO_4$  and water were mixed to obtain a reaction solution. The freshly cleaved mica<sup>9</sup> with or without the exfoliated MFI flakes on it was immersed into the reaction solution. The reaction solution was heated in a Teflon-lined autoclave at  $150^\circ C$  for 10-60 minutes. The mica with the product on it was washed with distilled water and dried in  $N_2$ . The complete recipes for tested further growth MFI nanosheets were summarized in Table 5.1.

**Table 5.1:** Recipes of the further growth MFI nanosheets

| Sample name | Seeds <sup>a</sup> | TEOS <sup>b</sup> | Reaction time |
|-------------|--------------------|-------------------|---------------|
| S1          | √                  | √                 | 10 min        |
| S2          | √                  | √                 | 30 min        |
| S3          | √                  | √                 | 1 h           |
| S4          | √                  | x                 | 30 min        |
| S5          | x                  | √                 | 30 min        |
| S6          | x                  | x                 | 30 min        |

<sup>a</sup> “√” represents the procedure that mechanical exfoliates the MFI nanosheets of a freshly cleaved mica, then put the mica with the exfoliated MFI flakes on it into the reaction solution. On the contrary, “x” represents that the reactions do not involve the exfoliated MFI nanosheets, and put the freshly cleaved mica into the reaction solution directly.

<sup>b</sup> The molar composition of the reaction solution was: 60 NaOH:4000 H<sub>2</sub>O:24 H<sub>2</sub>SO<sub>4</sub>:7.5 C<sub>22-6-6</sub>Br<sub>2</sub>:y TEOS. “√” represents that y was 100. “x” represents there was no TEOS in the reaction solution (without silicon source), that is y was 0.

### 5.1.2.2. Atomic Force Microscopy

The thickness of nanosheets has been measured by the *ex-situ* AFM, and all AFM images were obtained by the mode of PeakForce QNM in Air.

The as-synthesized exfoliated MFI flakes on the freshly cleaved mica have been used as seeds for further growth. C<sub>22-6-6</sub>Br<sub>2</sub> has been used as the precursor, and TEOS provide the silicon source for the growth. The molar ratio of the reaction solution shows in Table 5.1.

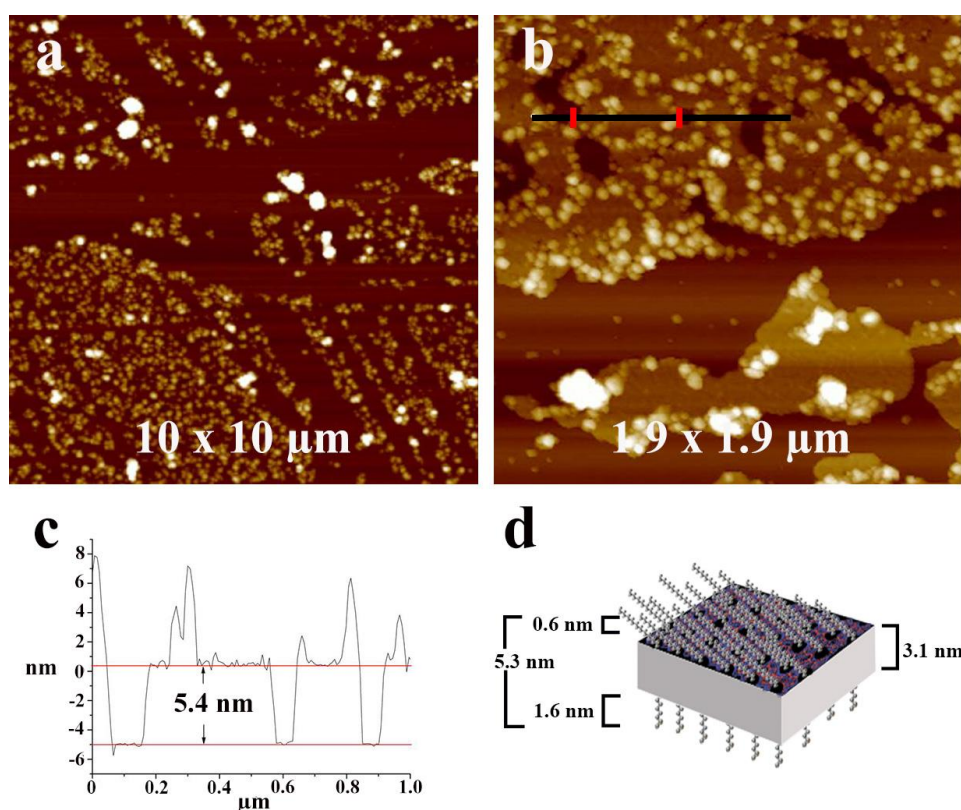


**Figure 5.6:** AFM height images of Sample S1 with size (a) 10 μm, (b) 1.9 μm. The height data of the line highlighted in (b) is plotted in (c), and the schematic representation of single MFI nanosheet after exfoliation shows in (d).

After heating in a Teflon-lined autoclave at 150°C for 10 minutes, the AFM height images of Sample S1 are as shown in Fig. 5.6. The height of the layer was measured along the line highlighted in Fig. 5.6(b), revealing regular  $5.4 \pm 0.1$  nm



height,(Fig. 5.6c) which is approximately equal to the thickness of mechanical exfoliated single MFI nanosheet, that are consistently  $5.3 \pm 0.1$  nm. The schematic representation of mechanical exfoliated single MFI nanosheet is shown in Fig. 5.6(d). The bright contrast features in the height images (Fig. 5.6a-b) correspond to some deposit on the MFI flakes, which could be the second layer or some precipitate from the surfactants.

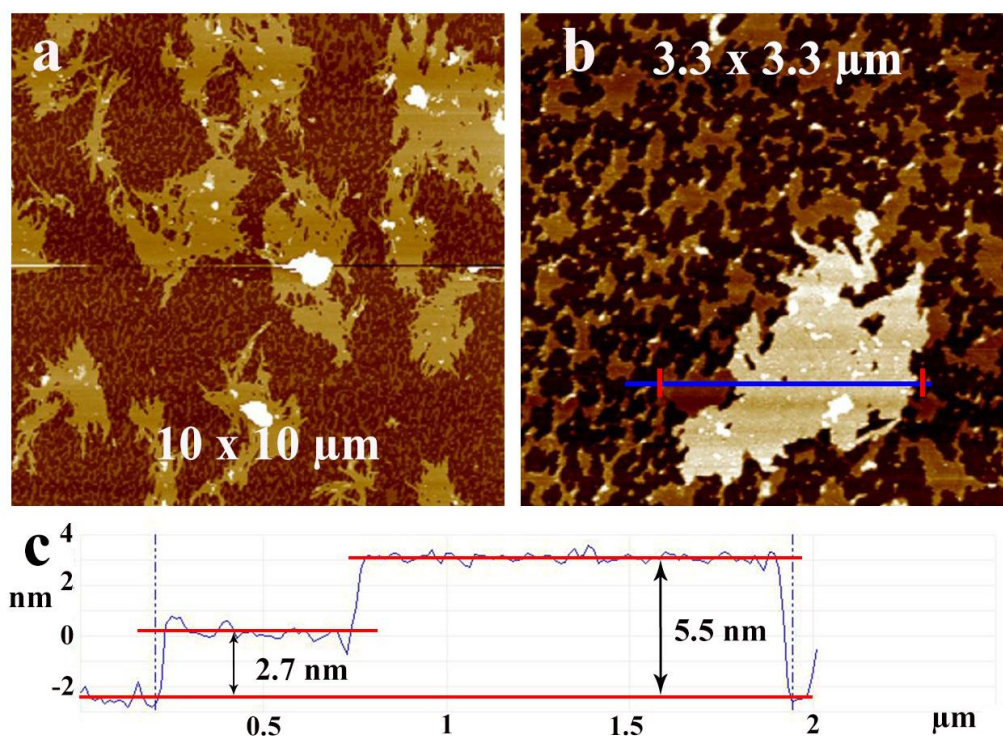


**Figure 5.7:** AFM height images of Sample S2 with size (a)  $10 \mu\text{m}$ , (b)  $3.3 \mu\text{m}$ . The height data of the line highlighted in (b) is plotted in (c).

Fig. 5.7 shows the AFM height images of Sample S2, after heating for 30 minutes. The height data of the line highlighted in Fig. 5.7(b) is plotted in Fig. 5.7(c). The thickness of the first layer is consistently  $2.7 \pm 0.1$  nm, and the thickness of the second layer becomes consistently  $5.5 \pm 0.1$  nm.

Fig. 5.8 shows the AFM height images of Sample S3, after heating for 60 minutes. Fig. 5.8 (b,d) are the height histogram of Fig. 5.8 (a,c), respectively. The first peak represents the height of the substrate mica, the second peak represents the height of the first layer, and in Fig. 5.8d the third peak represents the height of the second layer, which corresponds to the white layer on the top left corner in Fig.

5.8a. According to the height histogram (Fig. 5.8b), the thickness of the first layer is  $5.6 \pm 0.1$  nm, and the thickness of the second layer become  $11.5 \pm 0.1$  nm. The thickness of the layer in Fig. 5.8c is  $5.9 \pm 0.1$  nm. Some small rod-like crystals with about 30 nm thickness and 150-300 nm length, have appeared and shown as the brightest contrast features in Fig. 5.8c.

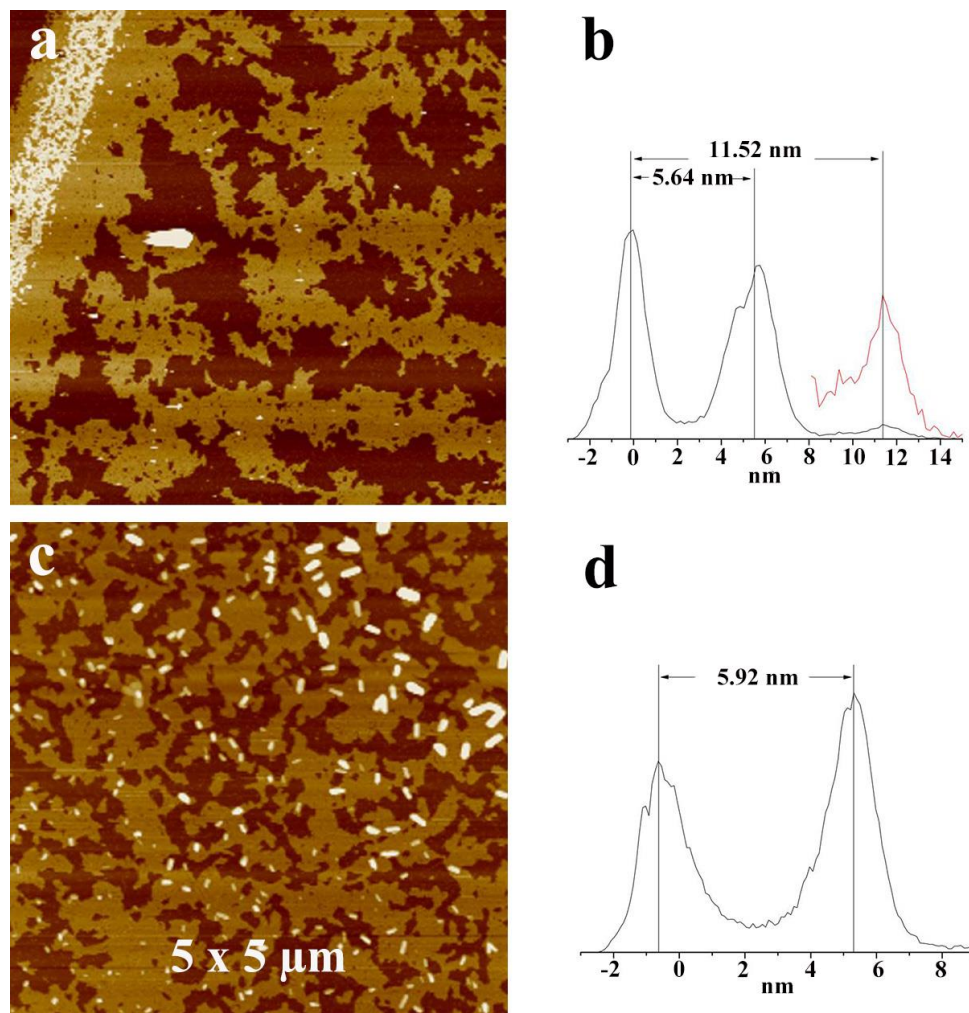


**Figure 5.8:** AFM height images of Sample S3 with size (a) 10 μm, (c) 5 μm. (b) and (d) are the associated height histograms of (a) and (c), respectively.

Comparing the AFM results (Figs. 5.6-8), the nanosheets continued to grow with the reaction time increasing from 10 to 60 minutes. Fig. 5.3b shows the d-spacing of the [010] facet is 6.3 nm. That means the basal plane spacing of the original single MFI nanosheet before calcination is 6.3 nm. In Chapter 3 paper 2 we suggest that before calcination the template molecules are essentially intact on both sides of the inorganic layer, however, it is probable that the organic template

molecules are no longer in their original configuration. Fig. 5.6d is the most likely arrangement after exfoliation where the nanosheet is 5.3 nm thick. The thickness of the further growth nanosheets is about 5.4-5.9 nm (Sample S1-3). It is close to the thickness of the exfoliated flakes (*ca.* 5.3 nm), and smaller than the thickness of the original single MFI nanosheet (*ca.* 6.3 nm). Therefore, we hypothesized that the uniform MFI nanosheets can continue to grow by using the exfoliated MFI flakes as seed,  $C_{22-6-6}Br_2$  as template and TEOS as the silicon source.

After heating for 10 minutes (Fig. 5.6), there were some deposits with 0-10 nm thickness aggregating on the layers (or island-like domains). After heating for 30 minutes (Fig. 5.7), the number of deposits on the layers decreased, and many small islands with size smaller than 200 nm appeared. Fig. 5.7(b,c) show these islands that have a thickness  $2.7 \pm 0.1$  nm. After heating for 60 minutes (Fig. 5.8), the small islands with thickness *ca.* 2.7 nm have not been found by AFM measurement. We surmised that the islands with 2.7 nm thickness could be the interphase by the self-assembly of organic templates, during the growth of the nanosheets. Fig. 5.8a shows the second layer with thickness  $11.5 \pm 0.1$  nm, i.e. about twice the thick of the first layer ( $5.6 \pm 0.1$  nm).

In conclusion from the experiments (Sample S1-S3), we suggest that the layers with thickness about 5.5 nm continue to grow by using the exfoliated MFI flakes as seeds (5.3 nm), and  $C_{22-6-6}Br_2$  as the template, and TEOS as the silicon source. The larger and flatter layer formed by increasing the reaction time, and after 60 minutes, the second layer aggregated on the first layer.

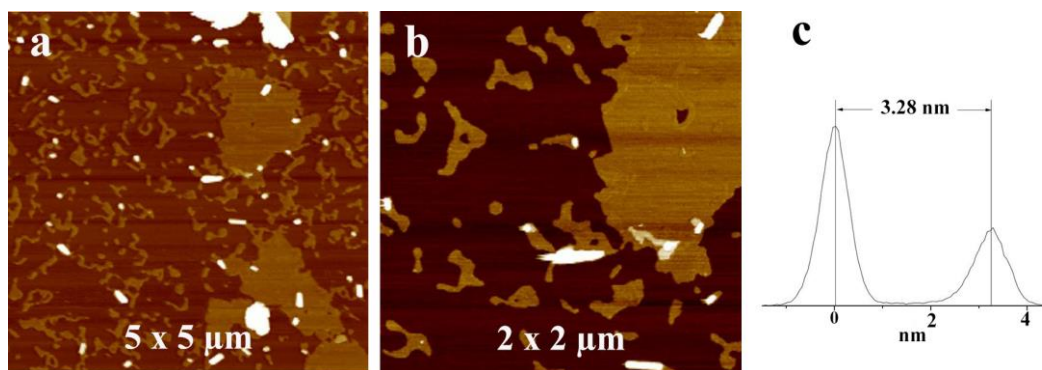


**Figure 5.9:** AFM height height images of Sample S4 with size (a) 5  $\mu$ m, (b) 2  $\mu$ m. (c) is the associated height histogram of (b).

$C_{22-6-6}Br_2$  has been used as the precursor, and the reaction solution does not involve any silicon source. The as-synthesized exfoliated MFI flakes have been used as seeds for further growth on the freshly cleaved mica. The molar ratio of the reaction solution is shown in Table 5.1. After heating in a Teflon-lined autoclave at 150°C for 30 minutes, the AFM images of Sample S4 are shown in Fig. 5.9. The bright contrast features in the height images correspond to some precipitation from the solution. The height histogram of Fig. 5.9b shown in Fig. 5.9c, reveals regular  $3.3 \pm 0.1$  nm spacing. (Fig. 5.9c)

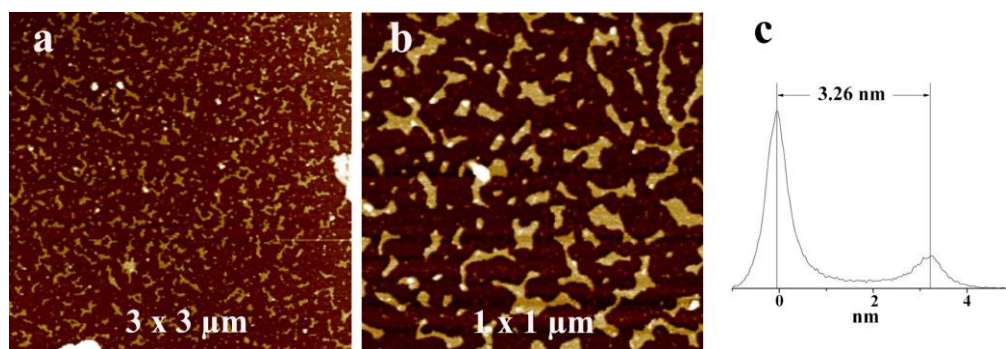


**Figure 5.10:** AFM height images of Sample S5 with size (a) 3  $\mu$ m, (b) 1  $\mu$ m. (c) is the associated height histograms of (b).

The freshly cleaved mica without exfoliated MFI flakes on it has been immersed into the reaction solution. The molar ratio of the reaction solution is shown in Table 5.1. After heating in a Teflon-lined autoclave at 150°C for 30 minutes, the AFM images of Sample S5 are shown in Fig. 5.10. The height histogram of Fig. 5.10b shown in Fig. 5.10c reveals regular  $3.3 \pm 0.1$  nm spacing.

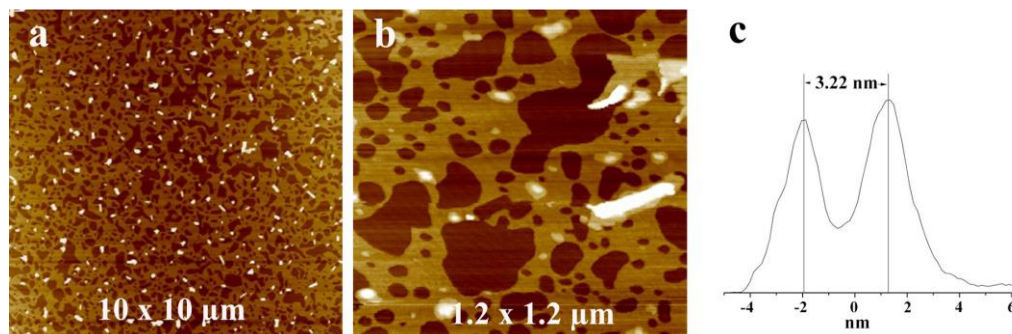


**Figure 5.11:** AFM height images of Sample S6 with size (a) 10  $\mu$ m, (b) 1.2  $\mu$ m. (c) is the associated height histograms of (b).

The freshly cleaved mica without exfoliated MFI flakes on it has been immersed into the reaction solution without any silicon source. The molar ratio of the reaction solution is shown in Table 5.1. After heating in a Teflon-lined autoclave at 150°C for 30 minutes, the AFM images of Sample S6 are shown in Fig. 5.11. The height histogram of Fig. 5.11b is shown in Fig. 5.11c, and reveals regular  $3.2 \pm 0.1$  nm spacing.

In conclusion of the experiments (Sample S4-S6), we removed these growing conditions: exfoliated MFI flakes as seeds (Sample S4), the silicon source in the reaction solution (Sample S5), and both the seed and the silicon source (Sample S6), respectively. Layers with thickness consistently  $3.2 \pm 0.1$  nm formed on the substrate mica, which could be the self-assembling of the organic surfactant  $C_{22-6-6}Br_2$ .

### 5.1.3. Future Work

Further work in this direction will enable to generate the large-scale ultra-thin zeolite MFI membrane. The immediate concern is to use TEM and GISAXS to provide more structure information of these further growth MFI layers.

## 5.2. Pt-containing Aluminosilicate Nanowires

One of the important applications of noble metal nanoparticles is their use as heterogeneous catalysts for various oxidation and reduction reaction. Encapsulating noble metals within the channels or cavities of zeolites has already drawn much attention because the well-defined zeolite structure is able to constrain the metal nanoparticle (NPs) aggregation size and enhance the diversity and activity for catalysis.<sup>10</sup> Zeolite MFI requires high synthesis temperatures (>150 °C) that decompose the ligand-stabilized precursor  $[\text{Pt}(\text{NH}_3)_4](\text{NO}_3)_2$ . Thus, the Pt particles precipitate before the zeolite crystallises, and it is inaccessible to encapsulate the Pt clusters within MFI via direct hydrothermal synthesis. Fluoride has been reported as a mineralizing agent to prevent the precipitation of the metal precursor during hydrothermal synthesis of zeolites and increase encapsulation selectivity.<sup>11</sup> Therefore, we seek here to use organic surfactant ( $\text{C}_{22-6-6}\text{Br}_2$ ) and  $[\text{Pt}(\text{NH}_3)_4](\text{NO}_3)_2$  as the structure and metal precursor to form Pt-containing MFI zeolites; and use  $\text{F}^-$  to inhibit the premature precipitation of Pt precursors. After involving  $\text{F}^-$ , the Pt-containing aluminosilicate nanowire structures were generated, and the resulting product has been characterized by XRD, SEM,  $\text{N}_2$  adsorption and TEM.

### 5.2.1. Preparation of Pt-containing aluminosilicate Nanowires

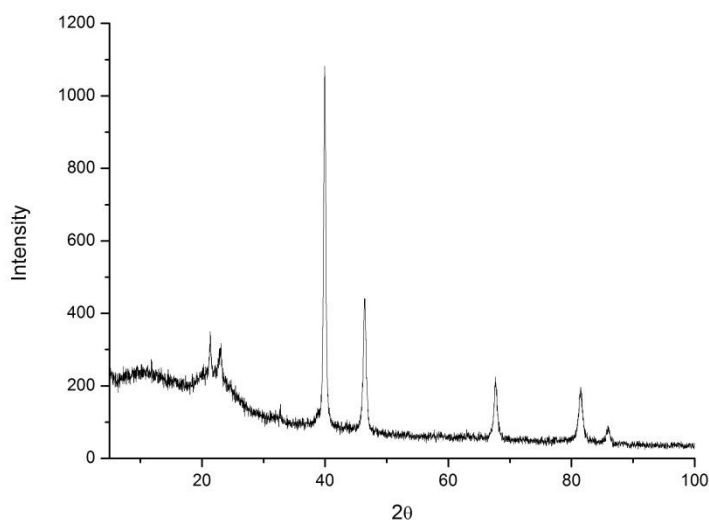
The Pt-containing aluminosilicate nanowires were synthesized by direct hydrothermal synthesis procedure that is similar to the multi-lamellar MFI zeolite nanosheets. (see Chapter 5.1.1.) Tetraethylorthosilicate (TEOS, TCI),  $\text{Al}_2(\text{SO}_4)_3 \cdot 18\text{H}_2\text{O}$  (Aldrich), NaOH, organic surfactant ( $\text{C}_{22-6-6}\text{Br}_2$ ),  $\text{H}_2\text{SO}_4$ ,  $\text{NH}_4\text{F}$ ,  $[\text{Pt}(\text{NH}_3)_4](\text{NO}_3)_2$  (Aldrich) and water were mixed to obtain a gel composition of  $30\text{Na}_2\text{O}: 1\text{Al}_2\text{O}_3: 100\text{SiO}_2: 10\text{C}_{22-6-6}\text{Br}_2: 18\text{H}_2\text{SO}_4: 120\text{NH}_4\text{F}: 5: [\text{Pt}(\text{NH}_3)_4](\text{NO}_3)_2: 3000\text{H}_2\text{O}$ . The gel was heated in a Teflon-lined autoclave at 150°C with rotation (~60 rpm) for 9 days. The solid product was recovered by filtration with distilled water and dried overnight at 120°C. These samples were treated in flowing air and

heated to 350 °C at 15 °C/min and held for 2 h, and reduced in flowing H<sub>2</sub>/N<sub>2</sub> and heated to 300 °C at 15 °C/min and held for 2 h. The resulting samples were calcined at 550 °C in air for 4h to remove the templates.

## 5.2.2. Results and Discussion

### 5.2.2.1. XRD analysis of as-synthesized Pt-containing nanowires

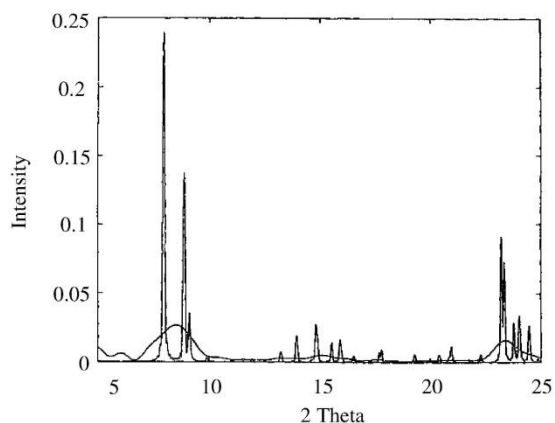
The XRD pattern of as-synthesized Pt-containing aluminosilicate nanowires is shown in Figure 5.12. The five well-resolved XRD reflections at 40.0°, 46.5°, 67.8°, 81.6°, and 86.0° correspond to the (111), (200), (220), (311) and (222) Pt facets, respectively, that indicate a good crystallization of Pt nanoparticles.<sup>12</sup> There is a bump at 6.75-15.5°, and two peaks at 21.36°, 22.98°. According to the Bragg's law  $\lambda = 2d \sin\theta$  ( $\lambda = 0.154184 \text{ nm}$ ),  $d_{21.36}=0.42 \text{ nm}$ ,  $d_{22.98}=0.39 \text{ nm}$ . Therefore, the characteristic two peaks of MFI structure at 21.36°, 22.98° corresponding to the (501) and (303) reflections, are sufficiently intense to be observed in the XRD pattern.



**Figure 5.12:** XRD pattern of as-synthesized Pt-containing nanowires.

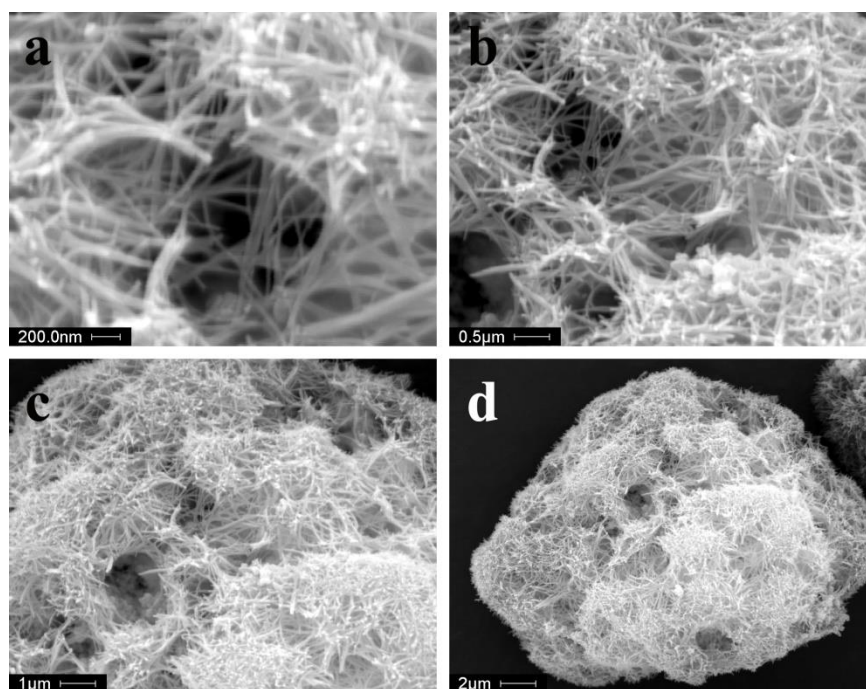
Schlenker *et al.* indicated that there is a concentration limit for all materials diffraction pattern.<sup>13</sup> When the concentration is below the limit, the diffraction pattern cannot normally be observed. Fig. 5.13 shows the theoretical pattern for

ZSM-5 crystals whose edges length is 4 unit cells. These materials would be indistinguishable from the amorphous pattern. Therefore, the reason that we did not observe an XRD pattern for MFI zeolites could be due to the very small size of the MFI-related component. It is also possible because the quantity of the samples that we obtained was below the detection limit.



**Figure 5.13:** Computed XRD patterns for ultra-small ZSM-5 zeolite crystals with edges 4 unit cells in length.<sup>13</sup>

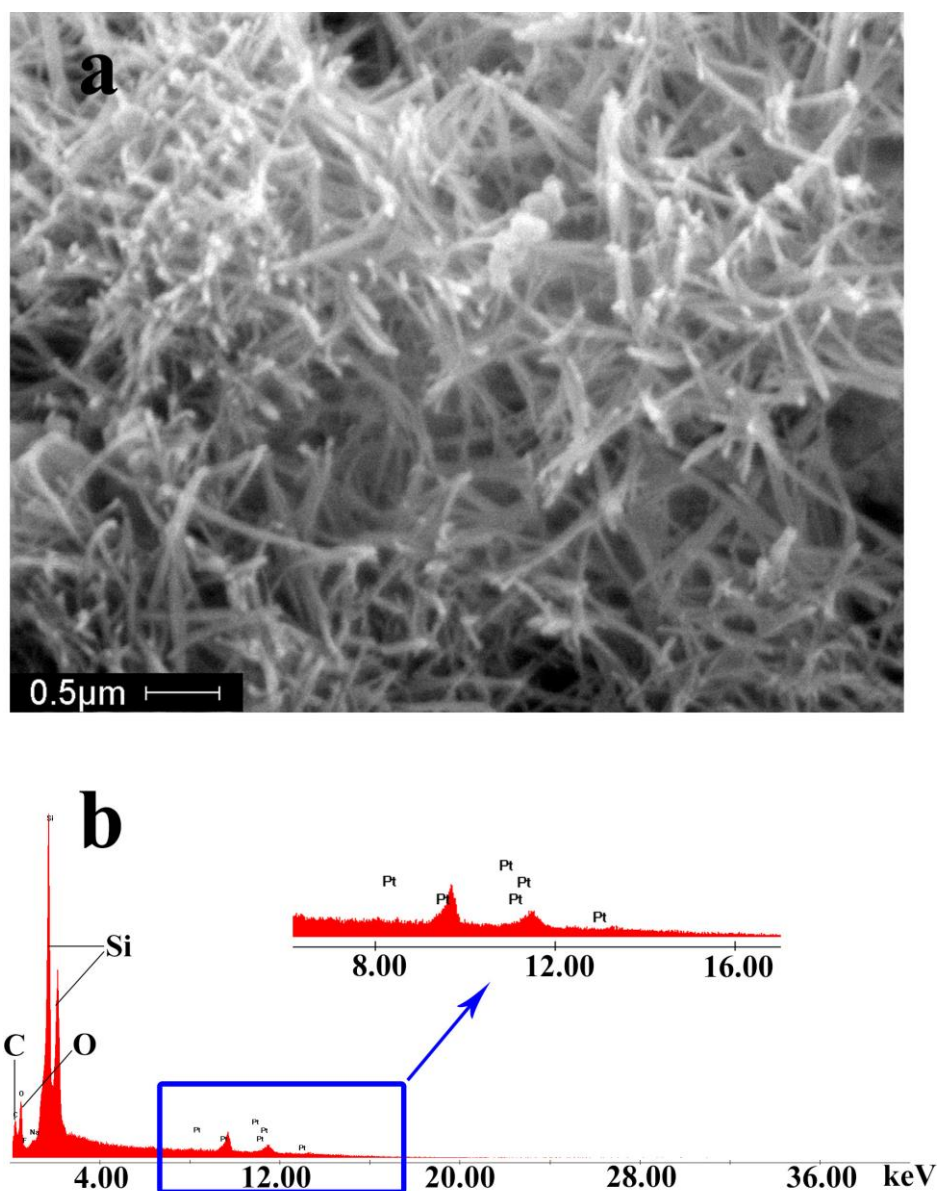
#### 5.2.2.2. SEM analysis of as-synthesized Pt-containing nanowires



**Figure 5.14:** SEM images of as-synthesized Pt-containing nanowires.



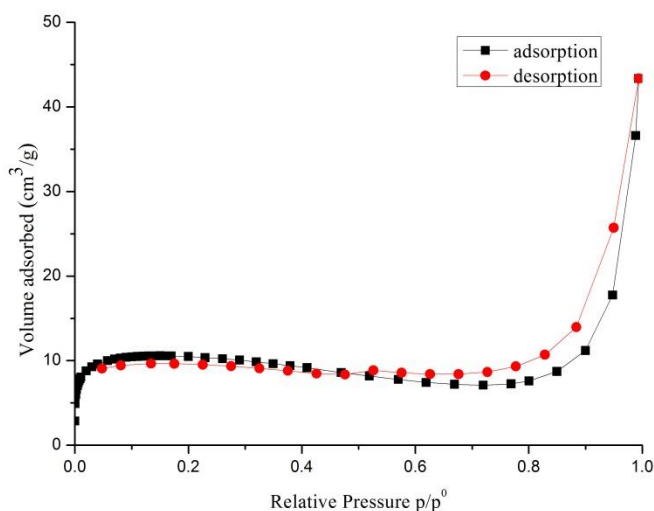
The SEM images show that the Pt-containing zeolite has a wire-like morphology. (Fig. 5.14) Energy dispersive X-ray spectrometry (EDX) measurements performed in tandem with the SEM has been applied to define the chemical composition of the sample. Fig. 5.15b proves that the samples are indeed some Pt containing materials, and the expected signals for additional elements C, O, Si are also present. The Si and O compose the crystal structure, and the C is readily explained as being present due to the carbon adhesive tabs have been used for attaching the samples on the SEM specimen stubs.



**Figure 5.15:** (a) SEM image of as-synthesized Pt-containing nanowires, and (b) EDX measurement performed in tandem with (a).

5.2.2.3. N<sub>2</sub> adsorption isotherm of Pt-containing nanowires

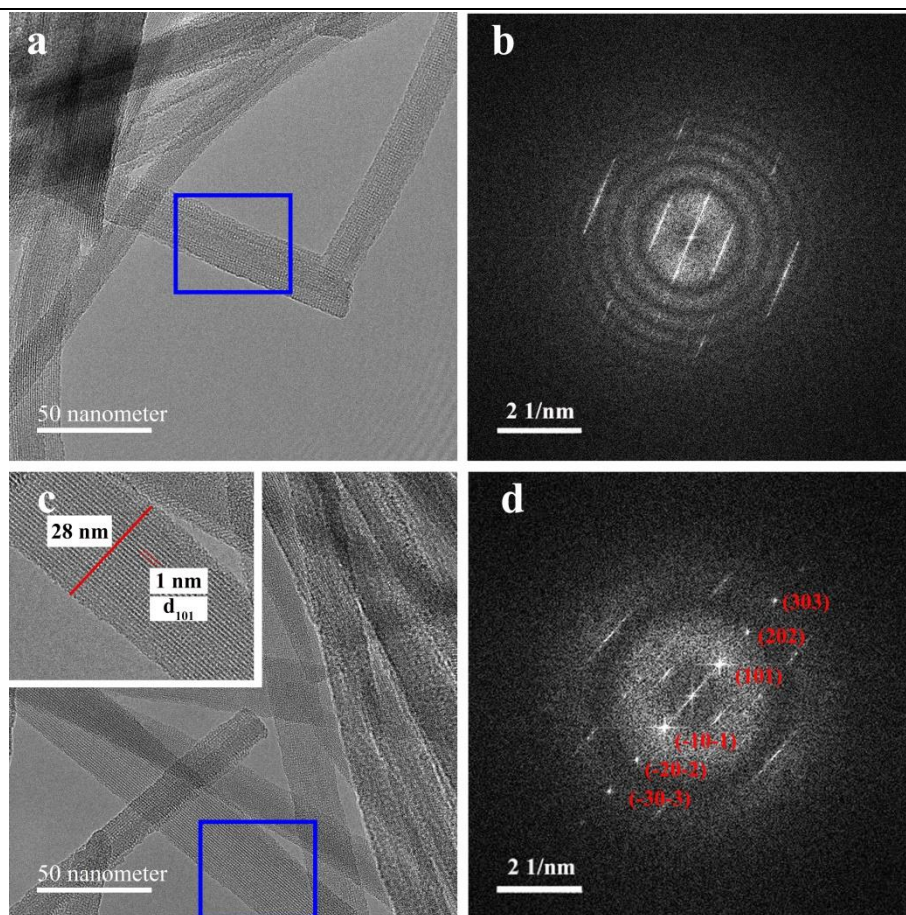
The nitrogen adsorption experiment was conducted to determine the properties of the Pt-containing nanowires, and the result is shown in Fig. 5.16. The hysteresis loop at  $p/p_0 > 0.4$  in the sorption isotherms confirms the formation of mesopores. The mesopore size determined by BJH method,<sup>14</sup> and the BJH adsorption average pore is 35 nm. Therefore, the Pt-containing nanowires with mesopores are successfully formed.



**Figure 5.16:** N<sub>2</sub> adsorption isotherm of Pt-containing nanowires.

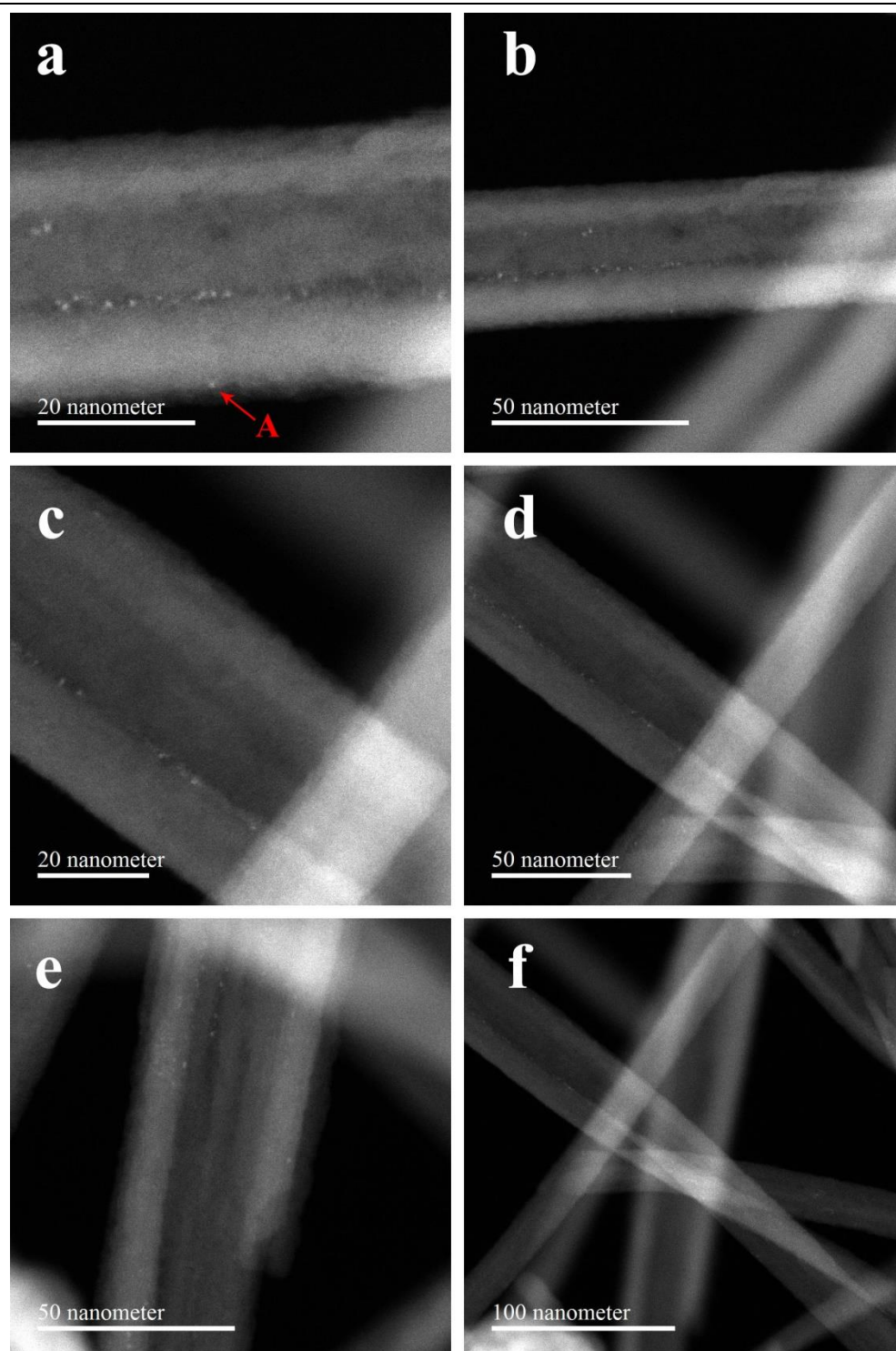
## 5.2.2.4. TEM analysis of Pt-containing nanowires

Fig. 5.17 shows high-resolution TEM images of Pt-containing nanowires after reduction and calcination to remove the templates. Fig. 5.17b and d are the FFT of the blue region in Fig. 5.17(a and c). Fig. 5.17d shows 6 sharp spots, which can be used to confirmed the crystallinity of the structure. The d spacing of the nanowires was calculated from the indexing of the selected FFT area (Fig. 5.17d).  $d_{101}=1.0$  nm,  $d_{202}=0.5$  nm, and  $d_{303}=0.34$  nm. Fig. 5.17c shows the uniform wires with 1 nm size which are parallel to the TEM grids, and each nanotube is about 28 nm. Since the nanowires and the nanotube are not perfectly straight, it would be difficult to present the indices from the HRTEM image with atomic-level accuracy.



**Figure 5.17:** (a,c)TEM images of Pt-containing nanowires. The FFT of the blue region in (a,c) is shown in (b,d), respectively.

In order to study the small nanoparticles that consist of heavy elements HAADF-STEM (high-angle annular dark field scanning transmission electron microscopy) was used to characterize the Pt-containing nanowires.<sup>15</sup> The HAADF-STEM images of Pt-containing nanowires are shown in Fig. 5.18, and Figs. 5.18(a,c,e) are the zoom in images of (b,d,f), respectively. These images confirm the Pt-containing nanowires have a tube-like morphology. The Pt NPs are identified in the HAADF-STEM images as the bright contrast features. (Fig. 5.18 and Fig. 5.20) The Pt NPs with *ca.* 0.5 nm located inside the tube wall (Fig. 5.18), but few of them have been measured outside the tube wall, for example, the particle A in Fig. 5.18a. The diameters of the tube which have been revealed in Figs. 5.18(a,c,e) are 33 nm, 45 nm and 46 nm, respectively. The diameter of the Pt-containing nanowires differed from place to place.



**Figure 5.18:** HAADF-STEM images of Pt-containing nanowires.

The TEM images of the pockmarked flakes with *ca.* 11 nm holes have been observed in Fig. 5.19, and the dark contrast features represent the Pt NPs. Each pocket contains one Pt nanoparticle. The size of the Pt nanoparticle is about 1-2 nm. Fig. 5.20 shows the HAADF-STEM images of the pockmarked flakes.

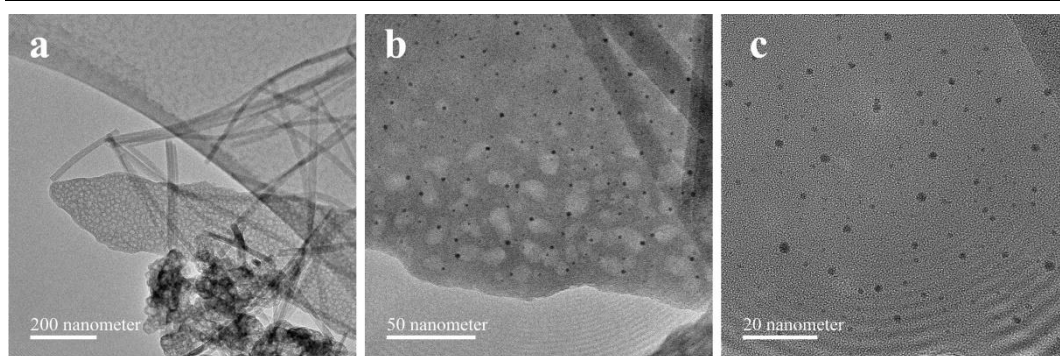


**Figure 5.19:** TEM images of the pockmarked flakes.

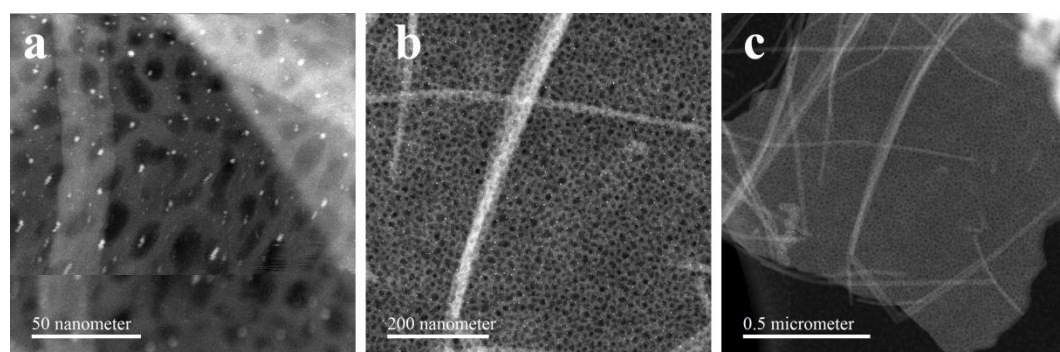


**Figure 5.20:** HAADF-STEM images of the pockmarked flakes.

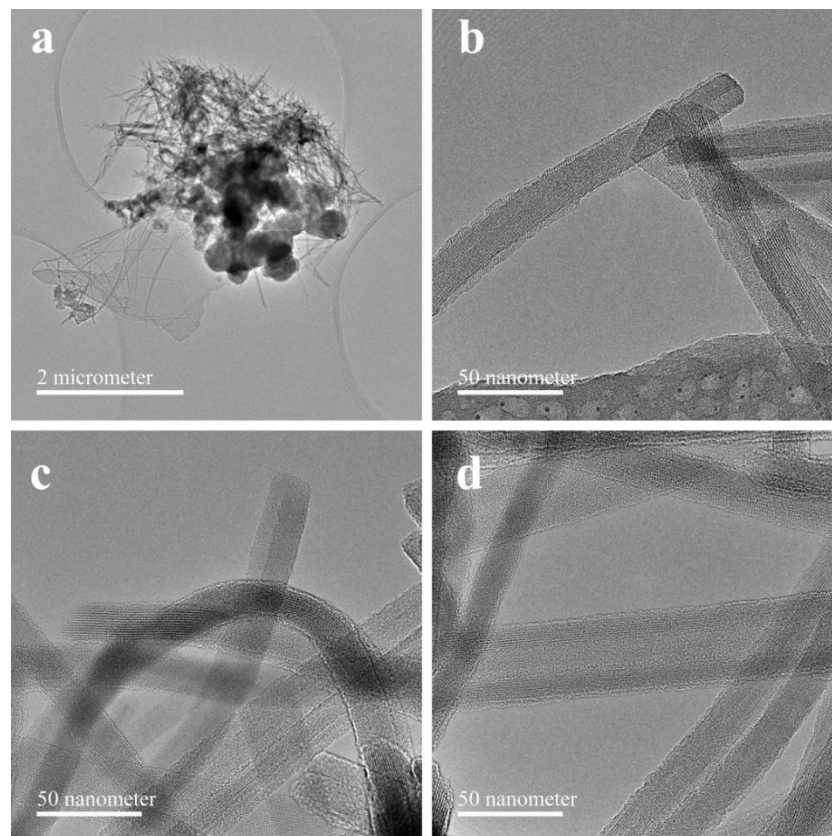


**Figure 5.21:** TEM images of Pt-containing nanowires.

Fig. 5.21a shows a low-magnification TEM image of Pt-containing nanowires. Figs. 5.21(b-d) show the Pt-containing nanowires with different diameter are bended in varying degrees.

### 5.2.3. Future Work

In summary, we have use organic surfactant ( $C_{22-6-6}Br_2$ ) and  $[Pt(NH_3)_4](NO_3)_2$  as the structure and metal precursor to form Pt-containing aluminosilicate nanowires; and use  $F^-$  to inhibit the premature precipitation of Pt precursors. After involving  $F^-$ , the Pt-containing nanowires were generated. The further work in this direction will be focus on the application of these Pt-containing nanowires.

### 5.3. Reference

- (1) Jeon, M. Y.; Kim, D.; Kumar, P.; Lee, P. S.; Rangnekar, N.; Bai, P.; Shete, M.; Elyassi, B.; Lee, H. S.; Narasimharao, K.; Basahel, S. N.; Al-Thabaiti, S.; Xu, W.; Cho, H. J.; Fetisov, E. O.; Thyagarajan, R.; DeJaco, R. F.; Fan, W.; Mkhoyan, K. A.; Siepmann, J. I.; Tsapatsis, M. Ultra-Selective High-Flux Membranes from Directly Synthesized Zeolite Nanosheets. *Nature* **2017**, 543, 690-694.
- (2) Varoon, K.; Zhang, X.; Elyassi, B.; Brewer, D. D.; Gettel, M.; Kumar, S.; Lee, J. A.; Maheshwari, S.; Mittal, A.; Sung, C.-Y.; Cococcioni, M.; Francis, L. F.; McCormick, A. V.; Mkhoyan, K. A.; Tsapatsis, M. Dispersible Exfoliated Zeolite Nanosheets and Their Application as a Selective Membrane. *Science* **2011**, 334, 72-75.
- (3) Choi, M.; Na, K.; Kim, J.; Sakamoto, Y.; Terasaki, O.; Ryoo, R. Stable Single-Unit-Cell Nanosheets of Zeolite MFI as Active and Long-Lived Catalysts. *Nature* **2009**, 461, 246-249.
- (4) Gottlieb, H. E.; Kotlyar, V.; Nudelman, A. NMR Chemical Shifts of Common Laboratory Solvents as Trace Impurities. *The Journal of Organic Chemistry* **1997**, 62, 7512-7515.
- (5) Database of Zeolite Structures. <http://www.iza-structure.org/databases/>
- (6) Lund, K.; Muroyama, N.; Terasaki, O. Accidental Extinction in Powder XRD Intensity of Porous Crystals: Mesoporous Carbon Crystal CMK-5 and Layered Zeolite-Nanosheets. *Microporous and Mesoporous Materials* **2010**, 128, 71-77.
- (7) Kim, J.; Kim, W.; Seo, Y.; Kim, J.-C.; Ryoo, R. n-Heptane Hydroisomerization over Pt/MFI Zeolite Nanosheets: Effects of Zeolite Crystal Thickness and Platinum Location. *Journal of Catalysis* **2013**, 301, 187-197.
- (8) Wu, L.; Magusin, P. C. M. M.; Degirmenci, V.; Li, M.; Almutairi, S. M. T.; Zhu, X.; Mezari, B.; Hensen, E. J. M. Acidic Properties of Nanolayered ZSM-5 Zeolites. *Microporous and Mesoporous Materials* **2014**, 189, 144-157.
- (9) Nagahara, L. A.; Hashimoto, K.; Fujishima, A.; Snowden - Ifft, D.; Price, P. B. Mica Etch Pits as a Height Calibration Source for Atomic Force Microscopy. *Journal of Vacuum Science & Technology B* **1994**, 12, 1694-1697.
- (10) Farrusseng, D.; Tuel, A. Perspectives on Zeolite-Encapsulated Metal Nanoparticles and Their

---

Applications in Catalysis. *New Journal of Chemistry* **2016**, 40, 3933-3949.

(11) Goel, S.; Zones, S. I.; Iglesia, E. Encapsulation of Metal Clusters within MFI via Interzeolite Transformations and Direct Hydrothermal Syntheses and Catalytic Consequences of Their Confinement. *Journal of the American Chemical Society* **2014**, 136, 15280-15290.

(12) Du, S.; Lu, Y.; Malladi, S. K.; Xu, Q.; Steinberger-Wilckens, R. A Simple Approach for PtNi-MWCNT Hybrid Nanostructures as High Performance Electrocatalysts for the Oxygen Reduction Reaction. *Journal of Materials Chemistry A* **2014**, 2, 692-698.

(13) Schlenker, J. L.; Peterson, B. K. Computed X-ray Powder Diffraction Patterns for Ultrasmall Zeolite Crystals. *Journal Of Applied Crystallography* **1996**, 29, 178-185.

(14) Barrett, E. P.; Joyner, L. G.; Halenda, P. P. The Determination of Pore Volume and Area Distributions in Porous Substances. I. Computations from Nitrogen Isotherms. *Journal of the American Chemical Society* **1951**, 73, 373-380.

(15) Girleanu, M.; Lopes Silva, S.; Ihiawakrim, D.; Chaumonnot, A.; Bonduelle-Skrzypczak, A.; Lefebvre, F.; Dufaud, V.; Gay, A.-S.; Ersen, O. HAADF-STEM High-Resolution Study of Nanometric MoS<sub>2</sub> inside Mesoporous SBA-15. *Microporous and Mesoporous Materials* **2015**, 217, 190-195.

---

## **Chapter 6 Conclusions and Future Work**

---



## 6.1. Conclusion

The aim of this project was to synthesise two different categories of thin nanoporous films (mesostructured films, and single zeolite nanosheet) in two different ways. From this project, we can conclude that:

(I) Four different mesoporous silicas powders with good regularities, MCM-41, MCM-48, SBA-15, SBA-16, have been prepared. The structures are calculated from the diffraction intensities, which are collected from the SAXS patterns of the samples, and be confirmed successfully as reported in the literature. The different morphology have been obtained depending on synthesis conditions and been examined and analyzed by SEM. The specific surface area, pore volume, and pore size distribution as well as the surface properties have been determined by N<sub>2</sub> adsorption. Two different structure mesoporous silicas thin films, SBA-16 with symmetry  $Im\bar{3}m$ , MCM-41 with symmetry  $P6mm$ , have been prepared by dip-coating. The structures have been confirmed by the GISAXS patterns of the samples. The molecular resolution AFM images of the thin film surface have been obtained by using AFM operating by Peak Force Tapping Mode in the liquid. The molecular defects and structural imperfections have been investigated by AFM.

(II) We synthesized mesostructured films at mica-soluton in acidic surfactant CTAB solution. The mesostructured films with cylindrical structures can be directly visualization by *in-situ* AFM. The cylinders are oriented parallel to the mica-solution interface and exhibited mesostructure with spacing 5.1 to 5.5 nm, did not vary with the concentration of surfactant CTAB and acid HCl. *In-situ* AFM also can be used to track the structure transformation process of the surfactant self-assembly on mica and reaction with the inorganic precursor after introducing TEOS. This valuable information at the molecular level is useful for developing architectural design strategies, and also provides important experimental support to the theory or model of interfaces and colloids science.

(III) In order to investigate whether it is possible to produce two-dimensional

nanoporous structures *via* a process that does not involve any chemical intervention and, thereby, is potentially applicable to a wide variety of structures with different chemical makeup, we have used a method similar to the original production of graphene from graphite whereby a solid is repeatedly cleaved by the application of a sticky tape. We have successfully produced three very different structure (UTL, MWW, and MFI) single nanosheet by the mechanical exfoliation. AFM and TEM have been used to confirm the thickness and structure of these single nanosheets.

(IV) Platinum nano-clusters are successfully encapsulated within exfoliated zeolite MFI nanosheets with 3 nm thickness (1.5 unit cells of each nanosheet along b-axis) by ion-exchange from aqueous solution of  $\text{Pt}(\text{NH}_3)_4][\text{NO}_3)_2$ . Simulation suggests that the Pt clusters are located in both the straight channels and the sinusoidal channels of the MFI structure. Moreover, the HAADF-STEM images show that the encapsulated Pt clusters size (~0.99 to 1.65 nm) within the exfoliated MFI nanosheets was followed by an Ostwald ripening process.

(V) Because of the property of the mechanically as-synthesised exfoliated MFI nanosheets that is the long hydrocarbon chains are essentially intact on both sides of the inorganic layer, and can prevent thickening of the zeolite MFI nanosheets along b-axis, we use the mechanically exfoliated MFI as seeds for further growth. The layers with thickness about 5.5 nm have been successfully formed on mica surface.

(VI) We successfully generated the Pt-containing MFI nanowires by using organic surfactant ( $\text{C}_{22-6-6}\text{Br}_2$ ) and  $[\text{Pt}(\text{NH}_3)_4][\text{NO}_3)_2$  as the structure and metal precursor,  $\text{F}^-$  to inhibit the premature precipitation of Pt precursors. HAADF-STEM images show the Pt-containing MFI nanowires have a tube-like morphology, and the Pt NPs with *ca.* 0.5 nm are located inside the tube wall.

## 6.2. Future Work

For the future, improving the resolution of the AFM image of the thin film into atomic resolution would be useful. In order to improve the ability to obtain high-resolution images by the AFM, the four artifact sources should be controlled: 1. noise (all source system including: building noise, deflection noise, positioning noise, *etc.*); 2. interaction localization (including tip geometry, *etc.*); 3. drift (thermal and creep); 4. contamination that can hide lattice.

Moreover, in order to confirm the structure of further growth nanosheets by using exfoliated MFI flakes as seeds, TEM and GISAXS would be used to provide more structure information. However, it would be important to find out a method to transfer the growth layer to the TEM grids.

Finally, because of the important applications of noble metal nanoparticles is their use as heterogeneous catalysts for various oxidation and reduction reaction., more catalyst testing would be useful to broaden the application of these Pt-containing MFI nanowires.

---

## **Appendix: List of conference presentations**

---

### Poster Presentations

1. Organisation in mesoporous thin films studied by atomic force microscopy, **BZA 37th Annual Meeting**, University of Glasgow, April 2014
2. Mechanical exfoliation of nanoporous materials, **BZA 39th Annual Meeting**, University of Bath, March 2016
3. Mechanical exfoliation of nanoporous materials, **18th IZC**, Rio de Janeiro, June 2016